UNIVERSITÀ
DEGLI STUDI
DI PADOVA

Sede Amministrativa: Università degli Studi di Padova

Dipartimento di Ingegneria Industriale

Corso di Dottorato di ricerca in Ingegneria industriale

Curricolo Ingegneria Energetica

XXX Ciclo

Advanced surface and volumetric receivers to convert concentrated solar radiation

Direttore della Scuola di Dottorato: Ch.mo Prof. Paolo Colombo

Coordinatrice di Curricolo: Ch.ma Prof.ssa Luisa Rossetto

Supervisore: Ch.mo Prof. Davide Del Col

Dottorando: Simone Dugaria

Padova 2017

I would like to dedicate this thesis to my parents Mauro and Rosetta Dugaria, who always supported all my pursuits, intellectual or otherwise.

Acknowledgements

Firstly, I would like to express my sincere gratitude to my advisor Prof. Davide Del Col for the continuous support of my Ph.D. study and related research, for his patience, motivation, and knowledge. I appreciate his contributions of time, ideas and discussion to make my Ph.D. experience productive and stimulating. His guidance helped me in all the time of research and writing of this thesis. The passion and enthusiasm he has for research were contagious and motivational for me.

Besides my advisor, I would like to thank the reviewers of my dissertation, Laura Fedele and Fabio Peron, for their time, interest and helpful comments.

The members of the STET research group have contributed immensely to my personal and professional time. The group has been a source of friendships as well as good advice and collaboration. I am especially grateful to my fellow lab mate Matteo Bortolato. We worked together on the experiments with the asymmetrical parabolic trough sharing good and bad times. I am thankful for the stimulating discussions, for the sleepless nights we were working together before deadlines, for all the fun we have had and for all what he taught me during the last three years. Other past and present group members that I have had the pleasure to work with or alongside are postdoc Andrea Padovan and the graduate students Enrico Bettin, Davide Rebellato, Erik Magro, Mario Smaniotto and Samy Jemy Artaky Hanalla.

In regard to the tests conducted on the nanofluid, I thank Filippo Agresti, Simona Barison and Laura Fedele for the preparation and the characterization of the nanofluid, and Elisa Sani for the optical tests. These coworkers share some of their knowledge with me and offer their support when it was needed.

I would like to thank, my parents who supported me in all my pursuits. To them, I dedicated this thesis.

Finally, for my loving, encouraging and patient Martina whose faithful support during the final stages of this Ph.D. is so appreciated, thank you.

Simone

Abstract

This thesis is the results of the work conducted during the three years of Ph.D. at the Department of Industrial Engineering of the University of Padova.

The conversion of solar energy into heat in the medium-temperature range (between 80°C and 250°C) has recently encountered a renewed interest in heating and cooling applications of industrial, commercial, residential and service sectors. Concentrating solar thermal collectors at medium temperature are suitable for many commercial and industrial applications, such as industrial process heat, solar cooling and desalination of the seawater. It is expected that in the future, a significant technological development can be achieved for these collectors, provided that the conversion of solar energy becomes more efficient and cost-effective. The proper design of the receiver, which is considered the heart of any concentrating collector, is essential to the future improvement in the conversion efficiency of this technology. In this context, the present thesis investigates the application of two innovative concepts of receivers in a prototype of an asymmetrical parabolic trough concentrator installed in the Solar Energy Conversion Lab of the Industrial Engineering Department, at the University of Padova.

In Chapter 1, a study on different estimation procedures for the assessment of the direct normal irradiance, which is the solar resource utilized by solar concentrators, is presented. The study includes an indirect evaluation from measurements of global and diffuse horizontal irradiances and the use of semi-physical/empirical models. A detailed analysis of the instrumentation and of the measuring technique as well as the expression of the experimental uncertainty is provided. In Chapter 2, the optical performance of the asymmetrical parabolic trough is experimentally characterized. As a result, a statistical ray-tracing model of the concentrator for optical performance analysis in different working conditions is validated and used to optimize the design of the proposed receivers. In Chapter 3, an innovative flat aluminium absorber manufactured with the bar-and-plate technology, including an internal turbulator, is tested in the asymmetrical parabolic trough collector under single-phase and two-phase flow regimes. A numerical model to predict its performance has been developed and validated against the

experimental data. In Chapter 4, this model is used to evaluate the performance of a small solar-powered ORC system by coupling the aforementioned concentrating solar system with direct vaporization of a low-GWP halogenated fluid or by using an intermediate solar circuit to heat pressurized water and evaporate the same organic working fluid in a separate heat exchanger. Finally, in Chapter 5 a new direct absorption receiver is proposed to investigate the capability of a suspension of single-wall carbon nanohorns in distilled water to absorb concentrated sunlight. The volumetric receiver has been designed through the development of a three-dimensional computational fluid dynamics model for its installation in the focus region of the asymmetrical parabolic trough. The capability of the nanofluid in collecting solar radiation when exposed to concentrated and non-concentrated solar flux are experimentally investigated thanks to the cooperation with National Council of the Research (CNR), that provided the aqueous solution. The nanofluid was tested in several conditions, with and without circulation, to investigate its stability with time.

List of publications

The material presented in this thesis is based on the following publications in peer-reviewed journals and conference proceedings.

Simone Dugaria, Matteo Bortolato, Davide Del Col
Modelling of a direct absorption solar receiver using carbon based nanofluids under concentrated solar radiation,
In Renewable Energy, 2017, (In press, corrected proof), ISSN 0960-1481,
https://doi.org/10.1016/j.renene.2017.06.029.
(http://www.sciencedirect.com/science/article/pii/S0960148117305335)

Matteo Bortolato, Simone Dugaria, Filippo Agresti, Simona Barison, Laura Fedele, Elisa Sani, Davide Del Col
Investigation of a single-wall carbon nanohorn-based nanofluid in a full-scale direct absorption parabolic trough solar collector
In Energy Conversion and Management, Volume 150, 2017, Pages 693-703, ISSN 0196-8904,
https://doi.org/10.1016/j.enconman.2017.08.044.
(http://www.sciencedirect.com/science/article/pii/S0196890417307562)

Matteo Bortolato, Simone Dugaria, Davide Del Col
Experimental study of a parabolic trough solar collector with flat bar-and-plate absorber during direct steam generation,
In Energy, Volume 116, Part 1, 2016, Pages 1039-1050, ISSN 0360-5442,
https://doi.org/10.1016/j.energy.2016.10.021.
(http://www.sciencedirect.com/science/article/pii/S0360544216314426)

Simone Dugaria, Andrea Padovan, Vincenzo Sabatelli, Davide Del Col,
Assessment of estimation methods of DNI resource in solar concentrating systems,
In Solar Energy, Volume 121, 2015, Pages 103-115, ISSN 0038-092X,
https://doi.org/10.1016/j.solener.2015.07.043,
(http://www.sciencedirect.com/science/article/pii/S0038092X15004144)

Simone Dugaria, Matteo Bortolato Davide Del Col
Direct vaporization of HCFO-1233zd(E) in a parabolic trough solar collector
(2017) ISES Solar World Congress 2017, Conference Proceedings

Matteo Bortolato, Simone Dugaria, Erik Magro, Davide Del Col
Coupled radiative and fluid flow modeling for a direct absorption solar receiver,
34th UIT Heat Transfer Conference, Conference Proceedings, 4 – 6 July 2016, Ferrara, Italia.

Simone Dugaria, Matteo Bortolato, Davide Del Col
Nanofluids application in direct absorption solar collectors: review and numerical model,
29th International Conference on Efficiency, Cost, Optimization, Simulation and Environmental Impact of Energy Systems (ECOS 2016), Conference Proceedings, 19 – 23 June 2016, Portorož, Slovenia.

Matteo Bortolato, Simone Dugaria, Davide Del Col
Concentrated flux measurement apparatus for an asymmetrical parabolic trough solar concentrator
(2015) ISES Solar World Congress 2015, Conference Proceedings, pp. 1065-1074.
DOI: 10.18086/swc.2015.10.22

Contents

List of Figures

List of Tables

Nomenclature

Acronyms

ALT	Atmospheric Life Time
CFD	Computational Fluid Dynamics
CPV	Concentrating Photovoltaic
CSP	Concentrating Solar Power
GWP	Global Warming Potential
HTF	Heat Transfer Fluid
MCRT	Monte Carlo Ray-Tracing
ODP	Ozone Depletion Potential
ORC	Organic Rankine Cycle
OWF	Organic Working Fluid
RTD	Resistance Thermal Detector
SWCNH	Single-wall Carbon Nanohorn

Symbols

A	Absorbance (*Eq. 5.5*)	-
A	Area	m^2
A_a	Aperture area of the collector	m^2
Bd	Boiling number	-
Bo	Bond number	-
c	Nanoparticles concentration	$g\ L^{-1}$
c_p	Isobaric specific heat	$J\ kg^{-1}\ K^{-1}$
C_g	Geometrical concentration ratio	-
CSR	Circumsolar ratio	-
d_h	Hydraulic diameter	m
DHI	Diffuse Horizontal Irradiance	$W\ m^{-2}$
DNI	Direct Normal Irradiance	$W\ m^{-2}$
e	Specific exergy	$J\ kg^{-1}$
e_h, e_d, e_m, e_s	Hourly, daily, monthly and seasonal prediction error	%
f	Fanning friction factor	-
f_c	Focal length of the solar concentrator	m
g	gravity acceleration	$m\ s^{-2}$
G_0	Extra-terrestrial solar irradiance	$W\ m^{-2}$
G_b	Direct component of the incident solar irradiance	$W\ m^{-2}$
G_d	Diffuse component of the incident solar irradiance	$W\ m^{-2}$
GHI	Global Horizontal Irradiance	$W\ m^{-2}$
h	Heat transfer coefficient	$W\ K^{-1}\ m^{-2}$
h_t	Height of the turbulator-strip	

H_h, H_d, H_m, H_s	Hourly, daily, monthly and seasonal direct normal irradiation	W h m^{-2}
i	Specific enthalpy	J kg^{-1}
i_L	Specific enthalpy of the saturated liquid	J kg^{-1}
i_{LV}	Specific enthalpy of vaporization	J kg^{-1}
I_{aur}	Radiation intensity in the aureole of the solar disc	W m^{-2} sr^{-1}
I_S	Radiation intensity in the solar disc	W m^{-2} sr^{-1}
$I_{bb\lambda}$	Spectral radiation intensity of a blackbody	W m^{-2} m^{-1} sr^{-1}
I_λ	Spectral radiation intensity	W m^{-2} m^{-1} sr^{-1}
k	Thermal conductivity	W m^{-1} K^{-1}
k_d	Diffuse fraction	-
$k_{d,h}$, $k_{d,d}$	Hourly and daily diffuse fraction	-
k_{pp}	'Pseudo-polytropic' parameter of the expander (Eq. 4.10)	-
k_t	Clearness index	-
k_t'	Modified clearness index	-
K	Global heat transfer coefficient	W m^{-2} K^{-1}
K_b	Incidence angle modifier for the direct radiation	-
K_d	Incidence angle modifier for the diffuse radiation	-
l	Length	m
l_t	Length of the turbulator-strip	m
l_{turb}	Effective length of the turbulator	m
m	Air mass	-
$\dot{m}$	Mass flow rate	kg s^{-1}
$n_{channel}$	Number of channel in the turbulator section	-
N_{pp}	'pseudo-polytropic' expansion index	-
Nu	Nusselt number	-
p	Pressure	Pa
p_{crit}	Critical pressure	Pa
P_{el}	Electrical power	W
P_{cross}	Perimeter of the cross-section	m
Pr	Prandtl number	-
q	Heat flow rate	W
q''	Heat flux	W m^{-2}
r_p	Pressure ratio	-
r_v	Volumetric built-in ratio of the expander	-
Re	Reynolds number	-
s	Specific entropy	J kg^{-1} K^{-1}
s_t	Width of the turbulator-strip	
S	Energy volumetric source term (Eq. 5.1)	J m^{-3}
SF	Shape factor	-
t	Thickness	m
t_t	Thickness of the turbulator-strip	m
T	Temperature	K
T_{crit}	Critical pressure	K
T_S	Apparent temperature of the Sun	
T_m^*	Reduced (mean) temperature difference	K m^2 W^{-1}
v_{wind}	Wind speed	m s^{-1}
We	Weber number	-
W_{exp}	Expansion specific work (Eq. 4.12)	J kg^{-1}
x	Vapor quality	-
x, y, z	Cartesian coordinates	m

Greek letters

α	Solar elevation (Eq. 1.5)	°
α_r	Absorbance of the receiver	-
α_λ	Spectral absorbance of the receiver	m^{-1}
$\alpha_{r,coat}$	Absorbance of the receiver coating	-
α_t, γ_t, δ_t	Dimensionless parameter of the turbulator geometry	-
γ_r	Intercept factor	-
δ_{kt}'	Stability parameter for the modified clearness index	%
ΔT_{mlog}	Logarithmic mean temperature difference	K
ε_r	Emittance of the receiver	-
η_0	Optical efficiency of the collector	%
η_{col}	Thermal efficiency of the collector	%
η_{ex}	Exergetic efficiency	%
η_{is}	Isentropic efficiency	%
η_{ORC}	Overall conversion of the ORC unit	%
η_r	Thermal efficiency of the receiver	%
θ_c	Acceptance angle of the solar concentrator	°
θ_z	Zenith angle	°
λ	Wavelength	nm
μ	Dynamic viscosity	Pa s
ρ	Density	kg m^{-3}
ρ_c	Reflectance of the mirror in the concentrator	-
σ	Total optical error of the concentrator	mrad
σ_λ	Spectral scattering coefficient	m^{-1}
φ	Inclination of the corrugation in chevron plates heat ex.	°
ϕ	Enlargement factor (Eq. 4.6)	-
ϕ_c	Rim angle of the solar concentrator	°
ω	Solid angle	srad
Ω	Clearness sky index	-

Subscripts

I	Primary fluid
II	Secondaty fluid
abs	Absorber
air	Ambient air
amb	Ambient
calc	Calculation (model)
col	Solar collector
cond	Condenser / condensation
conv	Thermal convection
eq	equivalent
ev	Evaporator / evaporation
exp	Expander /expansion
ext	External
EAS	External Absorber Surface
EIS	External Insulation Surface
f	Flow section
gen	Electrica generator
G	Gas (vapor) phase

glass	Receiver glass cover
GO	Only gas (vapor) phase
IAS	Internal Absorber Surface
he	Heat Exchanger
HTF	Heat Transfer Fluid
in	Inlet
inc	Incident
ins	Insulation
L	Liquid phase
LO	Only liquid phase
m	Mean (average)
meas	measurement
ORC	Organic Rankin Cycle
out	Outlet
OWF	Organic Working Fluid
p	Pump
r	Receiver
rad	Radiation
ref	Reference
S	Sun
s-p	Single-phase
sat	Saturation
sol	Solar
suc	Suction
t	Turbulator
t-p	Two-phase
w	water
w,h	Hot water
w,c	Cooling water

Introduction

The large use of photovoltaic, concentrated solar power (CSP) and solar thermal technologies is expected to play a crucial role in the future provided that the conversion of solar energy becomes more efficient and cost-effective. Concentration of solar radiation becomes necessary when high temperatures (above 100°C) are desired, or when, as in the case of photovoltaic cells, the cost of the absorber itself is much higher than the cost of the concentrator [1]. Significant technological development can be achieved for solar thermal collectors in heating and cooling applications of industrial, commercial, residential and service sectors.

The conversion of solar energy into heat in the medium-temperature range (between 80°C and 250°C) has recently encountered a renewed interest. After concluding tests in several pilot plants, solar collector manufacturers currently offer some proven solutions on the market. On the other hand, research institutions are investigating on several topics, including the improvement of the global system control, the cost-effectiveness, the building integration and innovative solutions to overcome the technical issues encountered in practice. There are several environmental, political and economic reasons that justify this interest. Medium-temperature solar collectors are very suitable for many commercial and industrial applications, such as the industrial process heat generation, the solar cooling and the desalination of the seawater. As these devices exploit a renewable energy source, they may contribute to the reduction of the energy supply from fossil fuels and greenhouse gases emissions. According to the IEA statistics [2], industry represented one-third of the total final consumption of energy worldwide of 2014. Electricity accounts for around the 25% of the final energy use for industry, while the rest is industrial heat demand. Market potential analysis performed in 2006 on medium-temperature solar collectors, [3] showed more or less the same share of the industrial heat demand and pointed out that, as a general tendency, about 50% of the industrial process heat demand is located at temperatures up to 250°C. *Vannoni et al.* [4] highlighted several industrial key sectors such as food, textile, transport equipment, chemical, metal and plastic treatment, that

present 60% of the thermal energy demand at a temperature level that encourages the use of solar process heat. Moreover, the air conditioning and refrigeration systems powered by solar thermal collectors are becoming an efficient and, in some cases, competitive alternatives to the conventional systems to meet the increasing cooling demand of big buildings and the refrigeration requirements in food processing and pharmaceutical products conservation. The most attractive prospect is the achievement of a temperature level high enough (150°C-200°C) to couple the solar collectors with double effect absorption chillers [5]. It is worth to remember that in most industrialized countries, the air conditioning demand shifts the yearly peak of electrical energy consumption in summer and may cause serious problems to the stability of the electrical grid. Furthermore, the flexibility of Organic Rankine Cycle to operate with different working fluids is well suited to work with medium-temperature solar power by adapting the fluid characteristics to the operating temperatures of the solar collector. The use of Rankine cycle power generation systems with organic working fluid are of particular interest for distributed electric generation which is becoming more and more widespread bringing significant contributions to the electrical system. In addition to these applications, solar desalination of the seawater might become one of the principal means to assure the access to drinking and safe water to everybody, given that the highest solar energy availability and the troubles of clean water supply pertain to the same regions.

Many researchers agree that, from a technical point of view, the parabolic trough collectors are the best proven and reliable solar technology to produce heat in the medium-temperature range, mainly thanks to the experience and the know-how gained in large commercial concentrated solar power plants. *Fernandez-Garcia et al.* [6] and *Zarza* [7] presented overviews on the components, efficiency and applications of these concentrating solar collectors, including commercial plants and new prototypes. Their conclusions highlighted that the proper design of the receiver is essential to the future improvement in the conversion efficiency of these concentrating solar collectors. The main function of this element, which is considered the heart of any concentrating collector, is to absorb the concentrated solar radiation and convert it with a high efficiency into heat. The receivers of medium-temperature collectors, depending on the operating temperature, may not need glazed and empty cavity covers and they can be manufactured with cheaper materials and selective coatings. This allows containing the

investment costs of the solar field, which nowadays it is the main cause that discourages the investments in the solar power industry due to the high capital required and the long payback time. In this context, the present thesis investigates the applications of two innovative technologies for flat receivers in a linear concentrating collector. The linear solar concentrator considered in this work is a prototype of an asymmetrical parabolic trough concentrator and it is installed in the Solar Energy Conversion Lab of the Industrial Engineering Department, at the University of Padova. The present concentrator can be seen as half of a more common symmetric parabolic trough for CSP applications. This solar concentrator, under clear-sky conditions, is capable to provide locally concentrated flux up to 100 kW m^{-2}.

The direct normal irradiance is the resource utilized by solar concentrators and its measurement is essential to determine the performance of any solar concentrator. This component of the solar radiation is not often measured due to practical reasons and is derived instead from measurements of global irradiance or satellite-based models. A study of different estimation procedures for the assessment of the DNI, using experimental data taken at two different latitudes in Italy is presented in the first Chapter. The study includes an indirect evaluation from measurements of global and diffuse horizontal irradiances and the use of semi-physical/empirical models. The capability of 1-min time series of direct normal irradiance and the accuracy in the estimation of hourly, daily, monthly and seasonal data of irradiation is investigated. A detailed analysis of the instrumentation and of the measuring technique as well as the expression of the experimental uncertainty is provided.

After the assessment of the estimation procedures of the solar input for concentrating solar collector, the second Chapter is focused on characterizing the optical performance of the considered concentrator. The definition of the concentrated solar flux distribution in the focal region is crucial to the design of the geometry and the configuration of the receivers. The optical performance of the asymmetrical parabolic trough is experimentally characterized by adopting a direct method based on the use of a radiometer mounted on a handling system to measure the solar flux map on the concentration region. The aim of this experimental activity is also to develop a statistical Monte Carlo ray-tracing model of the concentrator for optical performance analysis in different working conditions. This model constitutes an essential tool to the optimized design of receivers.

In the third Chapter, the numerical and experimental investigation on an advanced receiver for linear concentrating solar collectors is presented. This receiver presents an innovative flat aluminium absorber manufactured with the bar-and-plate technology, including an internal offset-strip turbulator, and is conceived for process heat and direct steam generation in a small linear concentrator. The performance of the new receiver is experimentally assessed in the asymmetrical parabolic trough collector under single-phase and two-phase flow regimes. For the latter case, a new test method is proposed and validated during the experimental tests conducted on water and on a halogenated fluid. A numerical model has been developed to predict the thermal performance of the receiver under single- and two-phase regimes. The model is validated against the experimental data and is used to study possible optimized configurations of the receiver.

In the fourth Chapter, a numerical model of a small size organic Rankine cycle for low-grade heat sources is proposed and validated by comparison with the datasheet of a commercial unit with a comparable size. Afterwards, the validated model of the receiver has been integrated into the ORC model in order to evaluate its performance by coupling the aforementioned concentrating solar system with direct vaporization of a low-GWP halogenated fluid or by using an intermediate solar circuit to heat pressurized water and evaporate the same organic working fluid in a separate heat exchanger.

In the last Chapter, a new direct absorption receiver is proposed to investigate the capability of the carbon-based nanofluid to absorb the concentrated sunlight. As compared to the conventional surface-absorption solar collectors, direct absorber solar collector may lead to higher thermal efficiency and lower cost due to the absence of a selective surface. The volumetric receiver has been designed through the development of a three-dimensional computational fluid dynamics model, for its installation in the focus region of the asymmetrical parabolic trough solar concentrator. The considered nanofluid consists of a suspension of single-wall carbon nanohorns in distilled water with a concentration of 0.02 g L^{-1}. The thermophysical properties are the same as those of the base-fluid, but the presence of carbon nanoparticles greatly enhances the optical characteristics. The stability of the nanofluid and its capability in collecting solar radiation when exposed to concentrated and non-concentrated solar flux with and without circulation are experimentally investigated.

Finally, the Conclusions of the experimental and numerical study on the application of the advanced technologies for linear concentrating solar collector presented in this thesis are drawn and the indications for possible future research are proposed.

Chapter 1 Assessment of estimation procedures of direct normal irradiance for solar concentrating systems

The availability of meteorological archives, based on satellite and ground station measurements, constitutes a precious support in the estimation of solar radiation availability. Nowadays, the development of solar concentrators calls for the assessment of direct normal irradiance (DNI). The DNI is the resource utilized by solar concentrators for energy production, in CSP and Concentrating Photovoltaic (CPV) applications, and thus, DNI forecasting is the basis for concentrating solar energy forecasting [8]. Solar radiation and specifically DNI has not been an objective in meteorological measurement over the time. Nowadays, while accurate datasets of global horizontal irradiance (GHI) are available for many sites, still efforts are required to fully characterize the DNI resource.

This Chapter describes a study of different estimation procedures for the assessment of DNI, which include an indirect evaluation from measurements of global and diffuse horizontal irradiances and use of semi-physical/empirical models. The analysed approaches include measuring techniques, using experimental data with a time scale of 1-min, taken at two different latitudes in Italy, and models. The capability of 1-min DNI time series and the accuracy in the estimation of hourly, daily, monthly and seasonal data of irradiation are tested. Since measurements of global and diffuse irradiance have good accessibility and availability, the study aims at clarifying to what extent such data can be used for deriving DNI time series.

1.1 Estimation procedures of direct normal irradiance

The DNI is an element of the total hemispherical terrestrial solar radiation flux on the Earth surface. This flux is referred as total hemispherical solar irradiance or more commonly as GHI. Hemispherical radiation comprises a combination of the nearly collimated DNI and some portion of the diffuse sky radiation extracted from the beam by scattering as the DNI propagates through the atmosphere [9], called diffuse horizontal irradiance (DHI)

1.1.1 Direct measurement of direct normal irradiance

The reference instrumentation for the direct measurement of DNI is a thermopile pyrheliometer installed on a Sun-tracker. In radiation detectors, several thermojunctions between dissimilar metals are in contact with the absorbing surface. These active junctions are located beneath a highly absorbing blackened surface and are heated by the radiation absorbed by the black coating. A thermal flux upon the junctions produces a voltage proportional to the difference in temperature between the active junctions and a similar set of passive junctions. The passive junctions are fully protected from solar radiation and are usually in thermal contact with the instrument housing, which serves as a heat sink. In pyrheliometers, the thermopile detector is placed at the end of a collimating tube, which is usually blackened on the inside to reduce the optical reflectance of the incoming radiation. This collimated detector is used for measuring solar radiation from the Sun and from a small portion of the sky around the Sun at normal incidence [9] The collimating tube contains several diaphragms in order to limit the angle of acceptance of the solar radiation. Its dimensions are such that the field of view for pyrheliometers is between 4° and 6°, or about ten times the solar disk angular diameter. As pointed out by *Myers* [10], this range of field was chosen to avoid lost data by permitting relatively large (1° to 1.5°) tracking errors to occur when only manually adjusted or clock drive tracking mechanisms were available. Sun-trackers allow tracking the Sun in its apparent path in the sky during the day. Reducing the fields of view of pyrheliometers would require significant reductions in tracker pointing error. Modern pyrheliometers require to be mounted on high precision Sun-trackers. Their typical pointing error is in the order of 0.01°.

Pyrheliometric measuring systems are quite expensive due to the combination of thermopile sensors, view-limiting apertures, and tracking equipment.

1.1.2 Indirect measurement of direct normal irradiance

An alternative measurement of DNI is to indirectly derive it from the measurements of GHI and Diffuse Horizontal Irradiance DHI. This method constitutes the first type of estimation procedure to derive DNI considered in this study. When the GHI and the DHI are measured, the direct horizontal irradiance can be obtained by subtracting the diffuse horizontal component from the global horizontal one. Since direct radiation has a geometric behaviour, by knowing the incidence angle of the direct radiation on a horizontal plane, which is the angle between the normal to the plane and the projection of the direct beam radiation on the intercepting plane, also called the zenith angle θ_z, the DNI comes from the direct horizontal irradiance divided by the cosine of the zenith angle:

$$DNI = \frac{GHI - DHI}{cos\theta_z} \qquad \textit{Eq. 1.1}$$

Global and diffuse irradiances are measured with pyranometers. A pyranometer is an instrument for measuring hemispherical solar radiation, which accounts the contribution of the direct and the diffuse radiation. These instruments must have a response independent of the angle of incidence of the solar radiation. Thermopile detectors present a more uniform response of the wavelength of radiation over the solar energy spectrum compared to silicon detectors, which response its limited only to the 300 nm to 1100 nm spectral region of the solar spectrum. However, in nearly all thermopile pyranometers, the detectors are protected from the ambient elements by one or two hemispherical glass. This cover limits the spectral sensitivity of thermopile-based instruments to either 290–2800 nm for glass dome, used in most pyranometers, or to 290–4000 nm for quartz dome, which is used in more advanced pyranometers. Furthermore, to prevent the uneven distribution of the radiation on the detectors, the covers should be very uniform in thickness. To measure the GHI a pyranometer should be placed on a horizontal surface free of obstacles that may shade the instrument, while to measure the diffuse irradiance a pyranometer should be shaded from the direct irradiance coming directly from the Sun. The best way to do it is to occult the solar disk with a ball driven by a

Sun-tracker. However, this technique, as for the direct measurement of the DNI, present a high cost due to the presence of the Sun-tracker. A cheaper and common technique involves the use of a shadow-band, which screens the pyranometer along the day. In this case, depending on the dimension of the shadow-band, it is required only a manual adjustment every few days as the declination changes, but the measured irradiance must be corrected because the band blocks also a part of the diffuse radiation from the sky [11]. However, the overall accuracy of this method cannot be equal to the one employing a shadow-ball driven by a tracker, even when corrections are applied [12]. The main problem in the indirect evaluation of DNI is that pyranometers can be affected by several sources of uncertainty, which should be properly considered, as discussed by *Gueymard and Myers*[13]. Moreover, the choice of the model to correct the shadow-band effect in the measurement of diffuse irradiance plays a role, as investigated by *Kotti et al.* [14]. Accurate estimations of DNI are obtained as derived from measurements of global horizontal irradiance and diffuse horizontal irradiance if the offset in pyranometers are properly corrected and the zenith angle is not too high [11]. A similar approach is to derive DNI from instruments that can measure simultaneously total and diffuse radiation, such as rotating shadow-band radiometers (RSR) and total hemispherical measuring radiometers with multiple fast thermopiles. RSRs are typically deployed using silicon photodiodes as detectors. *Myers* [15] presented a comparison of these two types of radiometers with respect to a reference pyrheliometric measurement of DNI. The comparison shows that the at DNI values useful for concentrating solar applications, the two radiometers system produces DNI estimates with similar uncertainty.

1.1.3 Estimation procedures using separation method

Due to practical reasons, the DNI is not often measured and is derived instead from models based on satellite data or measurements of global irradiance. The work of *Mohammed et al.* [16] represents a good example to stress out the difficulties encountered to build a large dataset for energy yield analysis, applicable to the concentrating system, based on radiation measurements in the field. Their study involved the measurements of a pyrheliometer, a pyranometer and a spectroradiometer made across a range of air mass values and atmospheric conditions. The system required regular maintenance to eliminate potential errors and the data

storage process has been set up to enable ease of data retrieval using a relational database. Approximately 422000 measurements were made across a range of air mass values and atmospheric conditions based on a two-year operation period.

In the last decade, many authors have been presented DNI estimation procedures based on satellite data. For instance, *Cogliani et al.* [17] present a physical model that provides hourly average GHI and hourly average DNI for Italy based on primary satellite images in the visible band. The validation of their model with data from ground-based stations highlighted the deep lack of solar data in Italy, in particular, DNI data. The potential of high concentration solar photovoltaic generation, based on satellite-derived data of DNI has been investigated by *Viana et al*. [18]. Their evaluation was carried out independently for different forecast horizons (1, 2 and 3 days ahead), different seasons of the year and three different sky conditions: clear, cloudy and overcast. Their results showed that their model presented a marked dependence on the sky conditions and season of the in forecasting both GHI and DNI. In a recent study, *Amillo et al.* [19] developed a database of global and direct solar radiation using the Eastern Meteosat Satellite and validation with high-quality data from ground stations. The sensitivity of satellite-based methods for deriving solar radiation to different choices of aerosol input and models has been explored by *Polo et al*. [20]. They observed that the most important contribution to the uncertainty of the satellite estimations comes from the impact of clouds to the GHI for clear and non-clear-sky conditions. However, also the input of aerosol information and the clear-sky model can have an important role in the uncertainty. In another study [21], a lidar-ceilometer has been adopted to establish a correlation between the daily variations of DNI and backscatter atmospheric extinction around solar noon, under cloud-free conditions. A 12-months experiment was carried out to obtain the correlation between DNI and atmospheric backscatter measurements. Their work shows the potential use of aerosols information as measured by lidar-ceilometer for solar radiation modelling. *Gueymard* [22] presented a study on the sensitivity of irradiance to precipitable water for various types of precipitable water measurement. The results suggest that the accuracy of the predicted clear-sky DNI and GHI is only a weak function of the uncertainty in the precipitable water data input, even in arid conditions, where the sensitivity of irradiance to precipitable water variations is largest.

When only the GHI is known, the DNI can be estimated by using separation models (semi-physical and empirical), which provide DNI or DHI; if a model provides DHI, DNI is then obtained from Eq. 1.1. Separation models constitute the second estimation procedure for DNI considered in this study. Due to their flexibility, semi-physical and empirical models are seen with interest by engineers and designers of solar energy installations. Moreover, a combination of ground measurements and statistical modelling data is often used in the development and validation of long-term and medium-term forecasting databases [23]. Statistical models are usually related to the use of local measurements and learning processes in order to derive future behaviour. Depending on the time-frequency and on the characteristic of the dataset of GHI, this behaviour can use data for years, months, days, hours, minutes, or seconds. In their basic form, such models are simple, because they are based on the correlation between the clearness index, k_t, defined as the ratio of the GHI to the horizontal irradiance available out of the atmosphere and the diffuse fraction (ratio of the diffuse-to-global irradiance), k_d, or the beam transmittance (ratio of the direct beam solar irradiance to the extra-terrestrial solar irradiance) k_b[24] . Figure 1 reports the dependence of the diffuse ratio k_d on the clearness index k_t in its typical shape as proposed by Muneer [25] describes the type of measurements at each area of the graph and the sources of possible errors. Each model is developed from the measurements taken on some specific stations as discussed by *Vick et al*. [15]; therefore, their accuracy must be carefully evaluated if they are used for locations different from the ones they were developed for. *Blanco et al.* [8] suggested that the spatial resolution of such models is usually related to less than 10 km around the measurements location depending also on the topography. Another critical point is that they were developed using mainly hourly irradiance measurements.

The separation models considered in this study are the model of *Erbs et al.*[26], the DISC model developed by *Maxwell* [27], the model of *Perez et al.* [28], the model of *Skartveit et al.* [29] and the models DIRMAX and DIRINT proposed by *Perez et al.*[30]. The model of *Erbs et al.* [26] is an extension of the *Orgill and Hollands's* correlation [31] to latitudes from 31° and 42° North based on 5 stations data. The diffuse irradiance was obtained as the difference of hourly values of direct and global irradiances on a horizontal surface these quantities. The proposed correlation combines a linear regression for k_t lower or equal than 0.22, a constant value for k_t greater than 0.8 and a polynomial correlation for k_t between these two limits:

$$k_d = \begin{cases} 1 - 0{,}09\, k_t & k_t \leq 0{,}22 \\ 0{,}9511 - 0{,}1604\, k_t + 4{,}388\, k_t^2 - 16{,}638\, k_t^3 + 12{,}336\, k_{Tt}^4 & 0{,}22 < k_t \leq 0{,}8 \\ 0{,}165 & k_t > 0{,}8 \end{cases} \qquad \textit{Eq. 1.2}$$

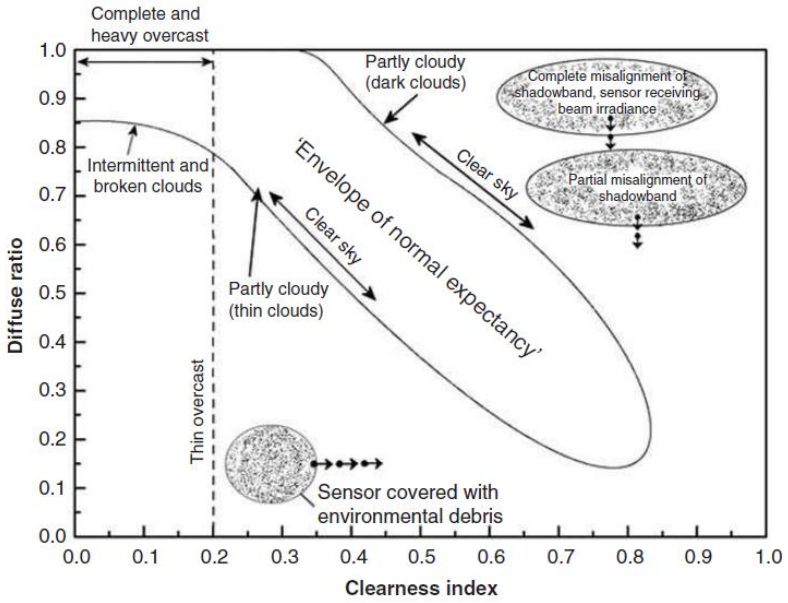

Figure 1 – Dependence of the diffuse ratio k_d on the clearness index k_t and sources of s possible measurement errors [25].

A quasi-physical model Direct Insolation Simulation Code (DISC) has been developed by *Maxwell* [27] for converting hourly global horizontal to direct normal irradiation. This model combines a clear-sky model with experimental fits for other sky conditions. The experimental regressions were deduced from radiation data recorded in 70 different stations during12 years. The direct normal irradiance is modelled as follows:

$$DNI_{DISC} = G_o \left(K_{nc} - \left(c_{DISC,1} + \left(c_{DISC,2} \right)^{mc_{DISC,3}} \right) \right) \qquad \text{Eq. 1.3}$$

where the coefficients $c_{DISC,1}$, $c_{DISC,2}$, and $c_{DISC,3}$ are functions of the clearness index k_t:

if $k_t \leq 0.6$:

$$c_{DISC,1} = 0.512 - 1.560k_t + 2.286k_t^2 - 2.222k_t^3$$
$$c_{DISC,2} = 0.370 + 0.962k_t k_t^2$$
$$c_{DISC,3} = -0.280 + 0.932k_t 2.048k_t^2$$

if $k_t > 0.6$:

$$c_{DISC,1} = -5.743 + 21.77k_t - 27.49k_t^2 + 11.56k_t^3$$
$$c_{DISC,2} = 41.40 - 118.5k_t + 66.05k_t^2 + 31.9k_t^3$$
$$c_{DISC,3} = -47.01 + 184.2k_t - 222k_t^2 + 73.81k_t^3$$

In Eq. 1.3, G_o is the normal incident extra-terrestrial irradiance and the parameter K_{nc}, is given by:

$$K_{nc} = 0.866 - 0.122m + 0.012m^2 - 0.000653m^3 + 0.000014m^4 \qquad \textit{Eq. 1.4}$$

This coefficient is an expression of the air mass m, which is evaluated with the formulation of *Kasten* [32] as a function of the solar elevation α:

$$m = \frac{1}{\sin(\alpha) + 0.15(\alpha + 3.885)^{-1.2253}} \qquad \textit{Eq. 1.5}$$

The model of *Perez et al.* [28] is a simple modification of the DISC model [27]. In this model, the direct normal irradiance DNI_{DISC} (Eq. 1.3) multiplied by a correction function CF_{Perez}, empirically obtained from a large pool of data:

$$CF_{Perez} = \begin{cases} 1 - 0.0124\left(100{\theta_z}^{1.2} - 60\right) & k_t < 0.7 \\ 1 - 0.0211(100(\sin\theta_z)^2 + 10sin(2\theta_z) - 25) & 0.45 < k_t \leq 0.7 \\ 1 - 00182\left(25\left(\sin(1.1\theta_z)\right)^4 - \left(\frac{0.125}{\frac{\pi}{2} - min(\theta_z, 1.4)}\right)\right) & k_t \leq 0.45 \end{cases} \qquad \textit{Eq. 1.6}$$

The models DIRMAX and DIRINT [30] are more comprehensive than the model of *Maxwell* [27] and *Perez et al.* [28]. In these models, the normal component of the direct irradiance is obtained from the direct normal irradiance DNI_{DISC} estimated with the Maxwell DISC model (Eq. 1.3) and a coefficient, which is a function of four parameters, which describe the insolation conditions. The first parameter is the solar zenith angle θ_z. The second and the third parameters are the modified clearness index k_t' and a stability index $\delta k_t'$ as defined in *Perez et al.* [30]. The

stability index $\delta k_t'$ derives from consecutive records of GHI accounting the dynamics of sequent time series. The last parameter is the atmospheric precipitable water content W, and is an optional input to the model. At Padova site, some tests have been run to analyse the effect of the precipitable water data in the performance of the models DIRMAX and DIRINT [30]. The analysis has shown that the use of precipitable water as additional input can lead to slightly better or even less accurate DNI estimations depending on the day conditions. Therefore, it was concluded that no overall improvement in the accuracy of the models is achievable at Padova climatic conditions if precipitable water data are used [33]. Moreover, since data of precipitable water was not available at Trisaia site, in the present paper both DIRMAX and DIRINT [30] models are used without using precipitable water data as an input, in order to get a more objective comparison of the model performance.

The last model evaluated in this study is the model of *Skartveit et al.* [29]. This model has been developed using a 32 years long record of hourly GHI and DHI taken in Bergen (Norway). The basic concept of this model is very similar to the DIRMAX and DIRINT model [30]. Analytical and continuous functions are adopted here rather than discrete values based upon lookup tables as in the models of *Perez et al.*[30]. Furthermore, the variability of the clearness sky index Ω is included as prediction variable. The clear-sky index Ω proposed in this model is given by the ratio of the clearness index and the cloudiness index as defined in [29], which is intended to account for the effect of the variability in the cloud cover. The variability of the clearness sky index is the root mean squared deviation between the clear-sky index Ω of a period and those of the former and next periods.

1.2 Experimental campaign on the measurement of direct normal radiation measurements and uncertainty analysis

Two experimental databases of solar irradiance are used for the present study. One is collected in Padova (45.4°N, 11.9°E), northern Italy, while the other is collected in Trisaia (40.2°N, 16.6°E), southern Italy. The two sites cover a wide range of climatic and sky conditions. Italy is a favorable site for solar energy installations; particularly Trisaia is interesting for solar concentrating applications. The measurement in Trisaia has been performed in collaboration with the ENEA Research Centre Trisaia. A detailed analysis of the instrumentation and of the measuring technique as well as the expression of the experimental uncertainty is a key aspect to get a more comprehensive understanding of the results provided by the models.

Data taken at Padova include a Kipp & Zonen CHP1 pyrheliometer mounted on a high precision EKO Instruments STR-22G solar tracker to measure the DNI; a Kipp & Zonen CMP22 pyranometer is used to measure the GHI and the DHI is measured with a Kipp & Zonen CM11 pyranometer placed under a shadow-band. Finally, an anemometer measures the wind speed on the horizontal plane and the ambient air temperature is gauged by a Pt100 RTD. Figure 2 reports a view of the solar radiation measurement instrumentations installed at the Solar Energy Conversion Lab on the roof of the Department of Industrial Engineering at the University of Padova. The values of the diffuse irradiance are corrected with the semi-physical model of *LeBaron et al.* [34]. This correction method accounts for both the band geometry and the sky conditions, that is how the diffuse radiation is distributed. Indeed, the anisotropy of the diffuse radiation is an important aspect to be considered when measuring diffuse radiation with shadow-band devices, as well as when modelling solar radiation. The effect of the reflection is considered minimal because of the black paint of the band.

Data taken at Trisaia include GHI, measured with an EKO MS-802 pyranometer, DNI, measured with an EKO MS-56 pyrheliometer and DHI, measured with an EKO MS-802 pyranometer shaded with a ball driven by the Sun-tracker. Pyrheliometers are first class instruments and pyranometers are secondary standards classified, according to ISO 9060: 1990 [35]. In both Padova and Trisaia stations, the status of the instrumentation is daily checked to avoid any sources of inaccuracy.

Figure 2 – Solar radiation measurement instrumentations installed on the roof of the Department of Industrial Engineering at the University of Padova.

To ensure high quality of the data taken in Padova, the agreement between the pyranometers used to measure global and diffuse irradiances has been checked. Both pyranometers were set up to measure the global irradiance on the horizontal plane on selected days; this check covers different periods of the year to include a wide range of zenith angles and sky conditions. Although the thermal offset had been corrected, when measuring clear-sky GHI a residual disagreement between Kipp & Zonen CM11 and Kipp & Zonen CMP22, up to 5% at the ends of the day, when irradiance is lower, has been observed. Such difference in the measured irradiances displayed a dependence on the zenith angle. Therefore, by assuming Kipp & Zonen CMP22 to be the reference pyranometer, a correlation has been developed to correct Kipp & Zonen CM11 readings. Such correction has been verified against independent data (not used to develop the correction). After the correction to Kipp & Zonen CM11 measurements, the difference in the measured clear-sky global irradiance between the two pyranometers has become lower than 1%. Similarly, the pyranometers used for measuring global and diffuse solar irradiances have been checked for Trisaia test site as well. The check has been performed by comparison with a reference secondary standard Kipp & Zonen CMP11 pyranometer, calibrated by a European accredited laboratory. The on-site calibration has been performed

outdoor according to ISO 9847 - Method Ia [36] in a wide range of zenith angles, sky and ambient temperature conditions. This calibration procedure has allowed correcting the sensitivity factors of the pyranometers used to measure the different components of solar irradiance during the monitoring period. Such corrections have been tested for a significant time period during which a complete agreement between the Kipp & Zonen CMP11 reference pyranometer and the EKO MS-802 pyranometers has been found.

To ensure the quality of the databases, further checks have been applied to irradiance measurements to find possible data showing a physical violation. Moreover, data points taken during rainy conditions have been rejected: as shown in [11] such data are not interesting for DNI characterization and their contribution on long-term estimation is absolutely negligible.

1.2.1 Uncertainty analysis

The uncertainty analysis, here adopted, is based on the procedure described by *Padovan and Del Col* [11], who show how to apply the method by ISO, Guide to the Expression of Uncertainty in Measurement [37] to the irradiance measurements with thermopile pyranometers. *Reda* [38] also proposed a method for calculating the uncertainty in measuring shortwave solar irradiance, which substantially agrees with that illustrated in [11].

All the radiometers used in the present study, are calibrated by comparison with reference instruments, calibrated from year-to-year by the WRC (World Radiometric Center). However, pyranometers and pyrheliometers operate at different conditions as compared to those occurring in calibration; thus, further sources of uncertainty should be added to the calibration uncertainty. Table 1 reports a list of uncertainties, which can affect the present instruments: in agreement to ISO guide [37], all the uncertainties reported in this table are considered as type B components of uncertainty with a rectangular distribution. An in-depth description of the measuring uncertainties affecting thermopile radiometers is reported in [11]. Both pyranometers Kipp & Zonen CMP22 and CM11 are equipped with thermistors and thermoresistance sensors to measure the instrument temperature. Although a posteriori correction of the thermopile signal was applied, as reported in the calibration certificates, the

contribution of the temperature dependence was considered in the calculation of the overall uncertainty budget.

Table 1 – Uncertainty sources in pyranometers and pyrheliometers.

Uncertainty source	Kipp & Zonen CHP1	Kipp & Zonen CMP22	Kipp & Zonen CM11	EKO MS-56	EKO MS-802
Directional response	-	±5 W/m^2	±10 W/m^2	-	±10 W/m^2
Temperature response	±0.5%	±0.5%	±1%	±0.5%	±1%
Non-linearity	±0.2%	±0.2%	±0.5%	±0.5%	±0.5%
Spectral response	±2%	±2%	±2%	±1%	±1%
Zero offset B	±1 W/m^2	±1 W/m^2	±2 W/m^2	±1 W/m^2	±2 W/m^2

The zero-thermal offset occurs when the pyranometer is shaded from solar radiation, but it provides a voltage output signal different from zero. The thermal offset error is usually divided into two parts: the contribution due to the infrared exchange between the radiometer and the sky (zero offset A) and the contribution due to the temperature change of the body of the instrument (zero offset B). From Table 1, the thermal offset B is small for all the present instruments, because of the careful construction of the thermopile sensor and use of compensation techniques for temperature.

The zero offset A is not reported in Table 1, but it is treated separately because it provides a systematic underestimation of irradiance, which should be properly evaluated and corrected. In particular, for Padova site, diurnal (with clear and cloudy sky) and nighttime tests have been run to measure type-A thermal offset. During diurnal tests, the dome of the pyranometers has been properly covered as recommended by the manufacturer and the response of the pyranometers has been observed. The response to solar radiation decays and before the instrument reaches the thermal equilibrium with the ambient the thermal offset A can be detected. Both tests have revealed that the Kipp & Zonen CM11 has a higher thermal offset A as compared to Kipp & Zonen CMP22. Such result is in agreement with the specifications of the manufacturer, which declares a lower thermal offset error for Kipp & Zonen CMP22, as a result of the improved construction of the instrument. Moreover, in agreement with independent experimental observations by *Gueymard and Myers* [13], it was found that the

thermal offset is higher with clear-sky conditions than with cloudy skies. Thus, two different corrections have been determined as a function of the sky condition. The thermal offset measured during day-time in clear-sky conditions is higher than the one measured during nighttime in agreement with experimental findings reported by *Vignola et al.* [39]. Moreover, the offset correction determined during day-time tests provides the best agreement when directly comparing irradiance measured with Kipp & Zonen CMP22 and Kipp & Zonen CM11 and therefore it was used to correct irradiance measurements by the two pyranometers. In the case of Trisaia site, instead, data of global and diffuse irradiance have been corrected by using the observations of nighttime thermal offset.

The overall uncertainty of GHI, DHI and DNI data is obtained by combining the uncertainty due to the calibration with the components reported in Table 1 and the uncertainty of the acquisition system. The procedure described by *Padovan and Del Col* [11] has been adopted for combining the various uncertainty components. For diffuse irradiance, the contribution of the directional response has been neglected. Moreover, zero uncertainty is attributed to the correction of *LeBaron et al.* [34]. The statistical type A uncertainty has also been calculated and taken into account. However, as discussed in [11], this contribution is negligible with clear and overcast skies, which is the case of stationary conditions.

1.2.2 Experimental results

The solar experimental data collected in Padova were measured from June 15, 2011 to April 23, 2013. During this period, solar radiation records of nearly 260 days have been acquired. The measurements at Trisaia were taken from August 2012 to August 2014, and 400 days were characterized. In both Padova and Trisaia databases, the irradiance measurements are taken with a time step of 5 s and then the minimum, average, maximum and standard deviation are stored every minute.

In Figure 3, the daily trend of DNI, observed in clear-sky condition on a summer (graphs on the left) and a winter (graphs on the right) day in Padova (top graphs) and in Trisaia (bottom graphs), is plotted as a function of the local time: the two sets, reported in each graph, correspond to the DNI measured with the pyrheliometer and the DNI calculated from the global

and the diffuse irradiance measurements. The bands of experimental uncertainty at 95% of confidence level are also drawn. For the site of Padova, the experimental uncertainty of the measured DNI is ±2.5%, while for Trisaia the uncertainty of it results ±2%.

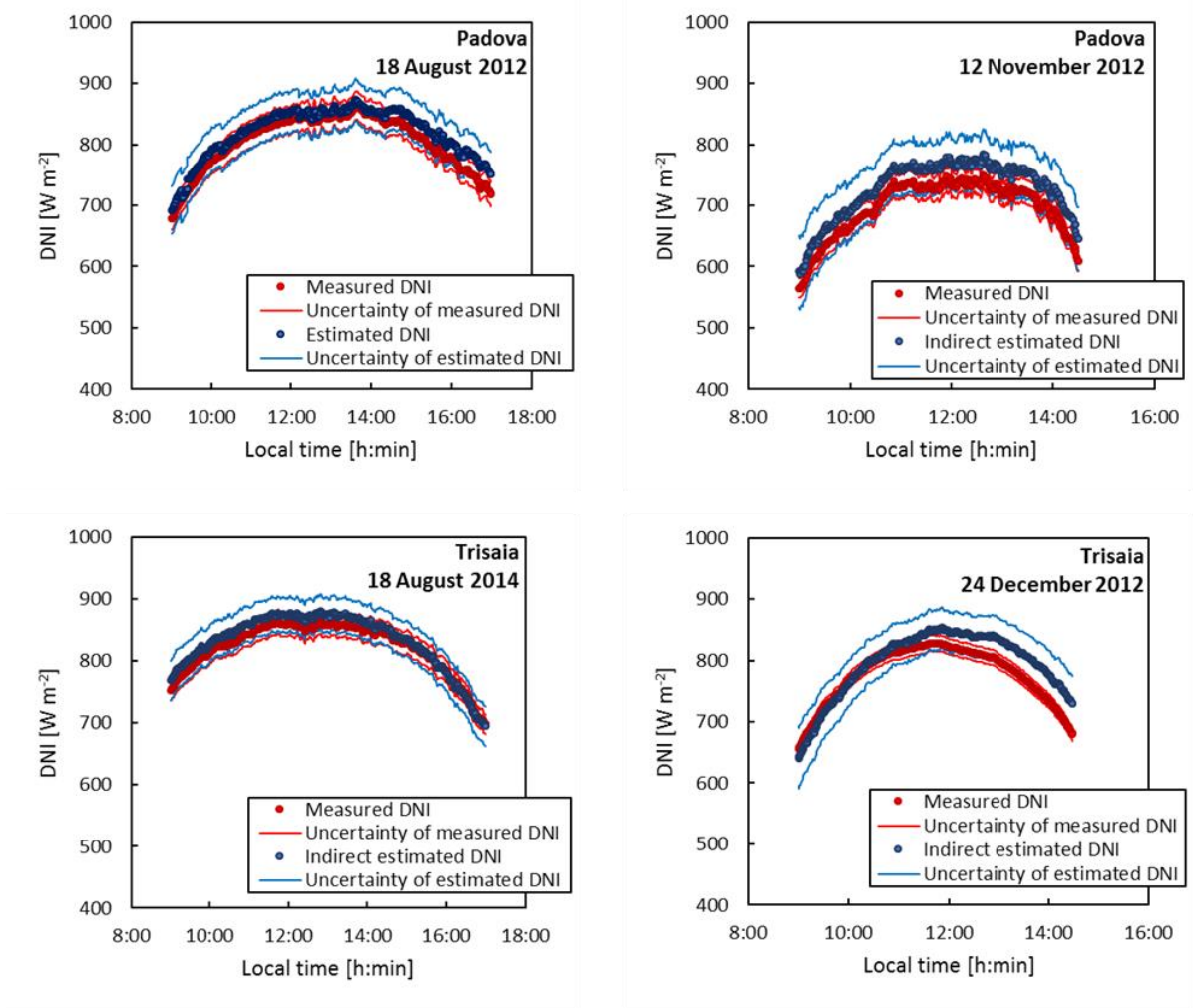

Figure 3 – Measured and calculated direct normal irradiances vs. local time for a clear-sky day in Padova (top) and Trisaia (bottom) in summer (left) and winter (right).

For both sites, close agreement between calculated and measured DNI is found on the summer day. In that case, at solar noon the uncertainty of DNI_{calc} is ±4% and ±3% in Padova and Trisaia respectively, but it increases in first morning and late afternoon due to the effect of the directional response. In Padova, at around 17:00 local time the uncertainty of DNI_{calc} is ±7%, while in Trisaia the uncertainty of DNI_{calc} remains lower than ±5% all day long.

On the winter day, the indirect method overestimates DNI more than on the summer day and on average its uncertainty is higher because of the higher zenith angles that characterize the sky conditions. At solar noon in Padova, the uncertainty of DNI_{calc} is ±5.5%, but it increases up to ±11% in the ends of the day, when higher values of zenith angle occur. At Trisaia site, the uncertainty of calculated DNI is ±3.5% at solar noon and ±7% at 15:00 local time. Two reasons can explain the higher disagreement between estimated and measured DNI found in winter days. The first is associated with the higher zenith angles of winter data, which, according to Eq. 1.1, affect the accuracy of the estimation of DNI more in winter than in summer. The second reason is due to the thermal offset error, which affects the diffuse irradiance measurement more in winter than in summer [13]. Thus, if diffuse irradiance is underestimated, to Eq. 1.1 DNI_{calc} is overestimated as a consequence. It should be noted that the present data were corrected by using an average measurement of thermal offset between winter and summer conditions. At Trisaia site, the offset correction obtained with night-time measurements is quite accurate for summer conditions, but it leads to underestimating diffuse irradiance in winter when the thermal offset error can be higher [13]. Besides, at Padova site, the model by *LeBaron et al.* [34], used for the correction of shadow-band effect in diffuse irradiance measurement, can play a role in the different prediction accuracy between summer and winter. However, for both sites, DNI_{meas} and DNI_{calc} are in agreement within their range of uncertainty for the summer days.

The graph of Figure 4 shows the importance of the thermal offset correction in pyranometers used for global and diffuse irradiance measurements. If it were not corrected, the indirect procedure would overestimate DNI. As a result, one can deduce that the measurement of the DHI is affected by a higher thermal offset as compared to the measurement of GHI and this leads to the overestimation of DNI when Eq. 1.1 is applied. The results have shown that the indirect derivation of DNI from measurements of GHI and DHI can lead to accurate estimations even when the diffuse irradiance is measured with a shadow-band, provided that the systematic error due to the thermal offset is evaluated and corrected. The experimental uncertainty associated with this procedure increases at irradiance conditions characterized by high zenith angles. Good accuracy is achieved when predicting DNI on summer days. The prediction accuracy decreases on winter days, due to the more severe conditions, particularly for diffuse

irradiance measurements, which are affected by a higher type-A thermal offset error as compared to summer conditions. Increase in accuracy is expected if using specific seasonal corrections for type-A thermal offset obtained with day-time tests.

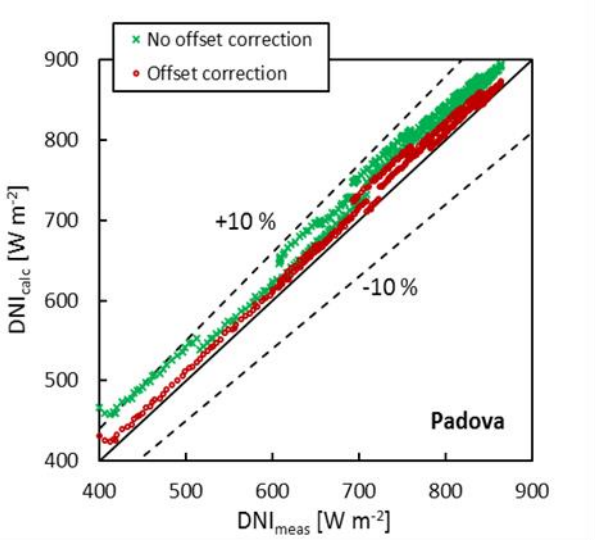

Figure 4 – Difference between DNI indirect estimation with and without offset correction for a summer clear-sky day in Padova.

1.3 Assessment of direct normal irradiance estimation procedures

Solar radiation data are used in several forms and for a variety of purposes. Nowadays, the most detailed information available is beam and diffuse solar radiation on a horizontal surface, by hours, which can be useful in simulations of solar processes [9]. Datasets with time resolution higher than one hour are adequate for design and simulation of concentrating systems. However, as process performance is generally not linear with solar radiation, the use of averages may lead to serious errors if non-linearities are not taken into account [9]. In the future, there will be the need to assess the performance of concentrating systems in the estimation of sub-hourly DNI. It is thus expected that detailed performance simulations of concentrating solar systems will be done with 1- to 10-min time steps to improve accuracy under transient conditions due to clouds [40]. Short-term DNI data are difficult to model because they are more sensitive to the variability of the sky conditions and in fact, high scattering can be found when comparing measurements with model predictions, as shown for example by *Gueymard* [41], and *Padovan and Del Col* [42].

1.3.1 Estimation accuracy of direct normal irradiance for short-term time series

Due to the nature of solar radiation, with a bimodal probability density function, its estimation is always improved when the situations of clear-sky and cloudy sky moments are considered separately [43]. In uncloudy sky situations, solar radiation can be accurately modelled by clear-sky models [44]. Figure 5 and Figure 6 show the prediction accuracy of different estimation procedures for a summer and winter day with clear-sky in Padova and Trisaia, respectively. For the sake of clearness, only some representative procedures (indirect estimation and models of *Erbs et al.*[26], *Perez et al.*[28] and *Skartveit et al.* [29] are shown in the graphs. As it can be seen, the indirect estimation allows good agreement with DNI data, provided that the thermal offset is corrected. With reference to summer case in Padova (Figure 5, left), the model of *Skartveit et al.* [29] and DIRINT [30] (not shown in the graph) agree with the measured DNI within ±10%. The models of *Perez et al*. [28] and *Erbs et al*. [26] estimate within ±10% the

high DNI values, but they become inaccurate when DNI decreases, both in the morning and afternoon. One reason can be the absence of the zenith angle as prediction variable. On the winter day (Figure 5, right), the accuracy of *Perez et al.* [28] and *Erbs et al.* [26] models increase, with estimating errors always within ±10%. On the contrary, the model of *Skartveit et al.* [29] overestimates the measured DNI slightly over 10%.

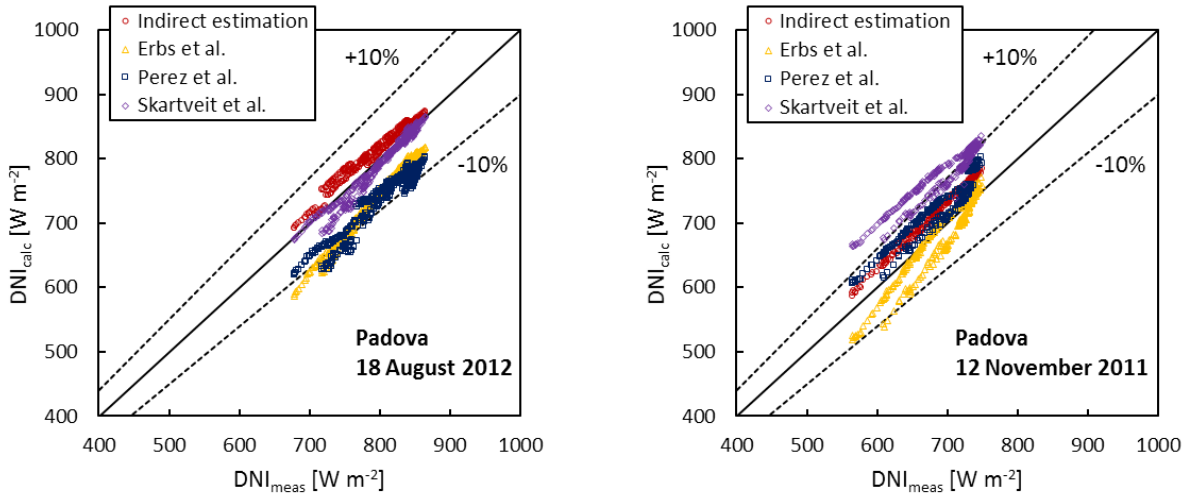

Figure 5 – Calculated DNI vs. measured DNI for a summer (left) and a winter (right) day with clear-sky in Padova.

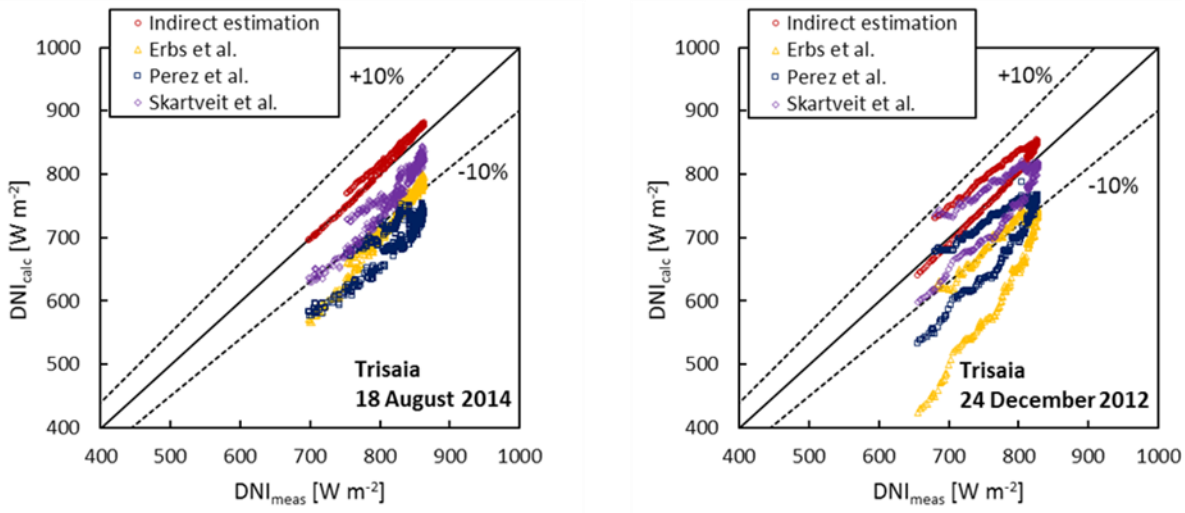

Figure 6 – Calculated DNI vs. measured DNI for a summer (left) and a winter (right) day with clear-sky in Trisaia.

At Trisaia site (Figure 6) the indirect estimation procedure shows higher accuracy as compared to the separation models on the summer day. On the winter day, the indirect procedure tends to overestimate DNI; however, the agreement with measured DNI is within ±10%. Similarly, the *Skartveit et al.* model [29] predicts most of DNI data within ±10% both in the winter and summer days. The *Erbs et al.* model [26], instead, shows a dependence on seasonal conditions, because it estimates within ±10% the measured DNI on the winter day, but the predicting accuracy degrades for the afternoon on the summer day. The model of *Perez et al*. [28] underestimates the measurement both on the summer and winter days.

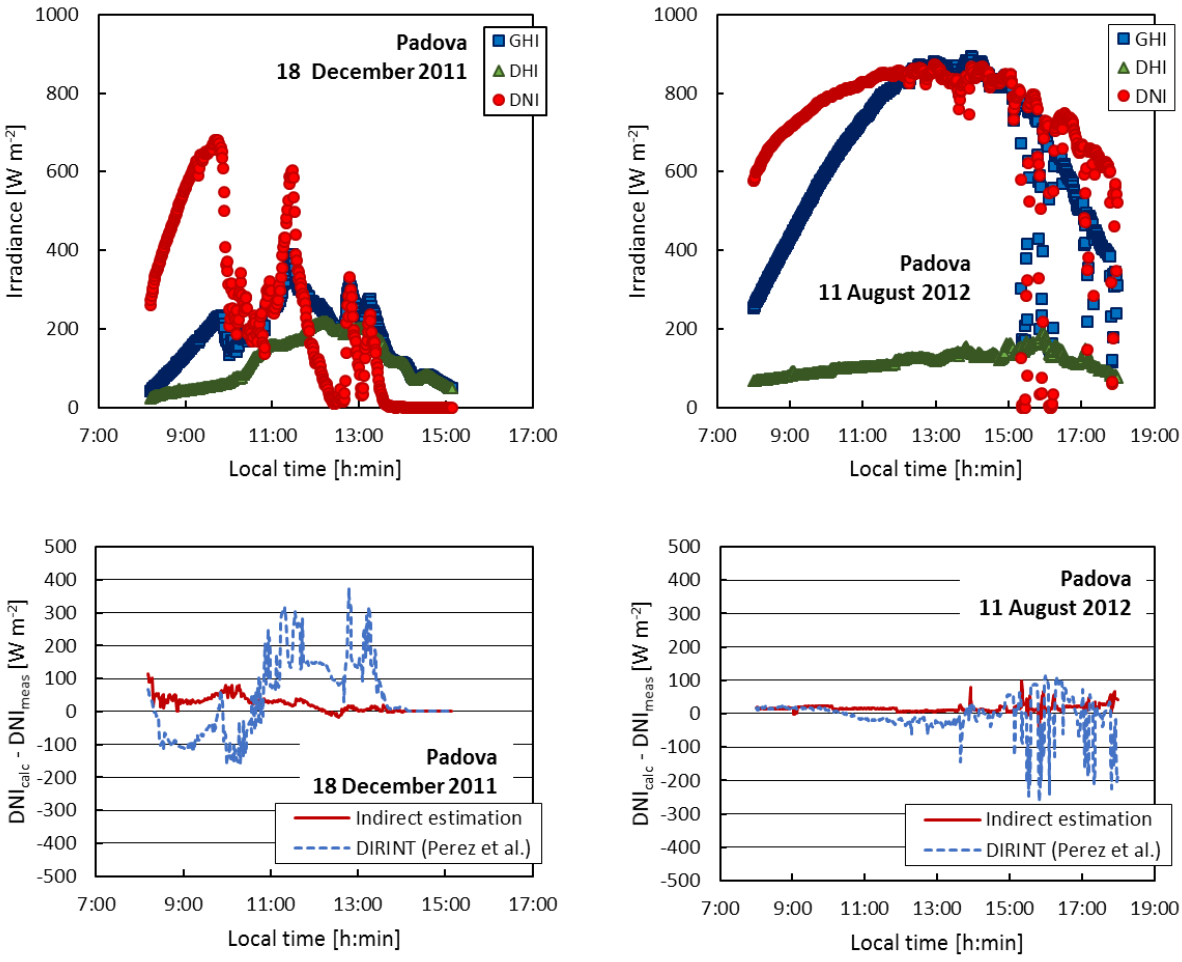

Figure 7 – Difference between calculated DNI and measured DNI for a winter (left) and a summer (right) day in Padova under variable sky conditions. The graphs at the top report the measurements of GHI, DHI and DNI for the same day.

The same effect is visible on the winter day (Figure 7, left). In this case, the indirect method shows a lower accuracy and the DIRINT [30] model has a fluctuating trend. This is probably due to the higher incidence angle as compared to the summer case. The scattering effect can be detected also in Figure 8 or Trisaia site.

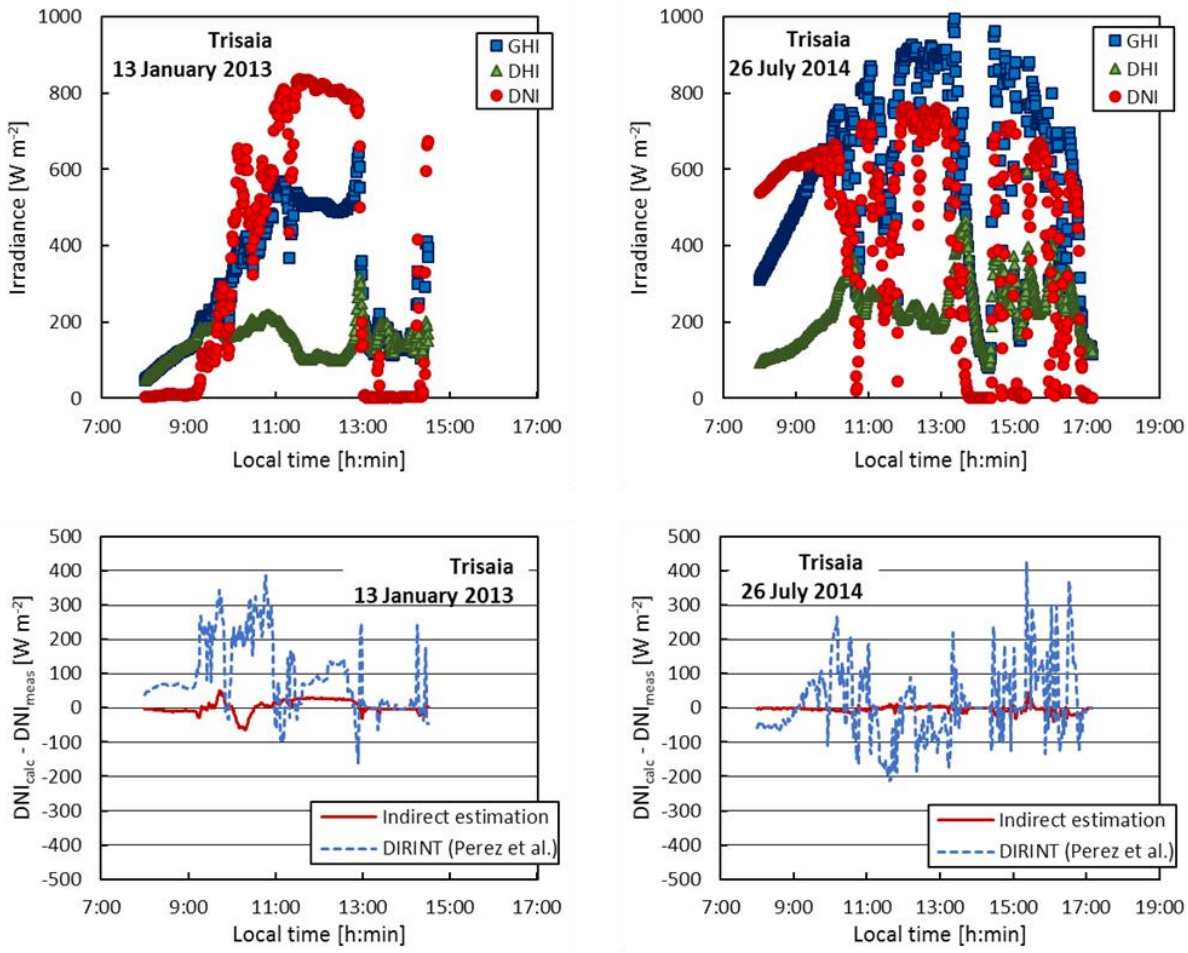

Figure 8 – Difference between calculated DNI and measured DNI for a winter (left) and a summer (right) day in Trisaia under variable sky conditions. The graphs at the top report the measurements of GHI, DHI and DNI for the same day.

The DIRINT [30] model shows opposite trends between winter and summer data during the early morning: on a winter day (Figure 8, left) the model overestimates the measured DNI values, whereas on a summer day (Figure 8, right) its predictions are lower than the measurements. With reference to the indirect method, the data of Trisaia show less scattering under cloudy and partly cloudy sky as compared to the data of Padova. This is particularly true

in winter conditions. The reason of this may be due to the difference between the measuring systems used in the two sites. At Padova site, the two different pyranometers used to measure GHI and DHI, are characterized by different time responses to quick irradiance variations. This can lead to a lower accuracy in DNI estimation in winter when variable sky conditions often occur. Furthermore, at Padova site, irradiance data are affected by the uncertainty contribution due to the adoption of the shadow-band coupled with the correction model of *LeBaron et al.* [34]. Finally, the average thermal offset correction used in Padova can be less accurate during the winter period when type-A thermal offset is higher. The two figures compare the performance of the indirect procedure and separation models at Padova and Trisaia sites, respectively, on a summer and on a winter day in variable sky conditions. The DIRINT [30] model is shown as a representative model. On the summer day at Padova site (Figure 7, right) in the morning, the sky conditions are stable and both the indirect procedure and the DIRINT [30] model shows a constant performance, with a good accuracy. When sky variability begins in the afternoon, both estimation methods show scattering, in particular, the DIRINT [30] model seems to be very sensitive to the variability in sky conditions.

Hourly direct normal irradiation H_h values were used to compare different indirect estimation procedures in summer and winter conditions for both Padova and Trisaia sites. Measured and estimated 1-min DNI values are numerically integrated over a time step of one hour to obtain the corresponding values of hourly direct normal irradiation H_h, which expresses the specific energy associated with direct normal solar radiation for one hour. In Figure 9, indirect estimated H_h is plotted against measured H_h. The indirect measurement procedure shows the good accuracy of estimation both in summer and in winter. The winter and summer periods for Padova refer to the data between November 2011 and January 2012, and between June 2012 and August 2012, respectively. For the Trisaia site, the winter period covers the data from November 2012 to January 2013, while the data between June 2014 and August 2014 are included in the summer period.

At Padova site (Figure 9, left) the indirect method slightly overestimates the measured data. This trend is clearer during the winter period, in particular, for low values of H_h. Winter data present higher scattering, whereas in summer the data distribution is more compact. As expected, closer agreement with the measured values in both summer and winter conditions

has been found for the indirectly estimated data in Trisaia (Figure 9, right). For this site, the scattering of the hourly data results reduced as compared to that present for the Padova dataset.

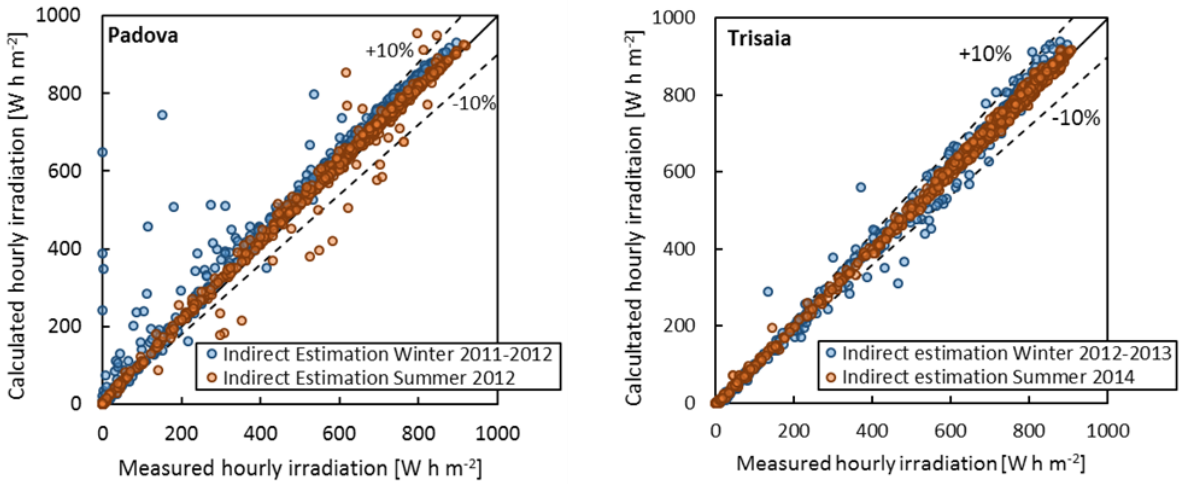

Figure 9 – Indirect estimated $H_{h,calc}$ vs. measured $H_{h,meas}$ hourly normal direct irradiation in summer (orange) and in winter (blue) for Padova (left) and Trisaia (right) sites.

The presence of scattered data can be explained by observing Figure 10, where hourly prediction errors eh are plotted as a function of hourly diffuse fraction $k_{d,h}$. The hourly prediction error e_h is defined as:

$$e_h = \frac{H_{h,calc} - H_{h,meas}}{H_{h,meas}} \qquad \textit{Eq. 1.7}$$

The value $k_{d,h}$ of the hourly diffuse fraction is calculated as the average ratio of diffuse fraction k_d over one hour:

$$k_d = \frac{DHI}{GHI} \qquad \textit{Eq. 1.8}$$

As can be seen in Figure 10, large hourly errors e_h are usually associated with high values of hourly diffuse fraction $k_{d,h}$, which characterize cloudy sky conditions. High values of error e_h are present at lower values of diffuse fraction $k_{d,h}$ too: these points refer to variable sky conditions with partial overcast sky and high instability. As shown in Figure 7 and Figure 8, the variability in the sky conditions has a strong influence in the estimation of the DNI and

this effect is still detectable in the predictions of H_h. Moreover, in winter, the variability in the sky conditions is combined with higher values of incidence angle, leading to a more evident scattering effect.

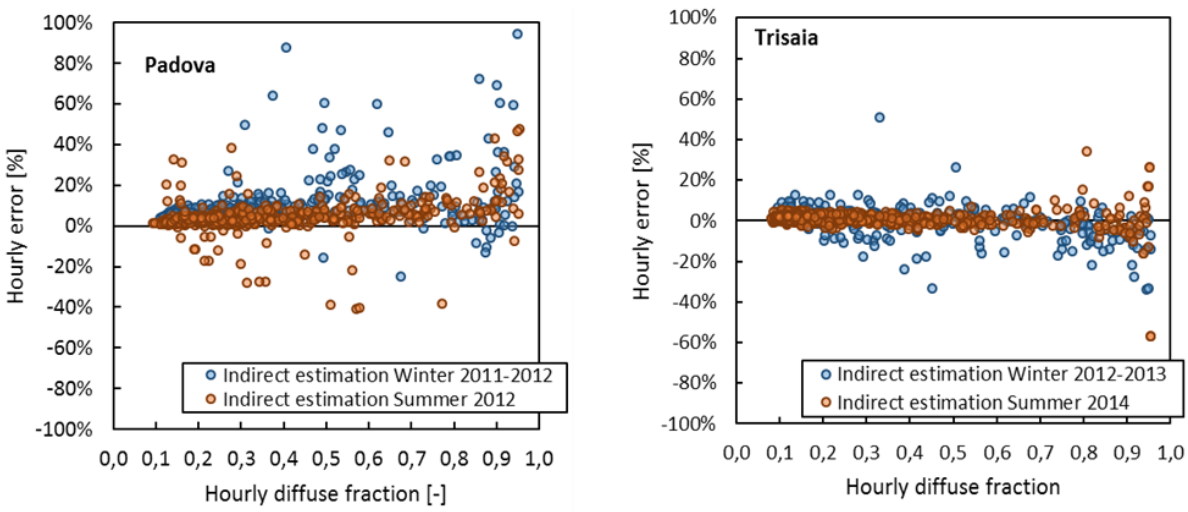

Figure 10 – Hourly prediction error e_h of the indirect method against hourly diffuse fraction $k_{d,h}$ in summer (orange) and in winter (blue) for Padova (left) and Trisaia (right) sites.

The separation models considered in this study to estimate the DNI have given quite different results for the two sites under investigation. At Padova site for the reported days, some models, such as the models of *Erbs et al.* [26] and *Perez et al.* [28] have shown a good accuracy in generating clear-sky short-term DNI time series. For Trisaia database, the separation models have shown higher inaccuracy in short-term predictions. Moreover, for the same site, the accuracy of the models in generating short-term DNI time series depends on sky conditions, showing better accuracy for clear-sky days. The accuracy of the models decreases significantly under variable sky conditions.

1.3.2 Estimation accuracy of direct normal irradiance for long-term time series

This section discusses how long-term effect can affect the evaluation of direct irradiation when using different estimation procedures to predict the daily H_d, monthly H_m and seasonal H_s direct

normal irradiation. Measured and estimated 1-min DNI values are numerically integrated over a time step of one day, month and season, respectively, to obtain the corresponding values of specific energy associated with direct normal solar radiation.

The daily direct normal irradiation H_d values were used to compare different estimation procedures in summer and winter conditions for both Padova and Trisaia sites. In the graphs of Figure 11, the daily prediction error e_d is plotted against the daily diffuse fraction $k_{d,d}$ for different estimation procedures.

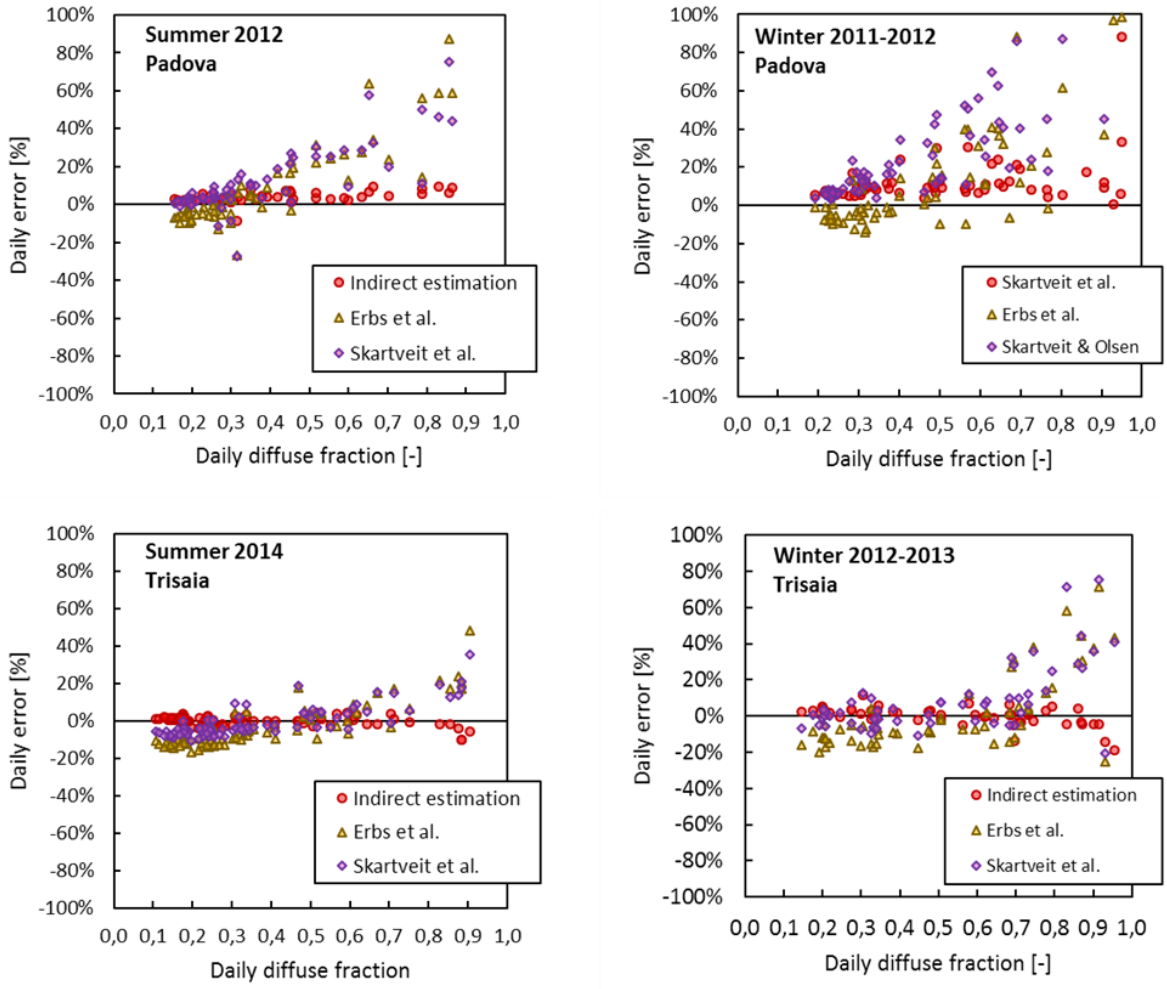

Figure 11 – Daily prediction error e_d as a function of the daily diffuse fraction $k_{d,d}$ in summer (left) and in winter (right) in Padova (top) and Trisaia (bottom) sites when different estimation procedures are applied.

For the purpose of clearness, only the *Erbs et al.* [26] and the *Skartveit et al.*[29] models are compared to the indirect measurement method. The daily error e_d and the daily diffuse fraction $k_{d,d}$ are evaluated according to Eq. 1.7 and Eq. 1.8 .Compared to the models, the indirect method shows a better accuracy in the evaluation of the daily direct normal irradiation H_d. The models tend to overestimate the measured H_d at high values of diffuse fraction related to cloudy sky days. The models tend to underestimate H_d in clear-sky conditions characterized by low values of the diffuse fraction. The summer datasets are mainly composed of days with daily diffuse fraction lower than 0.4, while in winter, the daily diffuse fraction is even higher than 0.5 and the variability of sky conditions is more frequent. These conditions are particularly unfavourable in the case of Padova where the variability in the sky conditions seems to have a stronger influence on the prediction of the models, as mentioned in the Paragraph 1.3.1. However, it can be seen that in the predictions of the daily direct normal irradiation H_d, the scattering at middle and low values of diffuse fraction results reduced compared to the hourly results. In summer at Trisaia site, the diffuse fraction reaches lower values compared to the Padova dataset, and the days characterized by diffuse fraction lower than 0.2 are more frequent. That reflects the presence of a higher number of clear-sky days during the summer period.

The previous observations can be useful to explain the monthly and seasonal results plotted in Figure 12 and Figure 13, respectively. Figure 12 presents the monthly prediction errors e_m for the different procedures under investigation. Each graph refers to a season and a site. Finally, Figure 13 highlights the difference in the performance of the models in summer and in winter for the two sites. This graph compares the indirect measurement procedure and separation models in terms of seasonal prediction error e_s.

Referring to Trisaia site, the separation models seem to perform better in winter than in summer (Figure 13). The reason of this can be related to the compensation between the cloudy days in the January dataset and the data of the other two winter months characterized by lower daily diffuse fractions $k_{d,d}$ (Figure 12). Instead, the summer months in Trisaia present mainly clear-sky stable conditions and lower values of the diffuse fraction. The result is that the separation models underestimate the measured H_s during the summer period. In this season, the most recent model, the one proposed by *Skartveit et al*. [29], provides the lower seasonal prediction error (around 3%).

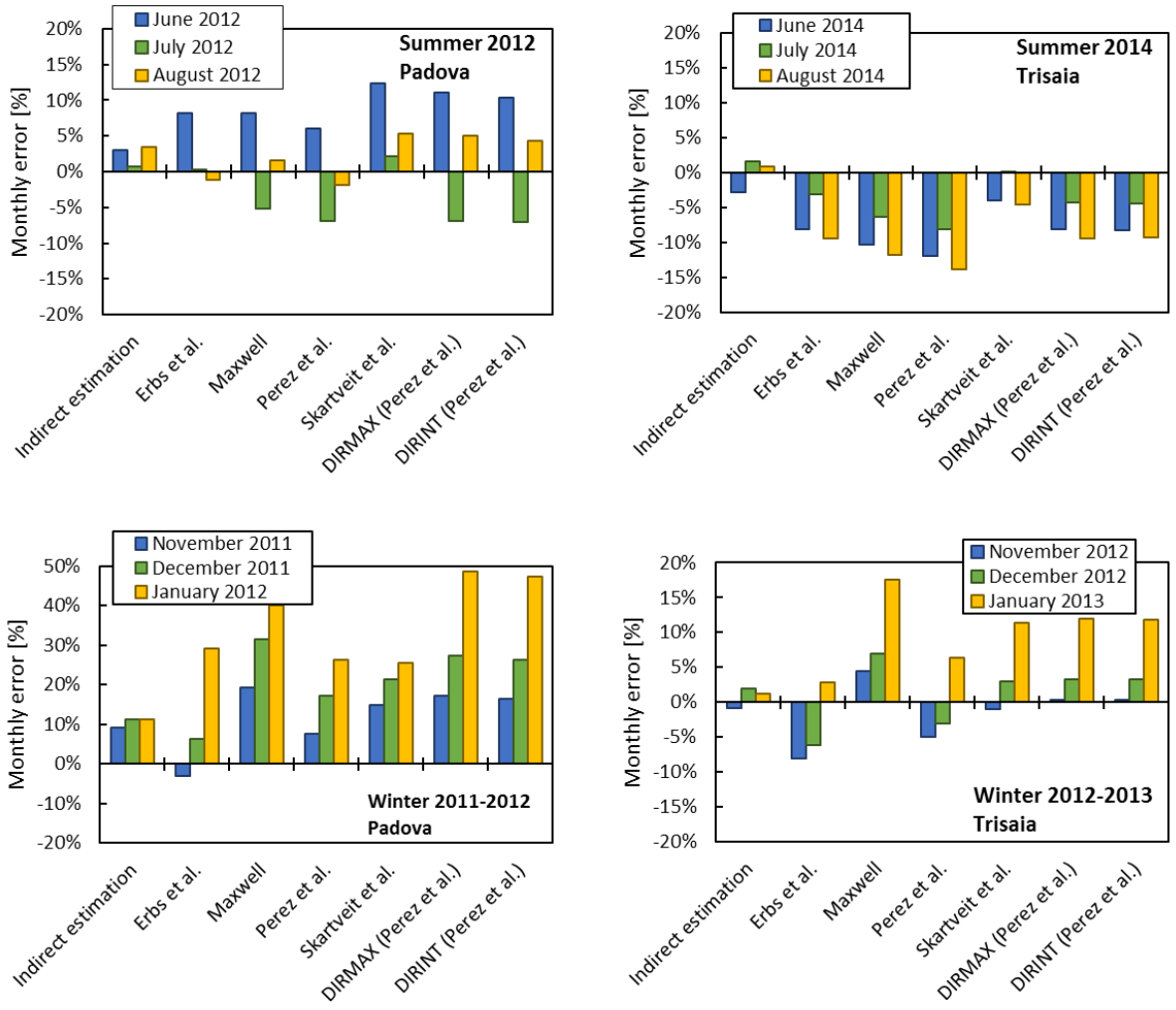

Figure 12 – Monthly prediction error e_m for summer (top) and winter (bottom) months in Padova (left) and in Trisaia (right) when different estimation procedures are applied.

Other models predicted the measured H_s with errors between –7% and –12%. On the contrary, in winter the models show a general tendency to overestimate H_s, with seasonal errors always below 10% (Figure 13). The model of *Erbs et al.* [26] shows the lowest seasonal dependence in the prediction accuracy; in winter, it presents an opposite trend with respect to the other models. In winter, the model of *Perez et al.* (Perez et al. 1990) has the highest accuracy (seasonal error lower than 2%), thanks to the compensation among the different months.

The summer case in Padova is characterized by the overestimation of all methods under investigation, however, the seasonal error e_s remains lower than 8%. An explanation of this can be the higher values of diffuse fraction during most of the days, as shown in Figure 11. In summer, the most accurate model for the Padova dataset is the one of *Perez et al.* (1990 Perez et al) (as for the winter case in Trisaia). During winter, the performance of the procedures strongly degrades. This is probably due to the higher incidence angle combined with higher variability in the sky conditions. The variability in the winter sky conditions can be seen in the fluctuations of H_h in the left graph of Figure 9 (blue points). Furthermore, the overestimation in the summer case is reduced thank to the opposite trend of the month of July (Figure 12) with respect to the other months. This reduction further emphasizes the difference between summer and winter cases.

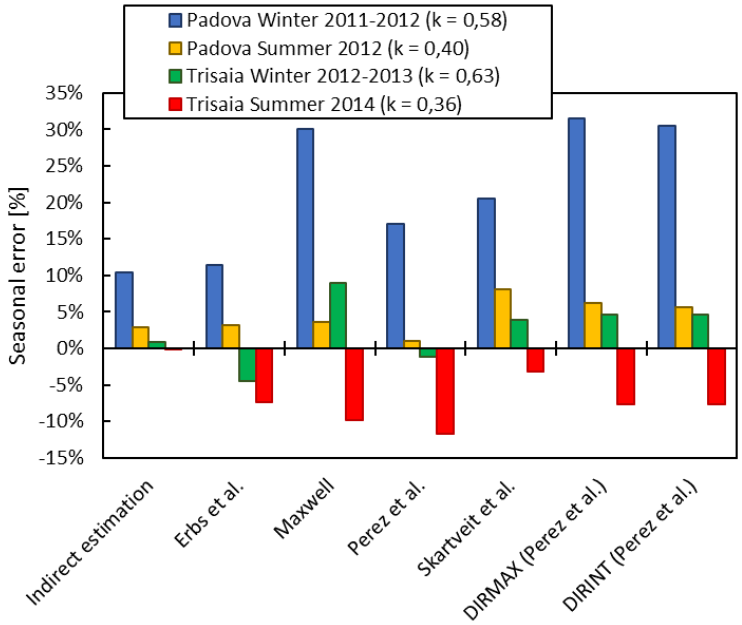

Figure 13 – Seasonal prediction error e_s for summer and winter in Padova and in Trisaia when different estimation procedures are applied. The values in brackets refer to the seasonal diffuse fraction $k_{d,s}$.

The indirect measurement method presents higher accuracy than the separation models and more stable seasonal performance. At Trisaia test site, the monthly estimation error e_m results lower than 3% for both summer and winter seasons. The resulting seasonal errors are between

±1%. The indirect estimation in Padova presents higher seasonal errors compared to the case of Trisaia. The reason for that must be searched in the difference of the measurement systems and adopted procedures in the two sites, as mentioned in Paragraph 1.2. In any case, the indirect method presents good accuracy with the measured data. In summer and winter at Padova site, the seasonal errors of prediction are +3% and +10%, respectively.

Concluding, sky variability affects the accuracy of the models in the estimation of long-term (daily, monthly and seasonal) DNI, proving the high sensitivity of the correlations to the sky conditions. When stable sky conditions characterize most of the database, the performance of the models is better than in the case with higher sky variability. Moreover, for low values of diffuse fraction, the models underestimate the measured values of DNI. On the contrary, when the days are characterized by high values of diffuse fraction, the separation models tend to overestimate the direct normal irradiation along the integration period. The models can show different behaviour for the two sites under investigation at the same daily diffuse fraction, even under clear-sky conditions; this suggests that their performance is also affected by climatic and atmospheric conditions, which can be site-dependent. Regarding the indirect measurement procedure, it shows good accuracy in estimating long-term DNI both in winter and in summer. Therefore, the indirect procedure presented in this work can be a valid method to produce long-term data of direct normal irradiation when measurements from pyrheliometers are not available.

Chapter 2 Concentrated solar flux in an asymmetrical parabolic trough concentrator

A solar concentrating collector consists of an optical system, named concentrator, and a receiver. The scope of the concentrator is to concentrate the solar radiation falling on a larger surface onto a smaller surface (receiver). Appropriate reflecting or refracting components are used to increase the flux density of the beam radiation onto a focal region, where the absorber (receiver) surface is installed to convert the solar radiation into heat or electric energy. The main advantage of using concentrating systems is the reduction of the heat losses from the absorber by reducing its area. The ratio of the aperture area of the concentrator to the receiver area is defined as the geometrical (or optical) concentration ratio and it qualitatively provides the operating temperature range of a concentrating collector. In ideal optics, parallel rays normally incident on the aperture area of a parabolic trough are concentrated along a focal line. To work efficiently throughout the day, the system must be equipped with a tracking system to maintain the Sun vector on the plane normal to the aperture area and containing the focal line. In real applications, there is a concentration region around the focal line, whose width depends on the Sunshape and the total optical error. The Sunshape represents the brightness intensity distribution across the finite angular size of the Sun disc and the circumsolar aureole and depends on the sky conditions. The total optical error includes the shape and specular reflectance errors of the mirrors, the tracking error and the imperfect positioning and alignment of the receiver.

In this Chapter, the optical performance of an asymmetrical small parabolic trough solar concentrator is characterized. The final performance of the solar collector results strongly influenced by the optical quality of the parabolic trough. Adopting a direct measurement method, the optical performance of the trough is experimentally characterized to define the solar flux map on the focal region. The aim of the present experimental activity is also to

develop a statistical ray-tracing model of the concentrator for optical performance analysis in different working conditions and optimized design of the receiver both for thermal and photovoltaic applications. By comparing the experimental results with the numerical optical performance predictions, it is possible to identify the most appropriate value of the total optical error for the investigated solar device.

2.1 Concentration in parabolic trough

Linear concentrators with parabolic cross-section have been largely studied and have been proposed and used for many applications requiring intermediate concentration ratios and temperatures in the range of 100 to 500◦C. Nowadays, parabolic trough concentrators (PTC) are the dominating technologies in the concentrating solar thermal power market. Parabolic trough systems representing the bulk of capacity that became operational in 2016 as well as most of the capacity expected to come online during 2017 [45]. Parabolic trough collectors are also used to provide process heat for a growing number of manufacturing facilities. Process heat accounts for around two-thirds of final energy consumption in the industry sector, and around the 50% of that heat demand is in the temperature range below 400°C and thus suitable for parabolic trough collectors.

Parabolic trough collectors feature a concentrator shell with parabolic sections in a cylindrical configuration. The focus of the cylinder parabola is a straight line (Figure 14).

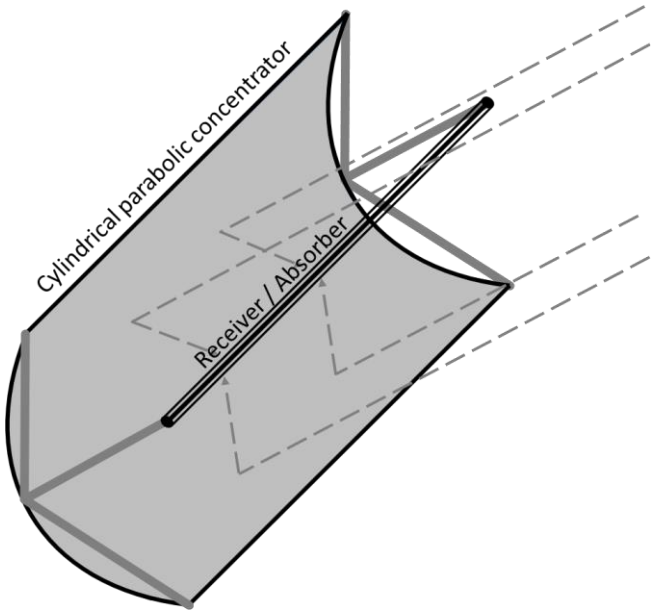

Figure 14 – Parabolic trough concentrator.

The receiver used with this concentrator is typically cylindrical and is enclosed in an evacuated tubular glass cover; flat receivers have also been used with reflectors of this type [9]. The heat

transfer fluid is heated as it flows through the absorber. The reflecting element of a solar concentrator should have high reflectance and good specular reflectance. Glass silvered either on the rear or a second surface is usually used as mirror materials in the parabolic trough. Glass is the most durable material with low-iron content. It can be used as a transmitting material whereas aluminium and silver are very good reflecting surfaces with a total reflectance of approximately 85% – 90% and 95%, respectively [46]. To increase the absorption capacity of the receiving a surface coating with a strong absorptivity is usually adopted. The coating should be stable at high temperatures and be cost-effective. Black-chrome appears to be one of the best selective coatings among the others. Other metal-oxide coatings, namely, black copper oxide and black nickel, are also used. Selective paints, such as lead sulfide particles in a silicon binder, can give better results but with increased cost.

The following four parameters are commonly used to characterize the form and size of a parabolic trough: trough length, focal length, aperture width and rim angle. Figure 15 reports a schematic of a parabolic trough where the geometrical parameters are highlighted.

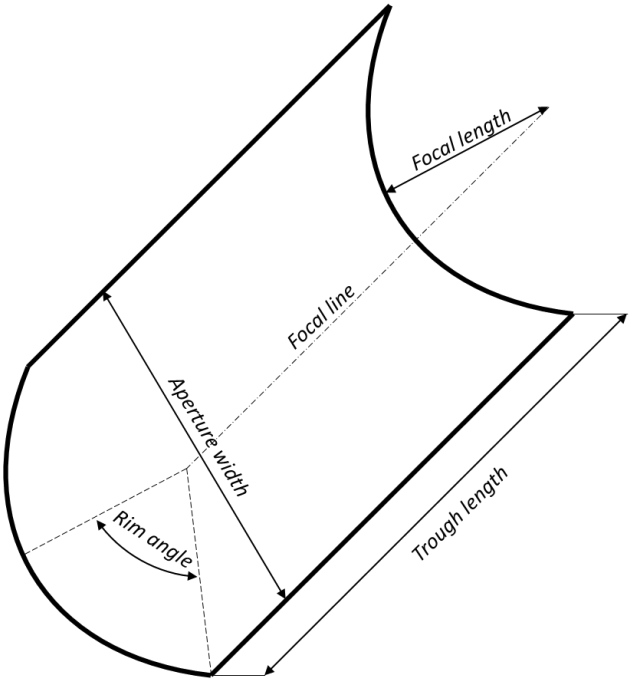

Figure 15 – Geometrical parameter of a parabolic trough.

The focal length f_c is the distance between the focal line and the vertex of a parabola. From a mathematical point of view, this parameter is sufficient to determine completely the parabola. The rim angle ϕ_c is the angle between the optical axis and the line between the focal line and the mirror rim. This parameter alone determines the shape of the cross-section of a parabolic trough. To determine the cross-section of a parabolic trough completely, i.e. shape and size, two of the three parameters rim angle, aperture width and focal length are sufficient. The limiting angle over which the incident solar radiation is accepted (reaches the absorber/receiver surface after reflection) without moving all or part of the collector, is called acceptance angle, $2\theta_c$. For larger acceptance angles, solar concentrators can be moved seasonally to track the Sun, whereas, for smaller acceptance angles, a continuous tracking system is required. Besides the specific geometrical linear measures of a parabolic trough, also surface area measures are very important for concentrating systems. The aperture area A_a is the area on the front of the solar concentrator that accepts the incident solar beam radiation. The receiver (absorber) area A_r is the total area that receives the concentrated solar beam radiation. The aperture area A_a, the acceptance $2\theta_c$ and rim ϕ_c angles, and absorber/receiver size A_r and shape may be used to characterize the ideal optical performance of the collector.

The ratio of the aperture area to the absorber/receiver area defines the geometric concentration ratio C_g, which qualitatively provides the operating temperature range of a concentrating collector. The solar concentration ratio for a cylindrical absorber in commercial trough varies from 5 to over 90. From the point of view of thermodynamic considerations, the upper limit of the concentration of any concentrating collector has been obtained by *Rabl* [47]. It has been observed that the maximum possible concentration is the reciprocal of the radiation shape factor between the Sun and the solar concentrator. With reference to Figure 16, it has been assumed that the Sun is a black body at the temperature T_S and that the collector is surrounded by vacuum; the fraction of the solar radiation that hits the aperture area A_{ap} of the concentrator is given by:

$$q_{S-ap} = A_a \frac{r_s^2}{d_{S-ap}^2} \sigma T_S^4 \qquad \textit{Eq. 2.1}$$

Considering a perfect concentrator optics, no radiation is lost between aperture and absorber, thus the heat radiated from the source to the absorber q_{S-r} coincides with the solar radiation that

hits the aperture area q_{S-a} of Eq. 2.1. The radiative transfer from the absorber at the temperature T_r to the Sun is:

$$q_{r-S} = \varepsilon_r A_r \sigma T_r^4 \qquad \textit{Eq. 2.2}$$

where the term ε_r expresses the fraction of the radiation emitted by the receiver which reaches the Sun. Obviously, this term cannot exceed unity.

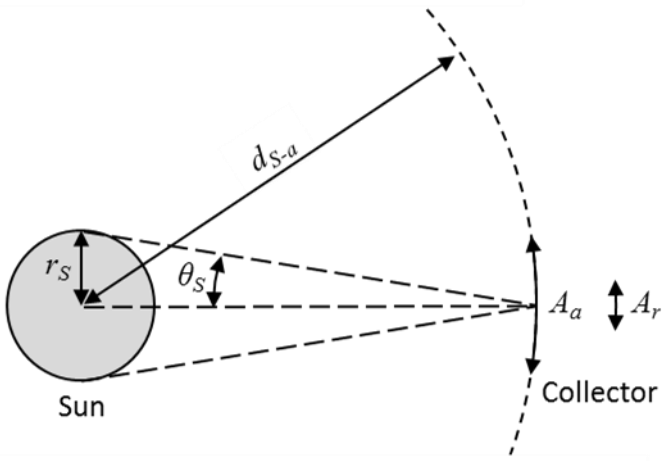

Figure 16 – Radiation transfer from the Sun through the aperture to the receiver of a concentrating collector.

By the second law of thermodynamics, between two bodies of equal temperatures, it cannot be any net heat transfer. Hence, it can be read off ideal concentration, as the maximum concentration permitted by the second law of thermodynamics, for any three-dimensional optics is

$$C_{g,ideal,3D} = \frac{d_{S-a}^2}{r_s^2}\varepsilon_r = \frac{1}{sin^2(\theta_c)} \qquad \textit{Eq. 2.3}$$

Linear focusing concentrators, such as a parabolic trough or linear Fresnel reflector present the thermodynamic concentration limit for two-dimensional geometries:

$$C_{g,ideal,2D} = \frac{1}{sin(\theta_c)} \qquad \textit{Eq. 2.4}$$

The maximum of this limit is determined by the minimum acceptance half-angle θ_c. Considering that the solar concentrator is always facing the Sun, the minimum acceptance half-

angle θ_c is equal to the half-angle of the solar disc θ_S, which is about 0.267°. According to Eq. 2.3 and to Eq. 2.4, the concentration limits for a three-dimensional concentrator and a two-dimensional concentrator are of the order of 40000 and 200, respectively. However, in practice, solar concentrations are different due to the finite acceptance angles [46]. Considering a parabolic cylinder, the concentration ratio for a flat absorber depends on whether it is one-sided or two-sided. A two-sided absorber does not lose any radiation because of shading, but its surface area is twice as large compared to a one-sided absorber [47]. The concentration ratio for a flat absorber (one-sided) is given by:

$$C_{g,pc,flat\ 1\ sided} = \frac{sin(\phi_c)cos(\phi_c + \theta_c)}{sin(\theta_c)} - 1 \qquad \textit{Eq. 2.5}$$

The concentration ratio for two-sided flat absorber is related to the concentration ratio for one-sided flat absorber as following:

$$C_{g,pc,flat\ 2\ sided} = 2 \cdot C_{g,pc,flat\ 1\ sided} - 1 \qquad \textit{Eq. 2.6}$$

and reaches a maximum at

$$\phi_{c,pc,ideal} = \frac{1}{2}\left(\frac{\pi}{2} - \theta_c\right) \qquad \textit{Eq. 2.7}$$

It is interesting to note the existence of a relationship between the geometrical concentration ratio and temperature at which a solar receiver can operate. The higher the temperature at which energy is to be delivered, the higher must be the concentration ratio and the more precise must be the optics of both the concentrator and the orientation system [9]. Assuming, the rest of the universe (other than the Sun and the absorber) is a black body at the temperature of 0 K. The radiation emitted by the Sun and absorbed by the receiver characterized by an absorbance α_r in a solar concentrator with a reflectance ρ_c is given by:

$$q_{S-r} = \rho_c \alpha_r A_a sin(\theta_s) \sigma T_S^4 \qquad \textit{Eq. 2.8}$$

The radiation losses from the absorber are

$$q_{r,rad} = \varepsilon_r A_r \sigma T_r^4 \qquad \textit{Eq. 2.9}$$

where ε_r is the emittance coefficient of the absorber in the spectral region corresponding to the surface temperature of the receiver. If a fraction η_c, of the incoming solar radiation (Eq. 2.8) is

extracted as useful heat and lost by convection or conduction, then the energy balance of the absorber reads

$$q_{S-r} = q_{r,rad} + \eta_c q_{S-r}$$
$$(1-\eta)\rho_c \alpha_r A_a sin(\theta_s)\sigma T_S^4 = \varepsilon_r A_r \sigma T_r^4 \qquad \textit{Eq. 2.10}$$

From the previous equations, it results that the temperature at which a solar receiver can operate in a concentrating collector depends on the actual and ideal geometrical concentration ratios:

$$T_r = T_S \left((1-\eta) \frac{\rho_c \alpha_r}{\varepsilon_r} \frac{C_g}{C_{g,ideal}} \right)^{1/4} \qquad \textit{Eq. 2.11}$$

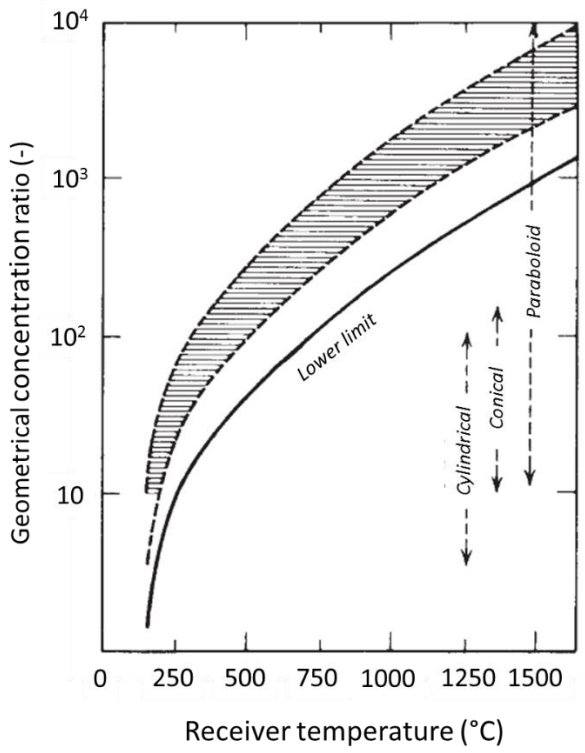

Figure 17 – Relationship between geometrical concentration ratio and temperature of the receiver [9].

The highest possible temperature of the receiver is T_S (around 6000 K). This condition can be reached only if no heat or radiation is lost, and if the actual geometrical concentration ration equals the three-dimensional ideal concentration ratio. For two-dimensional concentrators, due

to the limited ideal geometrical concentration ratio, the absorber temperature T_r is reduced by a factor $213^{-1/4}$ (around 1/4). Figure 17, proposed by *Duffie and Beckman* [9], shows practical ranges of concentration ratios and types of optical systems needed to deliver energy at various temperatures. The lower limit curve represents concentration ratios at which the thermal losses will equal the absorbed energy; higher ratios will then result in lower useful gain. The shaded range corresponds to collection efficiencies of 40 to 60% and represents a probable range of operation. Also shown are approximate ranges in which several types of reflectors might be used.

The work of *Hoffschmidt et al*. [48] contains an exhaustive survey of the evolution of the design and manufacturing of PTC as well as their constructions details. The following brief overview of the commercial model of PTC referred mainly to this work. At the beginning of the technical development in the early 1980s, the size of the trough has been increased from 34 m^2 for the Acurex model to 128 m^2 for the Luz LS-1 collector. The Luz LS-1 PTC presents an aperture of 2.5 m and a concentration ratio of 61. The next generations of the Luz collectors represent the standard by which all other collectors are compared [49]. The mirror aperture of the Luz LS-2 was increased to 5 m and its length was 49 m. For reducing manufacturing costs, Luz designed the larger LS-3 to lower manufacturing tolerance and steel requirements. The LS-3 reflectors were the last design produced by Luz and they were made from mirrored glass panels with a width of 5.76 m and a 4 m long receiver. The design of the EuroTrough PTC was based on the LS-3 collector technology of Luz. It has been developed for the generation of solar steam for process heat applications and solar power generation. The aperture length of the mirror is 5.45 m and its optical concentration is 94 [50]. The outcome of the EuroTrough project was above all the prototype of commercial products under test [48]. Under the US Department of Energy's USA Trough Initiative, Solargenix developed a new collector structure through a cost-shared R&D contract with NREL [51]. In 2005, Flagsol GmbH jointly with Schlaich Bergermann und Partner (SBP), Fraunhofer Institute for Material Flow and Logistics (IML), and DLR started the development and design of the next generation PTC, named HelioTrough [52]. Compared to the EuroTrough collector, this new approach provides the same thermal output with 10% smaller solar field. In 2010, SBP and Fraunhofer IML started the development of the next generation collector for parabolic trough power plants under the leadership of

FLABEG Holding GmbH. The new design of the Ultimate Trough collector was developed with an aperture width of 7.5 m [53]. As a further result of improved efficiency, the Ultimate Trough technology allows a reduction of the investment cost for the solar field. The latest version of the Abengoa Solar's PT-1 PTC system is the result of more than 20 years of continuous improvement aimed at increasing performance and durability while reducing costs and maintenance requirements [48]. The trough is 6.1 m long and has an aperture area of 14 m^2. A compact roof-mounted value-engineered version of the PT-1 of this collector was designed with a surface of about 4 m^2. It employs the same unique patented space frame design, but its smaller profile reduces wind loads to allow roof-mounting. The collector performance is similar, although the delivered energy is estimated to be 5–10% less than the original design of the PT-1 [54]. Other PTC models have been tested in experimental facilities or installed in demonstrative projects, however, their design is based on the older model that has been presented.

Nowadays, the investment on the research activities with the aim to develop, design, and optimize the first prototypes and introduce new models of PTC in the market has been significantly reduced as compared to the last three decades. Universities, research institutes as well as industries have focused their research activities in the development and optimization of system components, such as innovative receivers. The major thermal losses from a concentrator/receiver assembly for normal incidence are due to convection and irradiation from the absorber surface to the surroundings. To improve the performance of a solar concentrator, the rate of thermal losses from the receiver must be minimized. This implies the reduction of the receiver area. However, a small a size of the absorber can imply a reduction in the capacity of collecting the focused solar radiation and poor optical performance. Hence, a compromise must be made between the optical and thermal performance of the solar concentrator to obtain a suitable concentration ratio [46]. To reduce the outward losses from the absorber by convection and radiation to the atmosphere, receivers may have transparent covers. The cover should present a low solar absorption. Glass with low-iron content is generally used as glazed materials for the receiver. Plastic is usually avoided to due to low service temperature limit and ultraviolet degradation. Moreover, the addition of an insulating layer helps to reduce heat losses from the unirradiated portions of the receiver. Evacuated tube receivers have also been used to eliminate convection heat losses.

2.1.1 Solar tracking system

The solar tracking system plays a crucial role in the development of solar energy applications, especially in solar concentration systems. In these systems, high precision tracking is required to follow the Sun on its trajectory as it moves across the sky and to ensure that the solar collector can harness the maximum amount of solar energy throughout the day [55].

A solar tracking system is a sophisticated device comprising of electronic control circuitry and mechanical elements that orient the collector towards the virtual path of the Sun from Sunset to Sunrise. There exist two main classes of solar tracking systems: single-axis (or one-axis) tracking systems, used with large linear concentrators and dual-axes (or two-axis) tracking systems, which are needed with three-dimensional concentrators. In the former type, the tracking system drives the collector about an axis of rotation until the Sun central ray and the aperture normal are coplanar. Such systems can be distinguished in horizontal-axis tracker (tracking axis is to remain parallel to the surface of the Earth and it is always oriented along East-West or North-South direction), tilted-axis tracker (tracking axis is tilted from the horizon by an angle oriented along North-South direction e.g. Latitude-tilted-axis Sun-tracker) and vertical-axis tracker (the tracking axis is collinear with the zenith axis) also known as an azimuth Sun-tracker [56]. Single-axis trackers require only one degree of rotational freedom, but they cannot follow the Sun with absolute accuracy due to the seasonal variation of the tilt of the Earth's equatorial plane with respect to the Earth's orbital plane. Dual-axes Sun-trackers follow the Sun in the horizontal and vertical plane. This system is capable of perfect alignment with the Sun at all times, reaching optimal collection efficiency. Two-axis trackers may be distinguished the in tilt-roll solar tracking systems and in the more common azimuth-elevation systems. In azimuth-elevation systems, the tracking angle about the azimuth axis is the solar azimuth angle and the tracking angle about the elevation axis is the solar elevation angle. The enhancement in performance brought about by solar tracking compared to a fixed system is largely dependent on the latitude of the installation as well as the design. The study by *Cotfras et al*. [57], performed in Germany on a basis of 15 hours of sunlight, has shown that a dual-axes tracker has a relative fully power output of for 9 consecutive hours, while a single-axis tracker maximizes the power output for 5 h and a fixed system shows that the power output is at its limit for only 1 hour.

Any solar tracking system is provided with a electronic control system and must be designed for the continuous orientation or positioning of the solar collector with respect to the Sun vector. The Sun vector describes the solar azimuth and elevation angles from the perspective of a specific position and orientation on the Earth. Solar tracking system must be able to track the Sun at the right angle, even during periods of cloud cover. Different motion control logic approaches exist to assure a proper tracking accuracy. These concepts include open-loop control systems, closed-loop control systems, and a hybrid control system where open-and - closed-loop approaches are combined. In open-loop solar tracking systems, the Sun vector is calculated from astronomical algorithms and an open-loop sensor such as encoder will ensure the right positioning of the concentrator. Such tracking approaches may achieve tracking accuracies of around 0.2° provided that the mechanical structure is precise and the alignment is perfectly done [55]. Closed-loop Sun- tracking systems typically produce better tracking accuracy. In this tracking approach, one or more optical sensors, such as photodiodes, CdS Photo Cells or CMOS Sun sensors, may be utilized to sense the position of the solar image on the receiver. These sensors are typically mounted on the concentrator structure to inform the control mechanism with feedback signals whether the solar tracking system is precisely oriented and adjust the collector to a position directly facing the Sun. The main disadvantage of closed-loop solar tracking systems is that the optical sensors devices are dependent on solar visibility, which is easily affected by clouds, weather conditions and environmental factors. In fact, any closed-loop Sun-tracking systems will lose its feedback signal and subsequently its track to the Sun position when the sensor is shaded or when the Sun is blocked by clouds. Modern solar trackers combine open- and closed-loop approaches in a hybrid-loop control mode system able to track the Sun in any sky conditions with a high pointing accuracy. Any discrepancy between the angles calculated through an astronomical algorithm and real-time position of the solar concentrator provided by the optical sensor can be detected and corrected. With this feedback, the pointing control system ensures that any tracking errors due to wind effects, mechanical backlash, installation mismatches, accumulated errors or other disturbances in the positioning of the parabolic dish can be corrected or eliminated.

2.2 Prototype of an asymmetrical small parabolic trough concentrator

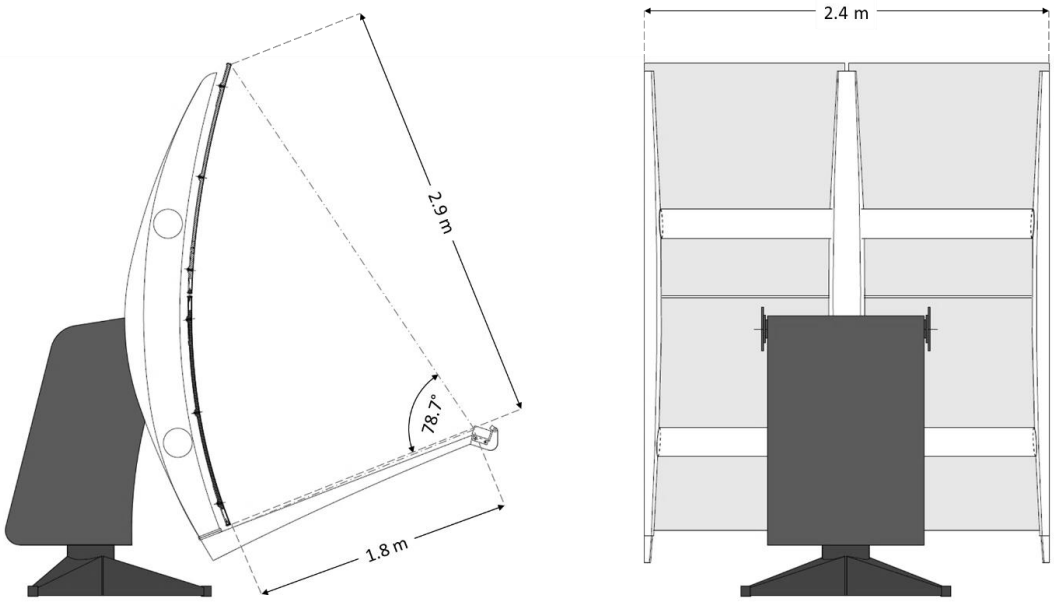

Figure 18 – Schematic of the prototype of asymmetrical parabolic trough linear solar concentrator.

The small prototype of linear solar concentrator considered in this thesis is an asymmetrical parabolic trough. Figure 18 reports a cross-section of the concentrator, whereas Figure 19 reports the concentrator in its installation at the Solar Energy Conversion Laboratory on the roof of the Department of Industrial Engineering at the University of Padova. The concentrator cross-section is a segment of a parabola that extends from the vertex to the mirror rim. More precisely, the lower rim of the reflective optics is on the parabolic profile at 35 mm from the vertex line, to allow the arrangement of the receiver without any shading. The concentrator exhibits an aperture width of 2.9 m, a rim angle of 78.7°, a focal length of 1.8 m and a trough length of 2.4 m, resulting in an aperture area equal to 6.96 m^2. The reflecting optical system is made up of four reflective panels produced by Ronda High-Tech S.r.l. arranged in two rows [58]. These reflective panels were initially developed in collaboration with the laboratories of the ENEA Research Center Casaccia in Rome and subsequently improved as a result of experiences during the Archimedes project at the ENEL Power Plant in Priolo Gargallo. Each

reflective panel is one-quarter of an arc of a parabola, and therefore comes in two types that together produce a cylinder parabolic surface with focus placed at around 1.8 m. The support panel is realized with a pre-impregnated thermosetting low-profile sheet moulding compound which allows the moulding of pieces of considerable size with very strict dimensional tolerances due to its very low shrinkage coefficient. The concave part of this support panels presents a smooth surface with a parabolic profile on which a back-silvered glass facet is applied with a thin double-sided adhesive film.

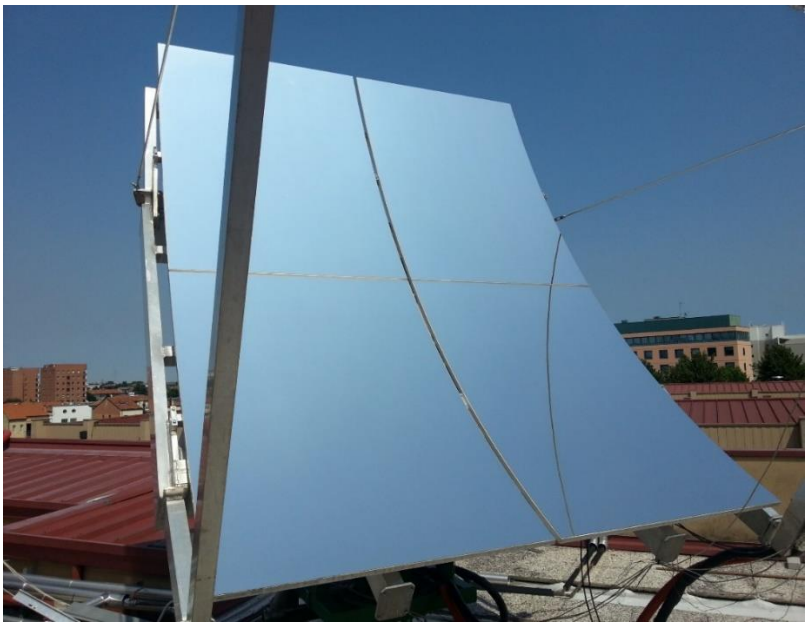

Figure 19 – Prototype of asymmetrical parabolic trough concentrator installed at the Solar Energy Conversion Lab of the University of Padova.

As reported by the manufacturer [58] , the achievement of values of thermal linear expansion coefficient close to the ones of the glass is fundamental both for not tensing the glass itself up to values close to or higher than those of breakage during the thermal excursions which it is subjected to during operation, and to prevent phenomena of detachment of the glass from the support and finally, to ensure a stability of shape suitable to different environmental temperatures. The use of a thin glass (1 mm) has two main advantages: reducing the effect of solar radiation absorption and reducing the effect of refraction, which are both proportional to the thickness of the glass. Figure 20 reports the solar reflectance of the mirror as a function of

the incident angle of the considered ray: the average value of the reflectance results assumed 96%.

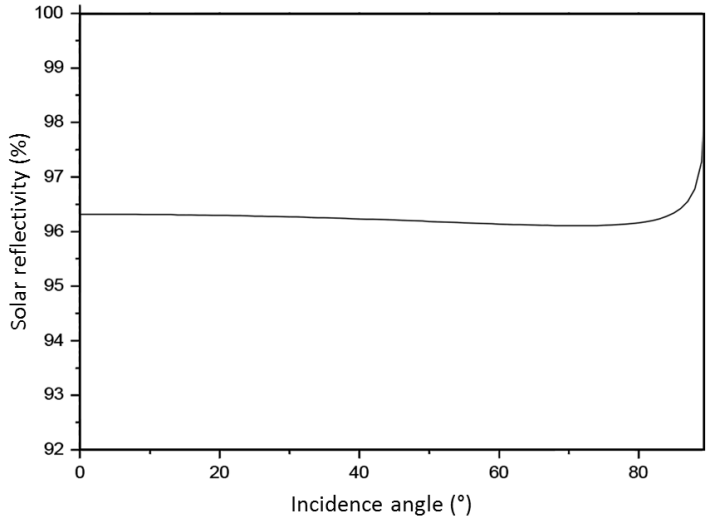

Figure 20 – Solar reflectance of the back-silvered mirror of the Ronda High-Tech reflective panel as a function of the incidence angle [59].

Due to its small dimensions, the considered prototype of the solar concentrator is equipped with a two-axis solar tracking. This tracking system points the concentrator to the Sun in order to have the direct irradiance normal to the aperture area avoiding any cosine loss while working. The motion of the tracking system is regulated by a solar algorithm when approaching the Sun and by a light sensor when achieving the best receiver alignment. The solar tracking accuracy is less than 0.2°. The particular geometry and tracking system of the present concentrator have been adopted for experimental research purposes to facilitate the access to the focal line, the arrangement of the sensors and the device control. Furthermore, the peculiar asymmetric geometry of this parabolic trough concentrator is suitable to be coupled with receivers displaying a flat geometry absorber rather than conventional tubular receivers. As an example, the receiver may be similar to some trapezoidal cavity receivers generally mounted on linear Fresnel solar collectors.

2.3 Concentrator optical losses and characterization of the concentrated solar flux

The geometrical concentration ratio depends only on the geometrical parameters of the concentrator and it does not incorporate the effects of any optical losses, which accounts for the solar beam dispersion occurring between the concentrator aperture and the receiver. The geometrical concentration ratio C_g as defined in Paragraph 2.1, is actually an average concentration over the receiver and it provides only a qualitatively indication of the operating temperature range of a concentrating collector. In real applications, there is a concentration region around the focal line, whose width depends on the optical errors of the concentrator and on the Sunshape, which represents the distribution of brightness from the centre of the solar disc. The concentrated solar flux is usually characterized by its distribution in the focal region and by defining the local concentration ratio. In contrast to the geometrical concentration ratio C_g, the local concentration ratio, or flux density concentration ratio, takes account of all the optical losses occurring in the concentrator and the non–uniformly illumination. This parameter is defined as the ratio of the concentrated radiation at any point on the absorber/receiver to the incident beam radiation at the entrance of the solar concentrator. Each optical element of the concentrator contributes to the concentrated solar flux on an appropriate area of the receiver. To determine the concentrated solar flux is thus necessary to sum over all elements of the concentrator, taking full account of the Sunshape, of the local angle of incidence on the receiver and of the displacement of the aim point of each element relative to the focal region. The characterization of the distribution of the solar flux density on the focal region has become pivotal for the design and improvement of concentrating solar collectors for both thermal and photovoltaic applications. In the development of new prototypes linear concentrating solar collectors, solar flux mapping on the focal region indicates if the fixing structure of the reflective mirrors is adequate to reproduce the desired ideal shape of the optical system. Moreover, periodical monitoring the concentrated solar flux and its distribution is recommended to assess the accuracy of the tracking system, the durability of the mirror reflectance and the stiffness of the mechanical structure over time

To optimize the performance, the geometry and the configuration of the receiver should be designed according to the width of the concentration region and the solar flux distribution. In fact, once the concentrated solar flux has been measured and the aperture width of the receiver is known, one can calculate the optical efficiency η_0 and the intercept factor γ_r. The first parameter is defined as the ratio of net thermal energy rate available at the receiver to the incident beam radiation available after the concentration process by the concentrator and the absorption by the receiver. It is often calculated according to equation *Eq. 2.12*, dividing the incident radiative heat flow rate intercepted by the absorber/receiver $q_{inc,Ar}$ by the radiative heat flow $q_{inc,Aa}$ on the portion of the concentrator aperture area, which is given by the of the product of the DNI and the considered aperture area A_a of the concentrator:

$$\eta_0(A_r) = \frac{q_{inc,A_r}}{q_{inc,A_a}} = \frac{q_{inc,A_r}}{DNI \cdot A_a} \qquad \textit{Eq. 2.12}$$

This efficiency includes the effect of the shape of the mirror surface, different sources of optical loss (reflection, transmission, and absorption), shading by the receiver, and the incident angle of solar beams [46]. However, it does not take account of the thermal losses occurring in the solar collector.

The intercept factor γ_r is a common parameter used to characterize the effect of the non-uniform distribution of the concentrated heat flux distribution on the area of the receiver. This parameter expresses the fraction of focused solar beam radiation intercepted by the absorber. It is calculated as the ratio of the incident radiative heat flow rate intercepted by the absorber for a given size of the receiver $q_{inc,Ar}$, and the radiative heat flow rate reflected by the mirrors, which is given by the product of the DNI, the considered portion of the concentrator aperture area A_a and the reflectance of the mirrors ρ_c:

$$\gamma_r(A_r) = \frac{q_{inc,A_r}}{DNI \cdot \rho_c \, A_a} = \frac{\eta_0(A_r)}{\rho_c} \qquad \textit{Eq. 2.13}$$

It easy to see that, once the reflectance of the mirrors ρ_c is known, the intercept factor γ_r can be determined from the optical efficiency η_0 and vice versa. The value of the intercept factor depends on the size of the absorbing surface. The receiver width must be just large enough to intercept most of the flux, otherwise fictitious geometric concentration ratios can be obtained

with arbitrarily large or small (if the receiver is oversized) receiver. To ensure an acceptable performance of the solar concentrating collector, the intercept factor should be higher than 90%. In the case of photovoltaic applications, the arrangement of the solar cells in the receiver and, when present, a secondary optics must be designed considering that the non–uniform incident flux is expected to cause hot spots, current mismatch and a reduction in the electrical efficiency [60]. On the other hand, in solar thermal collectors, the non–uniform distribution of the concentrated solar flux on the external surface of the absorber can lead to perimetral temperature gradients. This is associated with differential thermal expansions that cause thermal stresses, whose effect can be very serious in some working conditions as reported by many researchers [61-64]. In practice, to avoid this situation, a high mass flow rate is pumped in order to achieve a turbulent flow condition inside the tubular absorber. This approach is generally adopted CSP plants but cannot be always applied in medium-temperature concentrating collectors, especially for direct steam generation, where a certain flexibility of operation is required to maximize the working hours per day under stable conditions. In medium-temperature applications, the use of receivers with heat transfer enhancement represents an interesting solution and the solar flux mapping is of significant importance in their design.

2.3.1 Sunshape and concentrator optical errors

The Sun presents an object which is effectively at infinity, but the Sun-Earth distance causes the solar disc to subtend an angle of 32’ at a point on the Earth’s surface. Thus, because the Sun is not a point source, even a perfect optical system produces an image of finite size. An ideal image formed at a distance of 1000 m would have a typical radius of 5 m (common in central receiver systems) or at 10 m would have a radius of 50 mm (typical of distributed receiver systems such as in parabolic troughs) [65]. The brightness intensity distribution across the finite angular size of the Sun and the circumsolar aureole, shortly called Sunshape, depends on the sky conditions. In fact, in space, the Sunshape results well defined against the cold background space with a sharp rim. The extra-terrestrial irradiance is modified upon traversing the Earth's atmosphere due to absorption and scattering by fluid drops and different kinds of gases and solids. These atmospheric effects together lead to solar brightness distribution and

create the circumsolar aureole. For this reason, the simple flat top distribution is often replaced by a more realistic limb darkened distribution. Frequently, the bivariate Gaussian distribution is chosen as an approximation of the Sunshape. This distribution is well behaved everywhere and falls rapidly to zero for angles greater than two sigma. Furthermore, it is particularly easy to work with and is a suitable approximation for many error functions. In fact, by adding the standard deviations in quadrature, is possible to approximate the effects of optical errors of the concentrator to obtain the resulting distribution function [65]. The optical of error arising from many individual sources are usually combined in a single parameter called, total optical error.

The lack of perfection present in every real concentrator, such as the shape and specular reflectance errors of the mirrors, the tracking error, and the imperfect positioning and alignment of the receiver can affect the quality of the concentration provided by a concentrator. A proper characterization of the errors present in an optical system can become quite challenging because it depends on the application and on a number of other factors. However, as reported by *Winter et al.*[65], the nature of tracking collectors leads to a reasonably standard attribution of errors, from the microscopic level to the system level (Figure 21).

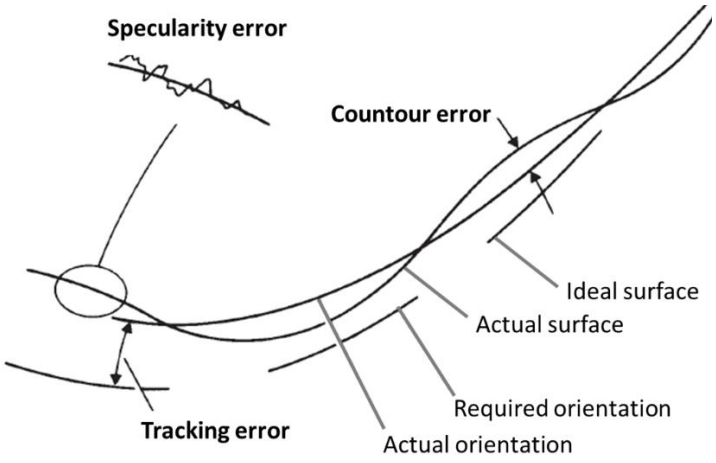

Figure 21 – A graphical representation of the several classes of optical errors [65].

Specularity error (or specular reflectance error) accounts for the local inhomogeneities and imperfections at the microscopic level that is present on the mirror surface. The displacements of the surface from the desired location are usually combined in the contour error. This error

can arise from manufacturing errors, thermal or gravity effects on the support structure, design approximations to the correct optical surface, etc. However, as these displacements only introduce a small fractional change in the distance to the focal region, they can generally be ignored under the guidelines of concentrator optics. Small distortions causing slope errors, on the other hand, deflect the beam through a large lever arm (the focal distance) and must be considered carefully[65]. Tracking error can have several origins such on-off tracking algorithm, drift, error in aim point and ambient effects on the tracking devices. This error produces an instantaneous degradation in the concentration, which may affect the performance of the collector. Because the subtended angle of the solar is equal to 32', optical errors which deflect the reflected beam substantially less than this value do not contribute to the reduction in the concentration of the solar radiation and can be neglected.

2.3.2 Concentrated solar flux

Concentrated flux is measured to determine the total amount of energy incident on a receiver aperture, or to examine the detail of the spatial distribution of the focal region. The measurement of the concentrated solar flux on the focal region of a concentrator can be performed through different techniques that can be classified as direct, indirect and measurement-supported simulation methods.

Direct measurement methods refer to the use of a flux sensor, whose response can be directly associated with the concentrated solar flux. In order to get a fine spatial resolution of the solar flux map, these sensors should have a small aperture and should be either distributed in the focal region or installed in handling systems to scan the concentration region[66]. In both cases, an interpolation of the experimental data collected at specific points of the concentration region is required to determine the solar flux map. In the former, many sensors are needed to obtain results with low uncertainty, but this entails that the measurement system has a very high investment cost. Furthermore, the spatial resolution may be modest. In the latter solution, the handling system should be suitable to the geometry of the investigated concentrator; this solution allows to scan quickly the focal region and to collect much more experimental points as compared to the case of stationary and distributed sensors, thus increasing the accuracy of the results. The most common sensors employed in concentrating collector analysis are

radiometers and calorimeters [67]. Radiometers deliver an electrical response that varies with the incident radiation. This electrical signal may be either a current generated by a photodetector or a voltage coming from a differential temperature sensor such as a thermocouple for the Gardon radiometer or a thermopile for the more recent heat flux microsensors (HFMs). Heat flux microsensors have been used by *Ballestrin* [68] to investigate the concentrated solar flux distribution on a central volumetric receiver of a heliostat field at the Plataforma Solar de Almeria. *Ferriere and Rivoire* [69] and *Parretta et al.* [70] designed and realized two different radiometers arranging a photodetector respectively inside a single integrating sphere and two integrating spheres optically interconnected. *Fernández-Reche et al.* [71] presented a comparative test performed in a solar furnace measuring concentrated solar flux using both a Gardon radiometer and a GaAs photovoltaic cell as photodetectors. *Riffelmann et al.* [72] developed the parabolic trough flux scanner (PARASCAN) to detect the solar flux on the tubular receiver of parabolic trough collectors having an aperture width of 5.76 m. The measurement system consists of two arrays of 96 photodiodes each, placed behind translucent Lambertian targets. The first array is arranged in front of the receiver tube, to detect the beam irradiance reflected by the mirrors towards the concentration region, while the second array is located behind the receiver, to measure the optical losses. The two arrays are fixed on a sliding carriage moved by a remote control. Integrating the data collected on the first and on the second array, the intercept factor of the parabolic concentrator can be calculated. When using a calorimeter mounted in the focal region of a concentrator, the solar flux can be derived from a thermal balance between the radiant power incident on the device aperture and the heat flow rate transmitted to a cooling fluid flowing through the sensor. *Pérez-Rábago et al.* [73], *Estrada et al.* [74] and *Jaramillo et al.* [75] employed calorimeters to measure the solar flux in point-focus concentrators.

Direct measurements techniques are rarely adopted, due to practical reason presented above. Reasonable approximations of the receiver flux density distribution are usually obtained through indirect measurement techniques or more commonly with the use of simulation ray-tracing tools Nevertheless, the models adopted in the simulations must be calibrated and validated by comparison with experimental data. In indirect measurement methods, digital cameras (CMOS cameras or, more often, CCD cameras) equipped with appropriate filters and

zoom lenses are used to capture one or more images that can be related to the solar flux distribution after processing. The captured images are in grey-scale map, so they can only give qualitative information. To correlate the grey-scale value of each pixel to a physical irradiant flux value, the system must be calibrated in situ. If accurately implemented and calibrated, indirect methods provide very high spatial resolution, high reliability and short measurement time. In most cases, the digital camera records the concentrated solar radiation reflected off a target which exhibits a diffuse reflectance very close to ideal Lambertian reflectance (camera-target method). This means that, whatever the angle of observation, the target surface appears equally bright. *Ballestrín and Monterreal* [76] evaluated the concentrated solar flux on a central receiver of a heliostat fields by capturing images with a CCD camera on a moving uncooled Lambertian target. This target swings in front of the receiver aperture area and intercepts the reflected solar beam radiation in a measurement plane. Moving or cooling the target is necessary for high concentration ratio systems, where the concentrated flux may overheat and damage it. Two water-cooled Gardon radiometers placed very close to the receiver aperture are used to calibrate the CCD camera. *Riffelmann et al.* [72] implemented the calibrated CCD camera-target method for flux mapping on the focal region of a parabolic trough concentrating solar collector. The Lambertian target has a notch which allows enclosing the tubular receiver and it can be moved through a telescopic arm along the focal region. On the target, higher and lower concentration areas, as well as solar rays missing the absorber tube, can be observed. After image processing, an approximate value of the local intercept factor γ_r can be calculated. A new method, that has been applied to few receivers so far [66,77], regards the use of only a digital camera, directly applied to external receivers, without Lambertian targets. It is related to many sources of error that should be carefully considered. First, the assumption of a perfectly diffusing material of the receiver is definitely not exact: its real reflectance should be characterized using a gonioreflectometer. Secondly, the receiver is provided with a selective coating with a high absorbance (and low reflectance) in the wavelength range of the solar spectrum. Besides, the temperature of the receiver surface is much higher than the ambient air temperature, hence, a special filter that can cut off thermal radiation emitted by the receiver in the infrared range should be adopted. Finally, the use of different filters during the calibration procedure and during tests may entail errors due to the difference between the actual attenuation factors and the manufacturers' specifications. Total errors associated with this

method can be up to 20% - 40%, mainly because of large uncertainty in receiver reflectance and in filters' attenuation factors. *Lüpfert et al.* [78] presented a second version of PARASCAN to evaluate the flux distribution on the focal region of a parabolic trough with great accuracy. Fiber optics are arranged instead of photodiodes, behind the translucent Lambertian targets of the two parts of the moving measurement system. Each sensor part is composed of 12 segments where 16 optical fibers are mounted at distances of 2.5 mm., giving a very high spatial resolution. The optical fibers transmit the beam radiation concentrated on the focal region to a CCD camera equipped with neutral density filters, out of the hot region. A direct calibration of the system under natural sunlight is possible. From the measured flux maps, intercept factor γ_r has been calculated with an experimental uncertainty of about ± 1%.

The last class of methods involves the use of ray-tracing codes, which have proved to be powerful tools to model many different solar concentrating collectors as they can be used to evaluate the solar flux on any surface. Nevertheless, the accuracy of the results depends on the quality of the input parameters: concentrator shape, tracking and receiver positioning errors, optical defects, optical properties of the materials and atmospheric conditions. In this regard, *Xiao et al.* [79] reviewed and discussed the advantages and the disadvantages of the three main methods for the measurement of surface shape and optical quality of solar concentrators: video scanning Hartmann optical test, photogrammetry and deflectometry. Furthermore, the results obtained from simulations should be validated against merely experimental measurements, in which, in this case, a high resolution and an extreme complexity are not required. *Schiricke et al.* [80] developed an optical model of a parabolic trough solar concentrator by implementing in a Monte Carlo ray-tracing software the photogrammetrically measured the geometry of the collector. The nominal optical properties of the materials, the incidence angle of the solar rays on the aperture area and the measured values of direct normal irradiance and assuming a typical clear-sky Sunshape have been implemented as inputs. The receiver has been represented as a linear tube without bowing and the errors in its positioning have been accounted for. Finally, a tracking error of 1 mrad has been assumed. The model has been validated by comparing the numerically calculated intercept factors and the flux map to those measured with an indirect method. It proved to be very accurate and reliable, hence it can be used to study the effect of different combinations of parameters on the collector performance. In the work by *Röger et al.*

[66], a ray-tracing code has been employed to simulate the flux density distribution on the focal region on a solar tower of a heliostat field. In the optical model, the heliostat shape errors were accurately measured using deflectometry, the receiver position relative to the heliostat field was determined by tachymeter measurements while the measured direct normal irradiance and a clear-sky Sunshape were taken as inputs. The heliostat reflectance is chosen in a way that the simulated and the measured solar flux on a radiometer mounted in the receiver area match. A random tracking error of 0.9 mrad for each axis has been considered. The simulations have been compared to the results obtained by applying an indirect solar flux mapping method which involved the use of a digital camera and the white radiation shield mounted around the aperture of the receiver as a target. A good agreement was found. Finally, to prove the reliability of the proposed technique, a comparison has been performed between the predicted receiver input power and the reference value derived from the previous application of a moving bar indirect method on the same system. As a final remark, the validated ray-tracing code proved to be able to predict the incident power on the receiver with a low deviation.

2.4 Experimental measurement of the concentrated solar flux of an asymmetrical parabolic trough concentrator

In this thesis, a direct method based on the use of a radiometer mounted on a handling system is used to measure the solar flux map on the concentration region of a PTC that has been designed for installing receivers equipped with flat absorbers [81]. The aim of the present experimental activity is to investigate the optical performance of the asymmetrical concentrator and to determine the appropriate parameters for a statistical ray-tracing modelling of the system. This experimental activity can be useful to identify weak points in the fixing structure of the mirrors for future improvement of the optical system.

A water-cooled heat flux microsensor HFM1000-1 manufactured by Vatell Corporation is used to measure the concentrated solar flux along the optimal concentration plane of the asymmetrical parabolic trough. A heat flux microsensor (HFM) consists of a thin thermal resistance layer sandwiched between many thermocouple pairs forming a differential thermopile that can measure very high heat flux. This kind of sensors is best suited for heat flux values above 1 kW m^{-2}, with no practical upper limit [82]. The HFM working principle was firstly described by *Hager et al.* [83]. The inner structure of a heat flux microsensor is reported in Figure 22.

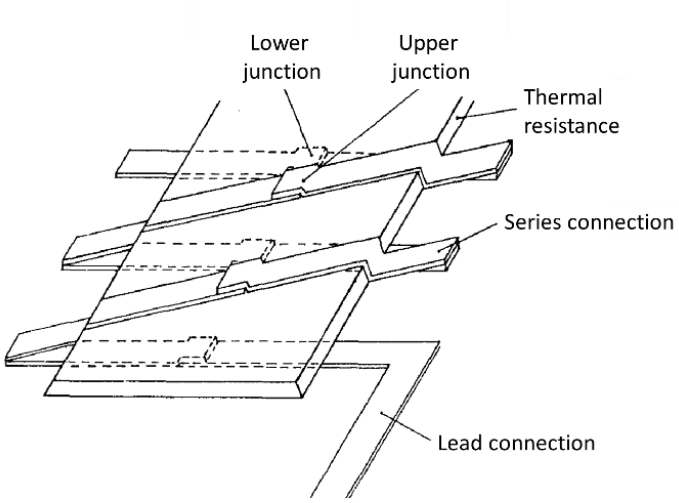

Figure 22 – Schematic of the inner structure of heat flux microsensor [83]

The output of the thermopile is a voltage signal directly proportional to the incident heat flux. Because it is made with thin-film sputtering techniques, the entire sensor is less than 2 mm thick [83]. Due to the small thickness of the thermopile, the HFM can assure high-frequency response. The response time of the Vatell Corporation HFM1000-1 is limited to 300 μs due to the present high absorptance black coating Pyromark 1200on the receiving face, as usual for radiant flux measurement and for applications in concentrating collectors. The coating is a high-temperature paint which has a solar emittance coefficient of 95 % as declared by the manufacturer. According to the study by *Song et al.* [84], the total infrared spectral emittance of this coating is higher than 93% in the wavelength range between 3 μm and 14 μm. Therefore, unlike other coatings such as Zynolite [85], there is no need to introduce corrective dimensionless factors to account for the differences between the solar irradiance spectrum and the irradiance spectrum of the black body (at about 850°C) employed for the calibration of heat flux microsensors. The combined use of high-temperature materials and water-cooled body allows the sensor to operate at temperatures that exceed 300°C. In the HFM-1000 series sensors, the sensor is put into a water-cooled copper body (Figure 23).

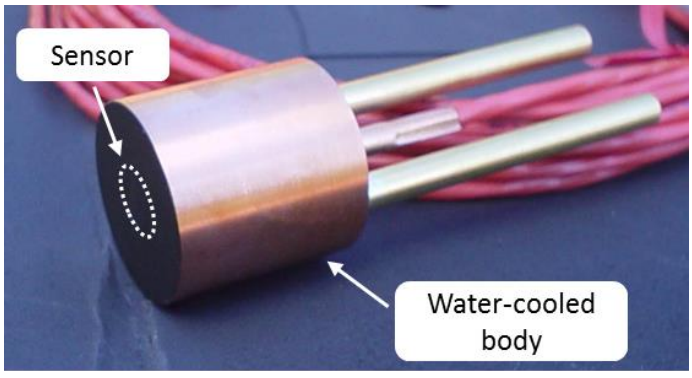

Figure 23 – Heat flux microsensor Vatell Corporation HFM1000-1 [86].

Water cooling is necessary for applications requiring a continuous monitoring of the concentrated flux or to reduce the influence of the ambient conditions on the measurement accuracy. In fact, if the average temperature of the cooling fluid (distilled water) passing through the sensor is close to the ambient air temperature, the effect of convection and radiation heat losses on the measurement of the concentrated flux can be neglected. A platinum thin film resistor which surrounds the heat flux sensor provides the temperature measurement. Sensor

temperature measurement is very useful for checking the heat flux calibration and determining the heat transfer coefficient.

The solar flux mapping system has been designed so that, during the experimental tests, the measuring plane corresponds to the optimal concentration plane. The water-cooled heat flux microsensor described above is mounted on a two-axes semi-automatic linear handling system to scan the focal region. reports the measuring plane identified by the *x* and *z*-axes. *Figure 24* shows the scanned area by solar flux mapping system installed on board the prototype of the small asymmetrical parabolic trough concentrator considered in this work. The motion of the sensor along the horizontal axis (*x*-axis) parallel to the focal line is allowed by an aluminium bar provided with a sliding carriage. The carriage can be stopped at ten fixed positions along the *x*-axis by appropriate blocking elements.

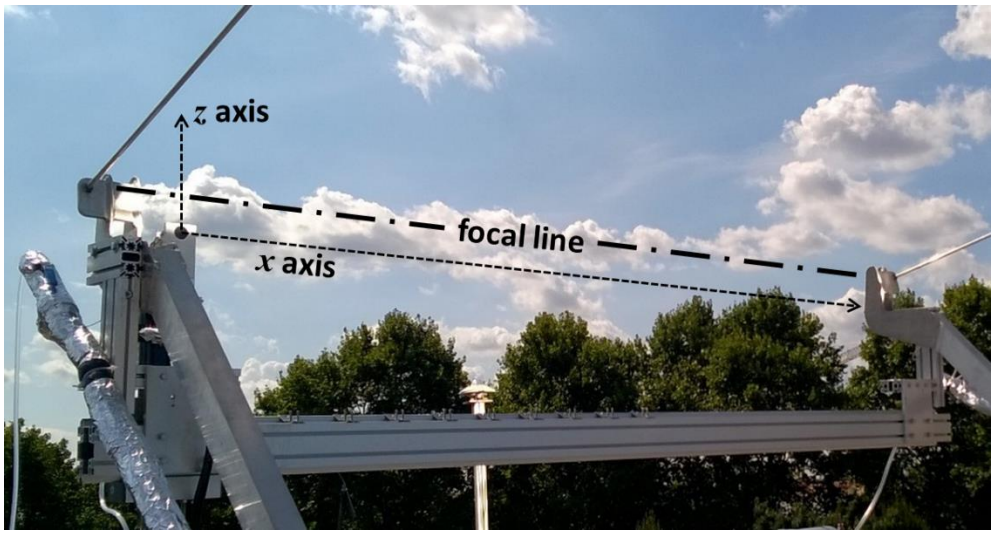

Figure 24 – Vertical (z-axis) and horizontal (x-axis) measuring axes of the solar flux mapping system and focal line of the asymmetrical small parabolic trough concentrator.

The sensor is moved along the width of the concentration (*z*-axis) by an electrical linear actuator connected to the sliding carriage. On the top of the actuator, an aluminium element supports the heat flux microsensor (Figure 25). This supporting element allows for fine adjustments of the sensor positioning.

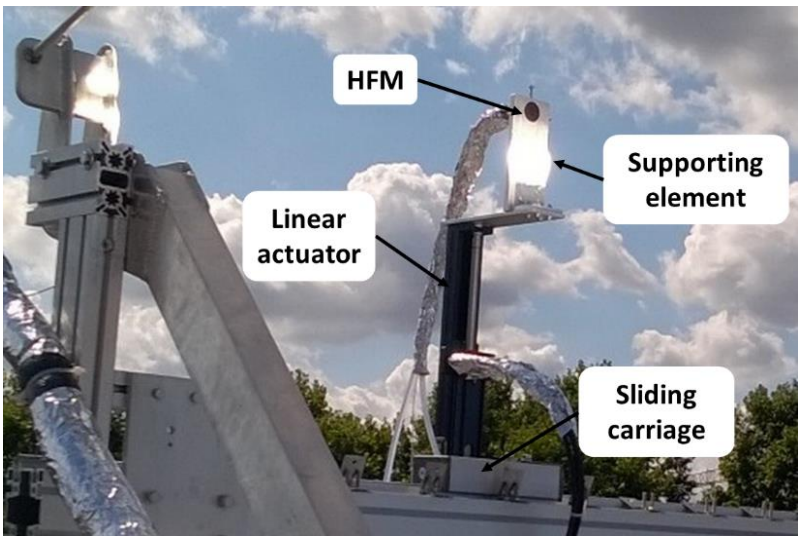

Figure 25 – Heat flux microsensor (HFM) arranged on its supporting element and electric linear actuator mounted on the sliding carriage of the x-axis.

The electrical linear actuator Gimatic LV25150 is based on a recirculating ball-bearing guide system and presents an integrated encoder. Its maximum stroke is of 150 mm at a variable speed from 0.001 m s^{-1} to 2 m s^{-1} and a maximum positioning repeatability of 0.1 mm. Figure 26 reports a schematic view of the electric linear actuator mounted on the sliding carriage

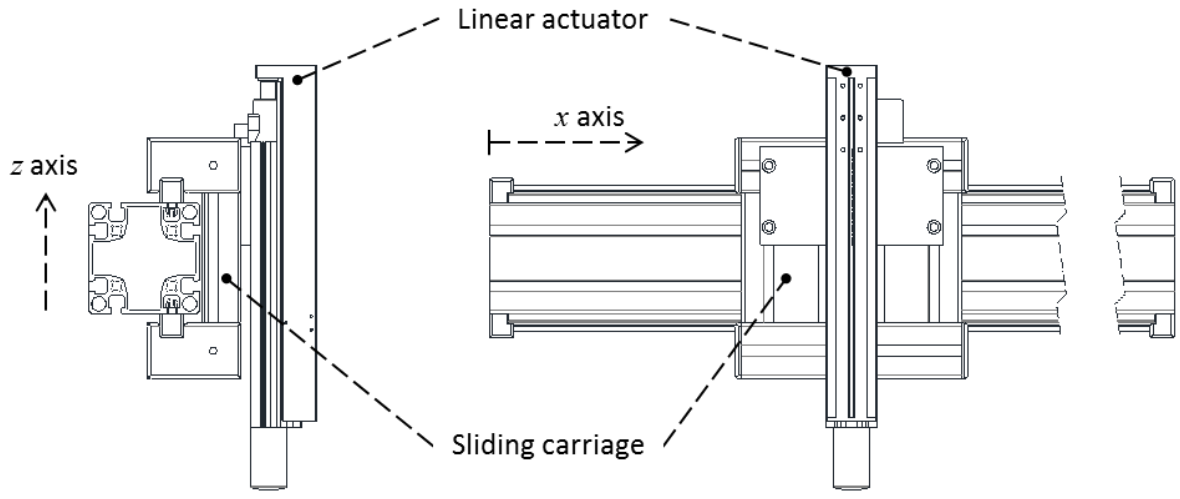

Figure 26 – Side and front schematic views of the of the two-axes semi-automatic linear handling system

The laboratory includes a first class Kipp&Zonen CHP1 pyrheliometer mounted on a high precision EKO Instruments STR-22G solar tracker that is used to measure the direct normal irradiance. An Agilent 34970A Data Acquisition / Data Logger Switch Unit registers the electrical signals coming from the actuator, the heat flux microsensor, and the pyrheliometer. Before every experimental test, the reflecting facets of the parabolic trough concentrator, the Sun sensor and the pyrheliometer have been cleaned.

The solar flux map has been experimentally characterized on a trough length of 1200 mm along the *x*-axis, corresponding to a single row of parabolic mirrors. During the test runs, the other row of parabolic mirrors has been shielded. Concentrated solar flux measurements have been performed according to the following procedure. First, the electrical linear actuator is brought at the first measuring point along the *x*-axis (at about 30 mm from the projection of the side rim of the mirrors row on the focal line), in which the heat flux microsensor is about 65 mm under the ideal focal line of the concentrator. Figure 27 reports the sensor in the starting position for a solar flux mapping test.

Figure 27 – Starting position of the heat flux microsensor. The electric linear actuator is completely down in its starting position, 65 mm under the ideal focal line of the concentrator.

Once the sensor reaches its starting position, the working cycle of the actuator is started: a slow rise for collecting the experimental data is followed by a quick descent to bring the actuator back to its initial position before moving it to the next measuring point along the *x*-axis. At the end of the slow rise phase, the sensor is 65 mm above the ideal focal line, thus the investigated width on the concentration region is of 130 mm, centred on the ideal focal line. During each test, four values are registered by the data acquisition system: the position of the sensor, given by the electrical output signal of the actuator's encoder, the heat flux and the temperature signals from the heat flux microsensor and the direct normal irradiance measured by the pyrheliometer. The series of data collected during a test are considered for data reduction if the variations of the direct normal irradiance are within the experimental uncertainty of the pyrheliometer (±3% of the average value, with a level of confidence of 95.45 %). The number of collected data for concentrated solar flux depends on 3 parameters: the number of measuring position along the *x*-axis, the actuator's speed along the *z*-axis and the sampling rate allowable by the data acquisition system. The higher the number of experimental data the more accurate the resulting solar flux map. The heat flux microsensor is cooled by a flow of 0.02 kg s^{-1} of distilled water. The temperature of the cooling fluid at the inlet of the sensor is kept constant by dissipating the heat flow rate coming from the concentrated solar radiation to the groundwater.

The uncertainty analysis has been performed in agreement with the guidelines provided by the "Guide to the Expression of Uncertainty in Measurement" [37]. Type B uncertainties of the measured parameters, resulting from calibration of instruments, calibration certificates, manufacturers' specifications and uncertainties assigned in reference handbooks, are reported in Table 2 with a level of confidence of 95%.

Table 2 – Type B uncertainty of measured parameters during the experimental measurement of the concentrated heat flux.

Ambient air temperature	± 0.07°C
Direct normal irradiance	± 4.5% of measured value
Horizontal coordinate	± 5 mm
Vertical coordinate	± 3 mm
Wind speed	± (0.1 m/s + 1% of measured value)

The experimental procedure reported in the work of *Bortolato et al.* [81] has been adopted to evaluate the optical performance of the present asymmetrical concentrator. To define accurately the solar flux map and to calculate the incident power on an area within the concentration region, an interpolation of the experimental data has been performed. The interpolant should be able to predict well local trends, therefore, the spline interpolants have been considered. Differently from the study by *Ballestrin* [68], where an aiming strategy on 25 heliostats was set up to obtain a uniform flux distribution on the central receiver, in the present parabolic trough concentrator, a strongly non-uniform flux distribution is expected. Consequently, the spatial resolution to interpolate should be quite high to get a more accurate estimation of the incident power q_{inc} on an area of interest included in the focal region. In fact, the incident power is calculated by a numerical integration of the solar flux distribution, dividing the area of interest into n equal rectangular elements and using the tiled method, according to Eq. 2.14:

$$q_{inc} = \sum_{i=1}^{n} q''_{r,i} A_{r,i} = \frac{A_r}{n} \sum_{i=1}^{n} q''_{r,i} \qquad \textit{Eq. 2.14}$$

where n is the number of data in the surface of interest, A_r is the total area of the surface of interest, $q''_{r,i}$ is the i-th value of solar heat flux associated with the portion of the area of interest $A_{r,i}$. Unfortunately, the spline interpolants do not allow the estimation of the uncertainty on predicted concentrated solar flux values. Therefore, in order to assess if the number of collected data is sufficient for a good definition of the solar flux map, different interpolants (linear, nearest-neighbour, cubic-spline and biharmonic) implemented in Matlab® have been considered and the results of the numerical integration have been compared. If the obtained value of the power incident on an area of the concentration region does not change significantly when varying the interpolant, the accuracy in the solar flux map definition can be considered satisfactory. Once the incident power onto an area of interest has been calculated, the associated optical efficiency and intercept factor γ_r can be determined according to Eq. 2.12 and to Eq. 2.13 for the average value of the direct normal irradiance during the considered test run, the part of the concentrator aperture area considered during tests and the nominal reflectance of the mirrors.

The experimental uncertainty of the calculated radiative heat flow rate q_{inc} is derived from the combination of the integration uncertainty, the interpolation uncertainty and the uncertainties related to the handling system positioning and movement. The interpolation uncertainty can be neglected because the chosen interpolant shall not affect the results as reported in the work by *Ballestrin* [68]. Furthermore, the geometry of the present asymmetrical parabolic trough concentrator allows checking accurately that the measuring plane matches the optimal concentration plane. Finally, the uncertainty of the intercept factor γ_r has been calculated applying the law of propagation of uncertainty for uncorrelated inputs [37] and neglecting the uncertainty of the nominal reflectance of the parabolic mirrors.

2.4.1 Experimental results

Experimental measurements of the solar flux distribution on the concentration region of the asymmetrical parabolic trough concentrator have been performed in two clear-sky non-consecutive days in Padova. Several tests have been conducted consecutively under very similar test conditions, to assess the proposed measuring technique. The measurements were performed for the first time the 28th September 2015 and they were repeated the 1st July 2016. In the first measurement day (28th Sept. 2015), 10 blocking elements have been arranged along the investigated trough length, at a distance of 120 mm, hence 10 measuring stations along x-axis are distinguished. In this day, the measurements were repeated for six times from 13:58 to 14:43. The average measured DNI was around 900 ±40 W m^{-2} and the ambient air temperature was around 23°C. In the second measurement day (1st July 2016), the measurements have been taken at 13:43 and repeated at 14:47. During these runs, the number of blocking elements has been augmented to 22, at an average distance of 55 mm. The average value of the DNI was around 750 ±34 W m^{-2} and the ambient air temperature was around 25°C.

The dimensions of the measuring area, which is the area scanned by the heat flux microsensor, are given by the actual stroke of the electrical linear actuator along the z-axis (130 mm) and by the distance between the first and the last of the blocking elements along the x-axis, 1115 mm and 1180 mm for the first and second measurement day, respectively. The speed of the electric linear actuator was set equal to 0.005 m s^{-1} in the rise phase and equal to 0.1 m s^{-1} in the descent phase. Data were collected with a sampling rate of 0.2 s. The resulting spatial resolution along

the width of the concentration region is 1 mm. During the first day, 1300 concentrated solar flux data were collected for each test, whereas during the second day the collected solar flux values were 2860 for each test.

Two single test runs, 28th Sept. 2015 13:58 and 1st July 2016 13:43, have been chosen as representative cases respectively for the first and the second day of measurement. In fact, the concentrated flux distributions obtained from the six test runs in the first day of measurement are all in the experimental uncertainty band. The same is true for the two set of data acquired during the second day of measurement. Figure 28 reports the three-dimensional maps of the dimensionless solar flux distribution obtained by interpolating the experimental data (dots) collected in these single test runs (28th Sept. 2015 13:58 - Figure 28 – a; 1st July 2016 13:43- Figure 28 – b). The dimensionless concentrated solar is defined as the ratio between the local solar flux registered by the heat flux microsensor and the corresponding DNI value acquired during the tests. The surface interpolation has been executed by means of the biharmonic spline method implemented in Matlab® over a grid with a spatial resolution of 0.1 mm x 0.1 mm. For the sake of clarity, the solar maps have been presented with a spatial resolution lower than that adopted for the calculation of the radiative heat flow rate on an area of interest included in the measuring area. Considering the first day of the experiment (28th Sept. 2015), which presents the lowest number of acquired data, the variation of the radiative heat flow rate of the concentred solar radiation is within ±0.2% when different spline interpolants are employed. That demonstrates that the number of experimental data collected during a single test run is high enough to get an accurate definition of the concentrated solar flux distribution on the measuring area. The origin of the z-axis corresponds to the ideal focal line, 65 mm over the initial position of the encoder integrated into the electrical linear actuator. The origin of the x-axis corresponds to the side rim of the investigated mirror row. As can be seen, the scanning range of the linear actuator was differently centred during the two days of measurement. In the first day, the HFM has been moved in the range z = -65 mm and z = 65 mm, while in the second day of measurement the range was between -55 mm and -75 mm. This difference does not affect the quality of the measurement.

As expected, the solar flux distribution is strongly non-uniform along the width of the concentration region (z-axis). Nevertheless, there are significant variations of the solar flux

even along the *x*-axis: the external rim of the investigated mirror row appears to be less efficient in concentrating the solar beams and the dimensionless solar flux is below 90 for the first 300 mm of the trough length. This can be due to the fixing system of the parabolic mirrors, which was manufactured expressly for lab tests only. In fact, the mechanical structure of the concentrator considered in this work does not include parabolic-shaped metallic ribs to sustain the mirrors arranged in a row. These elements may improve the optical performance of the system and make concentrated flux more uniform along the trough length.

While the plot in Figure 28 – a presents a smoother surface, in the plot of Figure 28 – b the peaks of the concentrated flux in the region around the ideal focal line can be detected more clearly. In fact, due to the higher number of sampling stations along the length of the trough (*x*-axis) the dataset of the second day can reproduce more in detail the local distribution of the concentrated flux. Since the coordinates of the blocking elements along the *x*-axis are not the same for the two days of measurements, the maximum peaks of the concentrated solar flux may not be located at the same location. The maximum peak value of the measured concentrated solar flux during the first day is 101217 ±7300 W m^{-2} (*q"*/DNI = 110 ±9) at *x* = 756±5 mm, while for the second day of measurement, the maximum peak is located at *x* = 505±5 mm (86194 ±6216 W m^{-2}, *q"*/DNI = 115 ±10). From the comparison of the local distribution at similar positions, it results that the differences between the values of dimensionless solar flux for the two datasets are lower than the resulting experimental uncertainty. The minimum peak values have been detected at the very beginning of the trough length. For the first day, the minimum peak is 68710 ±4955 W m^{-2} (*q"*/DNI = 76 ±6) (*x* = 33±5 mm), while for the second day it results equal to 54621 ±3939 W m^{-2} (*q"*/DNI = 76 ±6) (*x* = 30±5 mm). Despite the difference sampling resolution along the *x*-axis between the first and second day of measurement, three zones where the concentrated solar flux results more intense can be clearly distinguished, centred at 500 mm, 750 mm and 1000 mm from the beginning of the trough, respectively.

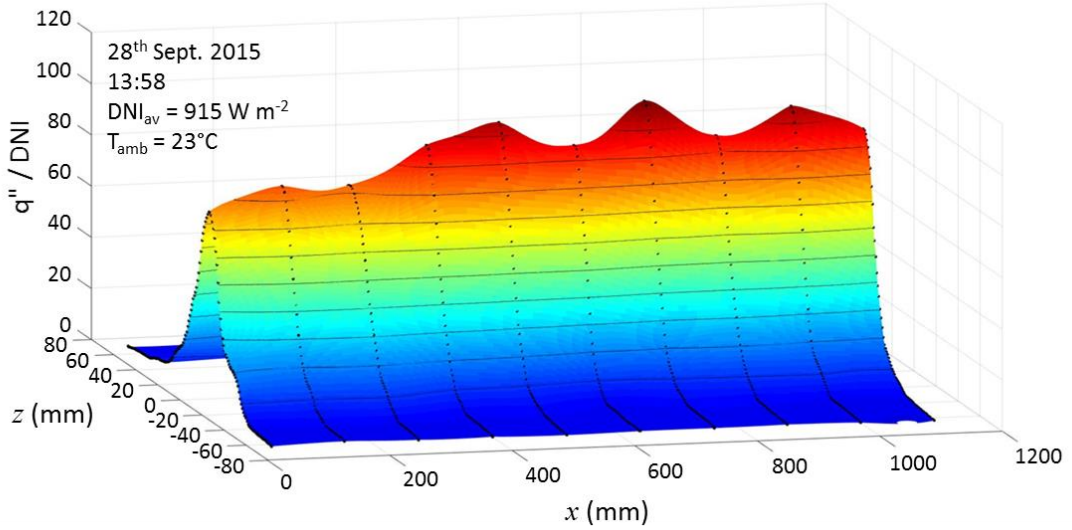

- a -

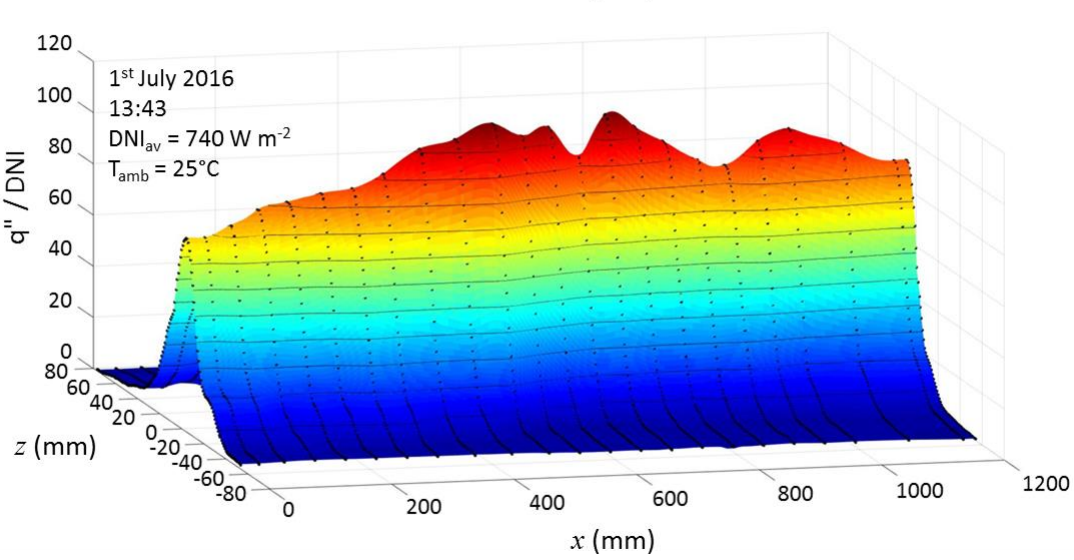

- b -

Figure 28 – Three-dimensional solar maps on the scanned area measured during the first (a) and second (b) day of the experimental investigation. The three-dimensional maps are obtained by interpolating the experimental data (dots) by means of the biharmonic method implemented in Matlab®.

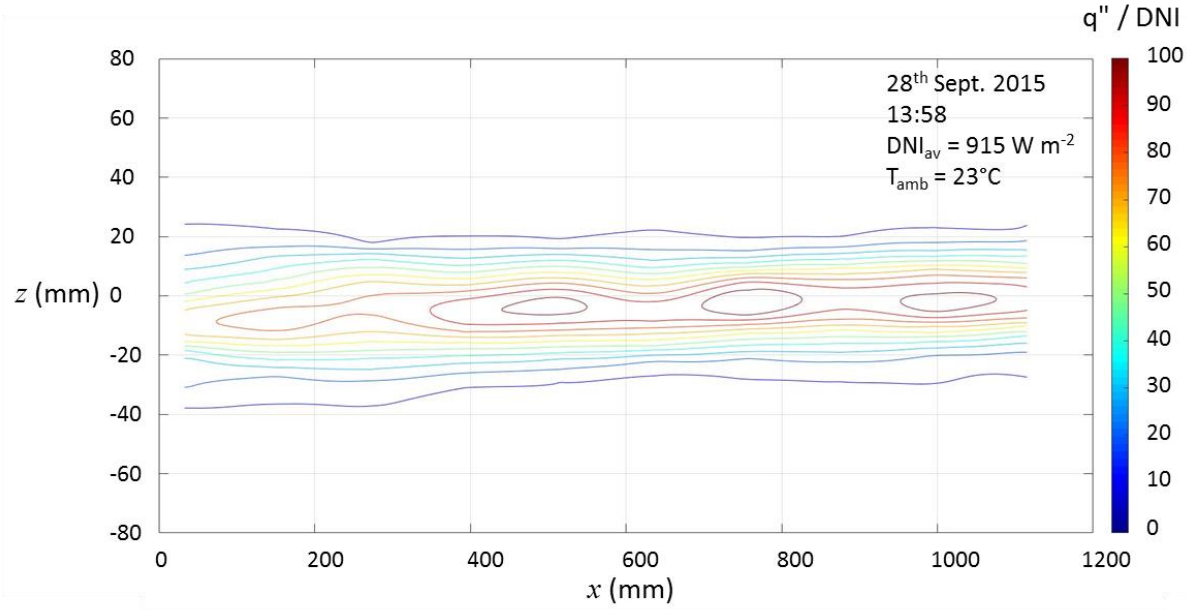

- a -

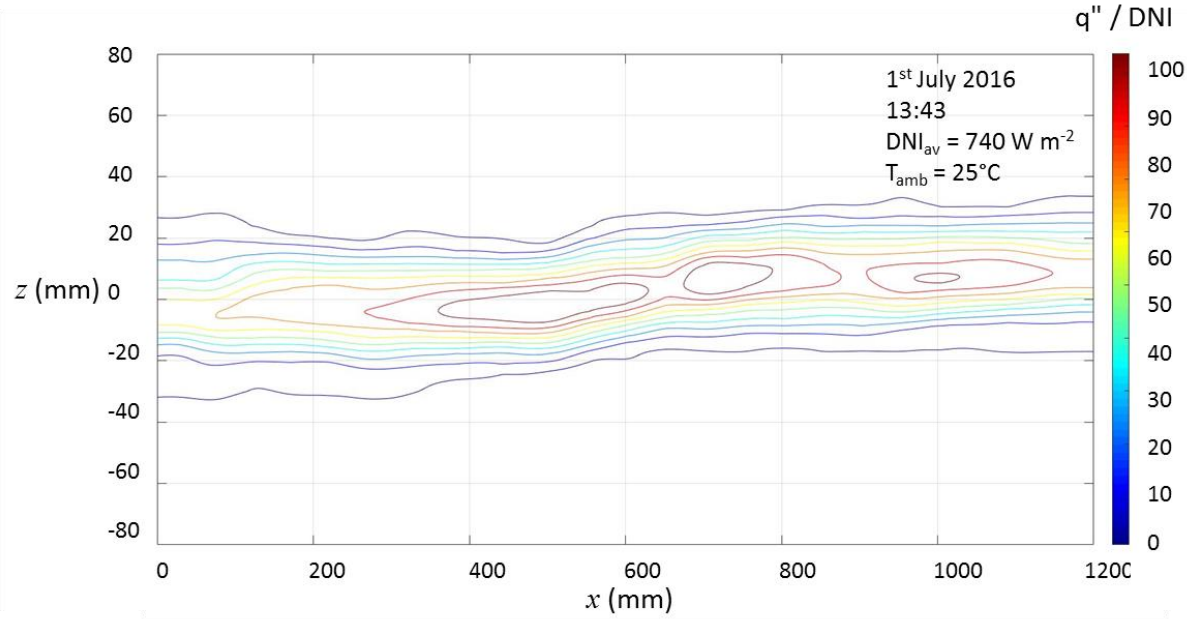

- b -

Figure 29 – Dimensionless concentrated isoflux contour plots on the scanned area measured during the first (a) and second (b) day of the experimental investigation.

From the isoflux contour plots of the dimensionless concentrated flux depicted in Figure 29, it can be noticed that the width of the concentration region with a dimensionless concentrated

flux above 10 is between 80 mm and 50 mm and it is centred on the focal line. On the central part of the mirrors composing the investigated row, the concentration of the solar beams is performed on the tighter width. The plots in Figure 29 refer to the same single test runs during the first (28th Sept 2015, 13:58 - Figure 29 – a) and second (1st Jul 2016, 13:43 - Figure 29 – b) day considered in Figure 28.

Figure 30 reports the resulting average distributions of the dimensionless concentrated solar flux for the two test runs for a receiving length of 1000 mm (Figure 30 – a) and 500 mm (Figure 30 – b). In this Figure, the distributions were limited to a width of 100 mm and the peak of the distributions were centred on the ideal position of the focal line (z = 0 mm) to better observe the asymmetry of the concentrated solar flux profile and to facilitate the comparison of the two sets of data.

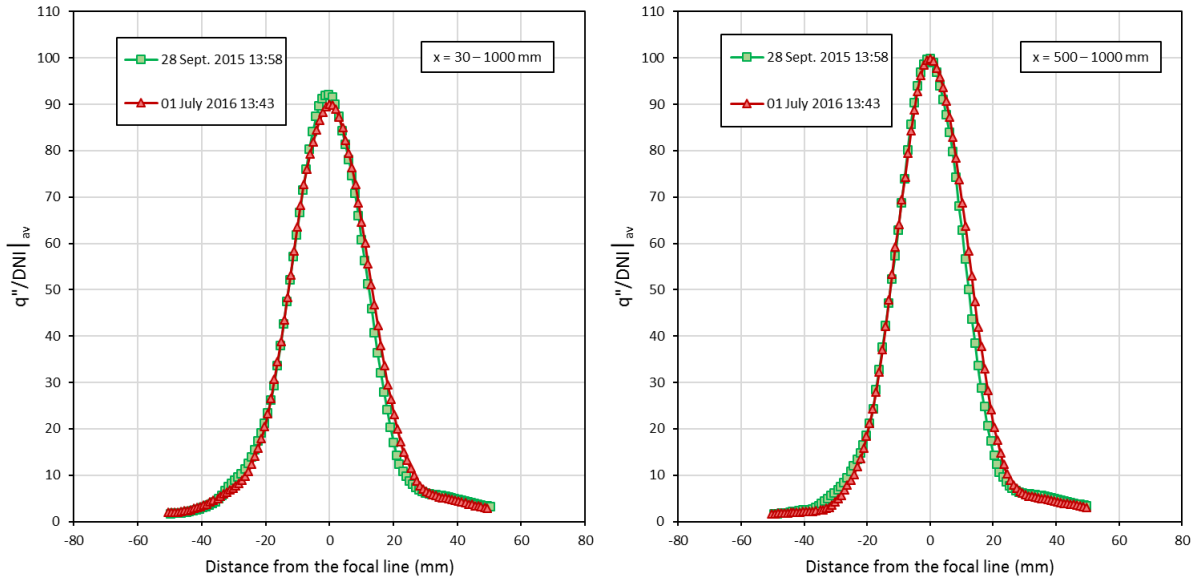

- a - *- b -*

Figure 30 – Average distributions of the dimensionless concentrated solar flux for the 28th Sept 2015 - 13:58 (green square) and the 1st Jul 2016 - 13:43 (red triangle). The distributions refer to a scanned area width of 100 mm and a length between 30 and 1000 mm (a) and 500 between and 1000 mm (b)

As can be seen in Figure 30 – a, the average distributions of the dimensionless concentrated solar flux for a length of around 1000 mm are very similar; the distribution of the 28th Sept.

2015, 13:58 (green square) is slightly shifted to the lower part of the receiving area (negative value of the coordinate z) and present a higher peak compared to the distribution of the 1st July 2016, 13:43 (red triangle). Considering only the concentrated flux distribution on the central part of the mirrors composing the investigated row between 500 and 1000 mm (Figure 30 – b), the difference in the peak between the two distributions is negligible but the slight shift of the 28th Sept. 2015, 13:58 distribution (green square) can still be observed. It must be mentioned that the differences in the average distributions of the dimensionless concentrated solar flux depicted in Figure 30 are all lower than the uncertainty band.

According to the previous considerations, the calculation of the concentrated heat flow rate q_{inc} and the determination of optical efficiency η_0 and the intercept factor γ_r has been performed by numerically integrating the distribution surfaces obtained from the interpolation of the different data sets for a trough length equal to 1000 mm (from 50 mm to 1050 mm) and different receiving widths from 100 mm to 0 mm. Considering the solar flux map on the measuring area of Figure 28 – a (28th Sept. 2015, 13:58), which has been obtained under an average direct normal irradiance of 915 ±40 W m^{-2}, equivalent to a radiative heat flow rate on the aperture area (1 m x 2.9 m) of 2653 ±120 W, the heat flow rate of the concentrated radiation incident q_{inc} on a receiving area having a width of 100 mm is around 2613 ±188 W, while it results equal to 2538 ±183 W for a 75 mm width, to 2359 ±170 W for a 50 mm width and to 1717 ±124 W when the width is 25 mm. When considering the solar flux map of the test run performed the 1st July 2016 13:43 (DNI_{av} = 740 ±33 W m^{-2} and 2147± 97 W on the aperture area), the heat flow rate of the concentrated radiation incident q_{inc} on an area of interest having a width of 100 mm is around 2147 ±155 W, while it results equal to 2088 ±151 W for a 75 mm width, 1959 ±141 W for a 75 mm width and to 1410 ±102 W when the width is 25 mm.

Table 3 includes the incident heat flow rate calculated from the data collected in six consecutive test runs during the first day of measurement, the related focal region widths and the relevant optical efficiency η_0 calculated according to the relationship reported in Eq. 2.12. All the data have been reported with their uncertainties values. The average experimental uncertainty on the concentrated power is ±7.5%, while that on the intercept factor γ_r is ±8.5% of the measured value.

Table 3 – Test results of the experimental measurement of the concentrated solar flux for four widths of the scanned area (100, 75, 50, 25). The length of the area is equal to 1000 mm (50 – 1050 mm) for all the test runs.

Width of the receiving area	Starting time of the test run	Average DNI during the test	Incident heat flow rate	Optical efficiency
mm	(year) hh:mm	W m^{-2}	W	%
100	(2015) 13:58	915 ±40	2613 ± 188	98.5 ± 8.4
	(2015) 14:04	913 ±40	2590 ± 186	97.6 ± 8.3
	(2015) 14:11	912 ±40	2608 ± 188	98.7 ± 8.4
	(2015) 14:31	890 ±39	2523 ± 182	97.7 ± 8.4
	(2015) 14:37	887 ±39	2521 ± 182	98.8 ± 8.3
	(2015) 14:43	887 ±39	2510 ± 181	97.6 ± 8.3
	(2016) 13:58	740 ±33	2147 ± 155	100.0 ± 8.5
	(2016) 14:47	770 ±34	2231 ± 161	99.9 ± 8.5
75	(2015) 13:58	915 ±40	2538 ± 183	95.7 ± 8.1
	(2015) 14:04	913 ±40	2511 ± 181	94.8 ± 8.1
	(2015) 14:11	912 ±40	2532 ± 183	95.8 ± 8.2
	(2015) 14:31	890 ±39	2455 ± 177	95.1 ± 8.1
	(2015) 14:37	887 ±39	2447 ± 176	95.1 ± 8.1
	(2015) 14:43	887 ±39	2441 ± 177	94.9 ± 8.1
	(2016) 13:58	740 ±33	2088± 151	97.9 ± 8.3
	(2016) 14:47	770 ±34	2171± 157	97.2 ± 8.2
50	(2015) 13:58	915 ±40	2359 ± 170	88.9 ± 7.6
	(2015) 14:04	913 ±40	2352 ± 170	88.8 ± 7.6
	(2015) 14:11	912 ±40	2371 ± 171	89.7 ± 7.6
	(2015) 14:31	890 ±39	2309 ± 167	89.5 ± 7.6
	(2015) 14:37	887 ±39	2301 ± 166	89.4 ± 7.6
	(2015) 14:43	887 ±39	2298 ± 166	89.3 ± 7.6
	(2016) 13:58	740 ±33	1959± 141	91.3 ± 7.8
	(2016) 14:47	770 ±34	2041± 147	91.4 ± 7.8
25	(2015) 13:58	915 ±40	1717 ± 124	64.7 ± 5.5
	(2015) 14:04	913 ±40	1739 ± 125	65.7 ± 5.6
	(2015) 14:11	912 ±40	1730 ± 125	65.5 ± 5.6
	(2015) 14:31	890 ±39	1712 ± 123	66.3 ± 5.6
	(2015) 14:37	887 ±39	1677 ± 121	65.2 ± 5.5
	(2015) 14:43	887 ±39	1700 ± 123	66.1 ± 5.6
	(2016) 13:58	770 ±34	1410± 151	65.7 ± 5.6
	(2016) 14:47	770 ±34	1466± 151	65.6 ± 5.6

The power and the optical efficiency on an area of interest do not vary significantly during the different test runs on performed on the first day of measurement. This proves the repeatability and the reliability of the proposed experimental technique. As a further proof of the repeatability of the adopted measurement technique, it can be observed that the values of the optical efficiency of the second day of measurements are in agreement with those of the first day. It has to be mentioned, that, since the nominal reflectance of the mirror is equal to 96%, it is physically impossible to reach optical efficiencies over this value, even at the maximum of the width of the receiving area. However, the calculated optical efficiency reported in Table 3 are considered plausible when the experimental uncertainty is taken into account.

The plot of Figure 31 includes the intercept factors obtained from the six consecutive test runs performed the first day and the two test runs of the second day of measurement. The scanned areas considered for this plot is given by the length of the single row of mirrors multiplied by the range of focal region widths from 0 mm to 100 mm.

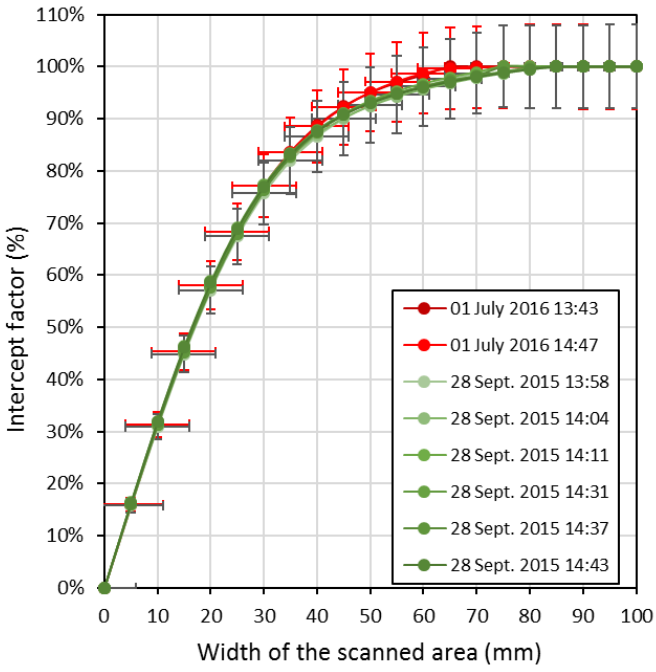

Figure 31 – Experimental values of the intercept factor γ_r obtained from the test runs performed during the 28th Sept 2015 (green square) and the 1st Jul 2016 (red triangle). The distributions refer to a scanned area with a length between 30 mm and 1000 mm.

The intercept factor γ_r obtained from the test runs performed during the 28th Sept 2015 (green square) and 1st Jul 2016 (red triangle) are in good agreement. Only for widths of the scanned area from 40 mm to 80 mm, the difference between the sets of data taken during the first day and the second day can be observed. These differences can be due to the asymmetry of the distribution of the concentrated solar flux with respect to the focal line (Figure 30) and the fact that the scanning range of the linear actuator was differently centred during the two days. However, the differences in the calculated values of the intercept factor are far below the experimental uncertainty. With reference to its average curve (dashed line in Figure 31), the intercept factor results 100% for a width of 75 mm, which means that flat receivers with a width higher than this value can collect all the solar radiation concentrated by the asymmetrical parabolic trough. The intercept factor decreases to 98% for a 65 mm width and to around 95% for a 55 mm. When considering a width lower than 45 mm, the intercept factor is less than 90% hence, it is recommended to include a secondary optics in the design of the receiver including the flat absorber with this width.

2.5 Ray-tracing modelling of the concentrated solar flux of an asymmetrical parabolic trough concentrator

In this investigation, the optical performance of the small prototype of asymmetrical parabolic trough considered in this thesis has been simulated and computed by Monte Carlo Ray-Tracing (MCRT) method. In order to generate a flux density distribution, numerical ray-tracing methods are combined with a convolution of the Sunshape with the shape of the ray-traced mirrors, which form the optical model of the concentrating system. Such methods allow the determination of the peak flux of the concentrated solar radiation as well as its spatial distribution. The experimental data obtained from the measurement of the concentrated solar flux have been used to validate the optical model of the concentrator adopted in the simulations and to identify the proper value of the total optical error σ to use in the simulations. Once validated, this model allows simulating the performance of the asymmetric parabolic trough under operating conditions different from the test conditions. Thus, it will be very useful for the optimized design of new flat absorber to be embedded into optimized receivers.

To develop an optical model of the present parabolic trough solar concentrator for performance analysis, the software SolTrace [87] has been used as MCRT tool. SolTrace is a software tool developed at the National Renewable Energy Laboratory (NREL) to model concentrating solar power (CSP) systems and analyse their optical performance. In the optical model developed in this work, all the factors influencing the solar flux distribution on the optimal concentration plane have been accounted for: the Sunshape, the geometry of the concentrator, the nominal reflectance of the mirrors and the total optical error σ. The rays coming from the Sun are considered to be normal to the aperture area, as ensured by the two-axes tracking system. The Sunshapes implemented in SolTrace refer to the work by *Neumann et al.* [88]. The circumsolar ratio (CSR) quantifies the average solar brightness profile and compares the energy contained in the solar aureole with the total energy. The CSR, which expression is reported in Eq. 2.15, is given by taking the integrated brightness or intensity over the solar disc I_S and the integrated intensity of the aureole around the solar disc I_{aur} (the circumsolar region):

$$CSR = \frac{I_{aur}}{I_S + I_{aur}} \qquad \textit{Eq. 2.15}$$

When CSR increases, the relative flux density of the Sun decreases, and vice versa. In addition to the derived characteristic Sunshapes, *Neumann et al*. [88]. developed frequency distributions of those Sunshapes for different levels of solar radiation explaining the conjunction between CSR and the energy density of the Sunshape ratio. From their statistical analysis, the Sunshape dubbed CSR0 resulted to be the most probable terrestrial Sun brightness profile on a clear-sky, therefore it has been considered appropriate to be implemented in the present investigation. According to the CSR0 profile, the circumsolar radiation represents up to 4% of the total energy contained in the solar disk plus aureole. The reflective surface considered in the simulation is half of a parabola that extends from the lower mirror rim, which is located on the parabolic profile at 35 mm from the vertex line, to upper the mirror rim. The defined parabola has a rim angle is of 78.7° and a focal length of 1.8. The length of the trough is of 2.4 m, resulting in an aperture area equal to 6.96 m^2. The reflectance of the mirror has been assumed equal to 96% as reported by the manufacturer [58]. The imperfections on tracking and mirrors shape and non-ideal reflectance are included in the total optical error σ which is the only parameter that can be varied in the simulations. A Gaussian distribution has been used to model the total optical error, thus it is expressed by its standard deviation expressed in milliradians: typical values within 3 mrad and 5 mrad have been implemented in the simulations. In the analysis, the total optical error is applied to the parabolic mirrors.

It has to be mentioned that the simplified model here proposed does not consider the effective shape of the facets of the concentrator. Therefore, local imperfections in the concentrator, like those observed close to the side edge of the parabolic mirrors, cannot be predicted. Nevertheless, the results obtained from simulations show the dependency of the concentration region width and of the intercept factor on the total optical error. In fact, MCRT tools can be used to calculate the amount of power reaching each surface of a given system. Therefore, some comparisons between experimental data and predictions have been done with the purpose of identifying the most suitable value of the total optical error. First, a comparison has been done between the experimental average profile of flux distribution along the width the concentration region (z-axis) and the simulated average profiles at different total optical errors.

Three sets of simulations have been performed in SolTrace considering a direct normal irradiance of 915 W m^{-2}, 890 W m^{-2} and 750 W m^{-2} and by varying the value of the total optical error σ between 3 and 5 mrad. Figure 32 reports the average distributions of the dimensionless concentrated solar flux resulting from these simulations using 25 bins along the z-axis and 40 bins along the x-axis (solid lines) and the average distribution obtained from the experimental data collected during the 28th Sept 2015 and the 1st Jul 2016 (dashed line). The use of a higher number of bins for exporting the simulated data does not entail any change in the predicted profiles.

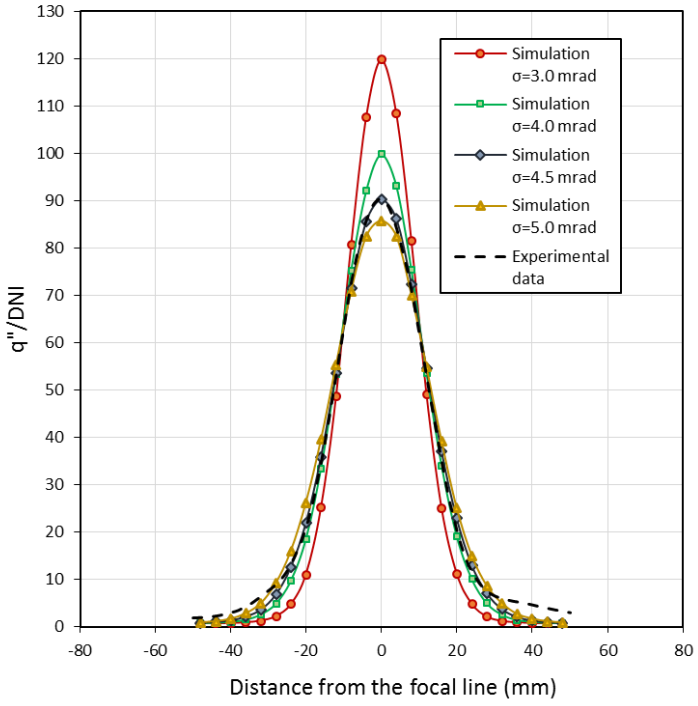

Figure 32 – Average distributions of the dimensionless concentrated solar flux. Solid lines represent the distribution obtained from the MCRT simulations using SolTrace at different values of the total optical error σ. The dashed line represents the average distribution calculated from the experimental data collected during the 28th Sept 2015 and the 1st Jul 2016.

The experimental average profile of the dimensionless concentrated solar flux distribution exhibits a peak value very close to z = 0 mm, which proves the accuracy of the positioning of the solar mapping system. From the comparison between experimental results and simulated

predictions, it can be observed that the central part of the experimental distribution profile, in the range around z = -30 mm and z = 30 mm, lies between the profiles simulated with a total optical error σ of 4 mrad and 5 mrad. The profile simulated with a total optical error σ of 4.5 mrad results to be in very good agreement. As the distance from the focal line increases, the optical error σ matching the experimental profile results higher than 4.5 mrad. Therefore, the trend of the dimensionless concentrated solar flux along the width of the receiver *z* can be mathematically expressed by the following expression (4.5 mrad):

$$\frac{q''}{\mathrm{DNI}}(z) = 81.451\, e^{-\left(\frac{z}{20.082}\right)^2} \qquad \textit{Eq. 2.16}$$

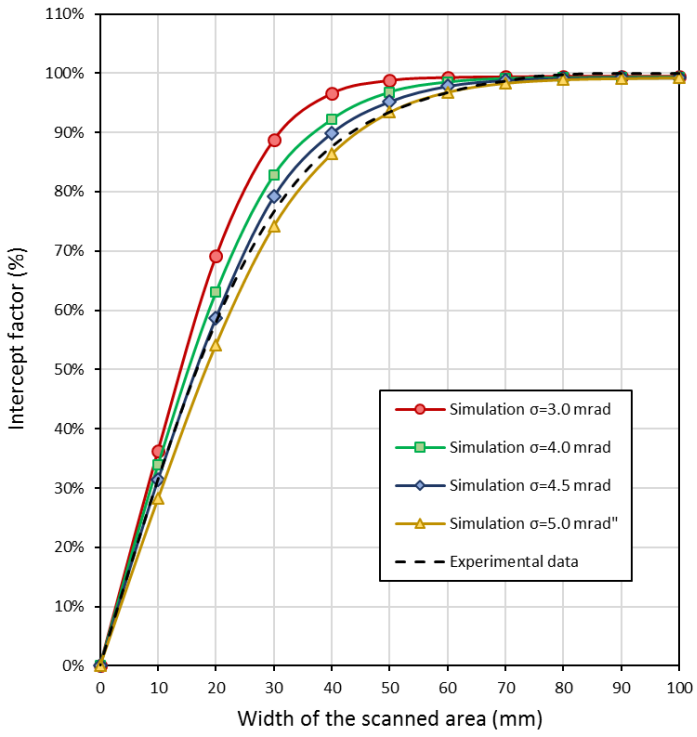

Figure 33 – Comparison between the experimental and predicted values of the intercept factor at different widths of the scanned area. Solid lines represent the intercept factor values obtained from the MCRT simulations using SolTrace at different values of the total optical error σ. The dashed line represents the experimental intercept factor obtained by averaging the experimental data collected during the 28th Sept 2015 and the 1st Jul 2016.

Similar findings come out from Figure 33, where the intercept factors obtained from the experimental data and from the numerical simulation are plotted as a function of the width of the scanned area in the concentration region. The experimental values of the intercept factor obtained by averaging the data collected during the 28th September 2015 and the 1st July 2016, lie between the MCRT predictions of the optical model implemented in SolTrace with a total optical error σ of 4.5 mrad and 5 mrad. Because of the model adopted for representing the total optical error σ, when increasing the width of the concentration region, the numerical predictions of the intercept factor tend asymptotically to a value between 99% and 100%. Nevertheless, this behaviour does not affect the present study. Considering the experimental uncertainty on the intercept factor and the previous comparisons between experimental data and numerical predictions, the values comprise between 4.5 mrad and 5 mrad are considered suitable for modelling the total optical error using a Gaussian distribution in a statistical ray-tracing model of the investigated concentrator.

Chapter 3 Planar surface receiver for single- and two-phase heat transfer fluids

The present work investigates an innovative aluminium flat absorber for medium-temperature linear concentrating solar collectors. After defining its optimal width through a Monte Carlo ray-tracing analysis, this absorber has been manufactured with the bar-and-plate technology, including an internal offset-strip turbulator. This technology is cost-effective and extremely flexible, giving the possibility to easily adapt the geometry of the absorber to different reflecting optics configurations. The combined use of a high thermal conductivity material and a passive heat transfer enhancement technique in a flat absorber is a promising solution for linear concentrating devices.

The present Chapter aims to present the results of the application of the proposed design for flat receivers in single-phase heating and direct vaporization of fluids in a small linear solar concentrator to form a solar collector with a concentration ratio of 42. After a brief introduction, the experimental investigation on the direct generation of steam and the production of process heat is presented. In particular, a new procedure proposed by *Bortolato et al.* [89] is applied and validated to characterize the thermal performance of the collector during steam generation. Afterwards, the new experimental procedure has been applied to determine the thermal performance of the innovative receiver during the vaporization of a halogenated fluid with a low Global Warming Potential (GWP), the R1233zd(E). This fluid can be a valid alternative to R245fa in various applications, such as power generation from low-temperature sources in ORC system and high-temperature heat pumps. A new numerical model to predict the thermal performance of the receiver has been developed. This model has been validated against the experimental data collected during single-phase heating and vaporization of the two fluids and has been used to study possible optimized configurations of the receiver.

3.1 Receivers in linear concentrating solar collectors

In linear concentrating solar collector, the receiver is the heart of the conversion system. The main function of the receiver is to absorb the concentrated solar radiation and convert it with a high efficiency to heat. In order to optimize the conversion process, the receiver must show high absorption of solar radiation as well as low heat losses due to thermal emittance.

In parabolic trough collectors, the receiver is generally formed by an inner steel tube provided with a selective coating on its external surface that acts as a surface absorber and an outer glass cover. In order to achieve high conversion efficiencies, in addition to the selective coating, vacuum is used between the inner absorber tube and the outer glass tube [48]. On the other side, Linear Fresnel collectors admit many configurations of receivers [90,91] and the following categories can be distinguished for a general classification:

- non-evacuated single tube and secondary optics,
- evacuated single tube and secondary optics,
- inverted trapezoidal cavity receiver [92,93]

In these collectors, the solar concentrated flux incident on the absorber element of the receiver is a function of direct normal irradiance, geometrical concentration ratio, optical properties of the materials and total optical errors of the system. In typical configurations, the distribution of the concentrated solar flux on the surface of the absorber is strongly non-uniform [63,64]. This can lead to a temperature gradient along the cross-section of the absorber which is associated with differential thermal expansions. The resulting thermal stresses may have serious effects, especially in some particular working conditions. As reported by *Wang et al.* [94], to allow a safe and reliable operation, the temperature difference on the cross-section of the absorber should not be too high. *Khanna and co-workers* [61-63] derived explicit expressions to calculate circumferential and axial distribution of the concentrated flux, temperature distribution, radial, circumferential and axial distribution of normal stresses and strains on the absorber of a parabolic trough receiver and the corresponding deflection in its central axis. As highlighted in the previous Chapter, the expression for the real distribution of the concentrated flux is achieved by implementing Gaussian Sun shape and optical errors in a

Monte Carlo ray-tracing tool. The use of these tools is of great importance to obtain reliable results when performing numerical investigations on the receiver of a concentrating collector. The presented expressions can be used to find the appropriate dimensions of the parabolic trough collector, design the support brackets, evaluate the appropriate gap between the glass envelope and the absorber tube in a typical receiver and define the optimal mass flow rate. In common practice, a high mass flow rate is pumped in order to achieve a turbulent flow condition inside the absorber tube, but this may not always be the optimal strategy. Circumferential and axial thermal gradients on the absorber tube included in a glass envelope represent a major concern in liquid heating concentrating collectors working with low mass flow rates. In fact, in these cases, due to the low heat transfer coefficients, a bending of the tube can occur and the possible breakage of the glass envelope jeopardizes the thermal efficiency. Furthermore, the deviation of the receiver from the focal line may also reduce the intercept factor and consequently the optical efficiency. This situation is worse when low conductivity thermal oil is used as heat transfer fluid: the peak temperature not only may damage the selective coating but also may provoke a chemical degradation of the oil.

In the literature, many passive techniques have been proposed for receivers in parabolic trough collectors to reduce circumferential temperature gradient, peak temperature, exergy losses, enhance the internal heat transfer and increase the overall collector efficiency. Passive heat transfer enhancement generally involves three mechanisms to promote the turbulence of the flow: decreasing thermal layer, increasing the flow disturbance and increasing the velocity gradient near solid walls. Most of the available works are numerical investigations comparing conventional and enhanced receivers in parabolic troughs for CSP plants. Some numerical works assuming a realistic non-uniform flux on the absorber tube, derived by a Monte Carlo ray-tracing method, are reviewed below. In the work by *Muñoz and Abanades* [95], the effect on pressure drop, thermal losses, thermo-mechanical stress and thermal fatigue of a set of internal helically-finned absorber tubes with a different number of fins and helix angles has been analysed by computational fluid dynamics (CFD) tools. *Cheng et al*. [96] carried out a numerical computation of several receivers with unilateral longitudinal vortex generators, located on the side of the absorber tube where the solar irradiance is concentrated. As compared to the smooth absorber, the different geometries of enhanced internal surfaces exhibit better

heat transfer performance in a wide range of working conditions. *Gadirijafarbeigloo et al.* [97] presented numerical simulations concerning the use of typically twisted tape inserts and innovative perforated louvered twisted tape inserts inside the absorber tube and showed that the latter allow higher thermal performance especially at low Reynolds numbers. Helical screw-tape inserts in absorber tubes have been suggested by *Song et al.* [84] as an improvement of commonly twisted tape inserts to level out the temperature distribution specifying that experiments are required to verify their performance. *Mwsigye et al.* [98,99] numerically optimized the geometry of perforated plate inserts centrally placed inside an absorber tube and fixed to a connecting rod. The optimization of orientation, spacing and diameter of the plates considers not only the heat transfer enhancement and the fluid friction but also the entropy generation in a wide range of operating conditions.

Reddy et al. [100] presented one of the few experimental works conducted on thermal receivers for heat transfer enhancement. They investigated the performance of six different receiver configurations in a 3 m long parabolic trough collector with an aperture width of 2.5 m. The external diameter of the absorbers was 60 mm. The investigated configurations included conventional receivers with and without glass envelope and enhanced receivers with bottom porous discs, U-shaped bottom porous discs, inclined bottom porous discs and alternative porous discs. Results showed that the use of inserts leads to a lower thermal gradient between the receiver wall surface and fluid and across the receiver cross-section. The best performance has been achieved using alternative porous discs which provided a negligible increase in pumping power. The authors proposed this solution both for solar power and process heat applications.

3.1.1 Receivers for steam generation in linear concentrating collectors

When direct steam generation is performed, above all, the non-uniform distribution of the concentrated flux on the absorber must be taken into account. In fact, the phase change occurring in the heat transfer fluid can be associated with a large variation of the heat transfer coefficient along the cross-section of the absorber with changing vapor quality when a stratified flow regime is established. As a consequence, a significant angular thermal gradient can appear. Nevertheless, in the medium-temperature range, solar direct steam generation is very

attractive. In these applications, the working pressure is not very high and cost reduction of the energy produced from the solar source and the increase in the efficiency of the system can be achieved. In fact, as compared to the use of liquid water, the phase change reduces the mass flow rate through the pumping system. Moreover, the heat exchanger between the solar collectors and the thermal user may be removed. With respect to the use of the thermal oil, direct steam generation allows to eliminate some auxiliary equipment and reduces the environmental impact of the system.

There are essentially two strategies to attain a strong reduction of the thermal gradient during direct steam generation [101]. The first one is setting a mass flow rate high enough to operate under annular flow pattern and avoid stratified regime. It involves the calculation of a lower limit of the mass flow rate that depends on the working conditions and the geometry of the absorber. This strategy is usually employed in the rare CSP plants working with direct steam generation. The second strategy concerns either the adoption of a high thermal conductivity material in the manufacturing of the absorber tube or the integration of enhanced heat transfer systems. This approach entails no lower limit of the operating mass flow rate and gives higher flexibility to the plant. In fact, it can work even under lower solar radiation and for a higher number of hours per day. This is of great interest especially in small linear concentrating collectors for medium-temperature applications; nevertheless, most of the relevant works available in the literature focus on big parabolic troughs for solar power. *Almanza et al.* [102,103] investigated mild steel and copper absorbers behaviour under two-phase stratified flow tests in a parabolic trough solar collector. When using the steel pipe, at around 160°C wall temperature, a maximum deflection of 6.5 cm has been observed causing the breaking of the glass envelope. In this case, the maximum circumferential temperature difference was around 60°C. Under the same test conditions, using a copper pipe, a bend of 2 mm has been observed and a maximum temperature difference of 10°C has been measured. The authors highlighted that thermal cycles at high temperature may cause copper annealing. On the basis of these results, *Flores and Almanza* [104] compared the thermal behaviour of a bimetallic copper-steel receiver for direct steam generation in parabolic trough solar collectors. Experiments have been performed in transient conditions, simulating the presence of clouds. The results prove that the high thermal conductivity of the internal copper layer contributes to uniform the wall

temperature of the receiver while the external steel layer improves the mechanical resistance. At a mass flow rate of 150 kg h^{-1} and a wall temperature around 200°C, the deformation was 70 mm in steel receiver and 18 mm in the bimetallic receiver. Moreover, the thermal behaviour of the bimetallic receiver resulted to be only slightly affected by the variation of the incidence angle of the solar beam irradiance. A numerical CFD simulation has been carried out by *Aldali et al.* [105] to assess the use of three types of tubes with different internal helical fins and an aluminium pipe without any fins as absorbers in a parabolic trough solar collector for direct steam generation under realistic heat flux distribution. The results show that the presence of fins improves the thermal distribution, but the smaller the pitch of the fins, the higher the pressure drop. The aluminium pipe has proved to be the best solution in minimizing the thermal stress. Thus, the thermal conductivity of the absorber tube may play a significant role in reducing the circumferential temperature gradient. An alternative solution for direct steam generation in parabolic trough solar concentrating collectors was presented by *Rojas et al.* [101]. They proposed the applicability of porous coating and etched microgrooves as capillary systems on the internal wall of the surface absorber tube.

3.2 Bar-and-plate flat receiver for concentrated solar radiation

In the present work, the use an innovative aluminium flat receiver in an asymmetrical parabolic trough collector for medium-temperature applications has been proposed under single- and two-phase flow regimes. The particular geometry of the parabolic trough concentrator considered in this study is suitable to be coupled with a receiver displaying a flat geometry rather than a tubular receiver. Figure 34 reports the numerical results of the comparison between a flat (Figure 34 – a) and a tubular geometry (Figure 34 – b) of the absorber collecting the solar radiation concentrated by an asymmetrical parabolic trough. The simulations have been performed with the MCRT software TracePro® [106]. From this Figure, it can be clearly seen that, while both flat and tubular absorbers are capable of receiving the totality of the concentrated solar rays, the latter geometry offers a much higher surface which is not used to collect the concentrated solar radiation and increases the thermal losses.

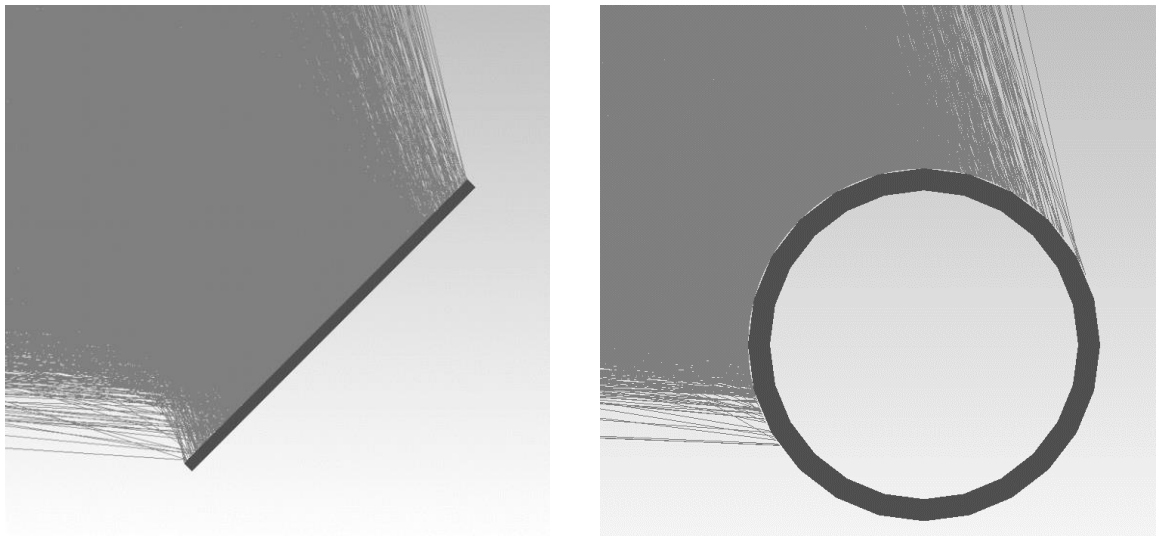

-a- *-b-*

Figure 34 – MCRT simulations of the reception of the concentrated solar flux coming by an asymmetrical parabolic trough on a flat (a) and a tubular (b) receivers.

To minimize the incidence angle of the concentrated beams on the flat receiver, without complicating the construction of the concentrator, the optimal concentration plane of this

system has been identified as the plane 45° tilted with respect to the plane containing the focal line and the vertex line and the aperture plane. This solution derives from a compromise between the needs to minimize the incidence angle of the concentrated beams and to simplify the positioning of the receiver. The receiver has been manufactured with bar-and-plate technology and provided with an internal turbulator. According to the cited studies in the literature, the combined use of a high thermal conductivity material and of passive heat transfer enhancement devices should make the direct vaporization of a fluid easier to control and less critical. The dimensions of the absorber front surface have been defined by adopting the developed optical model of the present asymmetrical concentrator using SolTrace [107] as Monte Carlo ray-tracing tool (see Chapter 2). A range of absorber widths from 40 mm to 100 mm have been numerical investigated. A value for the total optical error of 5 mrad has been prudently considered and the desired number of ray intersections has been set equal to 3×10^6. The use of more ray intersections has a negligible effect on the estimation of the optical performance parameters while implies a much higher computational effort. Because of the model adopted to represent the total optical error, when the width of the absorber increases, the numerical predictions of the intercept factor γ_r tend asymptotically to a value between 99% and 100%. This has a minor effect on the design of the receiver. The results of the simulations show that the intercept factor does not increase significantly for width higher than 70 mm. Furthermore, the bigger the absorber width, the higher the thermal losses towards the external surroundings. As a consequence, a width of 70 mm has been adopted for the absorber, thus the resulting geometrical concentration ratio C_g is equal to 42.

The optical model provides also the solar flux map on the front surface of the absorber. Considering this highly non-uniform heat flux profile, the use of a heat spreader is recommended to reduce the thermal load on the central line of the absorber and to use more effectively the heat transfer area on the working fluid side. It can consist of a front plate with a thickness of 5 – 10 mm made of a high thermal conductivity material. The bar-and-plate technology is suitable to manufacture an absorber with the features derived from the MCRT analysis. In fact, it allows creating a rectangular channel made of aluminium with high mechanical stiffness, including a heat spreader on the front surface reached by the non-uniform concentrated solar flux. Here, the heat spreader is made of a thick aluminium plate on the front

face. Furthermore, a turbulator is included inside the channel to enhance the heat transfer playing a pivotal role during direct steam generation. The internal structure of the bar-and-plate flat receiver is shown in Figure 35.

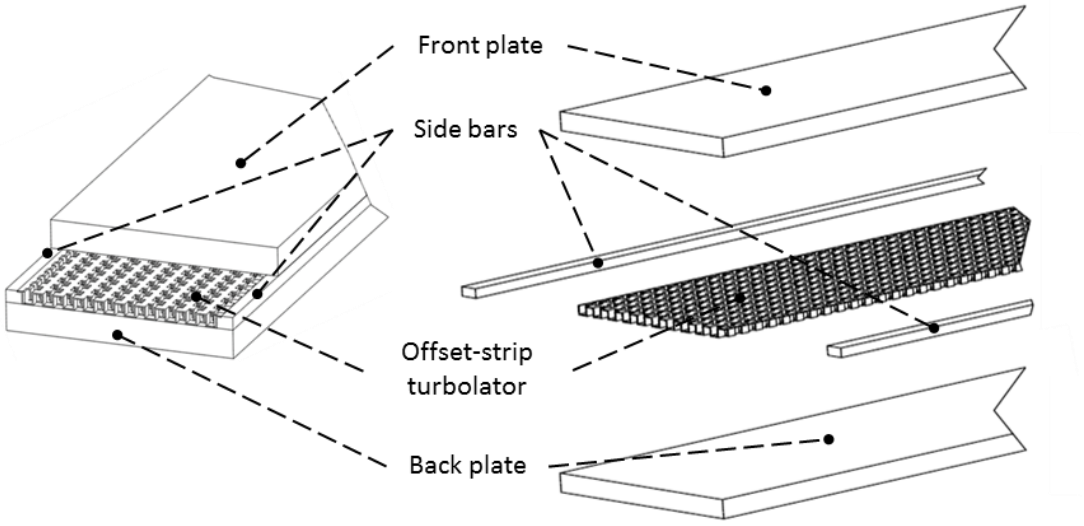

Figure 35 –Compact and exploited views of the bar-and-plate flat receiver internal structure.

The presence of the turbulator entails a uniform distribution of the mass flow rate on the absorber cross-section, hence stagnation points leading to hot spots can be avoided. Furthermore, the hydraulic diameter is reduced so that the occurrence of a stratified flow regime is limited. Finally, the turbulator helps to increase the nucleation sites and prompts the vaporization of the fluid. Given the above, throughout the length of the present absorber, there is an offset-strip turbulator, whose geometry is depicted in Figure 36. The height of the turbulator is of 3.3 mm and the resulting hydraulic diameter is equal to 2.5 mm according to the definition given by *Manglik and Bergles* [108].

The receiver has been thermally insulated on the back side by using a 20 mm layer of rockwool. The front surface of the absorber is provided with a thickness insensitive - spectrally selective black coating, that is characterized by a solar absorptance of around 90% and a thermal emittance at 100 °C of around 45%. The inlet and outlet of the working fluid are located at the ends of the absorber on the back face (Figure 37). According to some preliminary tests, the maximum working pressure is 30 bar and the maximum working temperature is around 200°C.

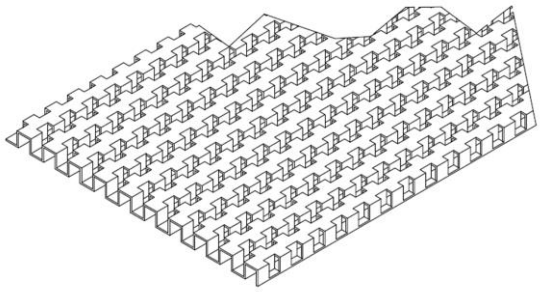

Figure 36 – Sketch of the offset-strip turbulator geometry inside the flat receiver.

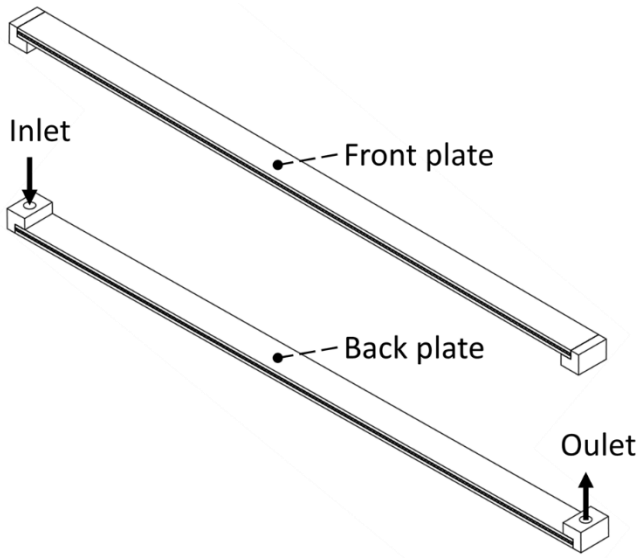

Figure 37 – Sketch of the bar-and-plate flat receiver including inlet and outlet fluid directions.

The length of the receiver is equal to 1.2 m, which corresponds to half of the total trough length. The present receiver has been coupled with the asymmetrical parabolic trough concentrator as shown in Figure 38 - a. The absorber has been arranged so that it receives the concentrated solar flux from a single row of back-silvered glass facets (Figure 38 – b). Due to the two-axis tracking system, the second mirror row does not influence the performance of the present absorber, thus, the thermal efficiency is computed considering a trough length of 1.2 m. A modular configuration can be considered for the system, which means that, in a real application, more receivers can be installed in series or in parallel.

- a -

- b -

Figure 38 – Bar-and-plate flat receiver arranged on the support bar of the collector (a) and receiver under concentrated solar radiation during a test run (b).

It is worth to mention that the bar-and-plate manufacturing process is extremely flexible. Thus, the dimensions of the absorber can be easily adapted in a cost-effective way to the primary optics of any considered medium-temperature linear solar concentrating collector. As an example, in a symmetrical parabolic trough, a V-shaped absorber consisting of two flat parts could be easily realized.

3.3 Experimental investigation of a bar-and-plate flat receiver for liquid heating and vaporization of fluids

The present flat bar-and-plate receiver has been mounted on the asymmetrical parabolic trough concentrator. An experimental test facility has been set up to evaluate the thermal performance of the collector during single-phase heating and vaporization of water in the receiver. The same test facility has been used to run tests with R1233zd(E). A sketch of the test rig is reported in Figure 39. The test runs presented in this Chapter have been performed in the Solar Energy Conversion Laboratory on the roof of the Department of Industrial Engineering at the University of Padova (45.416°N, 11.883°E)

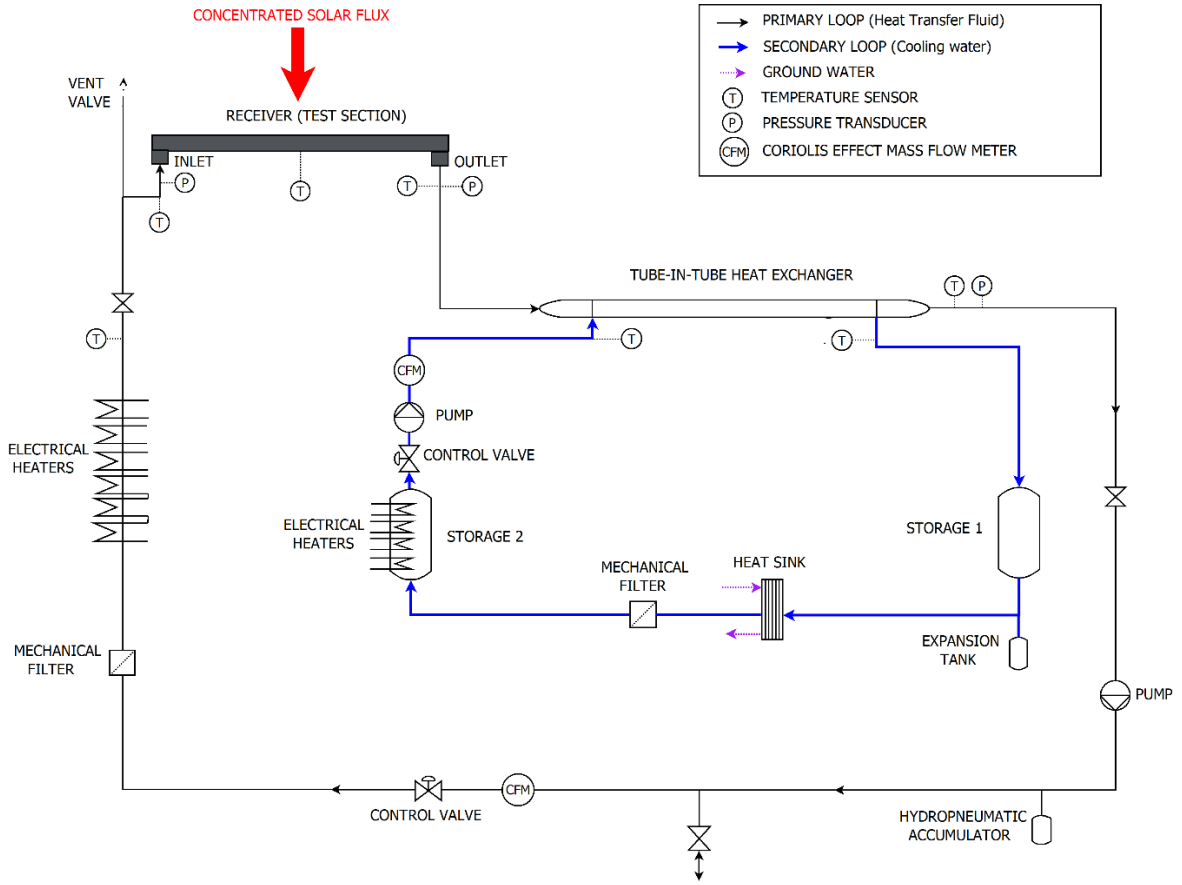

Figure 39 – Experimental test rig for single-phase heating and direct vaporization of water in bar-and-plate flat receiver under concentrated solar radiation.

The test rig is designed to measure the thermal efficiency of the solar concentrating collector during liquid heating but also when the heat transfer fluid (HTF) is directly vaporized inside the receiver. In the latter case, the experimental investigation should validate a test method compatible with the method available for liquid heating tests. Besides, possible instabilities during two-phase flow conditions must be carefully checked. Since the presence of a turbulator may penalize the hydraulic performance, accurate measurements of pressure drop have also been carried out. The test rig includes a primary loop arranged on board the concentrating collector and a secondary cooling loop. Both the loops are thermally insulated to limit heat losses towards the surroundings.

In the primary loop (Figure 39), after exiting the receiver, the HTF (distilled water or R1233zd(E)) enters a tube-in-tube heat exchanger that acts as a heat sink: the heat transfer rate provided by the concentrated solar irradiance is taken away by a secondary water flow. In the heat sink, the HTF flows inside the inner tube, while the coolant flows in the annulus. Afterwards, the HTF is sent to an independently controlled gear pump magnetically coupled to a variable speed electric motor. This pump is used to set the mass flow rate, which is measured by a Coriolis effect mass flow meter. The pressure of the primary loop is regulated by a hydropneumatics accumulator with a fluoroelastomer diaphragm: this device plays a key role in direct steam generation test runs as the working pressure determines the temperature of the generated steam. Before entering the receiver, the fluid passes through a preheating section which consists of a heating wire wrapped around a stainless steel tube. The electrical heater is connected to a solid-state relay which is governed by a PID temperature controller. The PID controller uses a T-type thermocouple as a probe to monitor the trend of the external wall temperature of the stainless steel pipe downstream of the preheating section. Three high precision absolute pressure sensors have been connected to the primary loop pressure taps to gauge the pressure at the inlet and at the outlet of the receiver and at the outlet of the tube-in-tube heat exchanger. The temperatures of the HTF downstream of the preheating section, at the inlet and at the outlet of the receiver and downstream of the heat exchanger are measured by Pt100 resistance temperature detectors (RTDs). In the two-phase tests for direct steam generation, with outlet vapor quality lower than 1, the presence of both the pressure transmitter and the RTD allows to check the agreement of temperature and pressure at the outlet of the

receiver under saturated conditions. During the test runs with water, two flat RTDs have been attached to the aluminium wall on the back of the receiver, under the thermal insulation layer. These temperature sensors were located respectively at 300 mm from the inlet and the outlet to measure the rear surface temperature of the bar-and-plate receiver. These measurements are used to check if the wall temperature exhibits marked peaks, which may be due to the onset of thermal dry out inside the receiver. During the test runs with R1233zd(E), the two flat RTDs have been substituted by five copper-constantan thermocouples attached 20 mm, 50 mm, 90 mm, 140 mm and 200 mm from the outlet of the receiver. In the secondary cooling loop (Figure 39), the water coming from the tube-in-tube heat exchanger enters a first storage and passes through a plate heat exchanger, where the heat gained from the primary loop is wasted to the groundwater of the building central plant. Afterwards, the cooling water enters a second storage which is provided with four electrical heaters. Given the cooling mass flow rate, it is possible to set the electrical power in order to control the coolant temperature at the inlet of the tube-in-tube heat exchanger. A pump is used to circulate the coolant, whose mass flow rate is set by a control valve and is measured by a Coriolis effect mass flow meter. The controls on secondary mass flow rate and inlet temperature are used to achieve constant conditions of the primary working fluid at the inlet of the receiver. The temperatures of the water at the inlet and at the outlet of the tube-in-tube heat exchanger are measured by Pt100 RTDs. The laboratory is equipped with a measuring system of the solar irradiance including a first class pyrheliometer mounted on a high precision solar tracker that is used to measure the DNI. Finally, an anemometer measures the wind speed on the horizontal plane and the ambient air temperature is gauged by a Pt100 RTD. All the measured quantities are recorded by a data logger with a sampling rate of 3 s and the collected data are reduced in a Matlab® environment by calculating the fluid properties with NIST Refprop Version 9.0 [109].

3.3.1 Experimental technique for single-phase test runs

The thermal performance of the linear solar concentrating collector working as a liquid heating device has been evaluated according to the quasi-dynamic test method described in the European Standard EN ISO 9806:2013 [110].

This method was originally conceived for non-concentrating solar collectors and for its relevant working temperature range and it was then extended to the concentrating technologies. As a consequence, when testing concentrating collectors, some procedures are hardly applicable and some rules are unclear [111], especially for prototype testing.

According to this procedure, the specific mass flow rate is set equal to 0.02 kg s^{-1} per square meter of the aperture area, computed considering the actual length of the receiver (1.2 m) and the projected height of the mirrors. Measurements are repeated at different values of the inlet HTF temperature, in order to produce a set of data points for the thermal efficiency of the collector η_{col}, defined according to Eq. 3.1

$$\eta_{col} = \frac{q_{th}}{\mathrm{DNI}\ A_a} = \frac{\dot{m}_I\ c_{p,I}\left(T_{out\ r,I} - T_{in\ r,I}\right)}{\mathrm{DNI}\ A_a} \qquad \textit{Eq. 3.1}$$

where $c_{p,I}$ is the isobaric specific heat capacity of the HTF at the mean temperature between inlet and outlet of the receiver.

The experimental results are presented in a diagram plotting the experimental thermal efficiency as a function of the reduced temperature difference T_m^* (Eq. 3.2), along with the obtained efficiency curve of the collector.

$$T_m^* = \frac{\frac{\left(T_{out\ r,I} + T_{in\ r,I}\right)}{2} - T_{amb}}{\mathrm{DNI}} = \frac{T_{m\ R,I} - T_{amb}}{\mathrm{DNI}} \qquad \textit{Eq. 3.2}$$

The mathematical expression of the efficiency curve of the parabolic trough collector in quasi-dynamic conditions is defined in the standard [110]. Its general equation is an energy balance including the dependence on direct and diffuse solar irradiance, wind speed, sky temperature, incidence angle effects and effective thermal capacity (Eq. 3.3)

$$\frac{\dot{q}_{th}}{A_{ap}} = \eta_{0,b}K_bG_b + \eta_{0,b}K_dG_d - c_6uG - c_1(T_m - T_{amb}) - c_2(T_m - T_{amb})^2 +$$

$$-c_3u(T_m - T_{amb}) + c_4\left(E_L - \sigma_{SB}{T_{amb}}^4\right) - c_5\frac{dT_m}{d\tau} \qquad \textit{Eq. 3.3}$$

In the present experimental study, concerning a concentrating system with two-axes Sun-tracker, the incidence angle modifier for direct radiation K_b is set equal to 1, the direct normal irradiance DNI is used instead of the direct solar irradiance G_b and the incidence angle for

diffuse radiation is equal to zero. In fact, the effective incident irradiance on the aperture area includes only the direct normal irradiance for all the concentrating collectors displaying a geometrical concentration ratio above 10 [9]. In the present work, the coefficients c_3, c_4 and c_6 are neglected right from the beginning, as it is recommended in the standard for concentrating collectors. According to the standard, it is not clear how the present concentrating collector prototype should be treated with respect to the effects of wind and long-waves thermal irradiance. In fact, the case of a unglazed receiver installed in a device with a high concentration ratio is not contemplated. It is worth to mention that the test runs presented in this work have been performed in Padova (45.416 °N, 11.883 °E) where the wind speed in clear-sky days is rarely higher than 1 m s^{-1}. Thus, the assumption of a negligible effect of wind is acceptable.

The experimental test rig does not include any storage and the working fluid and the HTF temperature at the inlet of the receiver can be maintained within the limits imposed by the standard only by a PID controlled electrical heaters and by varying the inlet temperature and the mass flow rate of the secondary fluid. As a consequence, the experimental tests have been conducted during clear-sky days, when the variation of the direct normal irradiance is quite small. Thus, the effect of the thermal capacity is not significant and is not included in the model ($c_5 = 0$). The final expression of the overall thermal efficiency is then:

$$\eta_{col} = \frac{q_{th}}{\mathrm{DNI}\ A_a} = \eta_0 - c_1 T_m^* - c_2 (T_m^*)^2\ \mathrm{DNI} \qquad \textit{Eq. 3.4}$$

Eq. 3.4 can be further simplified when the coefficient c_2 is negative or has no statistical significance because of the T-ratio, that is the ratio of the parameter value divided by its standard deviation, is lower than 3. As suggested by the standard EN ISO 9806:2013, the weighted least square method has been adopted to calculate the model parameters, starting from the measured quantities and their experimental uncertainties.

3.3.2 Experimental technique for two-phase test runs

The standard test methods to determine the thermal performance of solar concentrating collectors, namely the steady state method in the ASHRAE 93:2010 standard [112] and the quasi-dynamic method in EN ISO 8609:2013 standard [110], refer to liquid or air heating devices. This means that the useful heat gained by the working fluid can be calculated

considering its temperature increase inside the solar collector. There are no standard procedures to experimentally define the thermal efficiency of a solar concentrating collector performing direct steam generation when a latent heat transfer is involved.

Few authors in the scientific literature [113,114] proposed different procedures for thermal performance evaluation of steam generating concentrating collectors. *Bouvier et al.* pointed out that a proper definition of the reduced temperature difference should be introduced for two-phase systems. In the work of *Bortolato et al*. [89], a new test procedure has been outlined to characterize the thermal performance of a solar collector in a direct steam generation. The experimental procedure includes an expression for the reduced temperature difference in two-phase flow conditions that make the data collected in direct vaporization consistent with those collected in liquid heating mode under standardized conditions. This procedure has been adopted in the present study to evaluate the thermal performance of the concentrating solar collector during the vaporization of water and the halogenated fluid R1233zd(E).

During the test runs, the HTF enters the test section as subcooled liquid and its thermodynamic condition is completely determined by the temperature and pressure measurements at the inlet of the receiver. The working fluid exits the receiver as saturated vapor and then it is condensed and subcooled in the tube-in-tube heat exchanger. The thermodynamic state at the outlet of the heat sink is once again derived from pressure and temperature measurements. The tube-in-tube heat exchanger is installed very close to the outlet of the receiver, shielded from the concentrated solar beam and thermally insulated. The thermal balance in the tube-in-tube heat exchanger has been checked from the experimental points collected for water in single-phase test runs and it results to be within ±3%.

Given the above, the thermodynamic state of the working fluid at the outlet of the receiver under saturated conditions can be experimentally defined by applying the energy balance to the heat exchanger, under the reasonable hypothesis of negligible heat losses towards the surroundings. The specific enthalpy of the saturated vapor at the outlet of the receiver can be expressed as reported in Eq. 3.5

$$i_{out,r,I} = i_{out,he,I}\left(T_{out,he,I}, p_{out,he,I}\right) + \frac{\dot{m}_{II}\, c_{p,II}\left(T_{out,he,II} - T_{in,he,II}\right)}{\dot{m}_I} \qquad \textit{Eq. 3.5}$$

where $c_{p,II}$ is the isobaric specific heat capacity of the water flowing in the secondary loop at the mean temperature between the inlet and outlet of the tube-in-tube heat exchanger.

The thermodynamic vapor quality of the vapor exiting the receiver can be obtained from Eq. 3.6, after calculating the saturated liquid specific enthalpy i_L and the heat of vaporization i_{LV} corresponding to the saturation temperature gauged at the outlet of the receiver:

$$x_{out,r,I} = \frac{i_{out,r,I} - i_L\left(T_{out,r,I}\right)}{i_{LV}\left(T_{out,r,I}\right)} \qquad \textit{Eq. 3.6}$$

The saturation temperature is assumed equal to the temperature measured at the outlet of the receiver because, during two-phase test runs, the measured pressure drop across the receiver was very small: for instance, during the vaporization of water at 2 bar, the pressure drop entails a saturation temperature drop of 0.3 °C. The vaporization has been performed at different pressures of the HTF inside the receiver and thus at different saturation temperatures in order to obtain a set of overall thermal efficiency data under two-phase flow conditions, according to Eq. 3.7:

$$\eta_{col} = \frac{q_{th}}{\mathrm{DNI}\ A_a} = \frac{\dot{m}_I\left(i_{out\,r,I} - i_{in\,r,I}\right)}{\mathrm{DNI}\ A_a} \qquad \textit{Eq. 3.7}$$

The thermal efficiency of the receiver is calculated as the ratio between the heat gained by the fluid flowing in the receiver and the incident radiant power on the absorbing surface of the receiver. The latter, in the case of reflecting solar concentrators, can be estimated by considering the incident solar power on the aperture area of the collector A_a and the product of the intercept factor γ_r and the reflectance of the mirrors ρ_c. Hence the thermal efficiency of receiver in the present concentrator is given by

$$\eta_r = \frac{q_{th}}{G_{inc}} = \frac{\dot{m}_I\left(i_{out\,r,I} - i_{in\,r,I}\right)}{\mathrm{DNI}\ A_a\,\gamma_r\,\rho_c} = \frac{\eta_{col}}{\gamma_r\,\rho_c} \qquad \textit{Eq. 3.8}$$

According to the measurement of the concentrated solar flux conducted few days before the present test runs, the intercept factor γ_r of the present concentrating collector on a width of 70 mm resulted equal to 98.5%.

Considering Eq. 3.2, the definition of the reduced temperature difference under two-phase flow requires the introduction of the equivalent mean temperature of the fluid during direct vaporization of the HTF. Since the working fluid enters as a subcooled liquid, both sensible and latent heat transfers occur inside the receiver of the solar concentrating collector. Hence, the equivalent mean temperature of the vaporizing HTF shall be assumed as a weighted average temperature based on the enthalpy changes associated with the sensible and latent heat transfers (Eq. 3.9).

$$T_{m\,eq,I} = \frac{\left(\frac{T_{out,r,I} + T_{in,r,I}}{2}\right)\left(i_L\left(T_{out,r,I}\right) - h_{in,r,I}\right) + T_{out,r,I}\left(i_{out,r,I} - i_L\left(T_{out,r,I}\right)\right)}{i_{out,r,I} - i_{in,r,I}} \qquad \textit{Eq. 3.9}$$

3.3.3 Experimental procedure and uncertainty analysis

Before the test campaign, the primary loop is evacuated and then filled with the HTF. The residual air content is removed by circulating the HTF at high mass flow rate while keeping the vent valve open. The vent valve is located near the receiver, on the highest part of the primary test loop (Figure 39). Prior to each test sequence, the mirrors and the Sun sensor of the parabolic trough solar collector as well as the pyrheliometer have been cleaned.

When performing liquid heating tests, a preconditioning period of 20 min has been observed. During each test sequence, that has a minimum duration of 3 h, the experimental data are averaged every 10 min and the maximum permitted deviations of the main operating parameters are in agreement with the specifications included in the standard EN ISO 9806:2013 [110]. This means that each experimental point presented in this work is the average of 200 recordings while the collector is working under stable conditions.

During tests under two-phase flow regime, the new experimental procedure illustrated here below has been adopted. After a preconditioning period of 20 min, during each test sequence, that lasts for 3 h minimum, the collected data are averaged every 10 min and the following criteria have been satisfied during tests:

- the inlet temperature of the subcooled liquid is kept stable within ±1 °C as compared to its mean value;

- the HTF mass flow rate is kept stable within ±2% as compared to the mean value;
- the thermodynamic vapor quality at the outlet of the receiver must be higher than 0.1.

In order to validate this procedure, vaporization tests have been performed so that most of the useful heat (at least 90%) is transferred to the fluid flowing inside the receiver as latent heat. This entails that the maximum admitted subcooling degree for the data collected under two-phase flow regime with water is lower than 9 °C. During the test performed with R1233zd(E), the inlet subcooling ranges between 11°C and 24°C.

The uncertainty analysis has been performed in agreement with the guidelines provided by the "Guide to the Expression of Uncertainty in Measurement" [37] and briefly recalled here below. The experimental standard uncertainty of a measured parameter is made up of two terms: the type A uncertainty that arises from the statistical analysis of repeated observations and the Type B uncertainty that results from calibration of instruments, calibration certificates, manufacturers' specifications and uncertainties assigned in reference handbooks. Type B uncertainties of the measured parameters are reported in Table 4 with a level of confidence of 95%.

Table 4 – Type B uncertainty of measured parameters during single-phase heating and direct vaporization of water in bar-and-plate flat receiver under concentrated solar radiation.

Ambient air temperature	± 0.07°C
Fluid temperature in primary and secondary loops	± 0.035°C
Coriolis effect mass flow meters	± 0.3 kg h^{-1} for single-phase tests ± 0.07 kg h^{-1} for two-phase tests
Pressure of the fluid in the primary loop	± 0.023 bar
Direct normal irradiance	± 3% of measured value
Wind speed	± (0.1 m/s + 1% of measured value)

Usually RTDs manufacturers provide a Type B uncertainty that depends on the measured temperature: for the present sensors it is ±0.04 °C at 5 °C and ±0.1 °C at 90 °C. In Table 4, the type B uncertainty of the RTDs is reported as a constant value of ±0.035 °C, which is valid within the temperature test range from 20 °C to 150 °C. This value results from the calibration procedure performed using a high precision four wire RTD, that is calibrated up to 150 °C. The

reference RTD is connected to a Hart Scientific Super Thermometer II providing a measure chain with a global accuracy within ±0.01 °C. In order to calibrate the RTDs, a copper cylinder with a diameter of 60 mm and a height of 150 mm is employed. Several 100 mm deep holes have been manufactured on the top face of the cylinder to accommodate the temperature sensors. During calibration, all the RTD sensors and the copper cylinder are arranged inside a laboratory oven where the temperature set point can be varied (Figure 40). A correction function for each RTD is defined by comparing the temperatures measured by each RTD against the reference temperatures within the calibration range.

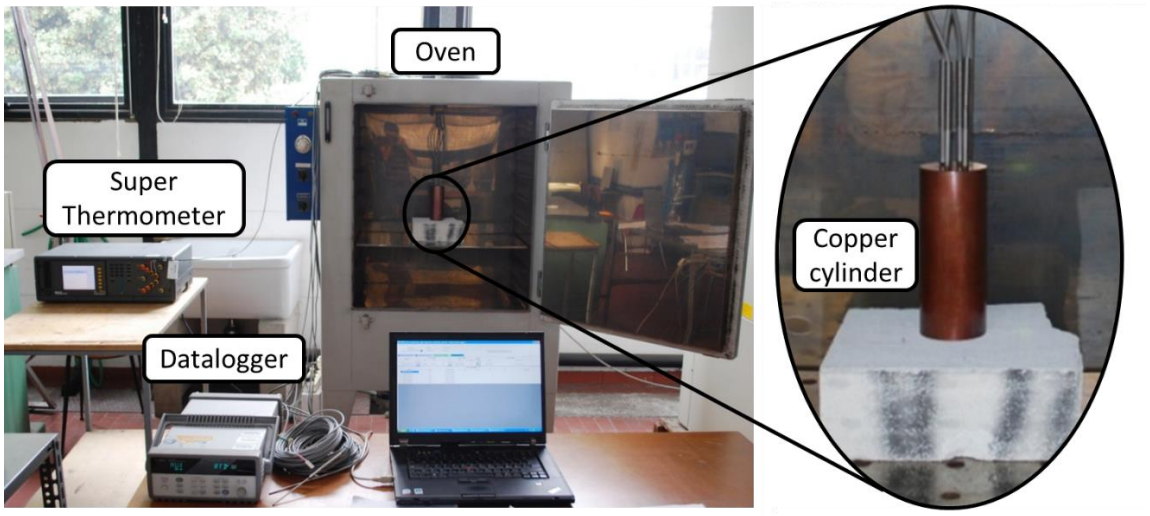

Figure 40 – Experimental apparatus for the calibration of the RTD sensors

With respect to the parameters which are not directly measured, their combined standard uncertainty can be calculated by applying the law of error propagation. For a given parameter, the expanded experimental uncertainty is obtained by multiplying the relevant standard uncertainty by a coverage factor equal to 2, which corresponds to a level of confidence of 95%. Finally, the uncertainties of the coefficients in the function of the efficiency curve result from the use of the weighted least square method, which is described in detail in the standard EN ISO 9806:2013. This method can be extended to the data collected during direct steam generation, considering the relevant parameters defined in Paragraph 3.3.2. Type A uncertainty is the standard deviation of the mean and, in the present tests, it comes out considering 200 readings collected over the averaging time period of 10 min.

3.3.4 Results of the experimental investigation on a bar-and-plate receiver for direct vaporization of water

The experimental campaign aimed to evaluate the performance of the concentrating solar collector composed of the bar-and-plate flat receiver and the asymmetrical parabolic trough concentrator in liquid heating and direct vaporization of water has been conducted from October 2014 to June 2015. Six test sequences with the parabolic trough working as a water heating solar collector have been carried out and 91 data points have been collected on clear-sky days. The direct normal irradiance was between 500 W m^{-2} and 860 W m^{-2}, the ambient air temperature between 8 °C and 33 °C, the mass flow rate of the distilled water in the primary loop was set equal to 0.02 kg s^{-1} per square meter of the aperture area, which corresponds to a total mass flow rate of 250 kg h^{-1}. The temperature of the water at the inlet of the receiver has been set at 37 °C, 48 °C, 50 °C, 81 °C, 109 °C and 117 °C to obtain experimental data in the reduced temperature difference range between 0.025 K m^{-2} W^{-1} and 0.140 K m^{-2} W^{-1}.

The experimental investigation performing steam generation consists of four test sequences, during which 26 experimental points have been collected at the saturation temperature of 120 °C, 123 °C, 131 °C and 138 °C. The maximum operating temperature of the working fluid inside the primary loop during present tests never exceeds the 140°C. Considering the collected data, averaged every 10 min, the deviation between the measured temperature and the saturation temperature calculated from the pressure at the outlet of the receiver is within ±0.05 °C, that is within the experimental uncertainty of the two employed instruments. During the steam generation tests, the subcooling at the inlet of the receiver was between 6 °C and 9 °C and the mass flow rate between 11 kg h^{-1} and 12.5 kg h^{-1} with a thermodynamic vapor quality at the outlet of the receiver between 0.15 and 0.3. These values are due to the small length of the tested receiver and to the minimum mass flow rate that can be pumped in the primary loop. Higher vapor qualities can be achieved in a longer receiver. The direct normal irradiance was between 650 W m^{-2} and 860 W $m^{-2}$and the ambient air temperature between 15 °C and 23 °C. In these two-phase tests, the range of the reduced temperature difference, calculated as reported in section 3.2, varies from 0.130 K m^{-2} W^{-1} to 0.160 K m^{-2} W^{-1}.

All the collected experimental points are plotted with the corresponding error bands in Figure 41 along with two efficiency curves expressed in the mathematical form of Eq. 3.4. The expanded experimental uncertainty on the thermal efficiency ranges between ±1.9% and ±3.1% while the maximum expanded experimental uncertainty on the reduced temperature difference is of ±0.005 K m^{-2} W^{-1}. The green dotted line represents the efficiency curve defined using only the experimental data collected in liquid heating mode, according to the guideline of the quasi-dynamic test method. In the same Figure, the black dashed line is the efficiency curve obtained considering all the data, i.e. the test runs both in liquid heating working mode and in direct steam generation

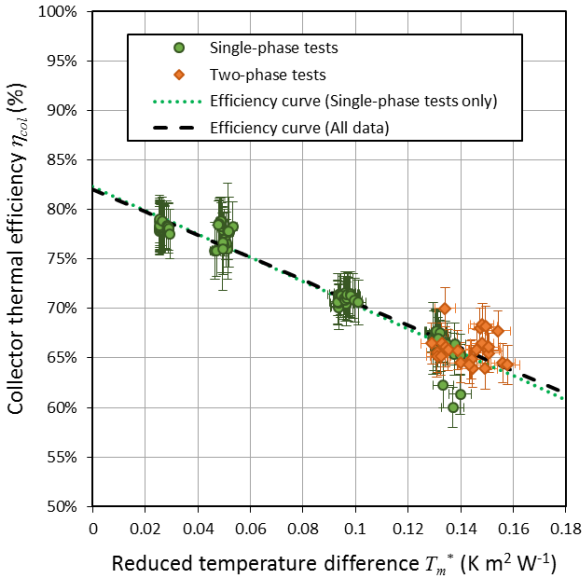

Figure 41 – Experimental thermal efficiency of the collector with a flat bar-and-plate receiver collected during single- (green dots) and two-phase (orange diamonds) test runs with water. The efficiency curves refer to the single-phase tests (green dotted line) and all tests (black dashed line).

From Figure 41, one can observe that there is a very good agreement between the two efficiency curves and that the experimental data measured during liquid heating and during steam generation overlap at reduced temperature differences between 0.130 K m^{-2} W^{-1} and 0.140 K m^{-2} W^{-1}. This means that the present new procedure proposed for data reduction during two-phase test runs gives results consistent with those derived from the standardized procedure. Therefore, it can be adopted to characterize the thermal performance of a solar concentrating

collector. In particular, controlling the inlet subcooling degree, one can reach an equivalent mean temperature of the fluid inside the receiver as close as possible to the maximum operating temperature for a given saturation pressure.

The coefficients of the collector efficiency curve calculated according to the weighted least square method are reported in Table 2, with the relevant expanded standard uncertainties (level of confidence 95%). From Table 2, it can be seen that both efficiency curves are straight lines: in fact, from the data reduction, the T-ratio of the coefficient c_2 is always smaller than 3, so c_2 has no statistical significance. Hence, the parameter identification has been repeated without c_2 included in the model.

Table 5 – Parameters of the parabolic trough collector's efficiency curve calculated according to the guidelines of the quasi-dynamic test method illustrated in the standard EN ISO 9806:2013 [110].

	Only liquid heating tests		Complete database (liquid heating + direct steam generation tests)	
Parameter	Value	Expanded uncertainty	Value	Expanded uncertainty
η_0	0.8230	0.0055	0.8203	0.0051
c_1	-1.1951	0.0649	-1.1455	0.0501

Since the efficiency curve derived from the whole database displays a lower uncertainty of the collector thermal efficiency η_{col}, the following discussion refers to that curve. The experimental optical efficiency η_0 comes out to be equal to 82%. This value is partly due to the high reflectance of the back-silvered glass facets forming the primary optics, but it also indicates that the coupling of the parabolic trough mirror with a flat geometry absorber may be an interesting option for medium-temperature applications. The thermal efficiency of the present parabolic trough collector at 0.16 K m^{-2} W^{-1} is equal to 64%, which constitutes a remarkable result as compared to some medium-temperature concentrating collectors available on the market and this value can still be increased. In fact, in the tested prototype, the receiver consists only of a flat absorber provided with a black coating, so it is not optimized for the minimization of the thermal losses. Higher efficiency may be achieved by arranging this absorber as a part of a cavity receiver provided with a front clear borosilicate glass. Furthermore, on the front

surface of the absorber, a selective coating with a lower emittance in the infrared region might be employed.

Figure 42 reports the effects of the outlet vapor quality (Figure 42 – a) and of the inlet subcooling (Figure 42 – b) on the thermal efficiency of the collector η_{col} during the steam generation tests. Considering that the extended uncertainty of the collector efficiency is ±2%, it can be concluded that the outlet vapor quality and the inlet subcooling had negligible effects on the collector efficiency.

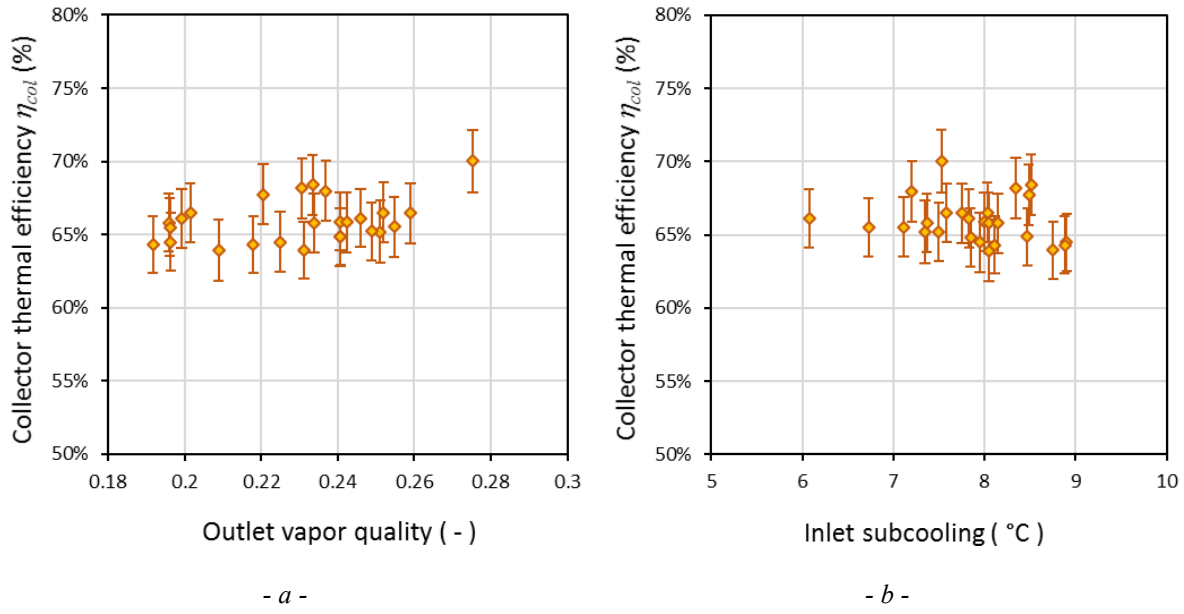

Figure 42 – Experimental thermal efficiency of the solar collector with a flat bar-and-plate receiver collected during the steam generation tests as a function of the outlet vapor quality (a) and the inlet subcooling of water (b).

As can be seen in Figure 43, during direct steam generation, the difference between the wall temperatures measured by the flat RTDs at the back surface of the absorber and the saturation temperature is always lower than 1 °C. This proves that the vaporization process can be performed at mass flow rates down to 11 kg h^{-1} without originating any hotspot or instability due to dry out of the liquid film at the wall. The hydraulic performance of the proposed receiver can be assessed by considering the difference between the measured pressures at the inlet and at the outlet of the receiver. Figure 44 reports the pressure drop through the bar-and-plate flat receiver as a function of the mass flow rate during the direct steam generation test runs. During

direct steam generation test runs pressure drop across the receiver is around 0.02 bar, that is within the experimental uncertainty of the pressure transducers, while during the test in liquid heating mode, it is in the range 0.10 – 0.13 bar with a mass flow rate between 245 kg h^{-1} and 250 kg h^{-1}.

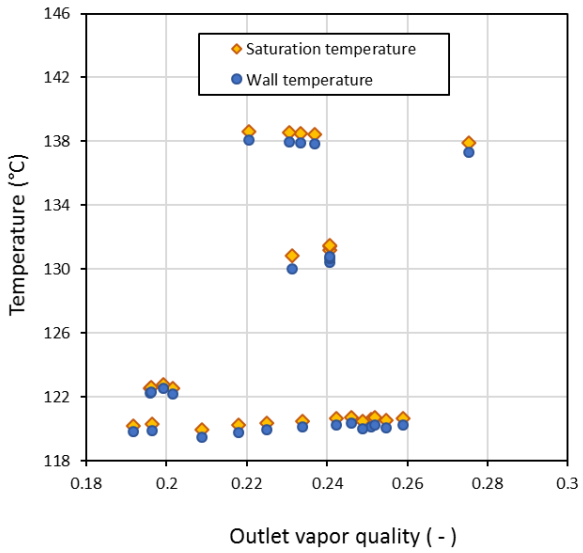

Figure 43 – Wall temperature (orange diamonds), based on measurements at the back surface of the receiver, and saturated temperature (blue dots) as a function of the outlet vapor quality during the two-phase test runs.

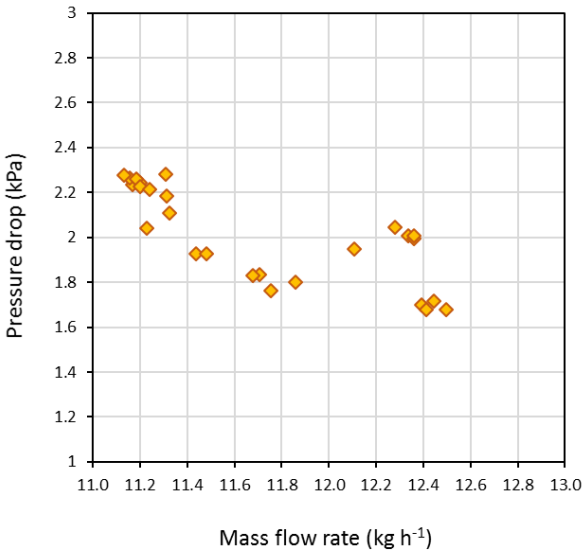

Figure 44 – Pressure drop through the receiver as a function of the mass flow rate during the vaporization of R1233zd(E) at a saturation temperature of around 85°C (blue diamonds) and 100°C (red square).

From the previous Figure, it can be concluded that the bar-and-plate absorber is particularly suitable for direct steam generation since the presence of the turbulator for heat transfer enhancement leads to low additional pressure drop. On the other hand, the geometry of the turbulator should be optimized for the application in single-phase flow regime.

Finally, the time constant of the collector has been calculated following the procedure reported in the standard EN ISO 9806:2013 [110]. At first, the concentrator is manually defocused so that no concentrated radiation reaches the receiver and the fluid inlet temperature is set close to the ambient air temperature. During this test, the electrical heaters of the preheating were switched off and the circulating mass flow rate was set equal to 250 kg h^{-1}, which is the same value used during liquid heating tests. The direct normal irradiance was around 830 W m^{-2}. Once reached a steady-state condition, the tracking system of the collector is switched on to focus the solar beams on the absorber within few seconds. Readings continue until the steady state conditions are reached again, which means that the outlet temperature of the fluid varies less than 0.5 °C per minute. In Figure 45, the difference between outlet fluid temperature and ambient air temperature is plotted against the elapsed time with the receiver on focus.

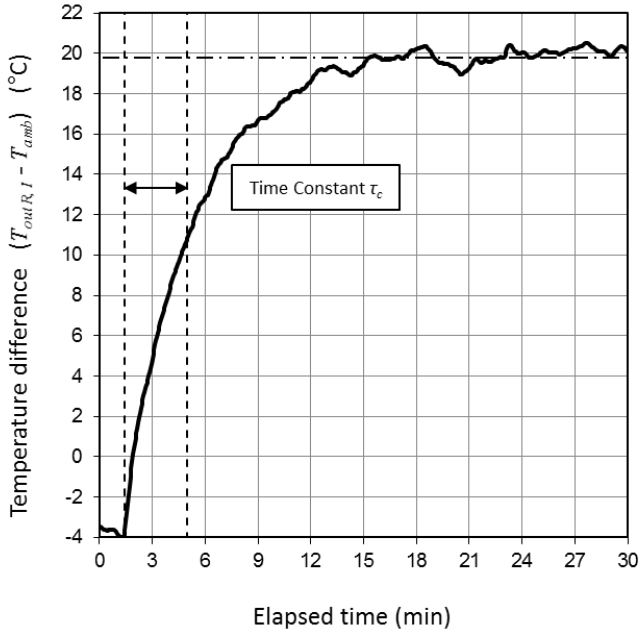

Figure 45 – Temperature difference between outlet fluid and ambient air against elapsed time during the time constant test run according to the standard EN ISO 9806:2013 (EN ISO 9806).

The collector time constant can be calculated as the elapsed time between the focusing of the concentrator on the absorber and the time when the difference between the outlet fluid temperature and the ambient air temperature rises to 63.2% of the total temperature increase from the starting to the final value. The time constant of the present asymmetrical parabolic trough solar collector results equal to 213 s, thus, the collector stabilizes quickly. The preconditioning period of 20 min adopted during test runs is long enough to ensure that the initial conditions of the system and it does not affect the experimental results.

3.3.5 Results of the experimental investigation on a bar-and-plate receiver for direct vaporization of R1233zd(E)

The experimental study on the direct vaporization of a halogenated fluid with a low Global Warming Potential (GWP) in the bar-and-plate flat receiver using concentrated solar flux has been carried out during the month of August 2016.

The selected fluid is R1233zd(E) and it represents a possible low-GWP substitute to R245fa as a working fluid for many applications, such as Organic Rankine Cycle (ORC). As reported in Table 6, the thermophysical properties of the R1233zd(E) are very close to those of the R245fa.

Table 6 – Thermophysical properties of the fluid R245fa and R1233zd(E) [115].

Thermophysical property	R 245fa	R 1233zd(E)
Normal boiling temperature	15.1 °C	18.3 °C
Critical temperature	154 °C	165.6 °C
Critical pressure	3.65 MPa	3.57 MPa
Latent heat at 25°C	190.32 kJ kg^{-1}	191.76 kJ kg^{-1}
Specific heat at 25°C and 0,1 MPa	1.32 kJ kg K^{-1}	1.24 kJ kg K^{-1}
Ozone Depletetion Potential (ODP)	0	0.0003
Atmospheric lifetime	~ 8 year	26 days
Global Warming Potential (GWP)	858	1

Two test sequences have been carried out at two different level of saturation pressure collecting 74 experimental points. During the tests, the ambient temperature was in the range 28 – 35°C

and the values of the direct normal irradiance were between 700 W m^{-2} and 920 W m^{-2}. Table 7 resumes the fluid conditions occurred during the experimental campaign.

Table 7 – Experimental conditions during the two test runs with the halogenated fluid R1233zd(E).

Saturation pressure	7.5 ± 0.16 bar	10.5 ± 0.10 bar
Saturation temperature	84 - 87 °C	100 - 101 °C
Inlet subcooling	10.6 - 14.3 °C	21.2 - 24.3 °C
Outlet vapor quality	0.37 - 0.99	0.35 - 0.89
Mass flow rate	46 -106 kg h^{-1}	40 - 94 kg h^{-1}
Equivalent mean temperature of the fluid in the receiver (Eq. 3.9)	82.55 - 86.4 °C	95.7 - 98.6 °C
Pressure drop	5 - 10.5 kPa	3 - 6.5 kPa

In the first test sequence, the saturation pressure varies between 7.24 bar and 7.77 bar, corresponding to a saturation temperature around 85°C. By varying the inlet subcooling between 10.6°C and 14.3 °C and the mass flow rate in the primary between 46 kg h^{-1} and 106 kg h^{-1} it was possible to obtain an outlet vapor quality that ranges from 0.37 to 0.99. During the second test sequences, the saturation pressure was between 10.42 bar and 10.65 bar with a saturation temperature around 100°C. The subcooling at the inlet of the receiver was between 21.3 °C and 24.3 °C, while the mass flow rate of the halogenated fluid assumes values between 40 kg h^{-1} and 94 kg h^{-1}. During this test run, the vapor quality at the outlet of the receiver was between 0.35 and 0.89.

During the two test sequences, the onset of the dry out was observed for an outlet vapor quality around 0.75. This value has been evaluated based on the trends of the surface temperatures at the back of the absorber, measured with five copper-constantan thermocouples attached at 20 mm, 50 mm, 90 mm, 140 mm and 200 mm from the outlet of the receiver (Figure 46). The onset of the dry out phenomena corresponds to the sharp increase of the difference between the saturation temperature and the wall temperature. In fact, during the dry out, the internal surfaces of the channel are in direct contact with the vapor phase without any liquid film. This situation leads to a drop in the internal heat transfer coefficient and thus to a sharp increase in the

temperature of the surface. In the test runs at 7.5 bar, close to the outlet, the temperature of the back plate of the receiver remained under 87°C for outlet vapor quality lower than 0.75, then it rapidly increased up to 93°C for outlet vapor quality of 0.99 (Figure 46 – a). With reference to the Figure 46 – b, at 10.5 bar saturation pressure, the closest thermocouple to the end of the receiver (at 20 mm from the fluid outlet) measured a temperature lower than 103°C when the outlet vapor quality was lower than 0.72°C. For the maximal value of the outlet vapor quality 0.89, this temperature raised to a value close to 106°C.

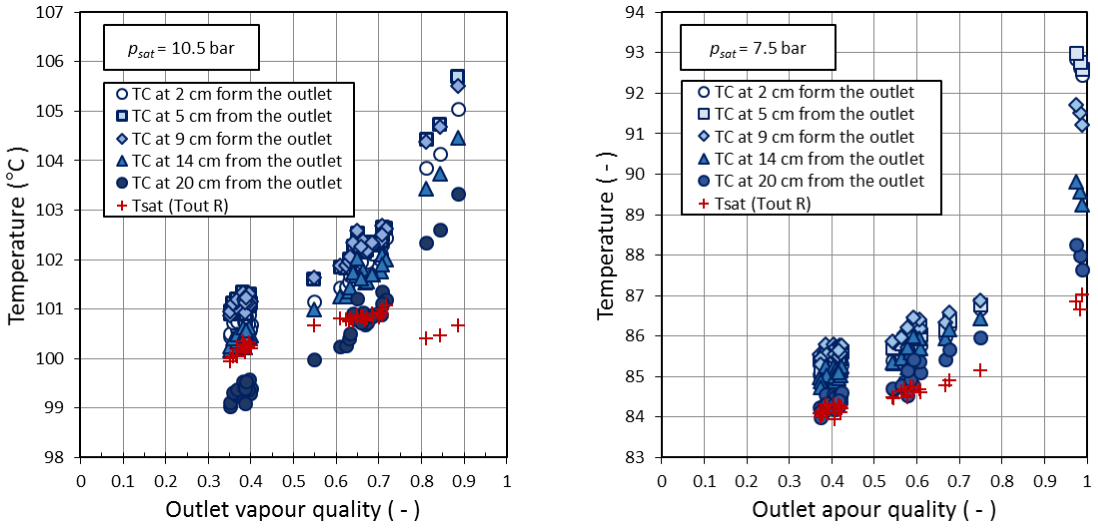

- a - *- b -*

Figure 46 – Surface temperatures at the back of the absorber, measured at 20 mm, 50 mm, 90 mm, 140 mm and 200 mm from the outlet of the receiver (blue symbols) and saturation temperature (red crosses) as a function of the outlet vapor quality during the vaporization of R1233zd(E). The plots refer to the test runs at 7.5 bar (a) and 10.5 bar (b) saturation pressure.

The experimental values of the collector thermal efficiency η_{col} calculated according to Eq. 3.7, are plotted with their corresponding error bands against the reduced temperature difference T_m^* in Figure 47. The results show that the average collector efficiency η_{col} at a saturation temperature around 85°C was around 73%, while it decreased to 70% when the saturation temperature was around 100°C. In the same Figure, it is plotted the efficiency curves derived from the experimental points collected during the present tests (continue black lined) and during the single- and two-phase tests with water in the same concentrating collector (dashed

black line). It can be observed that there is a good agreement between the two sets of data and the error between the efficiency curves derived from the test runs and the experimental data in vaporization of R1233zd(E) is lower than the experimental uncertainty. The difference that exists between the two curves may lie in the different test conditions and fluid properties. As known, water presents excellent thermophysical properties allowing its adoption for heat transfer applications with high performance. Moreover, due to the lower latent heat of vaporization of the R1233zd(E), higher outlet vapor quality, close to the unity, has been reached in the present test as compared to the tests with water at lower inlet subcooling and mass flow rates. The resulting average values of the receiver efficiency were 77% and 74% at 7.5 bar and 10 bar saturation pressure, respectively.

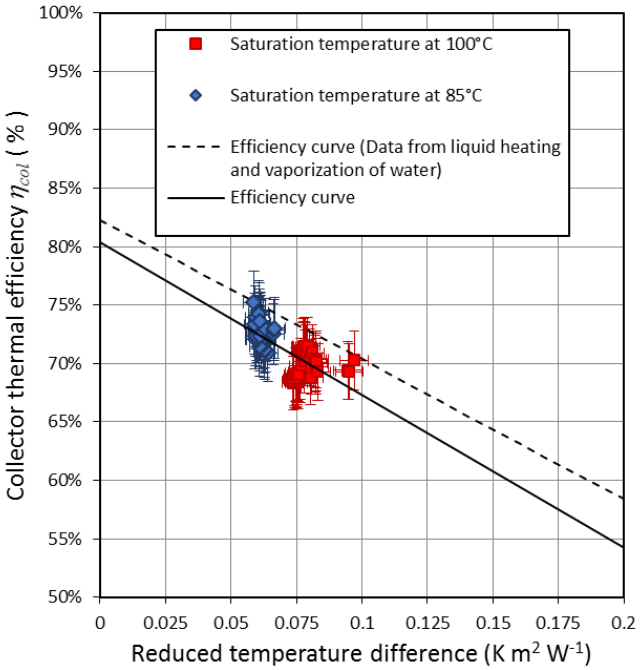

Figure 47 – Experimental thermal efficiency data of collector with a flat bar-and-plate receiver collected during the direct vaporization of R1233zd(E) at 85°C (blue diamonds) and 100°C (red squares) saturation temperature. The efficiency curves derive from the data collected during the present tests with R1233zd(E) (black continue line) and the single- and two-phase test runs with water (black dashed line).

Figure 48 reports the effects of the outlet vapor quality on the collector efficiency during the vaporization of the halogenated fluid at the two pressure levels. Considering that the extended uncertainty of the collector efficiency is ±3%, it can be concluded that the outlet vapor quality

had a negligible effect on the collector efficiency. Furthermore, the efficiency of the collector did not present any significant decrease when the dry out phenomena take over. This remarkable result suggests that it is possible to vaporize almost completely the halogenated fluid in the bar-and-plate receiver without any losses of efficiency.

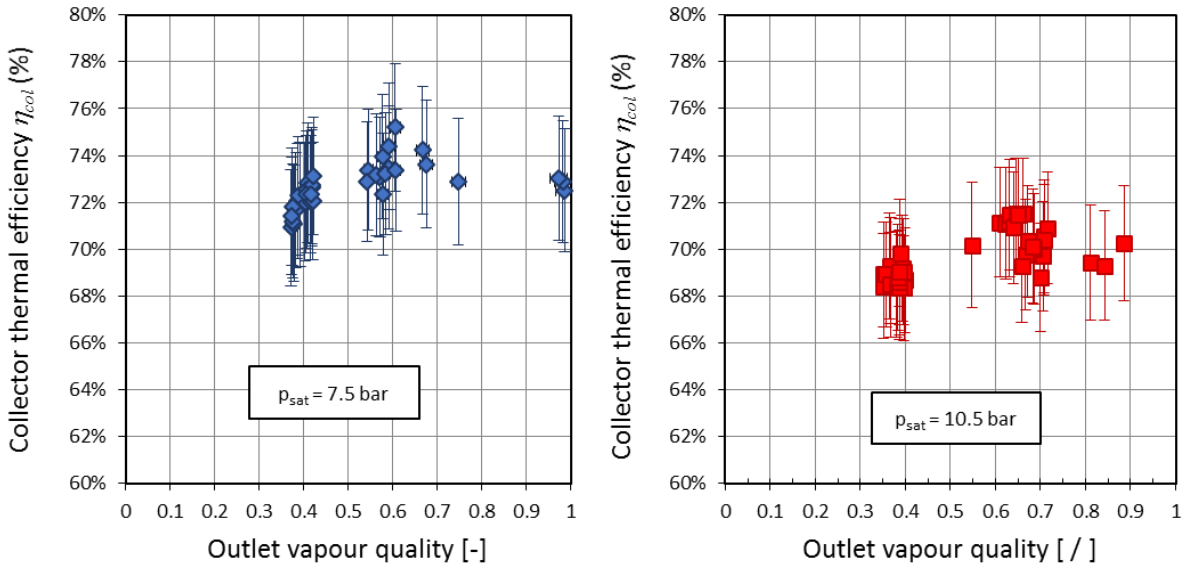

Figure 48 – Experimental thermal efficiency of the solar collector with a flat bar-and-plate receiver collected during the direct vaporization of R1233zd(E) as a function of the outlet vapor quality of the fluid. The plots refer to the test runs at 7.5 bar (a) and 10.5 bar (b) saturation pressure.

In the graphs of Figure 49, where the thermal efficiency of the collector is plotted against the inlet subcooling, it can be noted that also the inlet subcooling did not significantly affect the efficiency of the solar collector.

Finally, Figure 50 reports the pressure drop through the bar-and-plate flat receiver as a function of the mass flow rate during the vaporization test. It is worth to mention, that this Figure provides only a general trend of the pressure because the plotted values are lower than the experimental uncertainty of the pressure transducers. Anyway, the result confirms that the designed absorber is capable of vaporizing the fluid R1233zd(E) with a limited pressure drop, as happened during the vaporization of water, implying a low electrical consumption for the circulating pump.

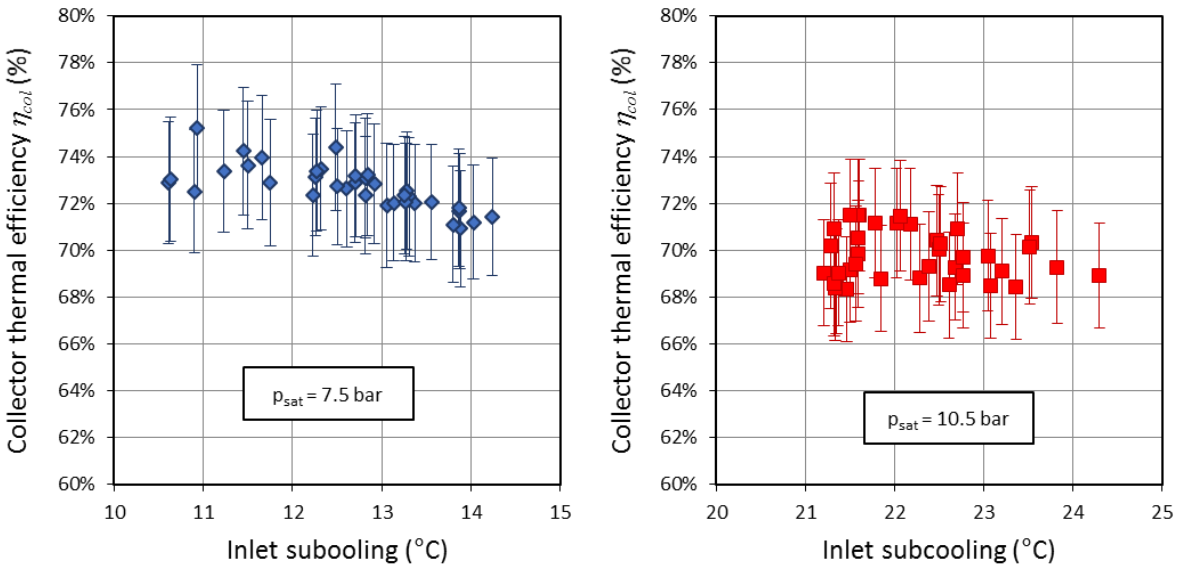

- a - *- b -*

Figure 49 – Experimental thermal efficiency of the solar collector with a flat bar-and-plate receiver collected during the direct vaporization of R1233zd(E) as a function of the inlet subcooling of the fluid. The plots refer to the test runs at 7.5 bar (a) and 10.5 bar (b) saturation pressure.

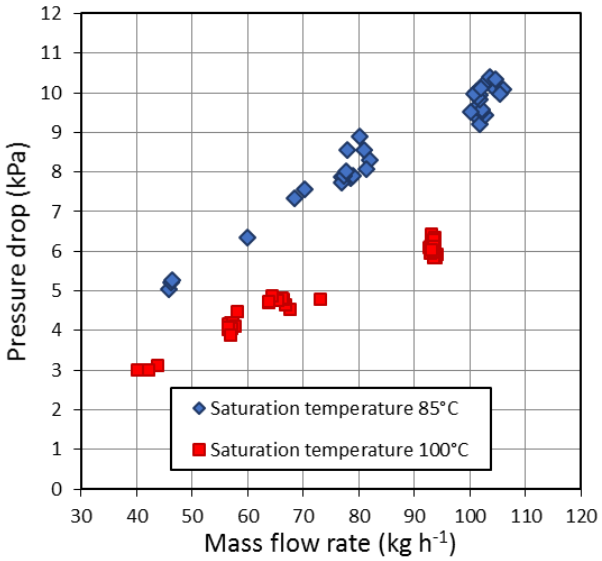

Figure 50 – Pressure drop through the receiver as a function of the mass flow rate during the vaporization of R1233zd(E) at a saturation temperature of around 85°C (blue diamonds) and 100°C (red square).

3.4 Modelling of single-phase heating and direct vaporization of fluids in a bar-and-plate receiver.

A new numerical model has been developed to predict the thermal performance of the bar-and-plate flat receiver in single-phase heating and in vaporization of a heat transfer fluid. The receiver has been discretized along its length in several segments. Each segment constitutes the control volume where a zero-dimensional steady-state energy balance is applied. The energy balance includes the concentrated solar radiation incident on the receiver, the thermal losses from the receiver to the surround and the heat gain into the HTF.

A preliminary simulation on the heat conduction in the absorber material has been conducted in order to evaluate the heat flux and temperature distribution inside the absorber. The simulations have been performed by means of the steady-state finite element solver Mirage [116]. This software is capable to solve steady-state heat conduction problems on two-dimensional planar domains. The main limitation to the solving capability of this software is the possibility to implement only one boundary condition for each surface. This limitation may cause some problem in the development of the receiver model, where the external surfaces are typically interested by convective and radiative heat transfer to the surround. This limitation has been bypassed considering equivalent convective heat transfer coefficients which take into account both convective and radiative heat transfer. Furthermore, the concentrated heat flux on the front plate of the absorber has been modelled by considering a heat generation in a fictive infinitesimal substrate adjacent to the front surface. This substrate has been divided into several parts along the width of the receiver and each of them accounts for the equivalent heat generation term according to the average flux distribution of the concentrated solar radiation determined in Chapter 2. The HTF considered in this preliminary simulation was water flowing at a mass flow rate of 250 kg h^{-1}. The correlations used to estimate the values of the heat transfer coefficients are presented in detail in the follows. The simulations have been conducted considering a direct normal irradiance equal to 980 W m^{-2}, an ambient air temperature of 25 °C and for values of the average temperature of the water inside the channel equal to 35 °C, 50 °C, 80 °C, 110 °C and 120 °C. Figure 51 reports the distributions of the temperature and the heat flux in the absorber material and in the insulation layer located at the bottom of the

absorber for the latter case, which presents the most intense thermal stresses. The following discussion of the numerical results refers to this case, but it can be easily extended to the other simulated cases.

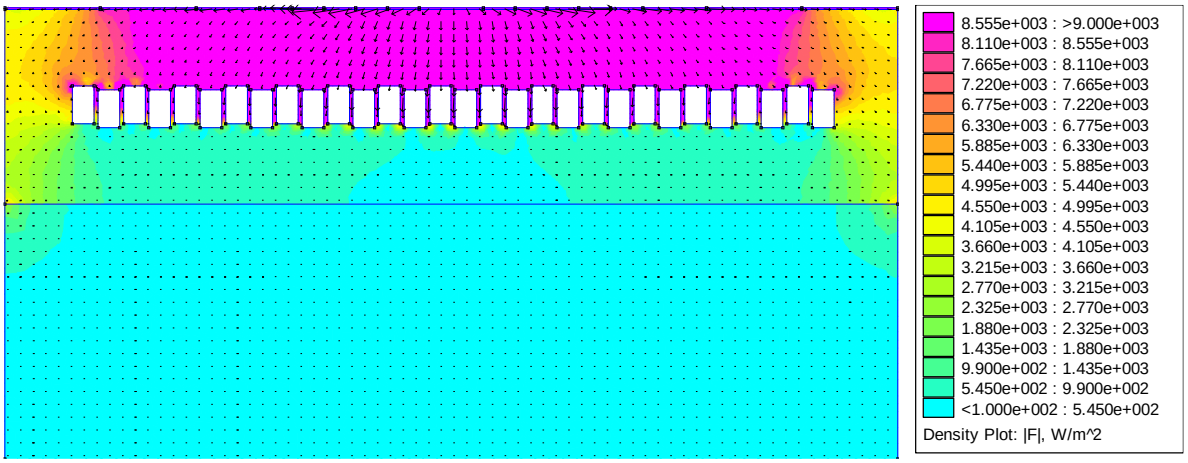

- a -

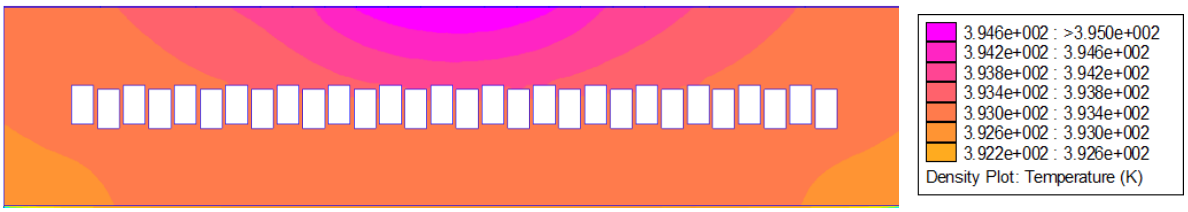

- b -

Figure 51 – Heat flux vectors and distribution (a) and temperature distribution (b) in the cross-section of the receiver obtained in the preliminary numerical simulation on heat conduction in the absorber and insulation material. For the sake of clarity, the temperature distribution plot (b) is limited to the absorber material.

As can be seen in Figure 51 – a, the heat flux through the absorber material is particularly intense in the central region adjacent to the front plate of the receiver in accord to the distribution of the concentrated solar radiation. The major part of the heat flow rate directs to the inner part of the absorber where it is diffused by the turbulator and gained by the HTF by convection. The rest of the heat flow rate is mainly dissipated through the front and lateral surfaces of the absorber in the ambient by convective and radiative mechanisms. The residual heat flux passes the insulating layer on the back plate of the receiver before being dissipated to the ambient. This heat flow rate is strongly reduced by the presence of the insulating layer. In

Figure 51 – b, it can be noted that the temperature of the absorber material is almost constant, with a thermal gradient lower than 4°C. In particular, the temperature on the inner surface of the absorber, which is contact with the HTF, results practically constant. The considered bar-and-plat flat absorber presents a thick aluminium plate on the front face reached by the concentrated solar flux, that acts as a heat spreader. Thanks to the high thermal conductivity of the aluminium, the plate entails the reduction of the transversal temperature gradient despite the imposed non-uniform concentrated flux. Hence, the thermal conduction resistance in the absorber material results is quite low compared to the thermal resistance at the external surface and that of the insulating layer. The previous considerations have been widely adopted as modelling assumptions in many numerical studies available in the literature and it has been confirmed by the results obtained for tubular absorbers of different materials arranged in large PTCs. *Forristall* [117] proved that a model of a tubular receiver in a parabolic trough solar collector developed with an analogous scheme to the one adopted in this study is suitable to predict the thermal performance of the receiver. Furthermore, the presence of the aluminium turbulator in the present receiver facilitates the heat transfer between the absorbing front plate and the back plate of the receiver. That entails a further reduction in the temperature gradient in the absorber.

Based on the previous observations, the numerical model of the bar-and-plate flat receiver developed in this study is based on the thermal resistance network depicted in Figure 52 where the external surfaces (front, back and lateral) of the absorber, the external surface of the insulation layer on the back of the receiver, the internal surface of the absorber in contact with the HTF and HTF itself constitute the thermal nodes of the model. In the model, the aluminium support bar in contact with the insulating layer has been considered to evaluate the radiative thermal properties of the back surface.

In the model, the effective incident concentrated solar radiation, net to the losses in the optical concentration, is mainly absorbed by the surface coating of the absorber (q_{abs}). Some energy absorbed into the coating is conducted through the absorber and transferred to the HTF $q_{EAS-HTF}$ by convection or by vaporization, while the rest is conducted through the insulating layer to the back surface $q_{EAS-EIS}$. The remaining energy is lost directly to the environment by convection and radiation ($q_{EAS-amb}$, $q_{EIS-amb}$, $q_{EAS-sky}$, $q_{EIS-sky}$). The model assumes that all

temperatures, heat flow rates and thermodynamic properties are uniform around the perimeter of the receiver. With the help of Figure 52, the energy balance equations are determined by conserving energy at each surface of the receiver cross-section:

$$q_{abs} = q_{EAS-amb} + q_{EAS-sky} + q_{EAS-IS} + q_{EAS-EBS} \quad \textit{Eq. 3.10}$$

$$q_{IAS-HTF} = q_{EAS-IS} - q_{IS-EIS} \quad \textit{Eq. 3.11}$$

$$q_{EAS-EIS} + q_{IAS-EIS} = q_{EBS-amb} + q_{EIS-sky} \quad \textit{Eq. 3.12}$$

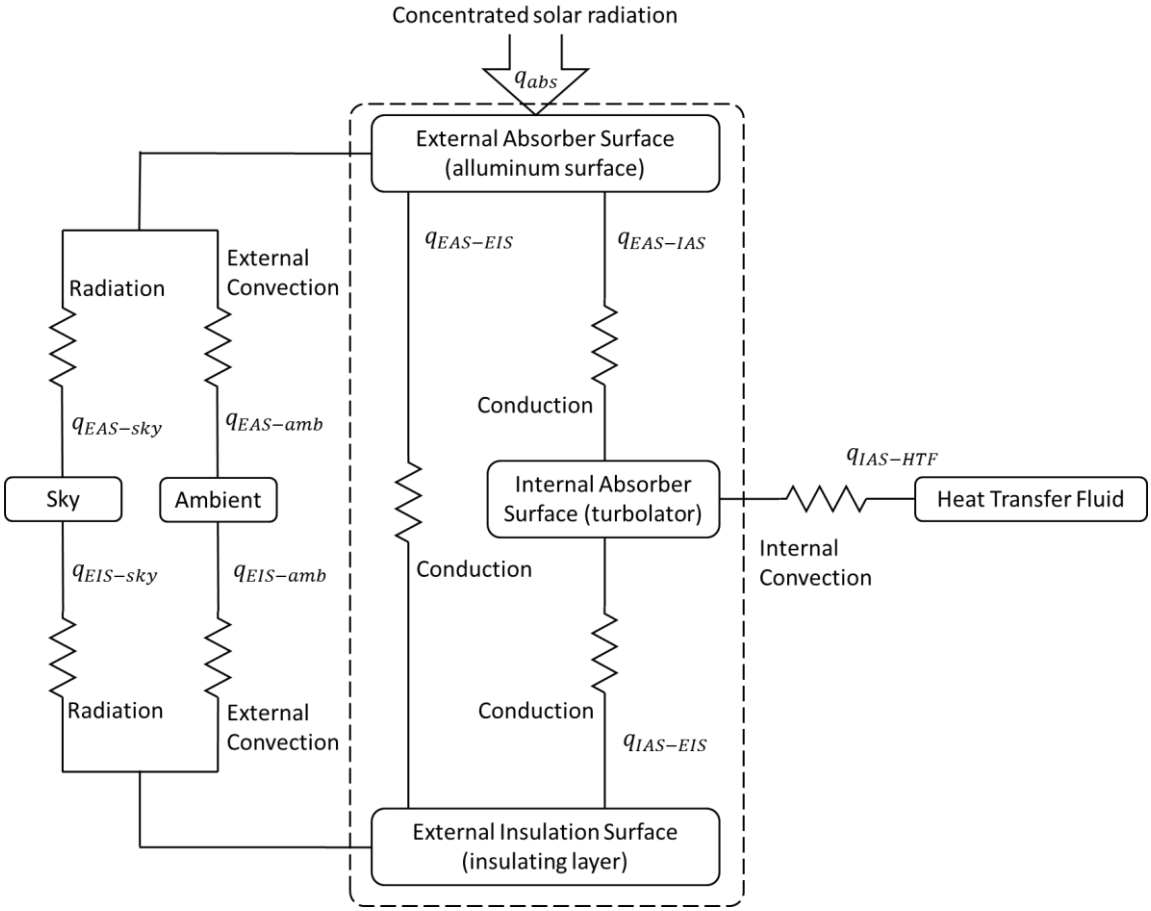

Figure 52 – Thermal resistance network representing the dimensionless model of the bar-and-plate flat receiver.

It must be mentioned that the solar absorption is simplified by treating the solar absorptance as a heat flow rate term terms instead of a volumetric phenomenon occurring in the volume of the absorber material [117]. However, most of the absorption in the absorber occurs very close to the surface (about 6 angstroms) [118]. Therefore, any error in treating solar absorption as a surface phenomenon should be relatively small. Furthermore, this assumption makes the heat conduction through the absorber material linear. In the model, the absorbed heat flow rate has been considered as reported in Eq. 3.13:

$$q_{abs} = DNI\ A_a \alpha_{r,coat}(\rho_c \gamma_r) \qquad \textit{Eq. 3.13}$$

where $\alpha_{r,coat}$ is the solar absorbance of the surface coating on the receiver, ρ_c is the reflectance of the mirrors and γ_r is the intercept factor associated with the width of the considered receiver.

The convective losses from the outer surface of the absorber have been modelled considering alternatively the natural convection with the external air and a forced convection mechanism in which the wind speed plays the main role. In both, natural and forced convection the external convective heat transfer coefficient $h_{ext,conv}$ has been evaluated according to the following expression

$$h_{ext,conv} = Nu_{ext} \frac{k_{air}}{d_{h,ext}} \qquad \textit{Eq. 3.14}$$

here the equivalent external hydraulic diameter $d_{h,ext}$ is calculated considering the external perimeter $P_{cross,ext}$ of the receiver cross-section:

$$d_{h,ext} = \frac{P_{cross,ext}}{\pi} \qquad \textit{Eq. 3.15}$$

When the natural convection is involved, due to the thermal buoyancy effect, the convective heat transfer coefficient $h_{ext,conv}$ strongly depends on the position of the dissipating element. Typically, due to the action of the two-axes solar tracking, the position of the considered receiver varies continuously when the collector is working. In the model, it has been considered an average position of the receiver assumed when the zenith angle is 45°. In this position, the front and back plates result in a vertical position, while the lateral walls are horizontal. The correlations adopted to calculate the natural convective heat transfer coefficient $h_{ext,conv}$ on each

external surface are taken from the book of *Rohsenow et al*. [119]. For the sake of brevity, these correlations are not reported here.

When the forced convection mechanism is considered, it has been assumed that the wind streams orthogonally the receiving surface with a speed of v_{wind}. The external Nusselt number Nu_{ext} is calculated according to the correlation of *Sparrow et al.* [120] reported in Eq. 3.16:

$$Nu_{ext} = 0.149\, Re_{ext}^{0.69} \qquad \textit{Eq. 3.16}$$

which is considered valid for a Reynolds number Re_{ext} between 2000 and 6300, calculated by considering an appropriate equivalent hydraulic diameter $d_{h,ext}$ according to the following formulations:

$$Re_{ext} = \frac{\rho_{air}\, d_{h,ext}\, v_{wind}}{\mu_{air}} \qquad \text{with} \qquad d_{h,ext} = \frac{P_{cross,ext}}{\pi} \qquad \textit{Eq. 3.17}$$

The external perimeter $P_{cross,ext}$ of the receiver cross-section in Eq. 3.17 is computed by including the insulating layer at the back of the receiver because the original correlation of *Sparrow et al.* [120] refers to a square cross-sectional parallelepiped in an air flow normal to its length, as shown in Figure 53. Considering also the presence of the thermal insulating layer, the dimensions of the sides of the transverse cross-section of the examined receiver are 70 mm and 40 mm; therefore, it is considered that the square cross-section approximation is acceptable.

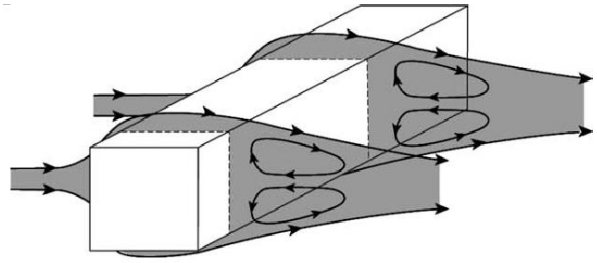

Figure 53 – Configuration of the airflow blowing on a square cross-sectional parallelepiped according to the formulation of Sparrow et al.[120].

The external surface of the receiver has been divided into two different portions to take into account the different convective dissipations from the absorber surface A_{EAS} at a temperature

T_{EAS} and the outer surface of the insulating layer A_{IS} at a significantly lower temperature T_{EAS}. The resulting convective heat flow to the ambient air at the temperature T_{amb} from the absorber surface and from the insulating layer can be calculated respectively by the following two equations:

$$q_{EAS-amb} = h_{conv,ext}\, A_{EAS}(T_{EAS} - T_{amb}) \qquad \textit{Eq. 3.18}$$

$$q_{EIS-amb} = h_{conv,ext}\, A_{EIS}(T_{EIS} - T_{amb}) \qquad \textit{Eq. 3.19}$$

The radiative heat losses to the environment depend on the difference between the temperature of the external surface of the receiver (T_{EAS} and T_{EIS}.) and the apparent temperature of the sky T_{sky}. By adopting the same simplification used in the model of Forristall [117], the apparent temperature of the sky T_{sky} is assumed 8 °C below the ambient air temperature. For computing the heat flow rates associated with this radiative dissipation, it is assumed that the receiver is a small grey body placed in a large cavity (sky) that behaves as a black body. Under this assumption, the thermal emittance coefficient of the receiver surface ε_r coincides with its absorbance α_r. As with the calculation of the convective losses, the external surface of the receiver has been divided into two different portions and the radiative heat flow rates have been calculated separately.

$$q_{EAS-sky} = \sigma_{bb}\, \varepsilon_{r,EAS}\, A_{EAS}\left(T_{EAS}^4 - T_{sky}^4\right) \qquad \textit{Eq. 3.20}$$

$$q_{EIS-sky} = \sigma_{bb}\, \varepsilon_{r,EIS}\, A_{EIS}\left(T_{EIS}^4 - T_{sky}^4\right) \qquad \textit{Eq. 3.21}$$

The thermal emittance of the external surface of the absorber $\varepsilon_{r,EAS}$ coincides with the emittance (at 100 ° C) of the absorbing coating and is equal to 0.45, while the emittance of the outer surface of the insulating layer $\varepsilon_{r,EIS}$ is estimated to be equal to that of the untreated aluminium of the support bar equal to 0.89.

The heat transfer from the external to the internal (turbulator) surface of the absorber can be treated as heat conduction in a rectangular cross-section hollow body with the inner and outer surfaces at constant temperatures. For this configuration, as reported in the book of *Rohsenow et al.* [119], it is possible to calculate the conductive heat flow rate by introducing a shape factor SF_r that characterizes the shape of the cross-section of the geometry.

$$q_{EAS-IAS} = k_{abs}\, SF_r\, (T_{EAS} - T_{IAS})\, l_r \qquad \textit{Eq. 3.22}$$

where k_{abs} is the thermal conductivity of the absorber material (aluminium) and l_r is the length of the considered segment of the receiver. The shape factor of the receiver SF_r is defined per receiver length unit ($l_{r,tot}$ = 1.2 m) in accordance with Eq. 3.23 and refers to a cross-section of a uniform thickness $t_{eq,abs}$ and internal perimeter $P_{cross,int}$. In the model, the uniform thickness $t_{eq,abs}$ has been considered equal to 8 mm, while the inner dimensions of the rectangular cross-section were 58 mm and 3 mm.

$$\frac{SF_r}{l_r} = \frac{2\,\pi}{log\left(1 + \frac{2\,\pi\, t_{eq,abs}}{P_{cross,int}}\right)} \qquad \textit{Eq. 3.23}$$

The dispersion heat flow rate conducted from the absorber surface through the insulating layer $q_{AES\text{-}EIS}$, can be calculated by applying the Fourier's law to the insulating layer itself. The calculation can be simplified under the assumption that the heat propagates mainly along the thickness of the insulating layer t_{ins}:

$$q_{EAS-EIS} = \frac{\lambda_{ins}}{t_{ins}} A_{EAS-EIS}(T_{EAS} - T_{EIS}) \qquad \textit{Eq. 3.24}$$

In Eq. 3.24 the symbol k_{ins} represents the conductivity of the insulating layer.

Finally, to calculate the useful heat flow rate gained by the heat transfer fluid flowing through the turbulator in the absorber, two heat transfer mechanisms have been considered. In fact, convective liquid heating occurs when the HTF is subcooled or saturated liquid and the wall temperature of the inner surface is lower than the saturation temperature, while a two-phase heat transfer occurs when the temperature of the internal surface in contact with the HTF is above its saturation temperature. To calculate the convective heat transfer coefficient when the liquid HTF is heated, the procedure proposed by *Manglik and Bergles* [108] was adopted. In their correlation for the heat transfer coefficient, the number of Nusselt Nu_{int} is expressed as a function of the internal Reynolds (Re_{int}) and Prandtl (Pr_{int}) numbers and the Colburn *j* number which depends on three dimensionless parameters (α_t, γ_t and δ_t) that define the geometry of an offset-strip turbulator.

$$Nu_{int} = j\left(Re_{int}\, Pr_{in}^{1/3}\right) \qquad \textit{Eq. 3.25}$$

The three dimensionless parameters that characterize the geometrical size of the turbulator are defined as follows:

$$\alpha_t = \frac{s_t}{h_t} \qquad \gamma_t = \frac{t_t}{s_t} \qquad \delta_t = \frac{t_t}{l_t} \qquad \textit{Eq. 3.26}$$

where the s_t, h_t, l_t and t_t are the width, the height the length and the thickness of a single strip in the turbulator, as reported in Figure 54.

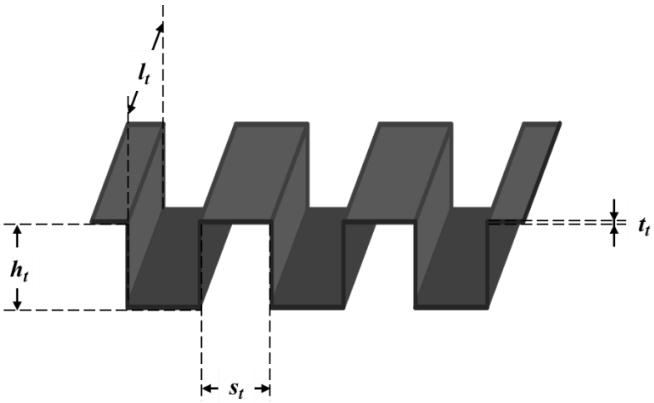

Figure 54 – Geometrical parameters of a single strip in an offset-strip turbulator according to Manglik and Bergles [108].

The geometrical parameters of the offset-strip turbulator inside the consider bar-and-plate flat absorber are reported in Table 8.

Table 8 – Geometrical parameters of a single strip in the considered offset-strip turbulator.

Width of the strip	2.4 mm
Height of the strip	3 mm
Length of the strip	18 mm
Thickness of the strip	0.3 mm

Once the geometry of the turbulator is known and the internal Reynolds (Re_{int}) and Prandtl (Pr_{int}) numbers are calculated at the mean temperature of the HTF in the heat receiver, it is possible to calculate the Colburn *j* number by the correlation of *Manglik and Bergles* [108]:

$$j = 0.6522\, Re_{int}^{-0.5403} \alpha_t^{-0.1541}\, \delta_t^{0.1499} \gamma_t^{-0.0678} \cdot \\ \cdot (1 + 5.269 \cdot 10^{-5}\, Re_{int}^{1.340} \alpha_t^{0.504}\, \delta_t^{0.456} \gamma_t^{-1.055})^{0.1} \qquad \textit{Eq. 3.27}$$

This correlation was developed over a moderate range of Prandtl numbers, that is, for fluids with *Pr* ranging from 0.5 to 15, and it was expected to be valid for all gases and most liquids with moderate *Pr* values [108]. The convective heat transfer coefficient $h_{IAS\text{-}HTF,s\text{-}p}$ between the internal surface of the absorber and the HTF in single-phase heating is given by

$$h_{IAS-HTF,s-p} = Nu_{int} \frac{\lambda_L}{d_{h,eq,int}} \qquad \textit{Eq. 3.28}$$

The internal equivalent hydraulic diameter $d_{h,eq,int}$ is given by Eq. 3.29:

$$d_{h,eq,int} = 4 \frac{A_f}{A_{IAS-HTF}} l_{turb} \qquad \textit{Eq. 3.29}$$

where heat transfer area $A_{IAS\text{-}HTF}$ to which the heat transfer coefficient is related is calculated by Eq. 3.30 and l_{turb} is the effective length of the turbulator in the considered segment of the receiver (total length of the turbulator = 1864 mm).

$$A_{IAS-HTF} = \left(\frac{w_{int}}{s_t + t_t}\right) \frac{l_t}{l_{turb}} (2\,(s_t\, l_t + h_t\, l_t + h_t\, t_t) + \, t_t s_t) \qquad \textit{Eq. 3.30}$$

Considering that the turbulator occupies the whole internal width of the absorber w_{int}, equal to 58 mm, the flow area of the heat transfer fluid can be obtained by calculating the number of channels $N_{channels}$ as reported in Eq. 3.31:

$$A_f = N_{channels}\, s_t\, h_t = \left(\frac{w_{int}}{s_t + t_t}\right) s_t\, h_t \qquad \textit{Eq. 3.31}$$

In the two-phase heat transfer, the HTF enters the receiver in subcooled liquid conditions, part of the incident solar radiation is firstly spent to heat it up the liquid to its saturation temperature (sensible heat) and then the saturated liquid is vaporized (latent heat). However, this separation is only useful to understand the two heat transfer mechanisms involved, because sensible and latent heat transfer occur simultaneously along the receiver and it is hard to observe them

separately. In the considered receiver, given the high conductivity of the aluminium, which the absorber is made, it is reasonable to assume that the internal surface temperature is fairly constant. This means that when the wall temperature is higher than the saturation temperature of the fluid, it is very likely that vaporization of the HTF can occur already in the presence of subcooled liquid. From this premise, it is possible to apply a formulation proposed by *Liu and Winterton* [121] to calculate the heat transfer coefficient between the inner wall and the vaporizing fluid at an average vapor quality which has been considered the average vapor quality between inlet and outlet conditions. In the formulation of *Liu and Winterton* [121] the heat transfer coefficient $h_{IAS\text{-}HTF,t\text{-}p}$ takes account of the joined effect of convection and pool boiling, calculated with the correlations developed by *Cooper* [122] (Eq. 3.33) and *Dittus-Boelter* [123] (Eq. 3.34), respectively.

$$h_{IAS-HTF,t-p} = \left(\left(e_s \, h_{pb} \, S \right)^2 + \left(e_f \, h_{conv} \, F \right)^2 \right)^{0.5} \qquad \textit{Eq. 3.32}$$

$$h_{pb} = 55 \left(\frac{p_{sat}}{p_{crit}} \right)^{0.12} \left(-\log_{10} \left(\frac{p_{sat}}{p_{crit}} \right) \right)^{-0.55} M^{-0.5} \left(\frac{q_{abs}}{A_r} \right)^{\frac{2}{3}} \qquad \textit{Eq. 3.33}$$

$$h_{conv} = 0.023 \frac{\lambda_{HTF,L}}{d_{h,eq,int}} {Re_{HTF,L}}^{0.8} Pr_{HTF,L}^{0.4} \qquad \textit{Eq. 3.34}$$

$$F = \left(1 + x_m \; Pr_{\mathrm{HTF,L}} \left(\frac{\rho_{HTF,L}}{\rho_{HTF,G}} - 1 \right) \right)^{0.35} \qquad \textit{Eq. 3.35}$$

$$S = \left(1 + 0.055 \, F^{0.1} \, {Re_{HTF,L}}^{0.16} \right)^{-1} \qquad \textit{Eq. 3.36}$$

where

$$Re_{HTF,L} = \frac{\dot{m}_I \, d_{h,eq,int}}{A_{FLOW} \, \mu_{HTF,L}} \qquad \textit{Eq. 3.37}$$

and the factors e_f and e_s are evaluated as a function of the Froude number *Fr*:

$$e_s = \begin{cases} (\mathrm{Fr})^{0.5} & for \quad Fr < 0.05 \\ 1 & for \quad Fr \geq 0.05 \end{cases} \qquad \textit{Eq. 3.38}$$

$$e_f = \begin{cases} (\mathrm{Fr})^{0.1-2\mathrm{Fr}} & for \quad Fr < 0.05 \\ 1 & for \quad Fr \geq 0.05 \end{cases} \qquad \textit{Eq. 3.39}$$

Finally, the heat flow rate $q_{IAS\text{-}HTF}$ exchanged between the inner wall and the heat transfer fluid is obtained by, where the heat transfer coefficient depends on the heat transfer mechanisms involved:

$$q_{IAS-HTF} = \begin{cases} h_{IAS-THF,1-p}\ A_{IAS-HTF}\ (T_{IAS} - T_{HTF}) \\ h_{IAS-THF,2-p}\ A_{IAS-HTF}\ (T_{IAS} - T_{HTF,sat}) \end{cases} \quad \textit{Eq. 3.40}$$

For the cases, where sensible and latent heats are transferred to the vaporizing fluid the vapor quality at the outlet of the receiver is calculated with this expression:

$$x_{out,R} = \frac{q_{IAS-HTF} - \dot{m}_I c_L (T_{HTF,sat} - T_{in,r})}{\dot{m}_I\ h_{LV}} \quad \textit{Eq. 3.41}$$

The pressure drop $\Delta p_{s\text{-}p}$ through the receiver in single-phase regime has been calculated according to the work of *Manglik and Bergles* [108], where it is provided a correlation for the average Fanning friction factor f in the offset-strip array:

$$f = 9.6243\ Re_{int}^{-0.7422} \alpha_t^{-0.1856}\ \delta_t^{0.3053} \gamma_t^{-0.2659} \cdot \\ \cdot (1 + 7.669 \cdot 10^{-8}\ Re_{int}^{4.429} \alpha_t^{0.920}\ \delta_t^{3.767} \gamma_t^{0.236})^{0.1} \quad \textit{Eq. 3.42}$$

and the pressure drop $\Delta p_{s\text{-}p}$ is given by

$$\Delta p_{s-p} = \frac{2\ f\ l_r}{d_{h,eq,int}} \rho_{HTF} \quad \textit{Eq. 3.43}$$

In two-phase regime, the pressure drop $\Delta p_{t\text{-}p}$ through the receiver have been calculated with the formulation proposed by *Friedel* [124]. The pressure drop results function of the specific flow rate of the HTF G_{HTF}, of the average value of the vapor quality in the considered segment of the receiver x_m, of the saturation pressure of the HTF, of the equivalent hydraulic diameter of the turbulator and of the thermophysical properties of the two separated phases.

$$\Delta p_{t-p} = 2 \frac{\phi_{LO}\ f_{LO}\ G_{HTF}^2}{d_{h,eq,int}\ \rho_{HTF,L}} l_r \quad \textit{Eq. 3.44}$$

$$\phi_{LO} = E_{Friedel} + \frac{3.24\ F_{Friedel}\ H_{Friedel}}{Fr^{0.045}\ We^{0.035}} \quad \textit{Eq. 3.45}$$

$$E_{Friedel} = (1 - x_m)^2 + x_m^2 \frac{\rho_{HTF,L}\ f_{LO}}{\rho_{HTF,G}\ f_{GO}} \quad \textit{Eq. 3.46}$$

$$We = \frac{G_{HTF}^2 \, d_{h,eq,int}}{\rho_{HTF,m} \, H_{Friedel}} \qquad \textit{Eq. 3.47}$$

$$Fr = \frac{G_{HTF}^2}{g \, d_{h,eq,int} \, \rho_{HTF,m}^2} \qquad \textit{Eq. 3.48}$$

$$\rho_{HTF,m} = \frac{\rho_{HTF,L} \ \rho_{HTF,G}}{x_m \, \rho_{HTF,L} + (1 - x_m)\rho_{HTF,G}} \qquad \textit{Eq. 3.49}$$

$$H_{Friedel} = \left(\frac{\rho_{HTF,L}}{\rho_{HTF,G}}\right)^{0.91} \left(\frac{\mu_{HTF,G}}{\mu_{HTF,L}}\right)^{0.19} \left(1 - \frac{\mu_{HTF,G}}{\mu_{HTF,L}}\right)^{0.7} \qquad \textit{Eq. 3.50}$$

$$F_{Friedel} = x_m^{0.78}(1 - x_m)^{0.224} \qquad \textit{Eq. 3.51}$$

The Fanning friction factors associated to the single liquid phase f_{LO} and to the single vapor phase f_{GO} are defined based on the flow regime, evaluated by the values of the Reynolds number in each phase:

$$f_{LO} = \begin{cases} \dfrac{16 \, \mu_{HTF,L}}{G_{HTF} \, d_{h,eq,int}} & for \quad Re_{LO} \leq 2000 \\ 0.079 \ \dfrac{G_{HTF} \, d_{h,eq,int}}{{\mu_{HTF,L}}^{-0.25}} & for \quad Re_{LO} > 2000 \end{cases} \qquad \textit{Eq. 3.52}$$

$$f_{GO} = \begin{cases} \dfrac{16 \, \mu_{HTF,G}}{G_{HTF} \, d_{h,eq,int}} & for \quad Re_{LO} \leq 2000 \\ 0.079 \ \dfrac{G_{HTF} \, d_{h,eq,int}}{{\mu_{HTF,G}}^{-0.25}} & for \quad Re_{LO} > 2000 \end{cases} \qquad \textit{Eq. 3.53}$$

3.4.1 Numerical model validation

The numerical model of the described in the previous Paragraph is implemented in Matlab® in a block diagram Simulink® environment. The model includes the parameters used to describe the concentrator's optical performance (i.e. the nominal reflectance of the mirrors, optical properties of the external surface of the receiver), the geometric properties of the receiver and of the internal turbulator. The inputs of the model are the value of direct normal irradiance, the inlet temperature and mass flow rate of the heat transfer fluid in the receiver, assuming that it is always in conditions of subcooled liquid, its saturation temperature and the temperature of the ambient air. When the external forced convection mechanism is considered in the model, it

is required to specify the wind speed. In the thermophysical properties of the fluids are calculated with NIST Refprop Version 9.0 [109]. The model estimates the temperatures at each of the considered thermal nodes in each receiver's segment as long as the convergence criteria based on the local and global thermal balances are not satisfied. Once a stationary converge is reached, the model provides the useful heat flow rate gained by the HTF, the average fluid temperature, the outlet temperature and vapor quality at each segment of the receiver, and finally, the thermal efficiency of the solar thermal collector

The developed model has been validated by comparing the numerical results and the experimental data collected during the test of the concentrating solar collector in liquid heating and direct vaporization of water and R1233zd(E), presented in the Paragraph 3.3.4 and 3.3.5, respectively.

The first simulations have been performed according to the test conditions during the six experimental sequences with the parabolic trough collector working as a water heating. According to experimental data, the direct normal irradiance ranged between 500 W m^{-2} and 860 W m^{-2}, the mass flow rate of the was equal to 250 kg h^{-1}, the ambient air temperature varied between 8°C and 33 °C while the temperature of the distilled water at the inlet of the receiver has been set at 37 °C, 48 °C, 50 °C, 81 °C, 109 °C and 117 °C. In order to evaluate the influence of the thermal losses due to convection on the external surface of the receiver, the wind speed in the model was varied from 0 m s^{-1}, corresponding to a condition where only natural convection takes place, up to 3 m s^{-1}.

As shown in the graph of Figure 55, where the collector thermal efficiency has been plotted against the reduced temperature difference, for a constant value of the reduced temperature difference, the thermal losses increase with the wind speed, leading a decrease in the collector efficiency. Furthermore, it can be noted that the results of the model are highly influenced by the value of the wind speed. The simulations present a very good agreement with the experimental data of the single test sequences for a wind speed lower than 2 m s^{-1}. The mean relative error made in the predictions of the thermal collector efficiency reaches its minimum (1.5%) for a value of the wind speed equal to 0.9 m s^{-1} (not showed in Figure 55).

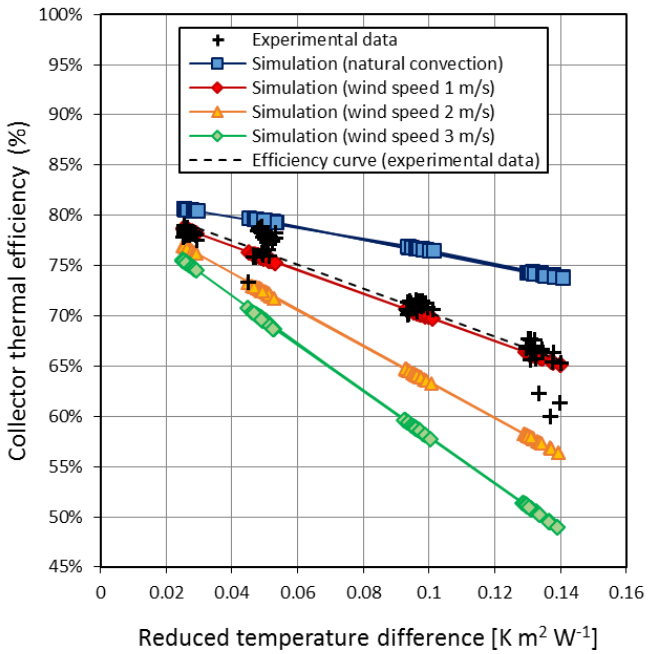

Figure 55 – Simulation results and experimental data for the collector thermal efficiency as a function of the reduced temperature difference. The simulations have been performed for different value of the wind speed.

Once the receiver model has been validated during the single-phase heating of water, the next step is its validation when two-phase heat transfer occurs. To carried out this validation, the dataset collected during the vaporization of the halogenated fluid R1233zd(E) was preferred over that collected during the vaporization of water because of the higher values of the outlet vapor quality. Thus, the numerical predictions of the model have been compared against experimental data collected during the two test sequences of direct vaporization of the fluid R1233zd(E) at the saturation temperature of 85 °C and 100 °C, respectively. The collected data of the collector efficiency have been plotted as a function of the outlet vapor quality with the values estimated by the numerical model. Figure 56 shows that the estimated thermal performance of the collector is in good agreement with that determined through the experimental tests. The predictions of the thermal efficiency at the saturation temperature of 85°C are quite accurate with a relative error lower than 2%. For the test at the saturation temperature of 100°C, the model tends to slightly underestimate the thermal efficiency obtained when the outlet vapor quality is greater than 0.8. In fact, the mean relative error in the prediction of the thermal efficiency was around 1%, 2.5% and 5% for outlet vapor quality lower

than 0.5, 0.8 and 0.9 respectively. For these last points, the numerical prediction exceeds the experimental uncertainty bar. In this regard, it must be mentioned, that the heat transfer coefficient of vaporization defined by *Liu and Winterton* [121] depends on the considered vapor quality, the specific flow rate of the vaporizing fluid and the heat flow rate of the incident thermal radiation. The experimental points for higher values of the vapor quality were obtained with lower mass flow rates of R1233zd(E) at the end of the test runs when the normal direct irradiance resulted lower than that collected during the test performed in the central hours of the day and that present low outlet vapor quality. As a consequence, the correlation of *Liu and Winterton* [121] loses accuracy and the prediction of the outlet vapor quality result slightly lower than its measured values, in particular for the data at a saturation temperature of 100°C. In these working conditions, however, the phenomenon of dry out has already been triggered and it is not recommended to use the developed model as it exits the validity range of the *Liu and Winterton* [121] correlation.

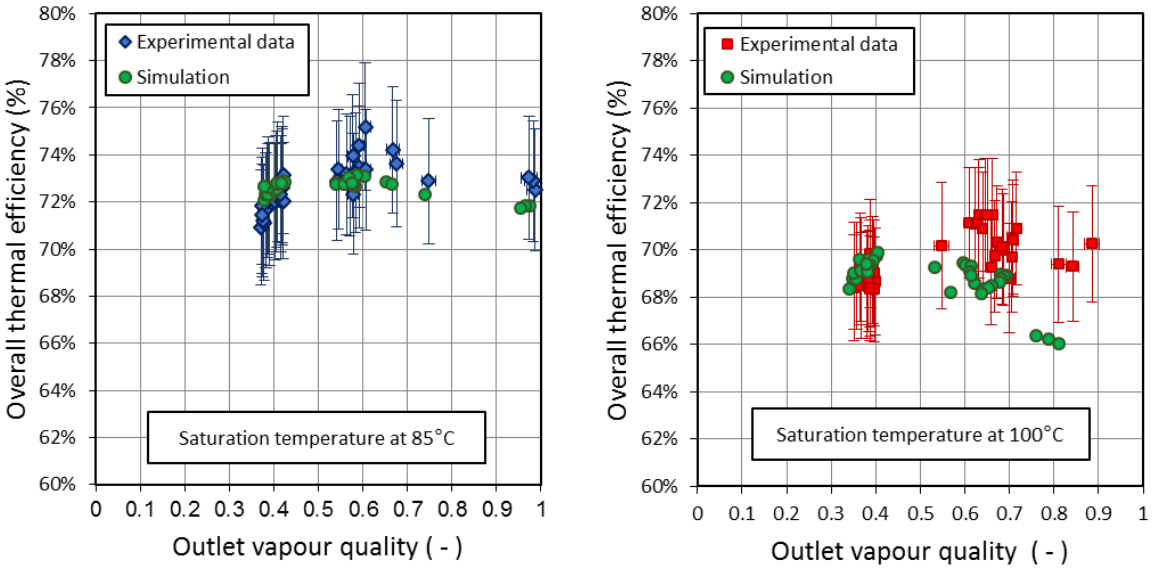

- a - *- b -*

Figure 56 – Simulation results and experimental data for the collector thermal efficiency as a function of the outlet vapor quality of the fluid R1233zd(E) at a saturation temperature of 85°C (a) and 100°C (b). In the simulations, the wind speed was set to 1 m s^{-1}.

The validated numeric model has been used to perform an estimation of the thermal performance of the collector including vaporization of the halogenated fluid R1233zd(E) up to

a saturation temperature of 130 °C. For these simulations, the values of the mass flow rate have been assumed according to the inlet subcooling, so that the outlet vapor quality resulted between 0.55 and 0.6. This was done to prevent the onset of dry out phenomenon and the use of the *Liu and Winterton* outside its validity range. The ambient temperature was considered equal to 30 °C. The result of these simulations is shown in Figure 57: from the numerical predictions, it results that it is possible to vaporise the halogenated fluid R1233zd(E) inside the modelled receiver at a saturation temperature of 130 °C with a thermal efficiency of the solar collector of more than 60%. For the sake of completeness, in Figure 57 the experimental data have also been plotted and the resulting efficiency curve. Even though the experimental efficiency curve (dotted line) plotted in Figure 57 is extended from its original range of definition, it results in very good accordance with the simulated efficiency curve (dashed line).

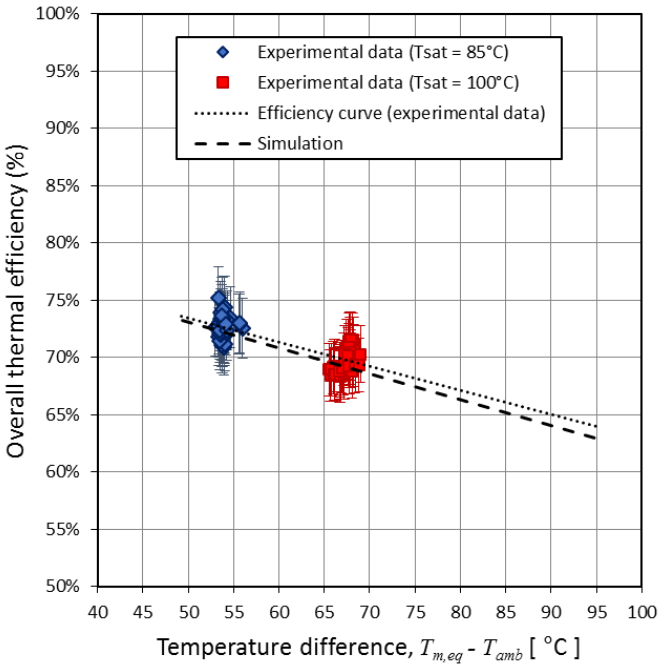

Figure 57 – Simulation results and experimental data for the collector thermal efficiency as a function of the temperature difference between the calculated mean condition of the fluid R1233zd(E) and the ambient. The outlet vapor quality ranges between 0.55 and 0.6 and the saturation temperature was up to 130°C. In the simulations, the wind speed was set to 1 m s^{-1}

3.4.2 Numerical comparison of the original and two modified receiver configurations during single-phase heating

Once the proposed model of the receiver has been validated, it has been adopted to predict the thermal performance of receivers which present small changing in the receiver configuration. The simulations performed on the modified configuration have been conducted only for single-phase heating of water. This choice was made in order to consider a heat transfer mechanism that has been largely studied in the past and for which correlations are considered largely reliable in the scientific literature.

In order to study the influence, the turbulator in the receiver on the thermal collector efficiency, the model has been modified in order to evaluate the heat transfer performance in the bar-and-plate receiver with the absence of the turbulator. In the new configuration, the receiver presents a simple hollow rectangular channel originated by the front and back plate and the side walls. In order to evaluate if the assumption of the constant temperature of the internal surface still holds, a heat conduction in the absorbing material simulation has been performed with the software Mirage. The simulation has been performed considering water as HTF flowing at a mass flow rate of 250 kg h^{-1}, a value of the direct normal irradiance equal to 980 W m^{-2}, an ambient air temperature of 25 °C and an average temperature of the water inside the channel equal 120 °C. The results of the simulations are reported in Figure 61.

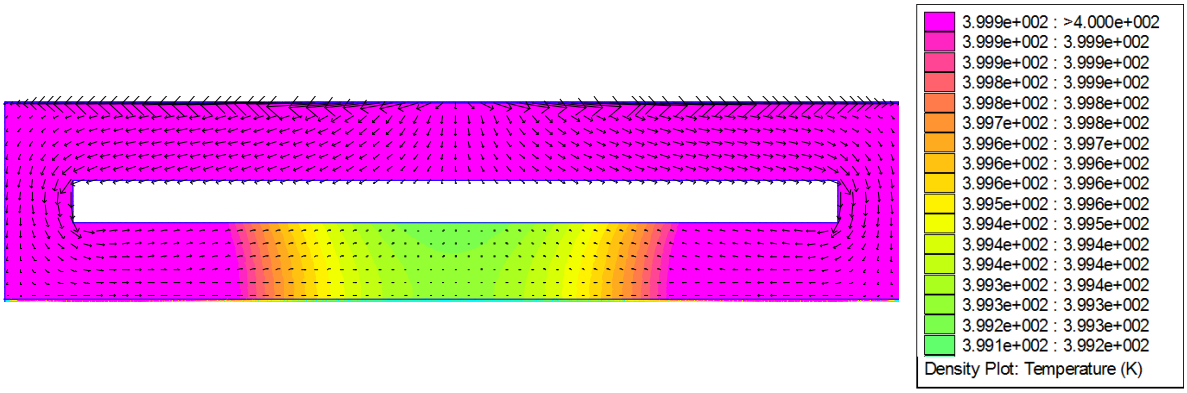

Figure 58 – Heat flux vectors and distribution and temperature distribution in the cross-section of the receiver without internal turbulator obtained numerical simulation on the heat conduction in the absorber.

As it was observed for the receiver with the internal turbulator, the heat flux through the absorber material is particularly intense in the central region adjacent to the front plate of the

receiver in accord to the distribution of the concentrated solar radiation. The major part of the heat flow rate directs to the inner part of the absorber where it is distributed around the channel walls where it is transferred to the HTF mainly from the upper and side wall of the channel (Figure 58). Furthermore, it can be noted that the temperature of the absorber material is almost constant, with a thermal gradient lower than 1°C. In particular, due to the high thermal conductivity of the aluminium the temperature on the channel surface, which is contact with the HTF, results practically constant as it happened when the turbulator was present. Thus, the assumption of a constant temperature of the internal channel can be considered valid also in the absence of the turbulator. Compared to the heat conduction simulation performed with the internal turbulator it can be noted, that the temperature of the absorbing material is higher leading to higher thermal losses in the environment.

To adapt the validated model of the receiver to the new configuration, some modifications are required. In particular, the calculation of the internal heat transfer coefficient can be no longer based on the correlations for off-strip turbulator, but it must be referred to a hollow channel with a rectangular cross-section. As suggested by *Incropera et al*. [125], the well-known correlation of *Gnielinski* [126] is a valid formulation to compute the internal heat transfer coefficient for this case:

$$h_{IAS-HTF,s-p} = \begin{cases} 4.44\dfrac{k_{HTF,L}}{d_{h,eq,int}} & for \quad Re_{int} \leq 2300 \\ \left(\dfrac{{}^{f}/_{8}\,(Re_{int}-1000)Pr_{HTF}}{1+12.7\sqrt{({}^{f}/_{8})}\left(Pr_{int}^{2/3}-1\right)}\right)\dfrac{k_{HTF,L}}{d_{h,eq,int}} & for \quad Re_{int} > 2300 \end{cases} \qquad \textit{Eq. 3.54}$$

where the Fanning friction factor f and the internal equivalent hydraulic diameter $d_{h,eq,int}$ are calculated as:

$$f = (0.79\,ln(Re_{int}) - 1.64)^{-2} \qquad \text{and} \qquad d_{h,eq,int} = \frac{P_{cross,int}}{\pi} \qquad \textit{Eq. 3.55}$$

The simulations have been performed according to the test conditions during the six experimental sequences with the parabolic trough collector working as a water heating. The wind speed in the model was set equal to 1 m s^{-1} in accordance with the result of the model validation.

Figure 59 reports the thermal efficiencies of the collector as a function of the reduced temperature difference resulting from the numerical simulations performed with the bar-and-plate receiver with and without turbulator. The values of the efficiency of the collector with a hollow receiver are lower than the obtained by the receiver with the inner turbulator. In fact, during liquid heating, the presence of the turbulator enhances the heat transfer area and promotes the onset of the turbulent regime. The resulting effect is a net increase in the collector efficiency around 5.5%. The same increase would be rather difficult to reach by operating on the collector optic and certainly, it would have a higher cost than the addiction of an off-strip turbulator in the assembling of the bar-and-plate receiver.

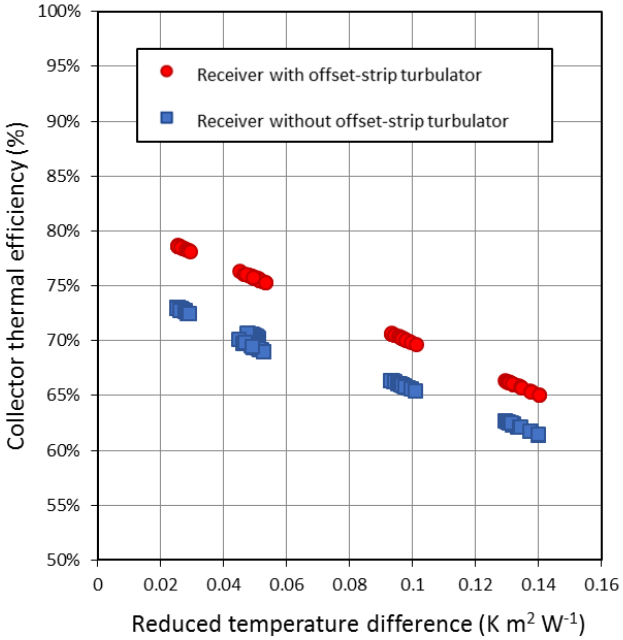

Figure 59 – Collector thermal efficiency as a function of the reduced temperature difference obtained from the simulations of the bar-and-plate flat receiver with (red dots) and without (blue squares) offset-strip turbulator. In the simulations, the wind speed was set to 1 m s^{-1}.

After having highlighted the key role of the turbulator in the increase of the thermal performance of the receiver, the developed model has been adopted to evaluate the effect of the addition of a glass cover on the front plate of the absorber as done in the receiver proposed for linear Fresnel collector. The glass cover has the function to reduce the convective heat losses from the absorber surface, which is the element at the highest temperature in the receiver.

In Figure 60, the cross-section geometry of the original bar-and-plate receiver, which model has been validated against the experimental data is compared to the new geometry of the optimized receiver.

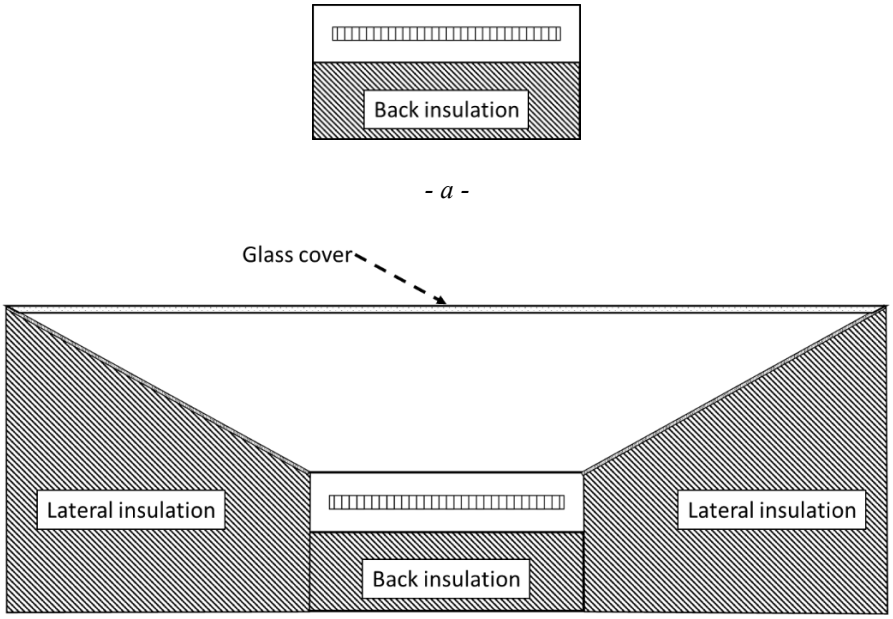

Figure 60 – Cross-sectional view of the bar-and-plate flat receiver in the original configuration modelled and tested during the experimental campaign (a) and of the modelled configuration after the addition of a glass cover and insulation layers (b).

In the new model, the presence of the glass requires the addition of a thermal node between the external absorber surface and the environment (ambient air and sky). The new model of the optimized receiver can be represented by the thermal resistance network depicted in Figure 61., The glass cover has been considered very thin so that its internal thermal resistance can be neglected compared to the other thermal resistances surrounding this element. With the help of Figure 61, the set of equations describing the energy balance of the receiver cross-section results:

$$q_{abs} = q_{EAS-glass} + q_{EAS-IS} + q_{EAS-EBS} \qquad \textit{Eq. 3.56}$$

$$q_{EAS-glass} = q_{glass-sky} + q_{glass-amb} \qquad \textit{Eq. 3.57}$$

$$q_{IAS-HTF} = q_{EAS-IS} - q_{IS-EIS} \qquad \textit{Eq. 3.58}$$

$$q_{EAS-EIS} + q_{IAS-EIS} = q_{EBS-amb} + q_{EIS-sky} \qquad \textit{Eq. 3.59}$$

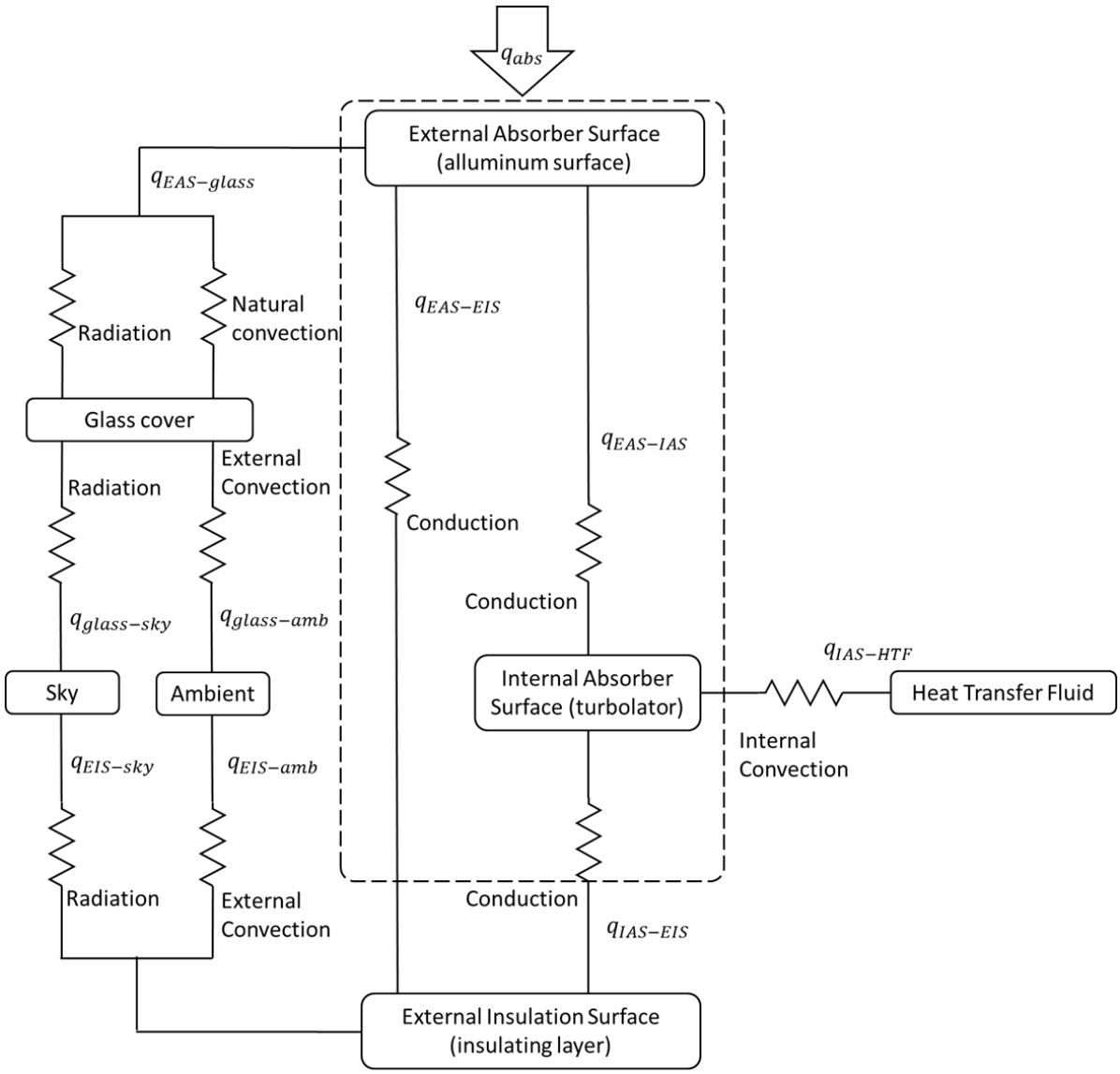

Figure 61 – Thermal resistance network representing the dimensionless model of the optimized configuration of the bar-and-plate flat receiver.

The heat losses $q_{EAS\text{-}surf}$ occurring between the absorber front plate and the glass cover are a result from the natural convective and radiative heat losses between the two surfaces. These

losses are modelled with the expression reported in Eq. 3.60, under the conservative assumption that the view factor F_{vf} between the two surfaces can be approximated to the 0.7.

$$q_{EAS-glas} = h_{conv,nat}\, A_{EAS}(T_{EAS} - T_{amb}) + \sigma_{bb}\, \varepsilon_{r,coating}\, A_{glass}\, F_{vf}\left(T_{EAS}^4 - T_{glass}^4\right) \qquad \textit{Eq. 3.60}$$

The convective heat transfer coefficient $h_{conv,nat}$ between the absorber front plate and the glass cover has been calculated with the correlation reported in the book of *Rohsenow et al.* [119] for parallel isothermal plates.

The convective heat flow $q_{glass\text{-}amb}$ from the glass surface to the ambient air at the temperature T_{amb} has been calculated according to the following expression:

$$q_{glass-amb} = h_{conv,ext}\, A_{glass}\left(T_{glass} - T_{amb}\right) \qquad \textit{Eq. 3.61}$$

where the external convective heat transfer coefficient can be computed according to Eq. 3.14. The radiative heat losses $q_{glass\text{-}sky}$ from the glass to the sky can be computed as

$$q_{glass-sky} = \sigma_{bb}\, \varepsilon_{glass}\, A_{EAS}\left(T_{EAS}^4 - T_{sky}^4\right) \qquad \textit{Eq. 3.62}$$

where the thermal emissivity of the external surface of the absorber ε_{glass} coincides with the emissivity of the glass in the far infrared region (considered at 100 ° C) and is assumed equal to 0.9, according to the values founded in literature.

Although the presence of the glass cover can reduce the convection losses it introduces a further optical loss linked to the transparency characteristics of the glass that can never be unitary. A fraction of the incident radiation will be reflected by the glass and the remaining radiation will be partly absorbed in the glass before reaching the absorber plate, although solar the absorption occurring throughout the thickness of the glass cover is relatively small ($\alpha = 0.02$). In the model, it has been considered that the glass cover is provided with an anti-reflective treatment, to achieve high transmittance in the wavelength range between 300 nm and 2500 nm, which is the most interesting band for solar thermal applications. For this glass, a transmission coefficient τ_{glass} equal to 95% was assumed and the solar absorption in the glass cover was neglected to simplify the analysis. Hence, in the new model of the optimized receiver, the heat flow rate that expresses the concentrated solar radiation absorbed by the front plate of the receiver, has been calculated according to Eq. 3.63:

$$q_{abs} = \mathrm{DNI}\, A_a \tau_{glass} \alpha_{r,coat}\, (\rho_c \gamma_r) \qquad \textit{Eq. 3.63}$$

The glass cover requires a support structure, that should present a trapezoidal geometry, in order not to shadow the front plate of the absorber. An aperture angle of the trapezoidal receiver equal to half of the collector's rim angle (78°) has been chosen and the distance between the receiver and the front cover has been assumed to be equal to 30 mm. Furthermore, the supporting structure of the glass allows extending the thermal insulation from the back plate to the side walls of the receiver in order to further reduce the thermal losses to the environment. From the numerical point of view, the extended insulation leads to a reduction in the area of the absorber at the highest temperature that was in contact directly with the external air A_{EAS} and an increase to the external insulated area A_{EIS} which is assumed to be at a constant temperature T_{EIS}.

Simulations have been performed in order to compare the thermal performance of the original and new optimized geometry of the receiver. The simulations have been conducted according to the test conditions during the six experimental sequences with the parabolic trough collector working as a water heating. The main result of the simulations is reported in Figure 62 where the efficiency of the collector is plotted against the reduced temperature difference. From this Figure, it can be noted that for the reduced temperature difference lower than 0.05 K m^2 W^{-1}, the efficiency of the unglazed receiver (red dots) is higher than that of the receiver with the glass cover and the additional insulation (green triangles). This is due to additional optical loss linked to the non-ideal transparency characteristic of the glass, that decrease the optical efficiency η_0 of the collector from 82% to 78%. The two values of the optical efficiency η_0 of the collector can be determined from the intersection between thermal efficiency curves of the ordinates axis (at 0 K m^2 W^{-1}). For values of the reduced temperature difference over 0.05 K m^2 W^{-1}, the efficiency curve of the collector obtained for the original receiver model always lower than the efficiency of the optimized receiver. The difference between the two efficiency curves increases with the reduced temperature difference, because the glass cover and the insulation layer on the sidewalls reduced the thermal losses between the absorber and the environment, leading to an increase in the thermal efficiency of the receiver and of the collector as a consequence.

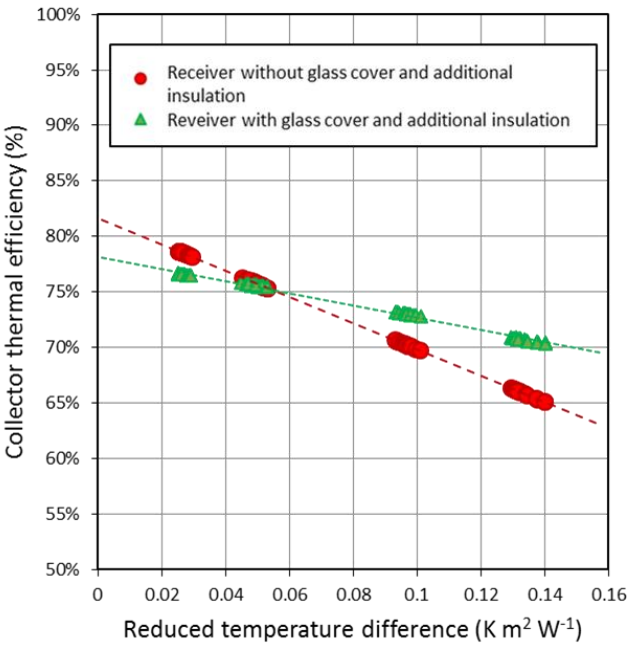

Figure 62 – Collector thermal efficiency as a function of the reduced temperature difference obtained from the simulations of the bar-and-plate flat receiver without (red dots) and with (green triangles) glass cover and additional insulation. In the simulations, the wind speed was set to 1 m s^{-1}.

Chapter 4 Numerical investigation on a small scale solar-powered Organic Rankine Cycle

Distributed electric generation is becoming more and more widespread bringing significant contributions to the electrical system. Distributed generation can be implemented in various forms, including conventional technologies such as diesel generators, microturbines, as well as advanced technologies such as fuel cells, systems involving the use of renewable energy (solar power, wind power, mini and micro-hydraulic, biomass and waste) and energy storage (electrochemical, electromagnetic, hydraulic). The use of Rankine cycle power generation systems with organic working fluid are of particular interest for the conversion of low-grade thermal energy (including solar energy) into electrical power. Organic Rankine Cycle (ORC) systems present reduced fluid dynamic erosion, the possibility to operate at moderate temperatures, the lack of rapid thermal cycling, such as those found in Stirling machines, and moderate vibrations and noise emissions that make these machines suitable to be installed also in residential area. In addition, the flexibility of ORC to operate with different working fluids is well suited to work with solar power by adapting the fluid characteristics to the operating temperatures of the solar collector.

In this Chapter, after a brief introduction on the ORC and its combination with a solar thermal system, a discussion on the most suitable organic fluid for this application is presented. A numerical model of a small size ORC for low-grade heat sources is proposed and validated by comparison with the datasheet of a commercial unit with a comparable size. Finally, the model of the solar concentrating collector with a bar-and-plate flat receiver developed in the previous Chapter is integrated into the ORC model. Some simulations are conducted in order to evaluate the performance of an ORC working with R1233zd(E) coupled to the aforementioned concentrating solar system with direct vaporization of the halogenated fluid or by using an intermediate solar circuit to heat pressurized water and evaporate the organic working fluid in a separate heat exchanger.

4.1 Organic Rankine Cycle

In thermal power plants, the use of water as a working fluid is, without doubt, the best choice to exploit heat sources available at temperatures over 300 °C and for powers exceeding 2 MWel. As the size of the plant increases, over a few tens of MW, the traditional Rankine vapor cycle is the best option. In fact, water as working fluid presents the advantage of being inexpensive and chemically stable at high temperatures, furthermore, its thermophysical properties allow to design and realize thermodynamic cycles with high conversion efficiencies for large size plants. On the other hand, for low power plants and low-grade heat sources, the use of water as a working fluid is no longer convenient due to technical and economic limits [127]. First, water presents a low molecular weight fluid, hence, the enthalpy drop elaborated by the expander will be high. This involves the use of high-cost specific turbines that can withstand high mechanical stresses on the disks/blades of the machine and which will inevitably work with modest expansion efficiency. A further limit on the use of water as a heat transfer fluid for small power plants is related to the simplicity of its molecule. The strong negative gradient of the upper limit curve in the specific temperature-entropy diagram implies that the final stages of the expansion will occur within the upper limit curve, with negative effects on the expansion efficiency and the life of the turbine. To cope with this and achieve high cycle efficiency, it is necessary to adopt cycles with an important superheating of the vapor. In addition, often the only superheating of the vapor is not enough and it is necessary to reheat the vapor to remove the remaining moisture carried by the steam at the final stages of the expansion process and to further increase the efficiency of the cycle. Both of these options are difficult to implement for applications with heat sources at low- to medium-temperature. Moreover, the consequential need for multiple stages in the turbine is not compatible with low power plants. Due to the high ratio between the evaporation heat and preheating or superheating heat for water, much of the heat in the cycle takes place at a constant temperature, while the heat sources are often at a variable temperature. The multi-level evaporation solution, commonly used in large power plants with combined cycles, is not feasible for small plants. Lastly, the high critical pressure of water implies that at high evaporation temperatures, which are necessary for high cycle performance, the pressures are very high, resulting in high prevalence for the circulating pump and high thicknesses of the tubes and collectors in the

steam generator. All these issues become accentuated by decreasing the size of the plant until they become predominant for powers of less than 1 MW_{el}.

The use of organic fluids in a Rankine cycle represents a valid alternative to convert heat from different heat sources to electricity where it is not possible or convenient to adopt conventional technologies such as steam Rankine cycle. In fact, due to the low phase change temperatures of the organic fluids used, ORCs are typically used for electrical or mechanical power generation in small power applications where the available heat source is at low- to medium-temperatures, such as wasted heat from industrial processes, solar thermal systems, and geothermal energy. Figure 63 compares the fields of application of ORCs and conventional Rankine steam cycles depending on the size of the plant and the thermal levels of the heat source [128]. In this Figure, the use of ORCs for high-temperature applications results limited by the thermal stability of the organic fluid, while the maximum power is limited by economic criteria. It exists a variable limit with the temperature of the thermal source, above which the ORCs are not economically competitive with traditional Rankine cycle. Due to the economic nature of this limit, it is expected, through technological progress and reduction of the production cost, that the applicability range of the ORC technology will increase. ORC systems represent an extremely competitive technology for applications where the power is lower than 1 MW_{el} and the average temperature of the heat source is below 250 °C, which is often associated with the renewable energy sector.

ORC systems present smaller conversion efficiencies than the conventional Rankine cycles: electrical efficiency of ORC systems ranges typically between 3% and 25% depending on the temperature of the heat source. These low values are not due to intrinsic inefficiencies resulting from the use of OWF instead of water, but they are a direct consequence of the lowest temperatures of the exploited heat sources, which limit the maximum achievable conversion efficiency, accordingly to the Carnot formulation. Because of the modest available temperature differences, the exergetic analysis, which considers the limits imposed by the second principle of thermodynamics, may be a more representative tool to evaluate the performance of the ORC system. Furthermore, when the size of the system is reduced, the economic competitiveness imposes a simplification of the system which often implies a possible decrease in the conversion performance of the system.

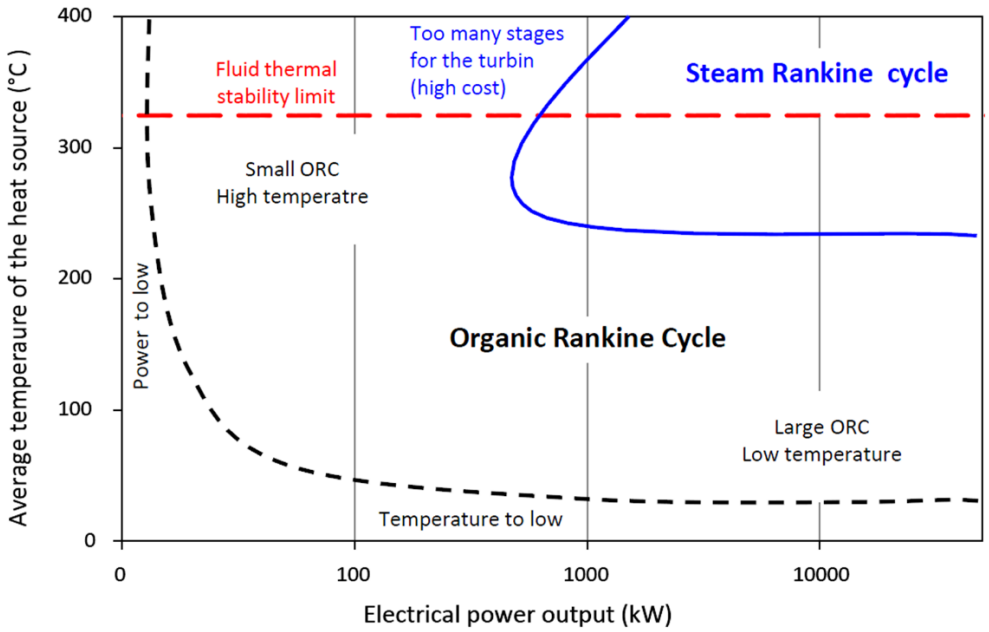

Figure 63 – Fields of application of ORC and convention Rankine steam cycle as a function of the electrical power output and the average temperature of the heat source accordingly to Gaia [128].

The first benefit in the use of an organic fluid for power generation with low-grade heat sources is a direct consequence of the high molecular weight of these fluids, which implies a low enthalpy drop and allows them to operate with low-cost, high-performance expanders. Typically, the organic fluids have molecules with a medium complexity presenting a quasi-isentropic upper limit curve or even with a positive slope. This characteristic implies that the expansion inside the limit curve can be avoided by a modest superheating. Furthermore, during its expansion, the fluid is only slightly cooled and the regenerative preheating of liquid may occur with very simple plant solutions, or it may be completely absent. Organic fluids exhibit a small ratio of vaporization latent heat to that needed to preheat the fluid or its superheating, hence the temperature profile of the fluid fits better a variable temperature heat source. Low values of the critical pressure allow operating at a high evaporation temperature without requiring either high pressures or high prevalence for the circulating pump and high thicknesses of the tube's wall. With the aim of recovering part of the heat discharged by the expander to preheat the liquid, it can be convenient to adopt an internal regeneration. In some cases, the use of a regenerator cannot be avoided, as in the case of ORC systems working with variable temperature geothermal sources. In these applications, it is advisable not to cool excessively

the fluid to avoid reaching the brine point, a condition where the mineral salts dissolved in the water precipitate. On the other hand, if there are no minimum hot water temperature limits, the use of a regenerator may be counterproductive as it reduces the heat recovered from the cycle, increases the pressure drop introducing a further complication in the circuit and increasing the initial investment [127].

4.1.1 Working fluids for ORC with low-grade heat sources

The selection of the working fluid for an ORC is a crucial choice in determining the performance and cost of the plant, in particular for ORC system for low-grade heat sources [129]. The thermophysical properties of the fluid strongly affect the size of the heat exchangers and the expander and have a great influence on the overall conversion efficiency of the cycle. In the literature, several works proposed different criteria to select the most suitable organic fluid for ORC depending on the heat source. *Chen et al.* [129] discussed extensively the properties of 35 potentials working fluids considering their thermodynamic and thermophysical properties, stability, environmental impact, safety and compatibility with materials. *Saleh et al.* [130] compared the performance of an ORC cycle (100 °C evaporation temperature and 30 °C condensation temperature) for 31 potential organic fluids focusing on the effect of superheating and internal regeneration. Their conclusions highlighted that the slope of the upper saturation curve and the critical temperature in relation to the heat source, the stability limits of the fluid, the flow rate in the evaporator and the volumetric expansion ratio play key roles. *Qiu* (Ren. En. 48, 2012) compared several criteria proposing a scale for the selection of the working fluid in ORC system. Although some specific requirements can reverse or modify the order of the applied criteria, his work provided a useful schema for the fluid selection. From this analysis, it resulted that particular attention must be paid to environmental impact (ODP and GWP) and safety aspects (toxicity and inflammability) of the fluid, normal boiling point, slope of the upper limit curve, specific enthalpy and latent heat of vaporization and some other thermophysical properties (low viscosity, high thermal conductivity) and finally to the cost and the commercial availability of the fluid. *He et al*. [131] proposed a theoretical formula for the calculation of optimal evaporation temperature for recovering heat from waste sources in order to maximize the power generated. Their results, in good agreement with the results derived

from numerical simulations, suggested that the highest power output can be obtained using fluids with a critical temperature slightly lower than the temperature of the heat source. Beyond the achievable power output and conversion efficiency, the authors individuated three fundamental parameters of the working fluid which influence the investment cost of the system: the evaporation pressure and heat transfer area provide first indications on the heat exchanger cost (thicknesses and size) while the expander size parameter SP_{exp}, originally defined by *Macchi and Perdichizzi* [132], can be representative of the cost of the expander. These parameters were considered decisive also in the study of *Lakew and Bolland* [133], where the performance of different working fluids for heat sources available at 80°C and 200 °C were numerically compared to identify the most appropriate fluid according to three distinct optimization objectives: maximum electric power generated, minimum heat transfer area and minimum expander size parameter SP_{exp}. The results indicated that the selection of the fluid varies according to the objective. The best compromise should be found through a multi-objective optimization, considering both the system performance and the size and cost parameters of the components.

From these studies, it is clear that is not possible to identify a single OWF that perform better in absolute terms and the selection of the optimal fluid is strongly dependent on the temperature and the nature of the available heat source. In addition, it emerges that it is necessary to find the best compromise between the different aspects of interest, not only considering the thermodynamic characteristics of the fluid. In this regard, safety aspects, as well as environmental impact, may play important roles in the selection of the working fluid. Using a non-flammable fluid reduces the risk of fire ignition and eliminates the need for measuring, prevention and extinguishment devices [134]. The use of toxic fluids is limited to systems operating far away from public places and requires trained and experienced. The need to protect the ozone layer and reduce greenhouse gas emissions have led to consider the environmental impact entailed by the direct emission of such organic fluids. Therefore, they were classified in terms of ODP (Ozone Depletion Potential) and GWP (Global Warming Potential). The ODP of substance defines the relative amount of degradation to the ozone layer by an equal mass of trichlorofluoromethane (R11, ODP = 1) that can be produced by the release of a unit of the considered substance. Fluids that contain chlorine atoms in their molecules present an ODP

value greater than one, as this element triggers tropospheric ozone destruction processes once the molecule is disrupted. For the preservation of the ozone, these fluids have been banned from the Montreal Protocol. The GWP is a relative measure of how much heat a greenhouse gas traps in the atmosphere by comparing the amount of heat trapped by a certain mass of the considered substance to the amount of heat trapped by an equivalent mass of carbon dioxide, whose GWP is standardized to 1. Under the Kyoto Protocol, the Conference of the Parties decided that the values of GWP calculated for the IPCC Second Assessment Report must be used for converting the various greenhouse gas emissions into equivalent amount carbon dioxide. Recently, the introduction of two directives, approved by the European Union and signed by the USA, Canada and Mexico, set the way to the progressive phase-out of high GWP HFCs. The F-Gas Regulation [135] aims to reduce the emission HFC presenting high GWP, by containing their leakages in existing systems and replacing them with alternative fluids with low environmental impact and similar performance. To achieve this objective, F-Gas Regulation imposes the dismission of HFCs with high greenhouse effect. Currently, the regulation is applied to civil refrigeration, commercial and HVAC system and it will probably be extended to electric power generation from heat sources at low- and medium-temperatures where high-impact HFC fluids are widely used (R134a, R245fa, R245ca). The MAC Directive, whose jurisdiction is limited to mobile air conditioning systems (mainly aimed at replacing R134a) is even more restrictive as it prohibits the use of HFCs with high GWP (> 150) in the air conditioning systems of vehicles produced from 2017.

From what presented above, it can be understood that the selection of the appropriate OWF cannot discern from the environmental considerations. Therefore, the use of natural fluids (carbon dioxide, propane, isobutane, propane, ammonia) and a new generation of synthetic low-GWP fluids, such as HFOs and HCFOs, have encountered a great interest in the last years. The latter type of fluids, is the most promising alternative for the replacement of existing fluids currently used for low-temperature ORC and for refrigerant, as their characteristics are very similar. The presence of a double bonding in their molecule accelerates their degradation in the atmosphere, thereby reducing their atmospheric lifetime (ALT) and consequently their ODP and GWP associated with their emission. Recently it has been proven experimentally that different HFOs show good stability in applications in low- and medium-temperature

applications [134]. Furthermore, these fluids also exhibit great compatibility with both metal and elastomer materials, commonly used in ORC and refrigeration circuits.

At the present, the fluid R245fa has been considered by many authors the most suitable choice for ORC systems coupled to low-grade heat sources. The main advantages offered by the use of this fluid for the exploitation of low-grade heat source are reported in the following:

- It is a non-flammable fluid, unlike the competing hydrocarbons at temperatures below 150°C. However, it is weakly toxic and therefore belongs to category B1 according to the classification ASHRAE 34:2010 [136].
- It presents a null ODP.
- It is a dry expansion fluid (positive slope of the upper saturation curve) and therefore, it does not form droplets during its expansion;
- It has a critical temperature of about 150°C (154 °C) which is perfectly compatible with typical temperatures of low-grade heat sources. Furthermore, it allows operating at high temperatures in order to obtain high conversion efficiency by keeping a certain distance from the critical temperature, in the proximity of which, small temperature variations can trigger instability phenomena.
- In the low-temperature range, it presents modest evaporation pressure which allows the use conventional heat exchangers well diffused on the market (at 100 °C its saturation pressure is just 12.6 bar)
- Above 13 °C its condensation pressure is higher than atmospheric pressure, allowing the possibility to operate without a system to eliminate the non-condensable gases under the typical operating conditions imposed by the thermal sink.
- Low evaporative pressure and high condensation pressure allow limiting the pressure ratio in the expansion process. This aspect is a great advantage in the use of volumetric expander both in terms of cost and efficiency.
- It present high thermophysical properties in both liquid and gaseous phases.
- It is very weakly corrosive, has good lubricating properties and it does not cause fouling;
- It is easily available on the market and has modest prices.

Datla and Brasz [137] compared the conversion efficiency, the size of heat exchangers and expander of a 100 kW_{el} ORC supplied by heat sources at temperature between 80 °C and 100 °C when different OWFs were used. Their results showed that the maximum efficiency was obtained using toluene. However, this siloxane oil presents several undesirable properties like high toxicity, flammability, furthermore, it required a high expander size, high expansion pressure ratio and sub-atmospheric condensation pressure which discourage its use. Very similar performance has been obtained with fluids presenting a lower saturation temperature and admit lower size and rotational speed of the expander such as pentane, R245fa and R123. However, the use pentane is often avoided do its high flammability, while R123 contains chlorine in its molecule. *Cataldo et al*. [138] compared the performance of an ORC plant for heat sources at 100 °C – 150 °C with different OWF, assuming constant isentropic efficiencies of the pump and the expander and minimum temperature difference at the heat exchanger. Evaporation temperatures and condensation have been adjusted to maximize the efficiency and minimize the specific cost of the heat transfer area for a unit of power generated. The results show that the fluids with the lowest critical temperature considered in their analysis (Novec649, RE347mcc, R245fa) maximize the efficiency while it is necessary to use fluids characterized by higher conductivity and higher latent heat of vaporization heat to minimize the specific cost of the heat transfer area. *Quoilin et al.* [139] claimed that, if all the aspects of interest are considered, only three operating fluids result interesting for ORC system supplied by so sources at the temperature around 150 °C: R245fa, Solkatherm® SES36 and n-Pentane. Solkatherm SES36 is the fluid that in their study showed the highest efficiency (7.9%), however, it required the largest expander. N-Pentane, in addition to being flammable, required the use of a large regenerator in order to operate with high efficiency. Despite the lower efficiency (6.9%), the best choice under the considered operating conditions resulted the R245fa. In the study of *Rayegan and Tao* [140], where a procedure for selecting the most suitable fluid for solar-powered ORC was developed, R245fa was recommended as potential working fluids in the case of collectors at low- and medium-temperature. In the study of *Li et al.* [141], the influence of the OWF on the performance of the ORC has been evaluated by varying the temperature of the heat source assuming a constant supplied heat flow rate. In this investigation it has been shown that among all the fluids considered, the R245fa was the optimal fluid for heat sources at the temperature lower than 150 °C. The fluid R245fa was also chosen an OWF in many

experimental studies on solar-powered ORC systems [139,142] or for waste heat recovery where it displayed good performance. The presence on the market of several commercial small ORC unit using R245fa provides a further proof of the technical and economic feasibility in the exploitation of low-grade heat source with this fluid. Despites the excellent thermodynamic performance of R245fa for the exploitation of low-grade heat source the growing sensitivity of society on environmental issues will increasingly limit its use due to its high GWP (1030 according to *Moles et al.* [143] although other authors in the literature indicate lower GWPs between 800 and 1000). In the work of *Juhasz and Simoni*[115], several potentially applicable fluids as a replacement for the use of R245fa in ORC systems were compared. *Moles et al* [144] limited their analysis to two fluids R1233zd(E) and R1336mzz(Z), which are the most valuable candidates for the future replacement of R245fa. Table 9 compared the thermophysical characteristics and the environmental parameters for the two substances considered.

Table 9 - Thermophysical properties of R245fa, R1233zd(E) and R1336mzz(Z) [143]

Parameters	R245fa	R1233zd(E)	R1336mzz(Z)
Chemical formula	$CF_3CH_2CHF_2$	$CF_3CH{=}CHCl$	$CF_3CH{=}CHCF_3$
T_{crit} (K)	427.16	438.75	444.45
p_{crit} (MPa)	3.65	3.57	2.9
Mol. w. (kg kmol^{-1})	134	130.5	164
Slope	Dry	Dry	Dry
Flammability	Non-flammable	Non-flammable	Non-flammable
ASHRAE Std 34 safety class	B1	A1	A1 (expected)
Tested thermal stability (K)	523.15	n.a.	523.15
ALT (year)	7.6	0.1096	0.0658
ODP	0	0.00034	0
GWP	1030	7	9
Boiling point (K)	287.96	291.12	306.55
Latent heat at boiling point (kJ kg^{-1})	196.23	195.52	165.67
Evaporating pressure at 400 K (MPa)	2.21	1.80	1.28
Condensing pressure at 300 K (MPa)	0.16	0.14	0.08

The trend of the saturation pressure with the temperature and the saturation curves in the T-s diagram for R245fa, R1233zd(E) and R1336mzz(Z) are reported in Figure 64.

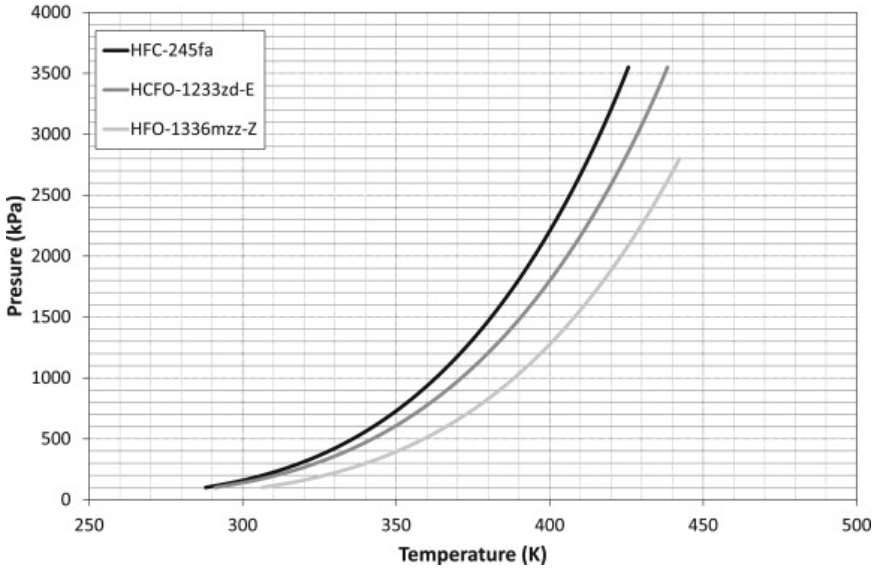

- a -

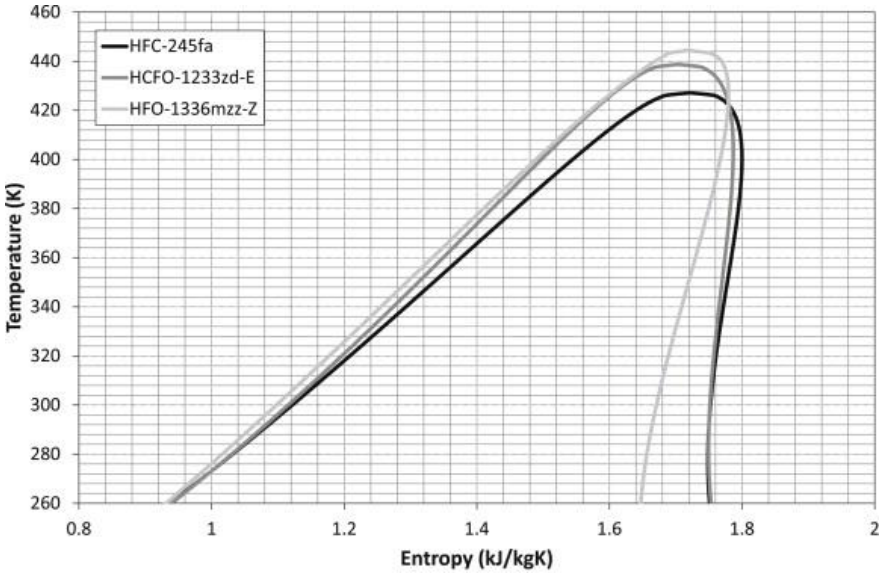

- b -

Figure 64 – Saturation pressure (a) and saturation curves in the T-s diagram for R245fa, R1233zd(E) and R1336mzz(Z) [143]

It worth to be mentioned, that because of the chlorine atom in the molecule of R1233zd(E) this fluid presents a non-zero ODP. However, due to its very low atmospheric stability, it presents

an ODP of only 0.00034. This negative aspect appears to be of lower relevance than the benefit achieved in terms of the greenhouse effect, thus it usually considered acceptable and not widely discussed. It is important to note that the GWP index associated with the R1233zd(E) is typically lees than 10, while the GWP value for the R245fa is much higher, typically between 850 and 1030.

Due to the only recent introduction in the market of R1233zd(E) and R1236mzz(Z), most of the publications aimed at studying the potential use these fluids as a replacement to the current R245fa are numerical study. *Kontomaris* [134] numerically compared the performance of an ORC cycle with R1336mzz(Z) and R245fa. The results have shown that the use of R1336mzz(Z) is technically possible and can even lead to an increase of the cycle performance. In the work of *Datla and Brasz* [145], the performance of R1233zd(E) and R245fa in a small low-temperature ORC (75 kWel) equipped with a radial turbine were compared. The use of R1233zd(E) can increase the efficiency by 8.7% compared to the competitor fluid. In comparison to the same system, however, the temperature of the heat source was increased so that evaporation temperature can be maintained the same.

Molés et al. [143] compared the performance of an ORC with both basic and regenerative configurations operating with R1336mzz(Z), R1233zd(E) and R245fa and powered by a constant heat flow rate at the evaporator. Both olefins gave similar performance to that obtained with R245fa. The analysis involved evaporation temperature ranging from 97 °C to 147 °C, and superheating from 0 °C to 50 °C while the condensation temperatures were between 27 °C and 77° C. According to the results of the simulations, both R1336mzz(Z) and R1233zd(E) require a pumping power from 37% to 41% and from 10% to 17% lower than that for the R245fa. The efficiency resulted 10.6% and 17% higher compared to that of the R245fa, for R1336mzz(Z) and R1233zd(E) respectively, depending also on the use or not of a regenerative exchanger. Both alternative fluids require a larger expander than the R245fa: in the case of R1336mzz(Z), the expander volume was 31% - 42% higher compared to R245fa, while that of the R1233zd(E) was only 8% - 10% higher. The difference between the conversion efficiency of the two fluids with respect to the R245fa, increases when the condensation and evaporation temperature rises, while the difference in size of the expander decreases.

Eyerer et al. [146] presented a work on the applicability of R1233zd(E) as a substitute for R245fa in ORC system supplied by a heat source at 120 °C by comparing system parameters such as cycle efficiency and power output. The influence of the process parameters mass flow rate, condensation temperature, and expander rotational speed was investigated experimentally for both fluids. The authors have concluded that R1233zd(E) can be successfully used to replace R245fa in existing systems without major modifications in the system. Comparing the highest achieved thermal efficiency, it was found that the use of R1233zd (E) can lead to an increase of 6.92% in the thermal efficiency with constant condensation and evaporation temperatures and constant isentropic expansion efficiency. However, the net electric power generated by the ORC working with R1233zd(E) was 12.17%. lower. It was observed experimentally that the largest volumetric flow rates of the R1233zd(E) required for the use of the system designed for R245fa, implied to increase the rotational speed of the expander to maintain the same volumetric efficiency and do not excessively penalize the power generation. In the work of *Molés et al.* [147], an experimental evaluation of the working fluid R1233zd(E) as R245fa replacement in ORC systems for low-temperature heat sources at different operating conditions has been conducted. Thermal and electrical powers resulted lower for R1233zd(E) than for R245fa, due to the fact that the different densities of the working fluids, implied that the mass flow rate for R1233zd(E) was approximately 20% lower than for R245fa. However, net electrical efficiency was similar for both working fluids, ranging from 5% to 10% in the tested operating conditions. *Guillaume et al.* [148], experimentally compared the performance of an ORC system fed by the waste heat of the exhaust gases of a long-haul truck and equipped with a radial-inflow turbine for R245fa and R1233zd(E). Measurements in steady-state were conducted in order to evaluate the performance of the turbine-generator set when varying the pressure ratio, the rotational speed, the inlet temperature and the mass flow rate of the turbine and the lubrication flow rate of the bearings for various oil temperatures and mass flow rates. Three types of comparison were proposed for the performance of the ORC components: same temperature levels for both fluids, same condensing temperatures and same evaporating pressures and finally, same pressure levels. The experimental results showed that R1233zd(E) represented a better choice compared to R245fa to recover waste heat, based on the given test rig.

4.1.2 Expander for ORC with low-grade heat sources

The selection of expander to be installed in an ORC is decisive in determining the performance and cost of the system. *Weiss* [149] highlighted that the cost of expander can weigh up to 50% of the total investment cost of the system, especially for small scale ORCs. With regard to performance in terms of conversion efficiency and power generated, for several authors the expander is the most critical component of the system because is the most influencing element on the overall cycle conversion efficiency. The selection of the best expander type depends on the size of the ORC system, the temperatures of the available heat source and heat sink and the operating fluid used, which define the expansion ratio. The performance of the expander at partial loads should also be considered when the heat source and/or the heat sink may present some variability.

Beside the thermodynamics aspects, there are several economic and technical aspects to consider, such as the availability on market, the reliability of the technology, the service, and maintenance cost and the longevity of the device. One of the most important parameters, is the rotational speed of the expander because it has significant implications in the coupling with the electric generator, the types of bearings for shaft rotation and the amount lubricant needed for its efficient operation. Working at high rotation speed makes necessary to use rotary gear or power conditioning systems for coupling with the electrical net, bearings present a high oil consumption for the lubrification. Furthermore, it is required to dissolve a higher amount of oil in the working fluid for the efficient lubrification and sealing of the device and to install an oil separator as a consequence. This device may prevent the counterproductive participation of the oil to the heat transfer processes in the condenser and evaporator. To limit the fluid leakage, great attention should be paid to the sealing of the expander housing, in particular, in the cases of fluids presenting high environmental impact, toxicity or flammability.

The expanders for ORC systems can be divided into two main categories depending on the different physical conversion mechanism that they exploit: volumetric (positive displacement) and dynamic (turbines) expanders. To the first group belong a series of very different devices such as scroll, single-screw or double-screw, reciprocal pistons and rotary vane expanders. For

small ORC units, in particular below 100 kW_{el}, positive displacement expanders like scroll or screw machines have been often applied (Figure 65).

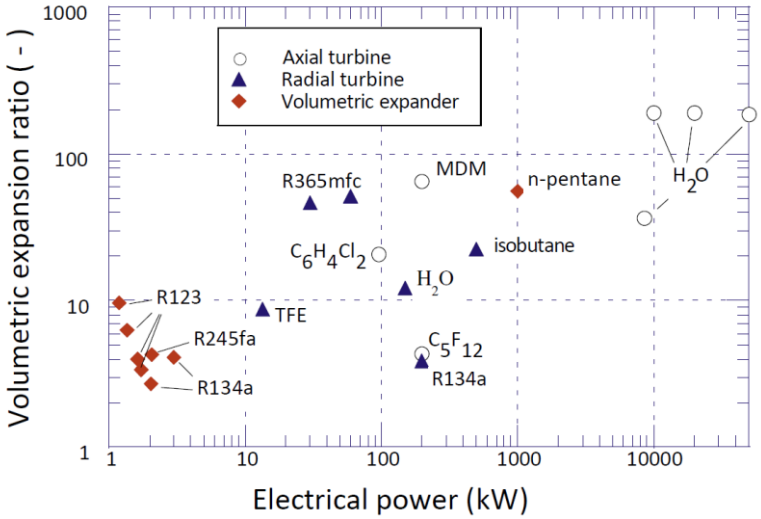

Figure 65 – Expander technology of existing ORC systems operating with different fluid plotted as a function of the actual volumetric expansion ratios and the electrical power output [150].

Many publications [151,152] showed that for small power output or rather small mass flow rate, volumetric expanders present considerable advantages regarding efficiency, rotational speed, size and cost. Such devices can process smaller flow rates and are suitable to elaborate high pressure ratio in a single stage. They can work at lower rotational speeds than turbines and allow in some cases the direct coupling with the electric generator without the need for a gearbox. Furthermore, working at low rotational speed reduces sound emissions, vibrations and stresses on rotor components ensuring the best reliability of the system. Volumetric devices are simpler to produce than turbines, which may present significant technological limits in reducing the size for the excessive miniaturization required. They also present a higher flexibility at partial loads. Finally, they are more robust and allow processing of high fractions of liquid without showing signs of wear or sharp reduction in the expansion isentropic efficiency.

Besides the above-mentioned reasons, there is another very simple reason for the frequent use of small volumetric expanders for small ORC systems: these machines were cheaply available in the past from refrigeration or compressed air technology where they acted as compressors

[149]. Currently, volumetric expansion solutions available on the market present high cost mainly due to the limited production dictated by the low demand on the market. Therefore, very often in experimental research volumetric compressor used in refrigeration and air conditioning are modified to be used as an expander. In fact, due to the absence of operating valves, some volumetric compressors can be easily converted to expander by means of minor adjustments, so as not to penalize excessively the efficiency of the reverse operation of the machine. This operation is associated with additional losses compared to the use of designed expander [153]. This is one of the reasons of the low overall efficiencies often experienced in experimental tests of small ORC unit. For this reason, volumetric expander presents a considerable margin to improve the performance and reduce the costs. The main disadvantage in the use of volumetric expansion is the limit imposed by the built-in volumetric ratio. In fact, all positive displacement devices present a fixed volumetric ratio. The fixed built-in volume ratio r_v, can generate two types of losses if the system specific volume ratio is not equal to the expander nominal volume ratio: namely blowback and blowdown losses. These two effects can considerably reduce the efficiency of the expansion process, the most common being the under-expansion [154]. Other sources of losses are friction, supply pressure drop, internal leakage of the fluid and heat losses from the fluid to the environment through the housing of the devices.

Although several solutions have been proposed as potential candidate technologies for the expansion process in ORCs, none of these has shown to be the best solution. From the studies of *Badr et al.* [155,156] where different types of expander, such as turbines (radial, impulse, reaction) and volumetric expander (screw, piston, Wankel) were compared for small power generation, screw and Wankel expander have been shown to be the most promising technologies among the others. Other theoretical and experimental studies confirm this the observation of *Badr et al*. For example, the works of *Kane*[157]*, Lemort et al.*[152,158] *Quolin et al.* [159] and *Singh et al.* [160] showed that in the range of small power, scroll and screw expanders present interesting values of the isentropic expansion efficiency, up to 70%.

Single- and twin-screw, scroll and rotary expanders are the most promising volumetric devices as they continuously expand the operating fluid. Among these, the twin-screw expander is considered to be the best candidate for ORC units with an electrical output between 10 and 300 kW_{el}. These devices have a nominal efficiency of up to 70% and show a high flexibility in

operating with partial loads. The presence of a sliding valve allows to efficiently vary the intrinsic volumetric ratio as well as the elaborated volume, maintaining high efficiency even under partial load conditions. In particular, these systems can fully cover the range of organic fluid expansion pressures commonly used for electrical generation from low-temperature heat sources. The volumetric ratio is generally around 5, limited by bending stress in the rotor, however, examples of screw expander with a volumetric built-in ratio up to 8 are present in the literature [161]. In comparison to scroll devices, the high volumetric built-in ratio allows their efficient used with elevated pressure ratio in a single expansion stage. Currently, on the market these devices present nominal power between 20 kW_{el} and 1 MW_{el} and fluid flow rates between 25 L s^{-1} and 1100 L s^{-1} [152]. The application of these devices to smaller size has encountered some difficulties due to the reduction in the constructive tolerances needed to avoid the decrease of volumetric efficiency. In the future, it expected that thanks to the improvement of manufacturing techniques, it will be possible to produce devices with smaller tolerances and consequently, this technology will be able to compete with the largest scroll devices currently used for small power [162]. In screw expander, the required gaps between the screws and between the screws and the housing strongly penalize their volumetric expansion efficiency. An internal pressurized lubrication system is usually implemented to ensure the high volumetric expansion efficiency. This technical solution is often adopted combined with the high rotational speed which improves the sealing due to the high centrifugal forces. *Lemort et al.* [152] reported that an oil-free double-screw expander indicatively requires a minimum speed around 10000 rpm to ensure an efficient sealing. Screw devices without lubrication are available on the market with 20000 rpm maximum rotation speed [152]. The presence of liquid in the expanding fluid may also contribute to the good seal of these devices [163].

Nowadays, only few companies around the world offer screw expanders on the market. Heliex Power [164] produces devices for the recovery of high-pressure streams. Their devices are applied for example to recover energy from the pressure reduction of natural gas in distribution stations or in industrial applications. *Smith and Leibowitz*, founders of the company ElectraTherm [165] have designed a twin-screw expander for ORC unit with low-grade heat from sources, capable of generating power from 20 kW_{el} to 110 kW_{el}. The investment cost of

their units was between 1500 and 2000 \$/kW_{el} with an estimated generation costs between 0.03 and 0.04 \$/kWh (20 years).

The main competitors to screw expanders in the exploitation of low-temperature heat sources in small ORC plant are scroll expanders. This technology is widely used in HVAC as compressor because it displays high efficiency, few rotating parts, low rotation speeds suitable for direct coupling with an electric generator, low vibrations and sound emissions, and high reliability. The scroll expander used in small ORCs present efficiencies below 70% [152,166] in the range from 1 kW_{el} to 10 kW_{el}. Compared to screw expanders, scroll expanders are more sensitive to changes in the operating conditions (flow rate, pressure ratio) and exhibit a sharper decline of its isentropic expansion efficiency. The main limit on the applicability of this devices is the modest intrinsic volumetric ratio, which generally is comprised between 1.5 and 3.5, although devices working with r_v up to 4 were reported in the literature [161]. The increase of the volumetric built-in ratio implies the increase of the size of the device (diameter, length, and number of spirals), its cost and the need for better sealing, which increase friction losses and the frequency of maintenance. Higher pressure ratios (which require greater intrinsic volumetric ratios) require larger spiral devices (cost greater) or the use of multi-stage serial devices. Although the high suitability of this devices for distributed generation from heat recovery at low temperature, scroll expanders are not still a mature technology and the design and production of scroll expanders have been only poor developed by the industry given their currently high specific costs. Even in the research works in the literature, scroll expander is usually modified compressors converted for their use as expanders. There is a lot of excitement for the introduction on the market of small size scroll expander. For example, Eneftech [167] is about to make available to the market a 5 kW_{el} ORC unit (ENEFCOGENplus), while a 10 kW_{el} unit (ENEFCOGENgreen) is already on the market at a price around 55000 €. Although ORC units adopting these devices are currently present on the market, screw expander presents a higher maturity level.

4.1.3 Solar-powered ORC

A solar thermal system can be combined with an ORC system according to two configurations: coupling with direct vaporization of the organic working fluid (OWF) or by using an

intermediate solar circuit to heat a heat transfer fluid and evaporate the OWF in a separate heat exchanger. A schematic representation of these configurations is provided in Figure 66. In the latter case, the heat transfer fluid circulating in the solar loop is heated during its passage in the receiver of the solar collector (Figure 66 - a). From this, it enters the heat exchanger given the gained heat to OWF, which is heated and evaporated. In order to perform a complete evaporation of the OWF, the mass flow rates in the solar and in the ORC loop must be carefully adjusted according to the solar input. In a solar-powered ORC system with direct vaporization of the OWF in the solar collector, the solar circuit, and the ORC circuit coincide so as the solar receiver coincides with the evaporator. By adopting this configuration, it is possible to simplify the system, in fact, the intermediate loop for transferring the heat from the solar collector to the OWF circulating in the ORC system is no longer needed (Figure 66 - b).

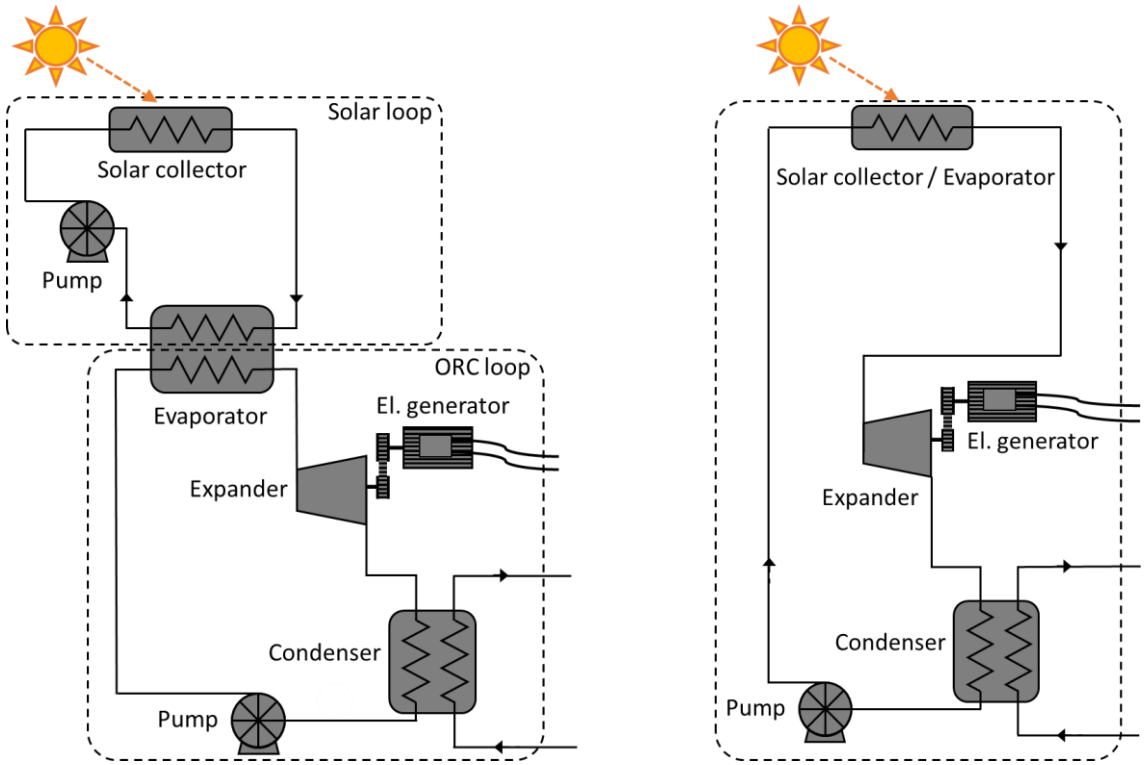

- a - *- b -*

Figure 66 – Schematic representation of a solar-powered ORC systems in the case of vaporization of the OWF by the heat transferred in a separate heat exchanger (evaporator) from an intermediate heat transfer fluid heated in the solar collector (a) and in the case of direct vaporization of the OWF in the receiver of a solar collector (b) (once-through configuration).

It is expected that the direct vaporization of the OWF in the solar receiver allows converting the solar energy collected by the solar system into the thermal energy of the OWF with higher efficiency than the case with indirect vaporization. In fact, this process takes place without the irreversibility associated with the heat transfer occurring in the heat exchanger/evaporator. This aspect is particularly important in ORC systems where the temperature differences between the heat source and the environment are quite low (around 100 °C). From another point of view, assuming the same inlet conditions of the OWF in the expander, the average temperature of the fluid inside the solar collector in the direct vaporization configuration will be lower and, as a consequence, the thermal efficiency of the solar collector will be higher. However, the solar circuit must be sized for a higher operating pressure which corresponds to the desired evaporation pressure of the OWF. This implies thicker tubes and better hydraulic sealing in the solar circuit and in the receiver, especially in the case of the use fluids with a high impact on the environment.

Although the feasibility of steam Rankine cycles with direct vaporization of water in PTC has been extensively demonstrated, it has not yet been proved with organic fluids. In addition, a direct vaporization of the OWF is characterized by a lower thermal inertia which requires a high adaptability of the load and makes the system more sensitive to the onset of instability which can occur at sudden variations of solar input. More complex control strategies are needed to control the two-phase flow inside the collector in order to avoid the onset of dry out and instability phenomena and guarantee a stable vaporization process. In the simpler solution, the so-called once-through strategy, which is equivalent to a conventional Benson boiler, the total amount of fluid flowing in the circuit is preheated, evaporated and superheated into the collector. The representation depicted in Figure 66. - b provides the schematic of a solar-powered ORC in once-through configuration. It must be mentioned that this strategy is not usually implemented in a direct steam generation system, due to the fact that the mass flow rate should be carefully regulated according to the solar input to have only a slightly superheated vapor at the outlet of the solar receiver/evaporator without thermal and flow instabilities. Commonly, in order to avoid the risk of dry out, more liquid is fed into the collector that can be evaporated within the collector. Thus, it becomes necessary to collect the liquid fraction of the non-completely vaporized fluid at the outlet of the solar receiver in a liquid-vapor separator.

The excess of liquid can be directly recirculated in the receiver or it can be laminated and sent to the condenser before being circulated in the solar collector Figure 67 shows two possible schematics of the direct vaporization configurations adopting a recirculation strategy. In the first solution (Figure 67– a), only a fraction of the total amount of liquid that feeds the solar collector/evaporator is circulated in the rest of the circuit. The remaining fraction is circulated by a secondary pump in the solar collector. In the second configuration (Figure 67– b), only the expander works with a reduced flow rate, while in the rest of the circuit elaborates the total amount of the working fluid. The economic optimum between the two configurations strictly depends on the real working conditions. In fact, depending on the design conditions of the systems, one configuration could present a lower initial investment than the other, but it could present higher maintenance and service costs.

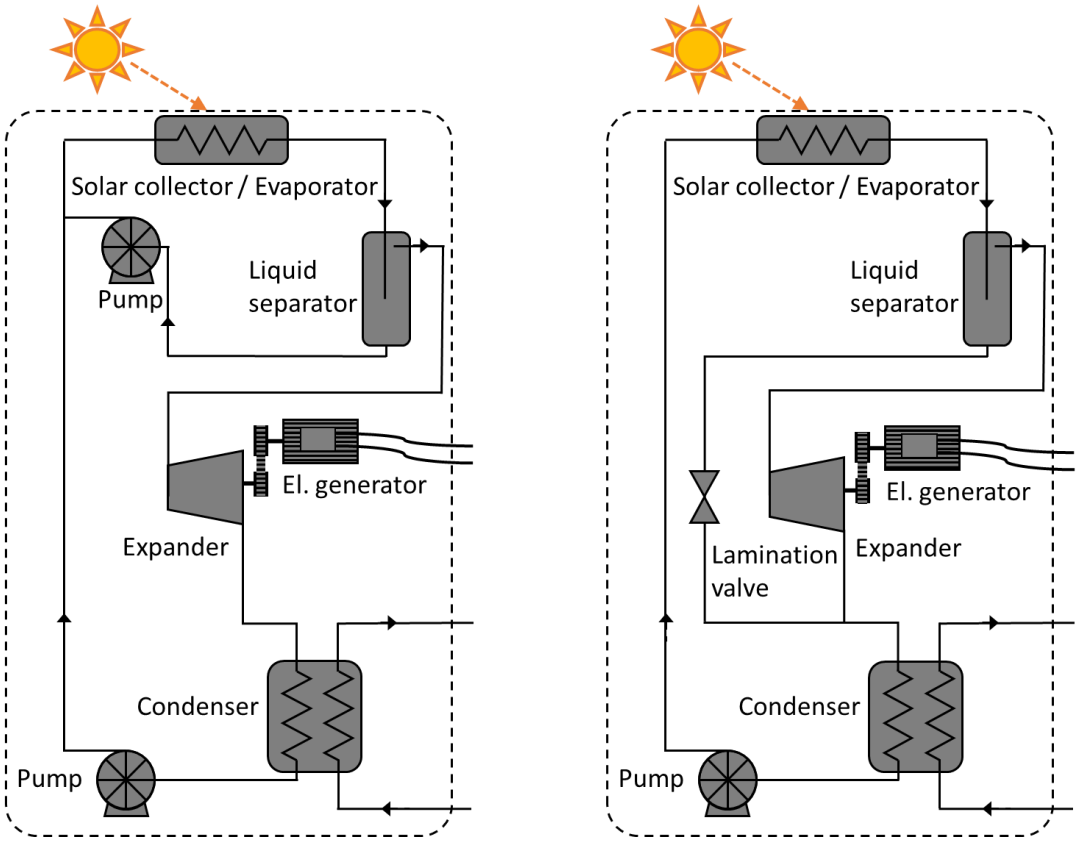

- a - *- b -*

Figure 67 – Schematic representation of a solar-powered ORC system in the case direct vaporization of the OWF in the receiver of a solar collector when the liquid from the separator is directly recirculated in the receiver (a), and when the separated fluid is laminated and sent to the condenser (b).

As the size of the system increases, the evaporator may be constituted by more collectors connected in series. In this case, the collector field can be subdivided into an evaporation and a superheating section by a vapor-liquid separator. At the end of the evaporation section, the excess liquid is separated from the vapor flow and recirculated to the collector inlet. If the subdivision of the collector field creates different single collector units divide by an injection element and gauging units, an injection control strategy can be performed. Both compact liquid-vapor separators for solar field portion or huge separation drums for the whole collector field are conceivable. Small compact liquid-vapor separators offer the advantage of a lower inertia, thus reducing the time for start-up and lower investment.

The liquid phase separation can be obtained through centrifugal forces, as in cyclone separators, or by inserting solid obstacles where to trap the liquid droplets, as in baffle separators. In the first kind of device, the two-phase fluid enters tangentially into the cylindrical device causing a spiral motion of the gas-phase. The axial flow is directed downwards in the outer region and upwards in the core region with the vapor leaves the cyclone through the so-called, vortex finder. For the separation of liquids, a simple cylindrical cyclone is used, which can be divided into an upper section where separation takes place and a lower section where the liquid is collected This design has the advantage of guaranteeing a well-defined flow situation in the upper part. In combination with a vortex breaker at the liquid outlet, a sufficiently high liquid level in the lower part avoids the problem of vapor being suctioned into the liquid outlet. Furthermore, only a flat liquid surface allows the measurement of the liquid level, which is necessary for the control of the liquid discharge. Baffle separators are a common device specially designed for droplet elimination from gas streams. Typical applications are air dryers in cooling devices and air cleaners for industrial exhaust streams with cut sizes in the range of 5 to 30 microns. In principle two different configurations are possible. In the first configuration, the vapor stream can be directed horizontally through a wave-plate package and the separated droplets move downwards on the walls or can be collected in drainage channels. In the second configuration, the vapor stream can be vertically directed upwards causing the separation of the small droplets on the wave-plates. There they form a film flowing downwards against the vapor stream. Larger droplets created by film break-up are now able to overcome the drag in the vapor stream and fall into a sump.

The European DISS and INDITEP projects have proven the feasibility of the direct steam generation process in parabolic trough collectors under real solar conditions at the Plataforma Solar de Almería (PSA) [168]. These projects have shown that the recirculating mode is the preferred operational mode in the case direct steam generation. However, it has to be mentioned, that the expander usually adopted in small ORC unit for lower-grade heat sources, are quite robust and allow processing of high fractions of liquid without showing signs of wear or sharp reduction in the expansion isentropic efficiency. Therefore, in these systems, the once-through configuration can be adopted without any particular requirement.

In the design of a solar-powered ORC system, it is essential that the choice of the collector is taken accordingly to the desired temperature that supplies the ORC. In fact, the performance of a solar-powered ORC system is given by the contribution of the electrical performance of the ORC system and the thermal performance of the solar collector/solar field. In first analysis, once the collector is set, higher temperatures at which the solar radiation is absorbed allow higher evaporation temperatures and higher conversion efficiencies of the ORC as a consequence, but penalize the thermal efficiency of the solar collector, whose losses by convection and irradiation increase due to the increased average operating temperature of the heat transfer fluid. Hence, to ensure higher collector efficiency the adoption of a more expensive solar collector is required. On the other hand, lower maximum temperatures allow the use of cheaper technical solutions for the collection of the solar radiation but involve lower conversion efficiencies ORC. Therefore, at the same electrical output generated by the system, it necessary to increase the solar field surfaces. The optimal value of the operating temperature at which the solar field and the ORC system will be dimensioned as result of a compromise between these two conflicting trends [169]. Compared to the large using traditional Rankine cycles plants for CSP, exploiting solar energy through an ORC cycles allows to of smaller size plants, with installed power from kW_{el} to some MW_{el}. The smaller power and the lower temperatures involved allow occupying a smaller area on the territory than the large solar power plants and the installation of solar collectors with a low concentration factor (typically lower than 20), which do not require high reflective surfaces and expensive solar tracking systems. Even though solar thermal collectors for medium temperature (between 80 °C and 250 °C) represent a niche sector, commercial models are available on the market [6]. The

receivers of these collectors, depending on the operating temperature, may not need glazed and empty cavity covers and they can be manufactured with cheaper materials and selective coatings. This allows containing the investment costs of the solar field, which nowadays it is the main cause that discourages the investments in the solar power industry due to the high capital required and the long payback time. Furthermore, the lowest operating temperatures can also reduce the costs and risks concerning the heat transfer to the power cycle by adopting safer heat transfer fluid (neither toxic nor flammable), such as water, rather than the high boiling diathermic oils used in CSP plants. For operating lower operating in temperatures (lower than 150 °C), stationary concentrating collectors, such as compounds parabolic or evacuated tube collectors, can be used without the need of expensive solar tracking systems. The feasibility of small ORC with such collectors has been proven obtaining conversion efficiency of 6% for a 120°C [170].

Nowadays, only few solar-powered ORC plants can be found all over the world. These installations are typically pilot plants operating in the medium-temperature range, i.e. between 100 °C and 500 °C, using concentrating solar collectors in order to guarantee high conversion efficiency. Moreover, the size of the plants is greater over the MW_{el} to profit of the scale effect. The National Renewable Energy Laboratory (NREL) constantly updates a dataset where it is possible to find information on the existing concentration solar plant for the production of electricity in the world among which ORC systems are also included [171].

Among the still operating solar-powered ORC plants, the demonstration plant (1 MW_{el}) Saguaro at Red Roch (Arizona - USA) is the oldest one and it is in service since 2006. In this plant, linear parabolic collectors (Starnet LS-2 by Solargenix) with tubular receivers (Schott PTR70) are coupled to an ORC system Ormat® operating with n-pentane. The solar collector field is characterized by an overall aperture area greater than 10000 m^2, capable to heat the heat transfer fluid Xcertherm® 600 from 120 °C to 300 °C. The ORC plant operates with a maximum evaporation temperature of 200 °C and a condensation temperature ranging from 15 °C to 35 °C, depending on the ambient temperature. The overall conversion efficiency is 12%, while the average annual conversion efficiency of the power plant is around 7.5% [171]. According to *Velez et al.* [172], the specific investment for this facility was around 5730 €/kW_{el} with an estimated cost of energy produced around 17 c€/kWh. In the last decade in the

Mediterranean area, the interest in solar-powered ORC system has increased and several demonstration plants have been constructed. In 2014 the ORC Airlight Energy plant (12 MW_{el}) in Ait-Baha (Morocco), which recovers heat from a cement plant, has been integrated a solar system which is capable to supply 3 MW_{el}. This pilot plant has been provided with linear parabolic concentrators with an innovative pneumatic cover (Figure 68 - a). The overall aperture area of the solar field is equal to 6160 m^2. The diathermic oil circulating in the solar circuit is heated from 270 °C to 570 °C and sent to a heat exchanger/evaporator of the ORC system.

- a - *- b -*

Figure 68 – Example of solar collector fields installed in demonstration solar-powered ORC plants: a - PTC with pneumatic covers installed in the Airlight Energy plant (Ait-Baha – Morocco); b – LFRs installed in the IRESEN CSP-ORC plants (Benguerir Morocco)

Another example of solar-powered ORC demonstration plant is located in Rende (Calabria, Italy). In this 1 MW_{el} plant, solar concentration is achieved through the use of LFC collectors with an overall aperture area of 9780 m^2. The outlet temperature of the diathermic oil from the solar circuit is equal to about 280 °C. The pilot plant IRESEN CSP-ORC (1 MW_{el}) under construction in Benguerir (Morocco) uses LFC collectors as well (Figure 68 - b). This plant is expected to use mineral oil as HTF for the solar circuit in the temperature range between 180 °C and 300 °C. The ORC will be present dry condenser and will be equipped with an oil storage capacity of about 20000 l, capable of supply the plant for about 4 hours. Recently, the Stillwater GeoSolar Hybrid Plant in Fallon (Nevada - USA) was expanded in March 2015 by adding a concentrating solar collector field. In this hybrid plant, aside the 33 MW_{el} produced from a geothermal source and the 26 MWel are provided with photovoltaic panels, 2 MW_{el} were

integrated by the solar thermal collector field (17 MW_{th}). The overall aperture area of the PTC field is approximately 656 m^2, demineralized water is used as HTF.

Since the early 1990s, small scale ORC system combined with solar systems have been the object of study by the scientific community. Small size solar-powered ORC systems are very interesting because they allow distributed generation on the territory even in a residential-civil area [139] and can help the electrification process of rural regions and the development of small off-grid isolated communities [173,174]. The requirements for simplification and containment of investment costs requires the use of more economical collectors that allow efficient operations at lower temperatures than the collectors used in the presented large demonstration plants. However, it cannot be found any commercial installation. One of the main reasons of that is the lack of small and efficient expanders available in the market. Although several solutions have been proposed as potential candidate technologies for the expansion process in ORCs, none of these has shown to be the best solution. From the studies of *Badr et al.* [155,156], where different types of expander, such as turbines (radial, impulse, reaction) and volumetric expander (screw, piston, Wankel) were compared for small power generation, screw and Wankel expander have been shown to be the most promising technologies among the others. Other theoretical and experimental studies confirm this the observation of *Badr et al*. [155,156]. For example, the works of *Kane* [157], *Lemort et al.*[158,175], *Quolin et al.* [159,176,177] and *Singh et al.* [160] showed that in the range of small power, scroll and screw expanders present interesting values of the isentropic expansion efficiency, up to 70%.

The analysis of the scientific literature reveals that there is a noticeable lack in the number of experimental studies on small scale ORC systems. The work *Orosz et al.* [139] reports the test results of the experiments carried out on a demonstration plant sited in the district of Berea in Lesotho. This system used linear parabolic concentrators with an opening area of 75 m^2 coupled with a 3 kW_{el} regenerative ORC system that used R245fa as OWF. The HTF in the solar circuit was ethylene glycol and a thermal storage system with quartzite elements (2 m^3) was used in order to make the plant more stable. A modified scroll compressor is used as an expander. The electrical conversion efficiency of the entire system resulted equal to 6% at a maximum temperature of 150 °C of the HTF. This system can operate in cogeneration mode providing

500 L/day of hot water. *Quolin et al*. [176] investigated the use of four different organic fluid (R134a, R245fa, Solkatherm® and n-pentane) in the experimental plant presented by *Orosz et al.* [139] by varying the vaporization temperature between 85 °C and 189 °C according to the type of fluid used. A thermal efficiency between 3.6% and 7% depending on the operative conditions. Another study of a small scale ORC solar system based on the use of scroll expanders was presented by *Saitoh et al.* [178]. The ORC system with R113 was powered by a solar CPC capable of heating water up to 140 °C. To ensure stable conditions of the system, a steam storage was present. From the results of the experiment performed in the laboratory, the overall conversion efficiency was 7% with an electrical output of 450 W. The conversion efficiency increases to 42% if the cooling water in the condenser was provided to a thermal user.

Wang et al. [179] proposed and implemented a low-temperature ORC Solar System for direct vaporization of R245fa using flat solar collect-mounted (12 m^2) or evacuated tube collector (10 m^2). The partially vaporized fluid inside the solar collector was collected in a reservoir that even the pressure to a value between 6 and 9 bar depending on the available solar radiation and the type of collector. The ORC system employs a Wankel volumetric expander capable of delivering a mechanical power of 1.64 kW with an average efficiency up to 45.2%. The authors concluded that due to the greater thermal inertia characterizing the evacuated tube collector, this collector was more efficient and guaranteed more stable operating conditions of the system. The average efficiency of the with the evacuated tube collector was 4.5%, whereas it is reduced to 3.2% when the flat collector was used. The difference in conversion efficiency was addresses to the lower conversion efficiency of the collector (71% vs. 55%) and the lower temperatures achieved by the operating fluid. In a subsequent work, *Wang et al*. [180] evaluated the possible application of a 1.2 m^2 flat collector for the direct vaporization of R245fa at a maximum temperature below 100 °C. Under the assumption that the expander worked with an isentropic efficiency of 80%, the maximum calculated conversion efficiency of the solar energy in the mechanical energy resulted equal to 3%. In the experimental study of *Wang et al.* [181], tests were conducted on the direct vaporization of low-temperature R245fa in a 0.6 m^2 flat solar collector combined with regenerative ORC system. This study has shown that the use of an internal regenerator in the ORC system does not give any performance improvement at a

constant flow rate. However, significant improvements have been observed with a variable flow rate, due to the possibility of limiting the superheating of the fluid entering the expander. Moreover, the variable flow rate improves the performance of the solar collector by reducing the volume of the vapor fraction inside the collector. The experimental results highlighted the importance of optimizing the mass flow rate setting, with an overall conversion efficiency of 2.42% and 0.84% with a variable and constant flow rate, respectively

More recently, *Helvaci et al.* [182] presented a solar-powered ORC system where the fluid HFE7000 was vaporized and superheated directly into a flat collector and subsequently sent to a rotary vane expander. In the ORC circuit, in addition to a water-cooled plate condenser, there were a regenerative heat exchanger and a circulation pump. The study included first and second principle analysis to evaluate the performance of the system. The collector was capable to transfer 3564 W to the working fluid with a thermal output of over 57%. The maximum fluid temperature reached was 45 °C. The mechanical power produced at the expander was 147W ($136W_{el}$) with an isentropic efficiency of 59%. Under these conditions, the thermal efficiency of the system was slightly lower than 4%. The exergetic analysis showed that the highest exergy destruction occurs in the solar collector (431 W) followed by expander (95 W), a condenser (32 W) and pump (4 W). The exergetic efficiency was 17.8% (reference ambient temperature of 15 °C). Finally, the authors suggested that increasing the pressure and the superheating of the fluid entering the expander can lead to improved performance.

Delgado-Torres et al. [169,183] published a series of theoretical works by investigating various possible configurations for a 100 kW solar-powerd ORC system with internal regeneration to be destined for a desalination system. The authors looked at the possibility of direct and indirectly vaporizing different fluids through two models of linear parabolic concentrators [169] and fixed solar collectors [183]. The results indicated that the most suited fluid for high-temperature, high concentration ratio solar collectors (e.g. PTC or LFR), was toulene whereas isobutane, isopentane, R245ca and R245fa should be used in the range of medium temperature. According to their analysis, overall efficiencies of 5% can be achieved with flat plate collector and around 8% with ETC or CPC. A further publication of *Delgado-Torres et al.* [184] contains the recommendations for the implementation of solar-powered ORC systems for desalination processes through reverse osmosis. Concentration solar collectors were preferred to flat

collector for the higher efficiencies in converting solar energy and the higher outlet temperatures. This choice is particularly indicated in the case of indirect coupling between solar and ORC systems, where the efficiency resulted more penalized when the maximum temperature is decreased as compared to the direct vaporisation configuration. Finally, in this publication, the authors emphasize that there is a lack of experimental evidence for the validation of models of direct vaporization in the concentrating system.

It has to be mentioned that hybrid ORC, where the heat is supplied alternatively from the solar collector or another external heat source offers could represent a cheaper alternative to the adoption of a thermal storage in solar-powered ORC to ensure the continuity of generation even in the absence of solar radiation. As an example, a small hybrid experimental system for the cogeneration of domestic hot water and electricity through ORC was studied by *Kane et al.* [157]. In this experimental apparatus, it is possible to integrate the thermal output of a solar system, consisting of linear Fresnel reflectors (aperture area of 100 m^2) with an evacuated tube absorber, using a diesel engine with a nominal power of 15 kW_{el}. Pressurized water was adopted as HTF. The solar circuit and the Diesel engine have been alternatively coupled to a cascade ORC system: in the top cycle (5 kW_{el}) circulates R123 with a maximum temperature between 120 °C and 150 °C, while the bottom cycle (8 kW_{el}) operates in cascade to the previous one with R134a. In this experimental study, hermetic scroll compressors have been modified to be used as expanders.

4.2 Modelling of a small size ORC for low-grade heat sources

A new numerical steady-state model is developed for a small size ORC system powered by a low-temperature (<120°C) water flow. The system configuration and the installed components are inspired by the design of a commercially available machine which constitutes a valid example of the current state-of-art in the design of ORC system for distributed generation from low- to medium-temperature heat sources [165].

The modelled system adopts brazed plate heat exchangers as pre-heater/evaporator and condenser. The OWF is circulated by a multi-stage pump that is composed of a motor and a stack of impellers that force the working fluid in a given direction. The feed pump is driven by a variable frequency drive. The model is aimed to evaluate the performance of small size ORCs with a maximum electrical power output less than 10 kW_{el}, hence the choice of expander technology must be restricted to volumetric devices. A twin-screw machine is chosen as expander which could be a compressor working in reverse mode. As seen in the previous Paragraph, twin-screw expander offers distinct advantages for small scale ORCs. The advantages include a simple and compact design, low-speed operation with the ability to run in a "wet" condition meaning that the refrigerant does not have to be completely vaporized to handle heat input variations and significant part load capability. It is assumed that the expander is directly coupled with an induction electric generator (asynchronous brushless construction), thus, a gearbox is not necessary. The small size of the ORC system requires to adopt simple configurations in order to maintain low initial investment, hence the use of an internal regenerator has not been considered. The potential benefits of the conversion efficiency of adopting a regenerative heat transfer are in fact quite modest in the case that R1233zd (E) is used as OWF due to its quasi-isentropic upper saturation curve. Furthermore, in the case that the heat is supplied through a solar collector, the absence of a regenerative exchanger leads to a lower inlet temperature of the fluid in the collector and to a higher efficiency in the conversion of the solar collectors as a consequence.

The block diagram of the ORC system considered in the model is shown in Figure 69. As with traditional water vapor Rankine cycles, it involves the pressurization (1 - 2) of the fluid in liquid phase through the use of a pump; subsequently, the pressurized fluid enters the

evaporator in subcooled liquid state (state 2) where it is heated up to the saturation condition (2 - 3) and evaporated inside the heat exchanger (3 - 3′) by the heat provided by the external source. At this stage, the vapor may be subject to a slight superheating (3′ - 3″). From the evaporator, the vapor is sent to an expander connected to an electric generator (3″ - 4). The expansion of the OWF provides the drive torque that allows the rotation of the shaft of the generator, resulting in the generation of electrical power at its external terminals. When an OWF with a quasi-isentropic upper saturation curve or with a positive slope is used, the low-pressure vapor after the expansion process can be found in a superheated conditions. This ensures the absence a liquid phase in the fluid at the end of the expansion process, without the need of a superheating in the evaporator. The fluid exiting the expander before being directed back to the pump is cooled (4 - 4′) and condensed (4′ - 1) into the second heat exchanger (condenser) connected to the external heat sink, which can typically be the ambient air or a cooling water stream when available. In the latter case, if the outlet temperature reached by the cooling water is high enough, the extracted heat from the condenser can be delivered to a possible thermal user.

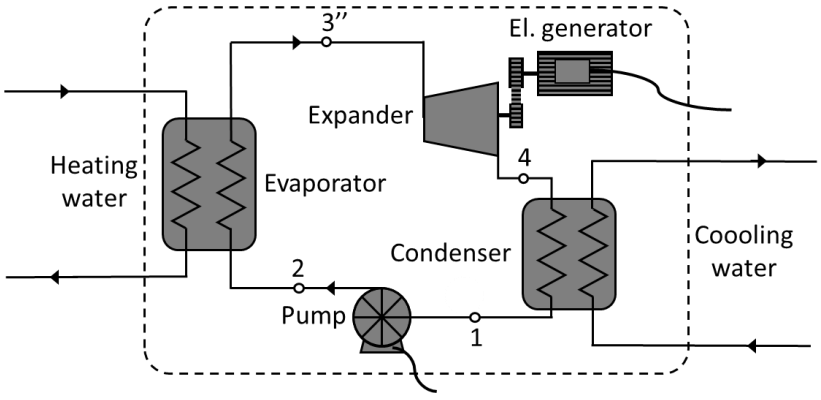

Figure 69 – Schematic of the typical configuration of an ORC system.

An example of the resulting thermodynamic transformations of the organic working fluid (in the case R245fa) in the model ORC system is depicted in in the isentropic diagram of Figure 70. For modelling the ORC cycle, the thermodynamic properties of heating and cooling water, as well as the properties of the OWF, are calculated using the properties implemented in the Refprop 9.0 database [109].

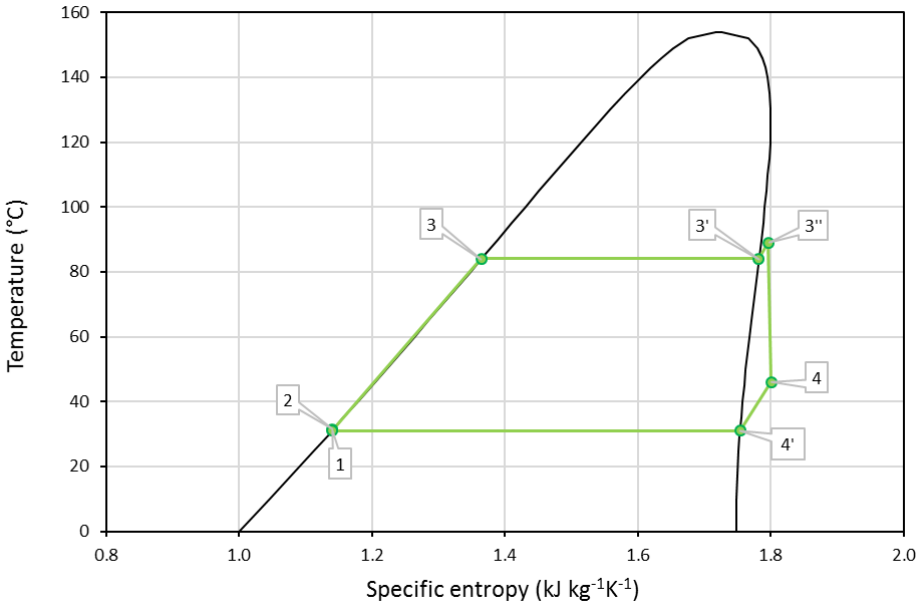

Figure 70 – Examples of the typical thermodynamic transformations involved for the OWF (R245fa) in the model of the ORC represented in the isentropic diagram.

Several assumptions have been made for simplified the model of the ORC system. All the components are modelled to work in stationary steady-state condition and are assumed adiabatic to the surrounding. Pressure losses occurring in the heat exchanger are neglected as well as in the pipes between the components of the ORC system. Therefore, the preheating, evaporation, cooling and condensation are considered isobaric processes. In the literature, this assumption is widely adopted in validated models of ORC, refrigerating and air conditioning systems working with mass flow rates and thermophysical properties of the HFC fluids similar to those considered in this model. Therefore, it is reasonable to consider contained pressure losses. In the model, the mass flow rate of the OWF is regulated in order to maintain a constant superheating at the outlet of the evaporator equal to 5 °C, independently from the operating conditions of the system. Superheating of the fluid does not imply any substantial increment in the conversion efficiency when fluids with dry or isentropic expansion are used [185]. This is particularly true in the absence of regenerative exchangers [186]. Moreover, the superheating involves heat transfer processes occurring with a fluid in the vapor phase, which is associated to lower heat transfer coefficients, higher volumetric flow rates (due to low density) and therefore higher pressure drops. However, superheating may facilitate to establish stable

working conditions and therefore it can be used as flow control parameter. Furthermore, it can prevent the unwanted presence of liquid drops in the suction section of the expander caused by evaporation temperature fluctuations that may occur during dynamic working conditions [134]. The fluid leaving the condenser is assumed in a saturated liquid state.

During the simulation, the evaporation and the condensation temperatures are not imposed as independent variables, but are the result of an iterative process that, starting with a first attempt solution, brings the system to the convergence until the following energy balances in the heat exchangers are satisfied:

$$\dot{m}_{OWF}\Delta i_{OWF} = \dot{m}_w c_{p,w}\,\Delta T_w \qquad \textit{Eq. 4.1}$$

$$\dot{m}_{OWF}\Delta i_{OWF} = K_{HE}A_{HE}\,\Delta T_{m,log} \qquad \textit{Eq. 4.2}$$

where the $\dot{m}_{OWF}$ and $\dot{m}_w$ are the mass flow rates of the OWF and water, respectively, Δi_{OWF} is the enthalpy difference between inlet and outlet conditions of the OWF, ΔT_w is the temperature difference and c_{pw} is the specific heat at the mean temperature between inlet and outlet conditions of the water flow in the heat exchanger characterize by a global heat transfer coefficient K_{HE} referred to the heat transfer area A_{HE}. The term $\Delta T_{m,log}$ in Eq. 4.2 refers to the logarithmic mean temperature difference used to determine the temperature driving force for heat transfer in the heat exchangers. The $\Delta T_{m,log}$ is computed as the logarithmic average of the temperature difference between the hot and cold feeds at each end of the exchanger:

$$\Delta T_{m,log} = \frac{(\Delta T_1 - \Delta T_2)}{log\left(\frac{\Delta T_1}{\Delta T_2}\right)} \qquad \textit{Eq. 4.3}$$

In order to reach the convergence for any considered operating conditions, it is necessary to adopt a subdivision of the total area of the evaporator, in preheating and evaporation section, and of the condenser, in cooling and condensation section, that can vary from iteration to iteration accordingly to the previous relationship; the converge is guaranteed by the adoption of a bisection algorithm applied to the heat transfer area.

In addition to the isentropic pump efficiency, the superheating, the nominal built-in volumetric expansion ratio, the evaporator and condenser geometries and the electromechanical efficiency, an additional input to the model, is the control map of the mass flow rate OWF as function of the heat source conditions, that are the inlet volumetric flow rate and temperature of the hot

water. It has been assumed that the OWF flow rate increases linearly with the inlet hot water flow rate and its temperature.

Through the developed model, an exergetic analysis of the ORC system can be carried out, which provides indications of the performance of the system and of each individual component adopted according to the second principle of the thermodynamics. The exergetic analysis may be in fact a more appropriate mean for the assessment of the efficiency of small ORC systems working with low-grade heat source with respect to the limits imposed by the Carnot's efficiency. Furthermore, the exergetic losses and the fraction of exergy destruction compared with respect to the global exergetic inefficiency of the ORC system can be computed for each component. Quantifying the inefficiencies of the processes taking place in the system components is useful to understand which components present the higher potential to increase the overall efficiency of the system through some modifications.

The model is implemented in Matlab® and is formed by four interconnected blocks representing the four components (pump, evaporator, expander-generator and condenser). of the system. The outputs of the model are the net electrical power generated by the ORC system, the thermal profiles of the OWF and the hot and cooling water streams, the thermal and exergetic performance of the system and of each involved component.

4.2.1 Model description

The evaporator and the condenser are copper-brazed corrugated stainless steel plate exchangers whose geometric parameters, such as such as thicknesses, distance and size of the plates and corrugation geometry, are typical of commercial models available on the market. The two fluids (water and OWF) are assumed to be in counterflow. From a modelling point of view, both exchangers are divided into two distinct sections, for the liquid heating, vapor cooling and the heat transfer processes during phase change (evaporation and condensation). Since the heat transfer processes are regulated by very different mechanisms, different correlations for the preheating and evaporation phases, and for the cooling and condensing phases are considered.

In the first section of the evaporator, where the heating of the pressurized OWF until its saturation condition is reached, both hot water and OWF evolve in single-phase regime. The

heat transfer coefficient of the OWF in this first section is calculated with the correlation of *Martin* [187], whose formulation to obtain the number of Nusselt *Nu* is reported below:

$$Nu = 0.122\ Pr^{1/3} \left(\frac{\mu_{fluid}(T_{fluid})}{\mu_{fluid}(T_{wall})} \right)^{1/6} \left(\psi\ Re^2\ sin^2(2\ \varphi) \right)^{0.374} \qquad \textit{Eq. 4.4}$$

where $\mu_{fluid(T_{fluid})}$ and $\mu_{fluid(T_{wall})}$ represent respectively the fluid viscosities evaluated at the bulk fluid and wall temperatures, ψ is the friction factor evaluated according to *Martin* [187] and φ is the inclination angle of corrugation on the plate. The properties of the fluids are calculated at the corresponding mean temperature in the heating section of the evaporator. By defining the number of Nusselt it is possible to calculate the convective heat transfer coefficient by approximating the hydraulic diameter by two times the width of the passage channel between the plates.

In the second section of the evaporator, where the OWF is vaporized and superheated by cooling the hot water stream, the heat transfer coefficient describing the heat transfer processes of the OWF is evaluated with the correlations of *Amalfi et al*. [188,189] depending on the number of Boiling number *Bd*:

$$Nu = \begin{cases} 982\ \varphi^{*1.101} We^{0.315} Bo^{0.320}\ \rho^{*-0.224} & Bd < 4 \\ 18.495\ \varphi^{*0.248}\ Re_{OWF,G}^{0.135}\ Re_{OWF,L}^{0.351}\ Bd^{0.235} Bo^{0.198}\ \rho^{*-0.223} & Bd \geq 4 \end{cases} \qquad \textit{Eq. 4.5}$$

In previous equations, φ^* is the ratio between the value of the actual corrugation angle of the plate and the maximum admissible value of 70° ("Chevron angle reduced" in [188,189]), *We* is the homogeneous Weber number, ρ^* is the density ratio between liquid and vapor phase and $Re_{OWF,G}$ and $Re_{OWF,L}$ are respectively the Reynolds numbers calculated in the case of vapor and liquid only flow, finally, *Bo* is the number of Bonds. The thermophysical properties of the OWF are calculated at the saturation temperature associated with the evaporating pressure and for a vapor quality equal to 0.5.

As the OWF heating liquid section, also in the evaporation/superheating section, the hot water flows in a single-phase cooling and Martin's correlation can be used to compute the water side heat transfer coefficient. Once the conditions of the OWF exiting the evaporator are evaluated, also the inlet expander conditions are known due to the assumption of isobar and adiabatic flow of the OWF in the connection pipes between the components of the ORC system.

In the model of the condenser model, the cooling process of the superheated vapor down to its saturation temperature and the following condensation of the saturated vapor is modelled separately. The cooling water undergoes a heating process without phase change through its entire flow across the condenser, hence the correlation of *Martin* [187] can be used to calculate the convective heat transfer coefficient. Assuming that the wall temperature of the plate surface in contact with the OWF is always lower than the saturation temperature, the superheated vapor starts to condense already in the first sections of the condenser, where, simultaneously, its cooling down to the saturation temperature occurs. The process of vapor cooling is therefore not completely separate from the process of condensation. Hence, it is possible to define a single heat transfer coefficient, which accounts for both cooling and condensation processes, through the correlations proposed by *Longo et al.* [190]. In their formulation, it is assumed that gravity forces are dominant over the forces of inertia for the values of equivalent Reynolds number Re_{eq} lower than 1600. Under these conditions, the authors adapted the original Nusselt expression valid for gravity controlled laminar film condensation on vertical smooth surface, to estimate the average heat transfer coefficient $h_{cond,sat}$ referred to the projected area of the corrugated plate:

$$h_{cond,sat} = \phi \left(0.943 \left(\frac{k_{OWF,L}^3 \ \rho_{OWF,L}^2 \ g \ i_{LV}}{\mu_{OWFL} \ \Delta T \ L_{cond}} \right)^{1/4} \right) \qquad \textit{Eq. 4.6}$$

where, ϕ is an enlargement factor (equal to the ratio between the actual area and the projected area of the plates) and k_L, ρ_L, and μ_L are the thermal conductivity, the density and the dynamic viscosity of condensate OWF, i_{LV} is the specific enthalpy of condensation, g is the gravity acceleration, ΔT is the difference between saturation and wall temperature and L_{cond} is the vertical length of the surface.

When the condensation occurs in forced convection conditions (equivalent Reynolds number Re_{eq} greater than 1600), the average heat transfer coefficient $h_{cond,sat}$ referred to the projected area of the corrugated plate is given by the following correlation [190]:

$$h_{cond,sat} = \phi \left(1.875 \left(\frac{k_{OWF,L}}{d_{h,eq}} \right) {Re_{eq}}^{0.445} \ {Pr_{OWF,L}}^{1/3} \right) \qquad \textit{Eq. 4.7}$$

In the model by *Longo et al.* [190], the previous correlations (Eq. 4.6 and Eq. 4.7) are coupled to the model developed by *Webb* [191] to account for the simultaneous transfer of sensible and latent heat in the forced convection condensation process:

$$h_{cond,sh} = h_{cond,sat} + F_{Longo}\, h_{conv,sh} = h_{cond,sat} + \left(\frac{T_{sh} - T_{sat}}{T_{wall} - T_{sat}}\right)\left(h_{conv,sh} + c_{p,OWF,G}\frac{\dot{q}_{lat}}{i_{LV}}\right) \quad \textit{Eq. 4.8}$$

where $h_{conv,sh}$ is the single-phase convective heat transfer coefficient for outflow between superheated vapor and the condensate interface, $c_{p,OWF,G}$ is the specific heat of the superheated vapor and q_{lat} is the heat flux due only to phase change. The properties of the condensing OWF are calculated at the saturation temperature and for an average vapor quality between inlet and outlet which corresponds to a value of 0.5.

For both heat transfer processes in the evaporator and condenser, the conduction through the plate has been neglected. In fact, the conductive thermal resistance of the plate results much lower than the thermal resistance on the water and the organic fluid side of the heat exchanger. Moreover, it is assumed the absence of fouling on the plate surfaces. Hence, the global heat transfer coefficient of this components is computed by the equation (Eq. 4.9), where the h_w and h_{OWF} are the heat transfer coefficients for water and OWF, respectively

$$K_{HE} = \left(\frac{1}{h_w} + \frac{1}{h_{OWF}}\right)^{-1} \quad \textit{Eq. 4.9}$$

The expander implemented in the model is a screw expander, despite the fact that the machines currently available in the market work with electrical output between 20 kW_{el} and 1 MW_{el} and mass flow rate ranging from 25 L s^{-1} and 1100 L s^{-1}, which are higher than those considered here. Nevertheless, this choice is justified by the fact that this technology shows a higher technological maturity level than large scroll expanders that should be better suited for the considered application [152]. Furthermore, as highlighted in the previous Paragraph, screw expanders offer a greater operational flexibility to partial load that allows them to operate without significant penalty in terms of efficiency in a wide range of temperature and flow rate supplied by the hot water source. In addition, screw expanders present higher volumetric built-in ratios r_v than those available for scroll expanders which allow them to be suited for

applications presenting higher pressure difference, such the one considered here. In this way, it is possible to operate with high single-stage expansion efficiency even in the presence of significant pressure ratio. Therefore, it is acceptable to consider that the current expansion efficiency of screw machines may be a reference also for other competing technologies. Albeit at the diminishing the size of screw devices, the expansion process is affected by higher leakage and consequently, it is necessary to increase the rotational speeds or adopt lubricating oil mixed with the working fluid. However, in the future, thanks to technological advances, above all, the decrease in the characteristic tolerances in the production of the screws, it is likely that screw devices expand their applicability range even to smaller sizes, becoming the reference technology.

The lack of experimental data in literature, where only the minority regards screw machines designed for expansion purposes, the strong variability of the analysed devices, the strong dependencies of the efficiency from the size of the device, the processed working fluid and thermodynamic parameters considered, constitute limits to the formulation of general semi-empirical correlation for the predict of the performance of screw expander. One of the few semi-empirical models of the screw expander was developed by *Ng et al.* [192,193] and it was recently implemented in the work of *Bamgbopa and Uzgoren* [194] on a quasi-dynamic model for a small ORC similar to the one considered in this work. This model considers that the expansion of the superheated vapor superheated deviates from the ideal isentropic process due to mismatch of the pressure of the exhaust fluid and the backpressure of the condenser, which causes unwanted blowdown or blowback effects. The empirical model of *Ng et al.* [193] is very dated (1988) and does not consider the significant technological improvements obtained for the screw expander; therefore, its predictions of the expansion performance, gives limited isentropic efficiency, surely smaller than what can be achieved today in the machines available on the market. The model of *Ng et al.* is, however, one of the few semi-empirical models of screw expander available in literature that does not require a detailed knowledge of geometry of the expander (dimensions, tolerances, and other specific geometry of the machine) for which usually no information is available, but it is based on a limited number of physically meaningful parameters of the expansion process. For this reason, this semi-empirical formulation was adopted to model the screw expander in the ORC system considered here. In their work, *Ng et*

al. [193] consider that the phenomena of blowdown or blowback affecting the expansion process, deviate the isentropic expansion to a process called "pseudo-polytrophic" characterized by an expansion index k_{pp} evaluated according to the built-in volumetric ratio and of pressure ratio of the expansion given by the following expression:

$$k_{pp} = \frac{{r_v}^{(1-n)} - n}{1 - n} \qquad \textit{Eq. 4.10}$$

where n_{pp} is the pseudo-polytrophic expansion index and is calculated accordingly to the following correlation:

$$n_{pp} = \left(a_1 \frac{1}{\log(r_v)} + a_1 \frac{1}{\log(r_v)^2} + a_3 \frac{1}{\log(r_v)^3} \right) \log r_p \qquad \textit{Eq. 4.11}$$

This model allows considering the major losses involved in the expansion process (non-adiabatic process, leakage, fluid dynamic attrition, and local pressure losses in the suction and discharge). The terms a_1, a_2 and a_3 are empirical values defined by *Ng et al.* [192] on the basis of experimental tests performed on a device (compressor) produced by Mycom [195]. This correlation originates from the comparison of the expansion power obtained from experimental tests with the values that could be obtained by performing an ideal isentropic expansion under the same condition of the test. For this reason, the overall isentropic efficiency calculated according to this model includes also the volumetric performance of the machine.

According to the proposed correlation, the specific work W_{exp} of the pseudo-polytrophic process is to be a function of the values of p_{exp} and density in the suction conditions, of the nominal built-in volumetric ratio r_v and the pressure ratio r_p available between evaporating and condensing conditions, as well as of the index k previously defined in Eq. 4.10.

$$W_{exp} = \frac{p_{exp,suc}}{\rho_{exp,suc}} \left(k_{pp} - \frac{r_v}{r_p} \right) \qquad \textit{Eq. 4.12}$$

Figure 71 shows the overall isentropic efficiency of the expander as a function of the pressure ratio for different values of the built-in volumetric ratio. These results were reported directly from a subsequent publication of *Ng et al.* [192].

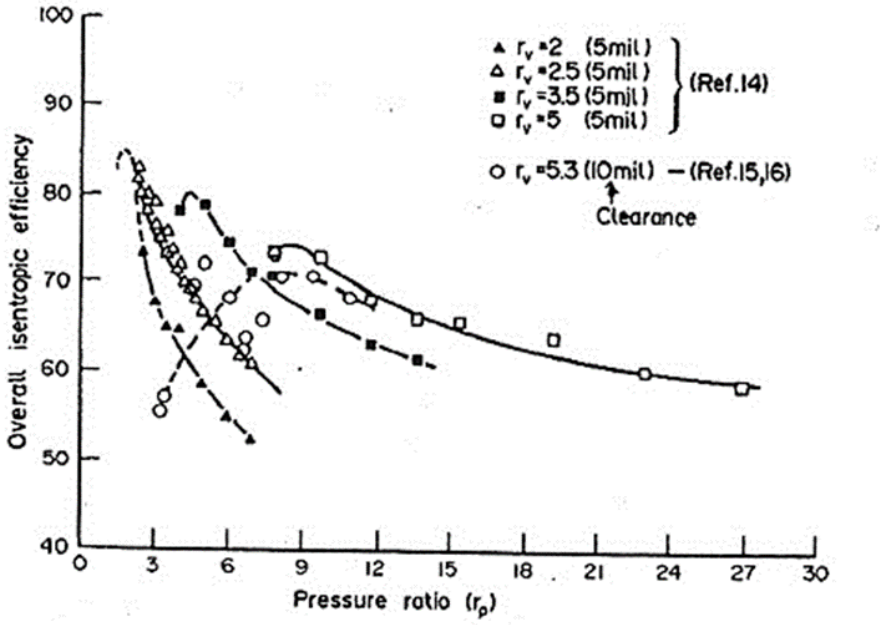

Figure 71 – Overall isentropic efficiency of a screw expander as a function of the pressure ratio for different values of the built-in volumetric ratio according to the model of Ng et al. [192].

The electrical machine for electrical power production connected to the expander considered in the model is an induction generator. This machine differs from synchronous generators or alternators which have standalone terminal voltage when they rotate and require synchronization before being placed on-grid. An induction generator is asynchronous in operation and does not require synchronization to the electrical power grid. Voltage regulation and frequency regulation are provided from the existing connection to the power grid. Because induction generators are not self-excited and have no magnetization or terminal voltage prior to coming on-grid, synchronization is rendered meaningless. Electrical and mechanical transmission efficiency of the expansion-generation block are combined in one single parameter assumed equal to 0.9.

The model of the pump is simplified by assuming a constant value of the electrical and isentropic efficiencies of independently from the operating conditions. In the literature, this assumption is often adopted [196,197]. The evaluation of the electrical pumping consumption is based the pressure drop through the circuit:

$$P_{p,ORC} = \dot{m}_{ORV} \frac{\Delta p_{tot}}{\rho_{ORV}} \frac{1}{\eta_{is,p}\eta_{el}} \qquad \textit{Eq. 4.13}$$

Typical values for the isentropic efficiency of the pump are comprised between 0.6 and 0.8 Although this assumption is not always reasonable from a physical point of view, it should be noted that the energy consumption occurring in the pumping phase is far smaller than the energy converted in the expansion process. Therefore, assuming a constant isentropic efficiency of the pump does not affect significantly the overall system performance, nor in terms of generated net electrical power, or conversion efficiency.

The most common parameter to qualify the conversion performance of an ORC system is the conversion efficiency. This parameter is defined as the ratio between the heat flow rate provided by the heat source q_{in} and the net electrical power output P_{el} of the ORC system.

$$\eta_{ORC} = \frac{P_{el}}{q_{in}} \qquad \textit{Eq. 4.14}$$

The exergetic efficiencies of the different components and the associated destruction of exergy as well as the exergetic irreversibility percentage with respect to global loss of exergy of the system can be computed by the model. The exergetic efficiency η_{ex} of each component can be calculated according to the definition of Eq. 4.15 where the definition of the Fuel (input) exergetic flux $\dot{E}_F$ and the Product (useful output) exergetic flux $\dot{E}_P$ depend on the processes involved in the considered component:

$$\eta_{ex} = \frac{\dot{E}_P}{\dot{E}_F} \qquad \textit{Eq. 4.15}$$

Once the Fuel exergetic flux $\dot{E}_F$ and the Product exergetic flux $\dot{E}_P$ are identified, the exergetic irreversibility in term of the destruction of exergy flux $\dot{E}_D$ that occurs in each component can be evaluated by the Eq. 4.16:

$$\dot{E}_D = \dot{E}_F - \dot{E}_P = \dot{E}_P(1 - \eta_{ex}) \qquad \textit{Eq. 4.16}$$

By adding all the destructions of exergy flux occurring in the components of the system, it is possible to obtain total irreversibility term of the system and calculate the percentage of total exergy destruction that occurs in each component.

The exergetic efficiency of the evaporator, the condenser, the expander, the electrical generator and the pump were calculated respectively with the equation from Eq. 4.17 to Eq. 4.21:

$$\eta_{ex,ev} = \frac{\dot{m}_{OWF}(e_{3''} - e_2)}{\dot{m}_{w,h}(e_{w,h,in} - e_{w,h,out})} \quad \textit{Eq. 4.17}$$

$$\eta_{ex,cond} = \frac{\dot{m}_{w,c}(e_{w,c,out} - e_{w,c,in})}{\dot{m}_{OWF}(e_4 - e_1)} \quad \textit{Eq. 4.18}$$

$$\eta_{ex,exp} = \frac{\dot{m}_{OWF}(e_{3''} - e_4)}{\dot{m}_{OWF}(e_{3''} - e_{4,is})} \quad \textit{Eq. 4.19}$$

$$\eta_{ex,gen} = \frac{P_{el}}{\dot{m}_{OWF}(e_{3''} - e_4)} \quad \textit{Eq. 4.20}$$

$$\eta_{ex,pump} = \frac{\dot{m}_{OWF}(e_2 - e_1)}{\dot{m}_{OWF}(e_{2,is} - e_1)} \quad \textit{Eq. 4.21}$$

In the previous equation, the numerical subscripts for the specific exergy *e* of the OWF are taken according to the thermodynamic state identified in Figure 70, whereas the subscripts for the hot water and cooling water refers to their inlet and outlet conditions.

In the simulation presented in Paragraph 4.3, the heat source of the ORC unit is provided by concentrating solar collectors. To evaluate the exergetic performance of a solar collector it is necessary to identify how much work can be extracted from solar radiation. The exergetic potential of thermal radiation is still a discussed subject of study. According to the theory of *Jeter* [198], the thermal conversion of the solar radiation it is considered that the reference temperature at which the solar radiation temperature available is the apparent black body surface temperature surface temperature of the Sun T_{Sun} (5777 K) and therefore the radiant exergetic flux is defined according to the following expression:

$$\dot{E}_{sol(Jeter)} = DNI\ A_{ap}\ \eta_{Jeter} = DNI\ A_{ap}\ \left(1 - \frac{T_{amb,ref}}{T_{Sun}}\right) \quad \textit{Eq. 4.22}$$

where T_{Sun} is the of the Sun, $T_{amb,ref}$ is the reference ambient temperature considered in the exergetic analysis. It can be argued, that the formulation of *Jeter* expressed the maximum work that can be extracted from a thermal device that operates between the apparent temperature of the Sun and that of the reference ambient conditions and it does not take into account the

necessary radiative absorbing process that occurs neither with a unitary absorbance nor a null emittance. At least two other different alternative approaches can be considered mainly depending on the different system considered to collect and convert the thermal radiation, The first alternative to Eq. 4.22, was presented by *Spanner* [199]:

$$\dot{E}_{sol(Spanner)} = DNI\ A_{ap}\ \eta_{Spanner} = DNI\ A_{ap}\ \left(1 - \frac{4}{3}\frac{T_{amb,ref}}{T_{Sun}}\right) \qquad \textit{Eq. 4.23}$$

and the second alternative is due to *Petela* [200]:

$$\dot{E}_{sol(Petela)} = DNI\ A_{ap}\ \eta_{Petela} = DNI\ A_{ap}\ \left(1 + \frac{1}{3}\left(\frac{T_{amb,ref}}{T_{Sun}}\right)^4 - \frac{4}{3}\frac{T_{amb,ref}}{T_{Sun}}\right) \qquad \textit{Eq. 4.24}$$

This last expression (Eq. 4.24) is obtained by assuming to match a Carnot's ideal thermal machine to an absorber surface and not directly to the Sun, as it was with Jeter's theory. It is interesting to see that by considering a T_{Sun} much higher than $T_{amb,ref}$, the second term in the parenthesis of Eq. 4.24 tends to zero and the Petela's expression coincides with one presented by Spanner. Bejan [201] provided a deep discussion on this argument. In his work, it has been shown that all these theories are correct and each occupies a well-deserved place in the theoretical domain. It is reported that what makes each theoretical result different is what is the considered "investment" made to extract work from the solar radiation and what is the appropriate state to refer the complete exploitation of the radiation.

In accordance with what *Al-Sulaiman* has already assumed in his exergetic analysis of a CSP systems [2], the approach presented by *Petela* [200] seems to be more suitable to evaluate the exergetic flux associated with the incident solar radiation on the aperture area of a concentrating collector, hence it can be computed in the model of a solar-powered ORC system.

4.2.2 Numerical model validation

The numerical model developed and described above has been used to simulate the performance of a small commercial ORC system using R245fa as OWF, the ElectraTherm® 4400+ Power Generator machine [165]. The POE oil used for lubrication is contained in the working fluid as part of ElectraTherm's proprietary in-process lubrication. Due to the low amount of oil present in the OWF, it is expected that it does not affect significantly the

thermophysical properties of the fluid and the processes occurring in the machine. Figure 72 shows the characteristic curves of this ORC unit where the generated power is plotted against the hot volumetric flow rate for different values of the inlet temperature. Curves are represented for a constant volumetric flow rate and temperature of the cooling water, respectively equal to 13.9 L s^{-1} and 21 ° C.

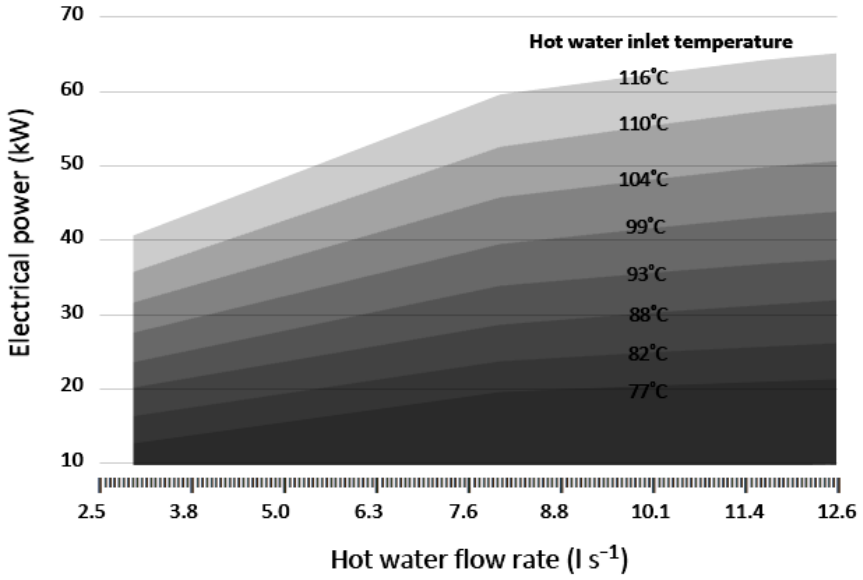

Figure 72 – Characteristic curves of the ElectraTherm® 4400+ Power Generator ORC as a function of the hot volumetric flow rate and for different values of the inlet temperature. The curves refer to a cooling water stream of 13.9 L s^{-1} at of 21°C (0% Propylene Glycol) [165].

Based on data published in the datasheet of the machine, the ElectraTherm® Power Generator 4400+ is capable to generate a variable electrical power of between 12 kW and 65 kW for an input thermal input included between 400 kW and 680 kW when it is powered by a volumetric flow rate of hot water between 3.2 L s^{-1} and 12.6 L s^{-1} at a temperature between 77 °C and 116 °C. From Figure 72, the characteristics curves of the machine are extrapolated by the adopting a polynomial interpolation with a second polynomial degree. In fact, it is reasonable to assume that there are no points of discontinuity and that those reported in the graph of Figure 72 are due to representation by means of linear functions starting from three operating points for each hot water inlet temperature. The heat exchangers inside this machine are designed to be used with water. When glycols are used with water, it is recommended that the percentage of glycol

to water does not exceed 40-50%, as the heat transfer decreases with increased percentages of glycol. The installed expansion device is a patented twin-screw expander and a multi-stage pump driven by a variable frequency drive. Since no other information about the ElectraTherm® Power Generator 4400+ unit is available, to simulate its performance, some assumption on the geometry, size and operative parameters of the modelled components have to be made.

The dimensions of the heat exchangers, in particular, their cross-sectional area of passage, are chosen so that the specific mass flow rates are below 40 kg m^{-2} s^{-1} which are typical values for systems working with halogenated fluids. The thickness of the adopted plates is 3 mm and the angle of inclination of the corrugations is 45° for both heat exchangers. The heat transfer surfaces are sized of to ensure an efficient thermal coupling between the OWF and the cooling and heating water. Once the geometry of the single plate is chosen, from the total heat transfer area of the two exchangers can be determined the respective number of plates. This value is generally adopted to reach the best compromise between reduced pressure drop and high thermal performance. The heat transfer of the evaporator adopted in the model is around 69.5 m^2 and it is composed of 147 plates with a heat transfer area of 0.42 x 1.14 m^2 each, with a typical value of the shape ratio about 2.5. The first reported dimension refers to the width of the plate while the second is the longitudinal length. The condenser consists of 162 plates with an area of 0.38 x 1.04 m^2, resulting in a total heat transfer area equal to 63.2 m^2. During the simulations, due to the specific mass flow rates imposed in the condenser, the equivalent Reynolds number Re_{eq} is always greater than 1600 and the condensation results always dominated by the inertia forces (Eq. 4.7). The value of the constant isentropic efficiency of the pump is set to 0.75. Finally, built-in volumetric ratio of the expander is set to of 3.5, which is a typical value for the available screw expander on the market [152] and implies a small size of the machine, with low its cost as consequence, maximizes the performance of the device in the mean condition of the in the simulated operational range and therefore, ensures an efficient performance of the device through the different operating condition. On the other hand, it implies that the maximum expander efficiency is not available at the highest evaporation temperature and pressure ratio r_p.

The generated electric power obtained from the simulations of this commercial ORC unit with the developed model is shown in Figure 73.

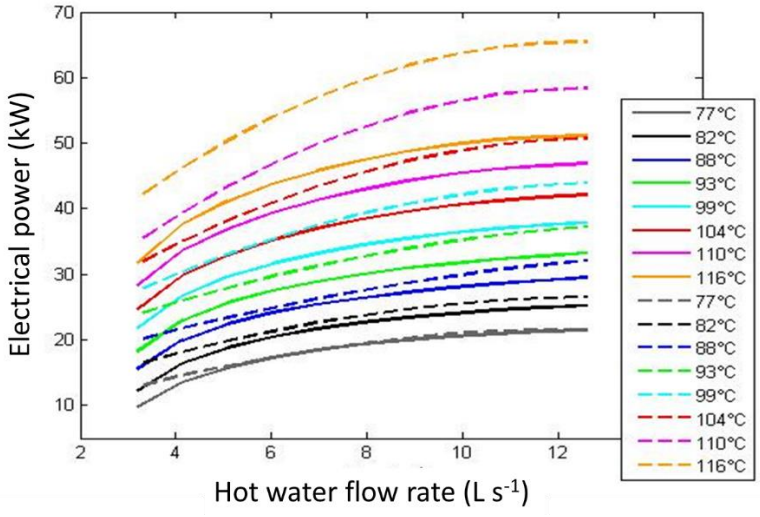

Figure 73 – Comparison between predicted (continuous line) and extrapolated (dashed line) characteristic curves for the ElectraTherm® 4400+ Power Generator [165]. *The curves refer to a cooling water stream of 13.9 L s^{-1} at of 21°C*

In this Figure, although the predicted values of the electrical power (continuous line) result lower than the curves extrapolated from the manufacturer's datasheet (dashed lines) for almost throughout the entire range of operating conditions, the simulations follow quite well the trend of the original curves. From a comparison between the predicted electrical power and the those declared by the manufacturer, the average value of the relative percentage prediction error of the model results lower than 12%. The relative error trend is very sensitive to the variation of hot water inlet temperature: the minimum relative percentage error (lower than 1%) is obtained for the minimum water temperature warm (77 °C) however the percentage error reaches its maximum, equal to 22%, for maximum hot water temperature (116 ° C) at maximum flow rate. Furthermore, it can be noted that the relative error is poorly influenced by flow rates, in fact, as the flow rate varies the relative error value variation s within 6% for each temperature value studied. A probable cause of the difference between the model prediction and actual performance of the machine can be the low expansion efficiency resulting from the application of the *Ng et al.* model which do not takes account of the technological improvement obtained. This expander model displays a particularly low nominal isentropic efficiency, between 53%

and 54% for the nominal built-in ratio. In the scientific literature, among other authors, *Lemort et al.* [152] and *Leibowitz et al.* [163] report current screw expander may present isentropic efficiency even higher than 70%. Figure 74 provides the isentropic efficiency curves obtained from the application of the *Ng et al.* model during the simulations.

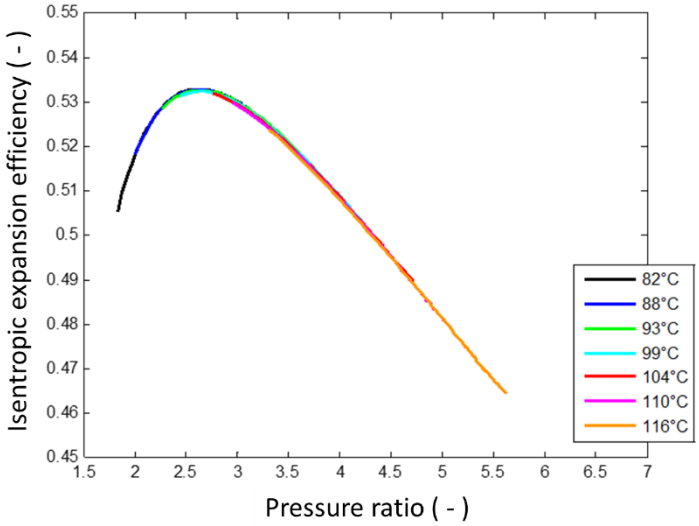

Figure 74 – Simulated isentropic efficiency of the expander as a function of the pressure ratio.

It can be observed that the efficiency increase quite rapidly for low pressure ratios r_p, reaches it maximum at the optimum pressure ratio and decreases more smoothly down to 46% for the highest pressure ratio obtained during the simulations, associated with the highest value of the evaporation temperature. The device designed by ElectraTherm® is most likely to exhibit a higher efficiency throughout the operational range than that predicted by the model; this aspect strongly affects the numerical results and constitutes the major source of discrepancy between simulated and declared performance by the manufacturer. In particular, the low value of the isentropic efficiency obtained at the maximum loads justifies the significant difference in predictions of generated electrical power (22%). Unfortunately, given the technological innovation, the manufacturer did not make any technical (e.g. built.in volumetric ratio) nor experimental (e.g. isentropic expansion efficiency curve) data available. An interesting field of research would be the recalibration of the correlation used [192] in the search for experimental constants updated to the currently available devices, or the development of a new model that reconsiders the decisive influence parameters for the performance of screw devices

(highlighted in literature by the use of CFD methods) providing an instrument of greater interest in modelling ORC systems which use screw expander. Other differences between the simulated and the characteristic curves declared by the manufacturer may derive from the assumptions made on the geometry and the fluid flow conditions in the heat exchangers or from the different logic adopted to define the control map for the flow rate of the OWF. The manufacturer does not provide any detail about this aspect. Since no information about component features adopted by the ElectraTherm® Power4400 + Power Generator unit was available or on the adopted control logic the adoption of different modelling assumption on its components would result equally arbitrary.

4.3 Simulations of solar-powered ORC systems

The numerical model of the concentrating solar collector with a bar-and-plate flat receiver, presented in Paragraph 3.4, is integrated into the developed model of the ORC system, in order to simulate the performance of small solar-powered ORC systems with an electrical output lower than 5 kW_{el}. Two configurations of the system have been considered: in the first configuration an intermediate solar circuit is used to heat pressurized water and evaporate the OWF in a separated heat exchanger (Figure 66); in the second system configuration, the OWF is vaporized directly in the concentrating solar collector field which coincides with the evaporator (Figure 68).

As seen in the Paragraph 5.1.1, the fluid R245fa has been considered by many authors the best choice for the exploitation of low-grade heat source. However, given the existence of alternative fluids that exhibit similar properties and thus similar thermodynamic performances and costs plant, the use of R1233zd(E) as OWF was preferred due to its low GWP.

In order to provide the sufficient thermal input, the solar collector field is composed of six parallel loops. Each loop presents a solar collector with the same dimensions of the asymmetrical solar collector tested during the experimental campaign but with a trough length increased to 6 m. This choice derives from the compromise between avoiding phenomena of non-uniform distribution of the flow between the loops in parallel and the containment of the pressure drop. The total aperture area of the solar collector field results equal to 105 m^2 and when it is subjected to a normal incident radiation of 1000 W m^{-2} can provide 81 kW_{th}. During the simulations, the solar input (DNI) varies between 450 W m^{-2} and 1000 W m^{-2}, which can be considered the maximum DNI available in Padua on a clear-sky day. The heat sink is provided by a cooling water flow with a constant inlet temperature of 21°C and a flow rate of 1.36 L s^{-1}.

The cross-sectional area of passage in the heat exchangers is chosen so that the specific mass flow rates are below 40 kg m^{-2} s^{-1}. The thickness of the adopted plates is 3 mm and the angle of inclination of the corrugations is 45° for both heat exchangers. The heat transfer of the evaporator adopted in the first configuration is 4.3 m^2 and it is composed of 22 plates with a

heat transfer area of 0.29 x 0.74 m^2 each. The condenser consists of 15 plates with an area of 0.45 x 1.13 m^2, resulting in a total heat transfer area equal to 6.6 m^2. These heat transfer surfaces are sized to ensure an efficient thermal coupling between the OWF and the cooling and heating water. Finally, the value of the isentropic efficiency of the pump is set to 0.75 and the built-in volumetric ratio of the expander is 3.5.

Trough this model is possible to evaluate the thermal performance of the solar collector field, the electrical output and the electrical and exergetic efficiencies of the ORC unit and of the solar-powered ORC system (ORC + solar collectors). In the exergetic analysis, the ambient reference temperature is set equal to the inlet temperature cooling water in the condenser (21 ° C) and the ambient reference pressure is equal to 1 bar.

4.3.1 Simulation results of a solar-powered ORC system with intermediate heat transfer loop

The performance of a solar-powered ORC system has been evaluated with an indirect vaporization of the OWF. During the simulations, a water stream with a design pressure of 3 bar flows in the solar circuit with a volumetric flow rate variable between 0.3 L s^{-1} and 1.25 L s^{-1} in order to obtain outlet temperature between 77 °C and 116 °C depending on the solar input. The mass flow rate of the OWF is adjusted in order to adapt the thermodynamic cycle, i.e. evaporation and condensation temperature, to the conditions of the heat source, that is the inlet temperature and mass flow rate in the evaporator. The flow of the OWF is adjusted accordingly to the control logic implemented in the code of the model, which tunes the OWF mass flow rate as a function of the hot water supply conditions (flow rate and temperature). As shown in Figure 75, in the simulations the mass flow rate of the halogenated fluid varies between 0.17 kg s^{-1} and 0.35 kg s^{-1}.

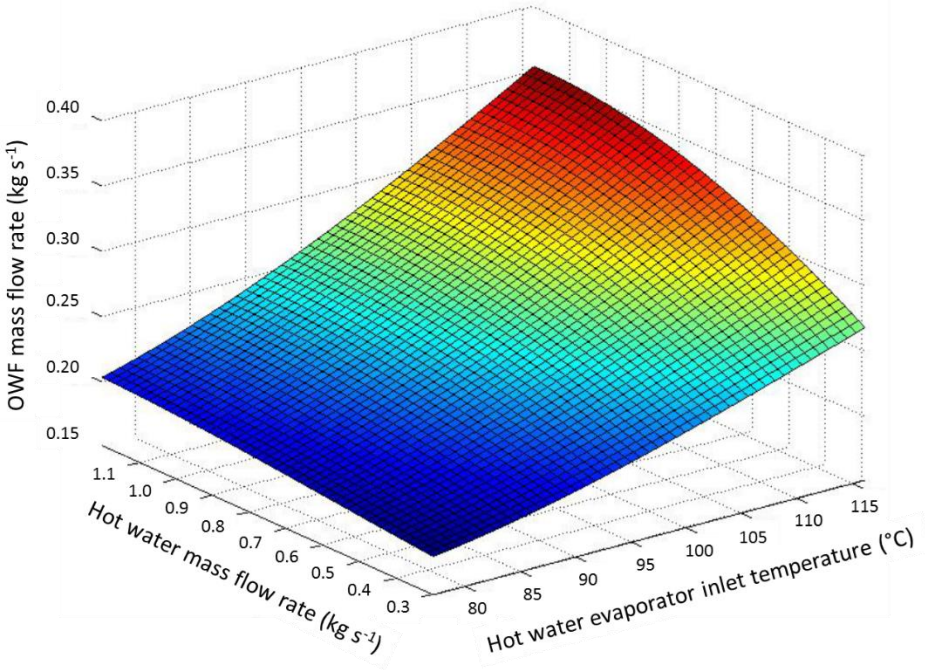

Figure 75 – OWF mass flow rate control map implemented in the model of the solar-powered ORC system with intermediate heat transfer loop.

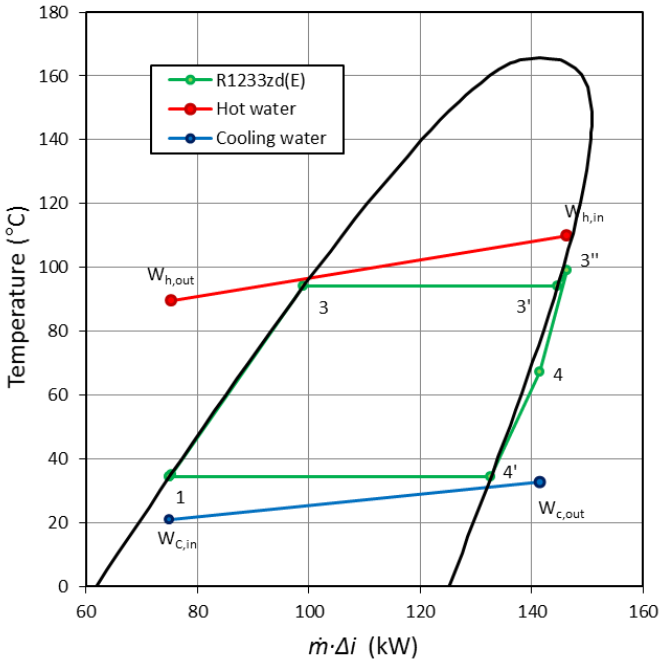

Figure 76 – Temperature profiles and heat flow rates transferred between the halogenated fluid and the water streams in the T- ṁ Δi diagram ($\dot{m}_{w,h}$ = 0.82 kg s^{-1}; $T_{w,h,in}$ = 110 °C; DNI = 882 W m^{-2}).

Once the DNI and the mass flow rate in the solar circuit are set, the thermal profiles of the three fluids involved result uniquely determined. An example ($\dot{m}_{w,h}$ = 0.82 kg s^{-1}; $T_{w,h,in}$ = 110 °C; DNI = 882 W m^{-2}) of the temperature profiles of the fluid flows in reported in the *T- ṁΔi* diagram depicted in Figure 76.

The net electrical output of the ORC unit is calculated by subtracting the electrical consumption of the pumps in the solar and ORC circuits, $P_{p,solar}$ and $P_{p,ORC}$ respectively, from the electrical power generated by the electrical generator $P_{gen,ORC}$:

$$P_{el} = P_{gen,ORC} - \left(P_{p,solar} + P_{p,ORC}\right)$$
$$= \dot{m}_{OWF}\Delta i_{exp,is}\,\eta_{is,exp}\,\eta_{el} - \left(\dot{m}_{w,h}\frac{\Delta p_{solar}}{\rho_{w,h}}\frac{1}{\eta_{is,p}\,\eta_{el}} + \dot{m}_{OWF}\Delta i_{p,is}\frac{1}{\eta_{is,p}\,\eta_{el}}\right) \qquad \textit{Eq. 4.25}$$

where $\Delta i_{exp,is}$ and $\Delta i_{p,is}$ are the enthalpy difference in the isentropic expansion and pumping processes, respectively. In Figure 77 the net electrical power output obtained from the simulation is plotted as a function of the DNI for different values of the collector outlet water temperature

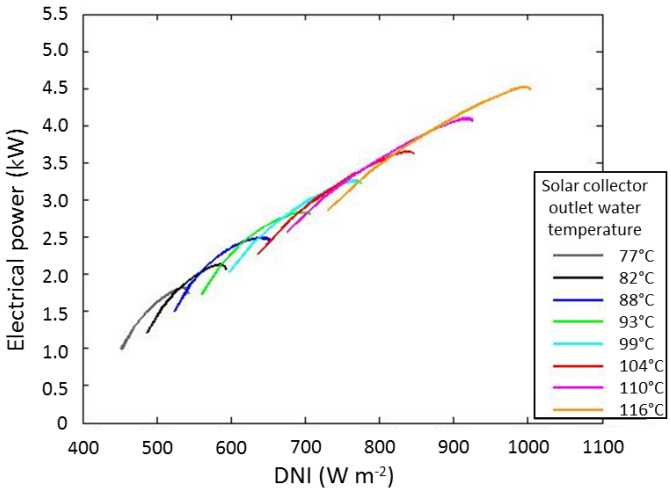

Figure 77 – Net electrical power generated by the solar-powered ORC system with intermediate heat transfer loop as a function of the DNI for different values of the collector outlet water temperature.

As the DNI increases, the mass flow rate of the water in the solar circuit is increased in order to provide a linear increment in net electrical power output. For each value of DNI, it is possible

to define the combination of mass flow rate and collector outlet temperature of the pressurized water, and therefore of the halogenated fluid, that maximize the electrical output

In Figure 78, the net electrical output power is plotted against the water mass flow rate for different values of the inlet evaporator temperature (coincident with the outlet collector temperature). In this Figure, it can be observed that the electrical power increases from 1 kW_{el} up to 4.5 kW_{el} with temperature and mass flow rate of water. Each curve refers to a different value of the inlet evaporator temperature of the water and shows an asymptotic trend. This trend is the result of the simultaneous evolution of evaporation and condensation temperatures which determine the enthalpy drop available for the expansion, influence the isentropic expansion efficiency and the pumping consumption in the solar circuit.

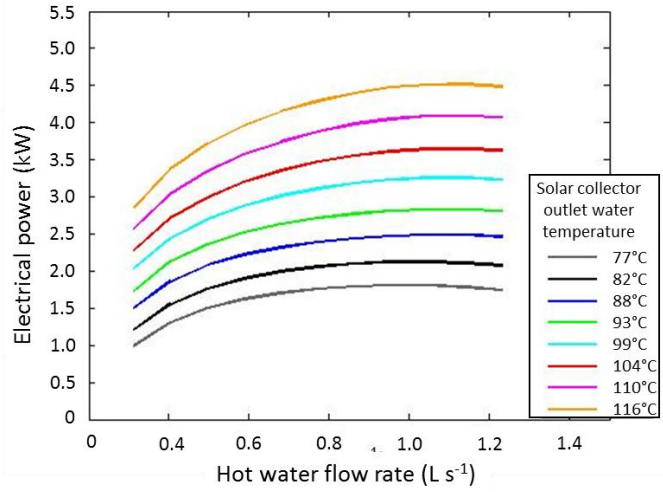

Figure 78 – Net electrical power generated by the solar-powered ORC system with intermediate heat transfer loop as a function of the volumetric mass flow rate and for different values of the collector outlet water temperature.

Since the inlet temperature and the flow rate of the cooling fluid in the simulations are constant, the variations in the OWF condensation temperature are due essentially to the variation in the mass flow rate of OWF. As shown in Figure 79 – a, the condensation temperature, increases from 29 °C to 37°C with water flow rate in the solar circuits and its outlet temperature, because of implemented control map for the OWF flow rate. Moreover, the outlet temperature of the water in the collectors leads to an increment of the heat flow rate that must be dissipated in the condenser, thus, a higher temperature decrease of the cooling water is required for the latter.

The increase of the condensation temperature, however, is modest because the higher OWF flow rate increases the heat transfer coefficients, improving the thermal coupling of the OWF and the cooling water as a consequence.

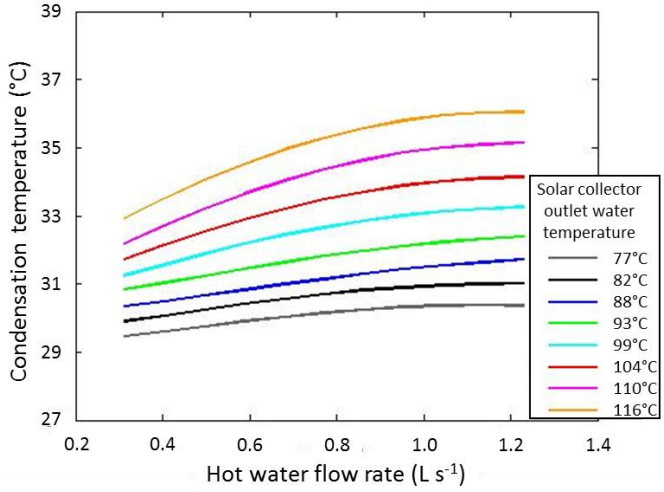

- a -

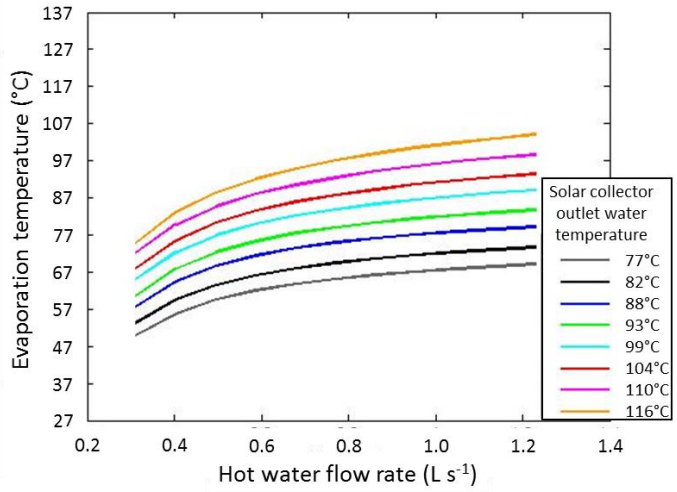

- b -

Figure 79 – OWF condensation (a) and evaporation (b) temperatures in the solar-powered ORC system with intermediate heat transfer loop as a function of the volumetric mass flow rate and for different values of the collector outlet water temperature.

The OWF evaporation temperature is strongly influenced by the temperature of the heat source and increases with it, as can be seen in Figure 79 – b. The evaporation temperature varies between 50 °C and 105 °C. Besides the influence of the hot water temperature in the evaporator,

the evaporation temperature increases with water flow rate in the solar circuits and therefore with the OWF flow rate due to the increased convective heat transfer coefficients obtained in the evaporator. At the same increase in the hot water flow rate, the evaporation temperature increase results higher than that obtained for the condensation temperature.

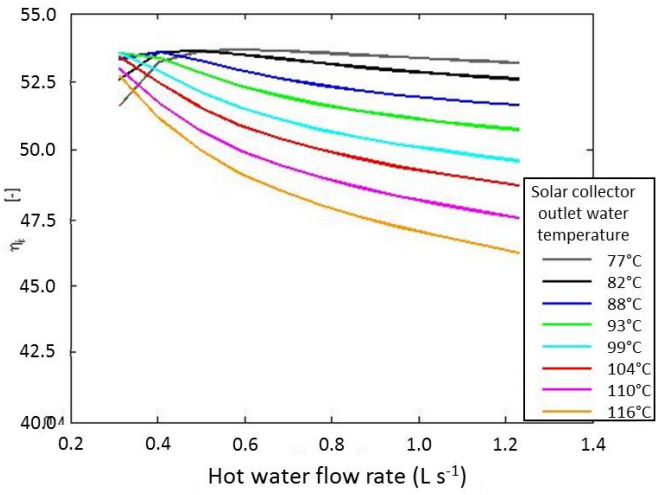

- a -

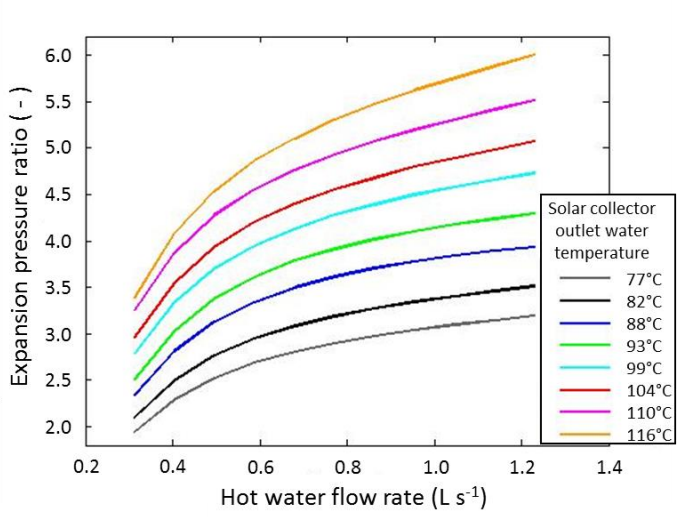

- b -

Figure 80 – Isentropic expansion efficiency (a) and pressure ratio (b) of the expander in the solar-powered ORC system with intermediate heat transfer loop as a function of the volumetric mass flow rate and for different values of the collector outlet water temperature.

If it the expander could work at constant isentropic expansion efficiency, an increase of the hot water flow rate would result in an increase of the generated electrical power. However, the

isentropic expansion efficiency given by the adopted expander model [192] displays a different trend as can be seen in Figure 80 – a. The isentropic efficiency reaches its maximum, around 54%, for different values of the water inlet temperature in the evaporator by adjusting its flow rate. In fact, due to the trends of the saturation temperatures illustrated above, the increase in the OWF flow rate leads to a larger isentropic enthalpy difference at the expander. for the temperatures and flow rates considered and the resulting pressure ratio at the expander varies between 2 and 6 as shown in Figure 80 – b. In particular, the curves associated with the water inlet temperature in the collector field from 77 ° C to 99 ° C show a non-monotonous trend with a rapid initial increase up to the maximum value followed by a decrease with a lower inclination to increase the water flow. The curves included between the isotherm at 104 °C and 116 °C instead present a monotonous decreasing trend with a higher slope for low values of the hot water flow rate. This is due to the progressive increase in the operating pressure ratio in the expander that drives the device to work at higher than its optimum value, between 2.5 and 3, as can be seen in Figure 81.

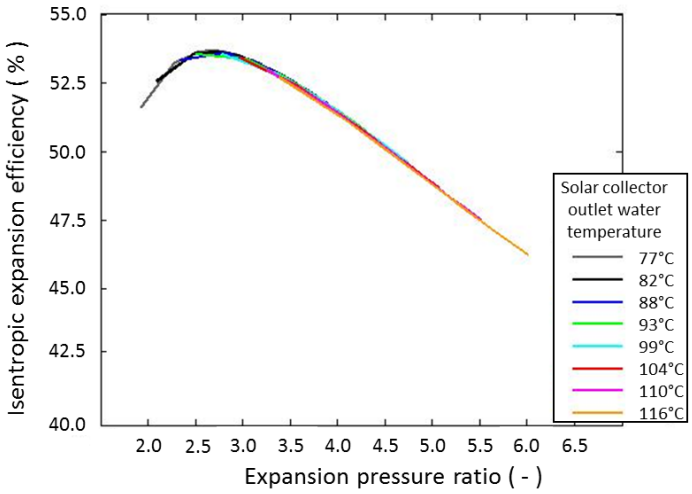

Figure 81 – Isentropic expansion efficiency of the expander in the solar-powered ORC system with intermediate heat transfer loop as a function of the pressure ratio and for different values of the collector outlet water temperature.

With respect to the considered solar-powered ORC system, the supplied heat flow rate provided by the heat source q_{in} is the heat flow rate gained by the OWF during the heat transfer process occurring in the evaporator. In the simulation, under the assumption that the ORC is adiabatic

to the environment, this heat flow rate coincides with the heat collected by the water stream in the solar collector field:

$$q_{in} = \dot{m}_{OWF}\, \Delta i_{OWF,ev} = \dot{m}_{w,h}\, c_{p,w,h} \Delta T_{col,w,h} \qquad \textit{Eq. 4.26}$$

where $\Delta i_{OWF,ev}$ is the enthalpy difference between inlet and outlet conditions of the OWF in the evaporator, $c_{p,w,h}$ is the specific heat of the water at its average temperature in the collector and $\Delta T_{coll,w,h}$ is its temperature difference. During the simulations, q_{in} varies between 37 kW and 81 kW accordingly to the variation of normal incident radiation between 450 W m^{-2} and 1000 W m^{-2}.

Figure 82 reports the conversion efficiency of the ORC unit (Eq. 4.14) for different values of the collector outlet water temperature when its volumetric flow rate is varied in the simulated range.

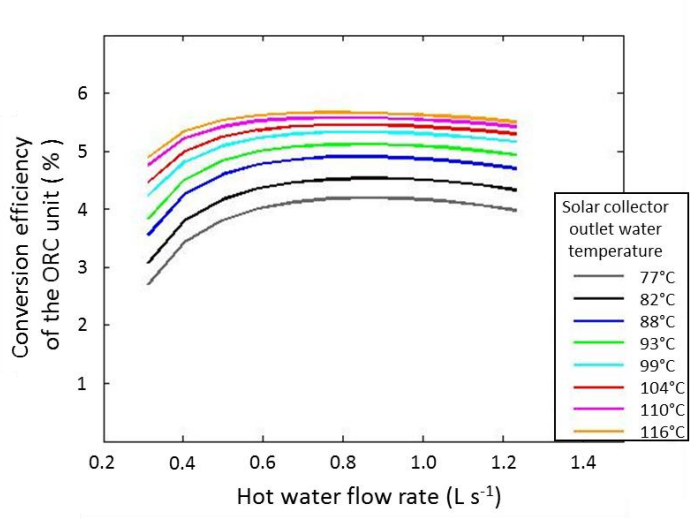

Figure 82 – Conversion efficiency ORC unit in the solar-powered ORC system with intermediate heat transfer loop as a function of the volumetric mass flow rate and for different values of the collector outlet water temperature.

The simulations show that the ORC unit works with an efficiency ranging from 2.7% to 5.7%. These values are in line with the results found the literature on the potentiality of electrical generation through ORC system powered by solar collectors working at low-temperature. Each efficiency curve lies above the curve obtained for a lower temperature of the water in the solar collector. The higher performance is obtained at the higher inlet water temperatures in the

evaporator which imply the higher evaporation temperature of the OWF. Due to the decrease of the isentropic efficiency of expansion and the increase of pumping power that reduce the net electrical output (Eq. 4.25), the conversion efficiency of the ORC does not show an increasing asymptotic trend as the water flow rate in the solar circuit increases, although the consequent increase in the evaporation temperature. At low values of water mass flow rate, despite the high isentropic efficiency of the expander, convection in the heat exchangers limit the efficiency of the heat transfer processes. The decrease of the isentropic expansion efficiency becomes more relevant on the performance of the ORC unit as the flow rate of the water in the solar collectors increases.

The effects of the solar input (DNI) on the conversion efficiency of the ORC unit is reported in the graph of Figure 83. Here, it can be observed that each is isotemperature efficiency curve increases with the at the DNI, in particular at low values of DNI (lower than 700 W m^{-2}) where the simultaneous increase of thermal input and the isentropic efficiency of expansion entails a stronger increase of the generated electrical power. For high values of DNI instead, the decline in the isentropic yield of expansion and the augmented solar circuit pumping consumption attenuate the increase of net power generated, although the increase in thermal input. The combination of these effects reflects into the asymptotic the of the conversion performance of the ORC unit. For each considered DNI range, it is possible to determine the mass flow rate a and outlet temperature of the water flowing in the solar collector field that maximize the conversion efficiency of the ORC unit.

The conversion efficiency of the ORC unit does not take into account the performance conversion of the solar radiation in heat occurring in the collector field. The conversion efficiency of the collectors can be evaluated according to Eq. 3.1. In the simulations, the high specific flow rates of the water considered in the solar circuit allow maintaining the receiver temperature only slightly higher the temperature of the water, limiting in this way the thermal losses. Therefore, in the simulation the considered concentrating solar collector is capable to operate with high efficiency between 76% and 78%.

The overall conversion efficiency of the solar-powered ORC system can be calculated as the product of the solar collector efficiency (Eq. 3.1) and the overall conversion efficiency of the ORC unit (Eq. 4.14):

$$\eta_{solar-ORC} = \eta_{ORC}\,\eta_{col} \qquad \textit{Eq. 4.27}$$

The overall conversion efficiency of the solar-powered ORC during the simulations varies between 2.1% and 4.4% with a trend that reflects the combined performance of the solar collector and the ORC system as can be seen in Figure 84.

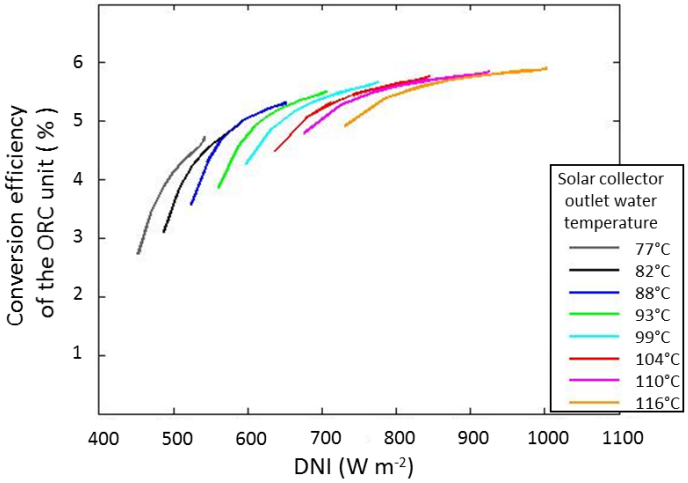

Figure 83 – Conversion efficiency of the ORC unit in the solar-powered ORC system with intermediate heat transfer loop as a function of the solar input (DNI) for different values of the collector outlet water temperature.

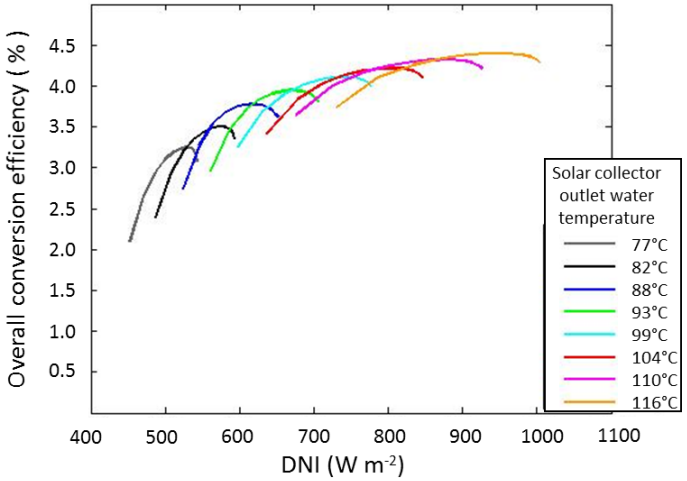

Figure 84 – Overall conversion efficiency of the solar-powered ORC system with intermediate heat transfer loop as a function of the solar input (DNI) for different values of the collector outlet water temperature.

It worth to mention, that the efficiency of the system can be considerably increased in a cogeneration configuration, where the heat transferred to the condenser is delivered to a thermal user instead of being dispersed by the cooling water. In the considered configuration, due to the chosen cooling water flow rate, this water stream reaches a maximum temperature only about 35 °C, which can be hardly exploited by a thermal user. However, through a reduction of the flow rate, it is expected that higher outlet temperature could be reached without excessively reducing the electrical performance of the system.

The modest values of the overall efficiency, rather than by the intrinsic inefficiencies of the conversion system, are limited by the low temperatures of the water coming from solar collectors and therefore depend on the low potential of the heat source in agreement with the Carnot theorem. To better understand the conversion potential of the considered system an exergetic analysis is performed. The exergetic efficiency of the ORC unit is given by the following expression:

$$\eta_{ex,ORC} = \frac{P_{el}}{\dot{m}_{w,h}\left(\Delta i_{w,h,ev} - T_{amb,ref}\,\Delta s_{w,h,ev}\right)} \qquad \textit{Eq. 4.28}$$

where, P_{el} is the net electrical output of the ORC (Eq. 4.25) and $\Delta i_{w,h,ev}$ and $\Delta s_{w,h,ev}$ are the specific enthalpy and entropy differences between the inlet and outlet conditions of the hot water in the evaporator. The reference ambient temperature $T_{amb,ref}$ is assumed 21 °C.

The simulated exergetic efficiency of the ORC unit is reported in the graph of Figure 85. for different values of the collector outlet water temperature. As for the conversion efficiency of the ORC unit, the exergetic efficiency is subjected to the opposite trend of the irreversibilities associated to the expander and the evaporator. At low-temperatures and low flow rates of the hot water, the evaporator provides the largest destruction of exergy. As the hot water flow rate increases, the dominant source of irreversibility is switched from the heat transfer process in the evaporator to the expansion of the halogenated fluid. These aspects can be better observed in the graph of Figure 86, where the curves of the are plotted as a function of the hot water flow rate. This Figure refers to 104°C outlet temperature of the water in the collectors but can be considered representative also for the other considered condition, since the outlet temperature of the water from the solar collector field does not affect significantly the trend of the percentage fraction of the total irreversibility.

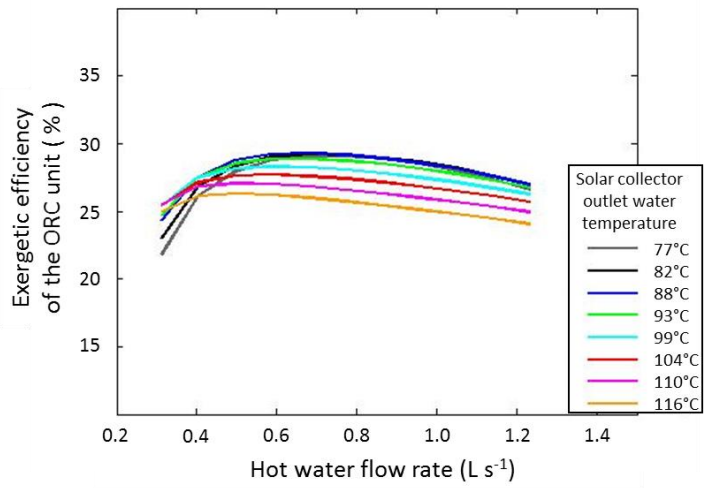

Figure 85 – Exergetic efficiency of the ORC unit in the solar-powered ORC system with intermediate heat transfer loop as a function of the volumetric mass flow rate and for different values of the collector outlet water temperature.

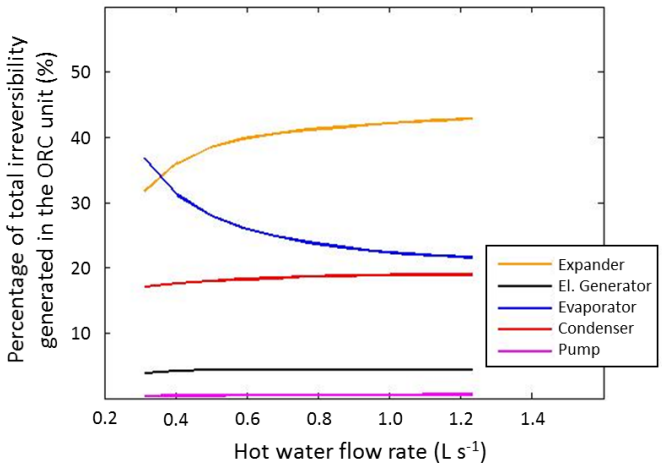

Figure 86 – Percentage of the total irreversibility generated in the ORC unit of the solar-powered ORC system with intermediate heat transfer loop as a function of the volumetric mass flow rate of the water in the collector. The curves refer to the components present in the ORC unit. (104°C outlet water temperature).

As the flow rate in the solar collectors increases, the irreversibility generated during the heat transfer in the evaporator decreases. This is due to the improvement of the conditions of thermal transfer: higher convective coefficients of thermal exchange are realized as the flow rate

increases and thus, the incidence of this process on the total irreversibility of the ORC unit is reduced.

The irreversibility in the condenser remains almost constant because the positive effect due higher convective heat transfer coefficients achieved on the OWF side (evaporator heat exchange improves on both sides) is compensated by the higher temperature difference between cooling water and OWF needed with the increase of the thermal input. During the simulations, the exergetic efficiency of the evaporator and the condenser are between 69% and 86% and between 36% and 40%, respectively. Despite the fact that the exergetic efficiency of the evaporator results significantly higher than that of the condenser, the latter contributes less to the total destruction of exergy in the ORC unit due to the fact that it operates at a lower temperature. The condenser and the evaporator have in fact a percentage exergetic destruction respectively between 18% and 22% and between 22% and 42% respectively.

As the water supply increases, the irreversibility associated with the expander increases with a monotonous trend and is results the most incisive component in terms of exergy destruction in most operating condition. The exergetic efficiency of the screw expander decreases from 56% to 49%. The reason of this is the reduction in the isentropic expansion efficiency for the progressive deviation from design condition as of the evaporator temperature increase. The expansion process can cause up to 48% of the total irreversibility of the ORC unit. The irreversibility generated in the pump and the generator are much lower than the those of the other components. Their exergy efficiencies components coincide with the constant value of the isentropic pumping and electrical efficiency set in the model, thus, their percentage irreversibilities have modest variations as the operating condition varied.

The results obtained from the exergetic analysis are apparently in contrast to those reported in the study on ORC systems presented in the literature, which identified the evaporator as the most critical component. *Tchanche et al*. [202] observed that the largest exergy destructions in ORC cycle occur in the order in evaporator, expander, condenser and pump. *Barse and Mann* [203] reported that the losses in the condenser were higher than those occurring in the expander and indicated the evaporator as the component in which the largest destruction of exergy. Such studies, however, considered large ORC system with expander characterized by very high

isentropic efficiency. For instance, in the work of *Barse and Mann* [203], a constant 80% isentropic efficiency is assumed. In addition, the temperature differences between the fluids involved were larger (10 °C at the pinch point) and, therefore, the heat transfer processes were less efficient than those considered here. In our model, the low temperatures of the heat source impose instead a small minimum temperature difference between the fluid (2 °C – 6 °C at the pinch point) in order to not reduce the small potential of the low-grade heat source, which requires large heat transfer areas at the evaporator and condenser.

As what has been done in the energetic analysis, to compute the overall exergetic performance of the solar power ORC system, the conversion of the solar radiation available at the concentrator aperture area into heat must be considered. The exergetic flux connected to the solar radiation is evaluated by using the equation Eq. 4.22 it was possible to calculate the exergetic flow of direct normal solar radiation incident on the aperture area of the collector field. Known the exergy difference between inlet and outlet conditions of the water in the collector field, it is possible to evaluate the exergetic efficiency of the solar collector as

$$\eta_{ex,col} = \frac{\left(\dot{E}_{w,h,out} - \dot{E}_{w,h,in}\right)_{col}}{\dot{E}_{sol}} = \frac{\dot{m}_{w,h}\left(\Delta i_{w,h,col} - T_{amb,ref}\,\Delta s_{w,h,col}\right)}{DNI\,A_a\left(1 + \frac{1}{3}\left(\frac{T_{amb,ref}}{T_{Sun}}\right)^4 - \frac{4}{3}\frac{T_{amb,ref}}{T_{Sun}}\right)} \qquad \textit{Eq. 4.29}$$

The results of the simulation show that the exergetic efficiency of the conversion of solar radiation into heat results higher at higher values of the outlet temperature and flow rate of the water in the solar collectors. Although the solar collectors allow an efficient conversion of the incident radial flow into thermal energy (77% thermal collector efficiency), very low exergetic efficiencies are obtained, with values ranging between 10.2% and 18.8%. This result was expected due to the large temperature difference between the reference ambient temperature and the apparent temperature of the Sun. The solar field becomes the source of the largest irreversibility generation in the solar-powered ORC system. The percentage exergetic destruction in the solar field is in fact results between 86.3% and 94.4% of the total. The exergetic analysis carried out highlights how crucial is to improve the performance of the solar collectors in order to increase the overall exergy performance of the system.

The overall exergetic efficiency of the solar-powered solar ORC as a function of the DNI is shown in Figure 87. The trend of the exergetic efficiency curves is very similar to that reported for the overall conversion efficiency in Figure 84.

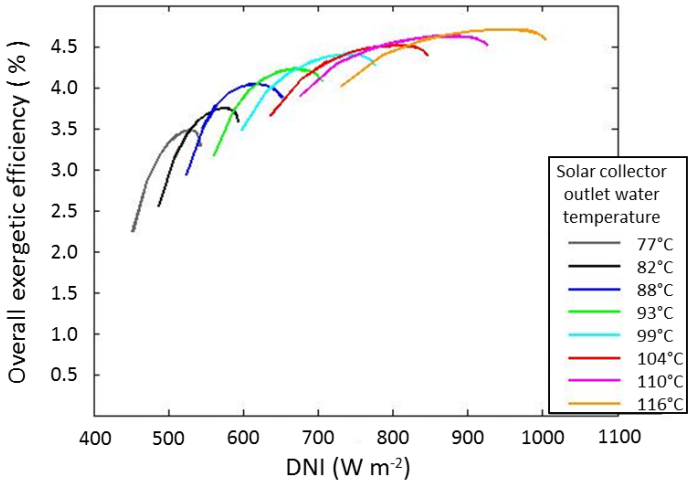

Figure 87 – Overall exergetic efficiency of the solar-powered ORC system with intermediate heat transfer loop as a function of the solar input (DNI) for different values of the collector outlet water temperature.

4.3.2 Simulation results of a solar-powered ORC system with direct vaporization of the working fluid

The performance of a solar-powered ORC system has been evaluated with direct vaporization of the OWF in the solar collector by adopting the once-through configuration presented in Paragraph 4.1.3. The pressurized OWF coming from the pump is directly sent to the solar collector where it is heated and vaporized. Afterwards, the vapor is expanded in the screw expander and condensed before entering the pump. As compared to the configuration considered in the previous Paragraph, in this case, the pump and the heat exchanger/evaporator, whose function is directly carried out by the solar collector field, are no longer required. A schematic representation of the considered system is reported in Figure 66 – b. In this configuration, it is not convenient to superheat the vapor as it would cause a decrease in the performance of the solar collectors, due to low heat transfer coefficients in the receiver obtained in the presence of vapor flow. This would imply a substantial increase of receiver length, thus

of the aperture area of the collector with a higher cost of the system. Moreover, these disadvantages would be accompanied by higher thermomechanical stress on the receiver, due to the higher thermal gradients in the terminal section of the receivers. Therefore, it has been assumed a reference thermodynamic cycle for the halogenated fluid with a complete evaporation of the halogenated fluid and no superheating of the saturated vapor at the outlet of the collector (Figure 88)

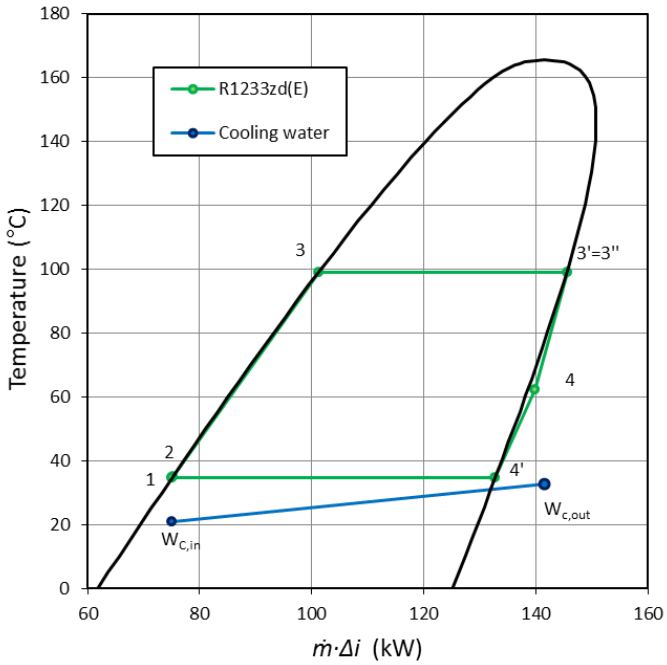

Figure 88 – Temperature profiles and heat flow rates transferred between the halogenated fluid and the cooling water streams in the T- ṁ Δi diagram ($\dot{m}_{OWF}$= 0.33 kg s^{-1}; DNI = 882 W m^{-2}).

The simulations are performed under the same solar input (DNI) and environmental conditions (air temperature and wind speed). In order to assess a fair comparison, the solar-powered ORC system with direct vaporization of the R1233zd(E) in the solar collector solar-powered ORC that operates with the same components (collector field, pump, expander and condenser) considered in the simulation of the solar-powered ORC systems with intermediate heat transfer loop. In the model, geometries and design parameters of the components have been maintained unaltered. Furthermore, the evaporation temperature of the OWF has been adjusted to operates with the same reduced temperature difference in the collector field under the different operating conditions tested reduced to which the solar field operates. This assumption assures that the

comparison between the two configurations is not affected by the thermal efficiency of the solar collectors.

For the sake of simplification of the comparison, the reference of the curves in the following figures is kept to the outlet water temperatures from the solar collector field obtained with the intermediate heat transfer that provides the same reduced temperature difference in the collectors.

Working at the same reduced temperature difference in the solar field requires operating at a higher evaporation temperature than it has achieved with the configuration with intermediate solar circuit it also increases significantly. The evaporation temperature obtained during the simulation of the solar-powered ORC system with direct vaporization of the OWF in the solar collector field is plotted as a function of the DNI in Figure 89. The evaporation temperature increases almost linearly with the DNI.

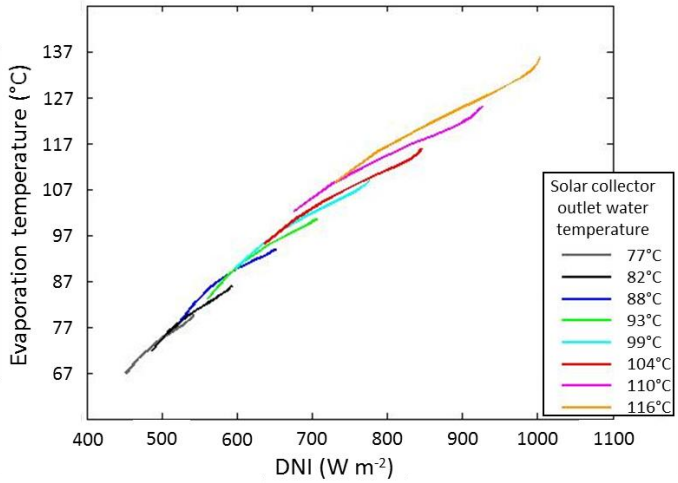

Figure 89– Evaporation temperature in the solar-powered ORC system with direct vaporization of the OWF in the solar collector field as a function of the solar input (DNI). The curves refer different values of the collector outlet water temperature providing the same reduced temperature difference in the collectors.

The increased evaporation temperature implies that the system will operate at higher pressure level: at the maximum values of the evaporation temperature achieved in the simulation, 135 °C, the R1233zd (E) present 21.1 bar saturation pressure which results significantly higher than

the maximum evaporation pressure (11.2 bar) in the evaporator working at 105°C with the intermediate solar circuit. This implies that the solar circuit must be sized for a much higher pressure (21.1 bar) with respect to the 3 bar of the water in the intermediate solar circuit.

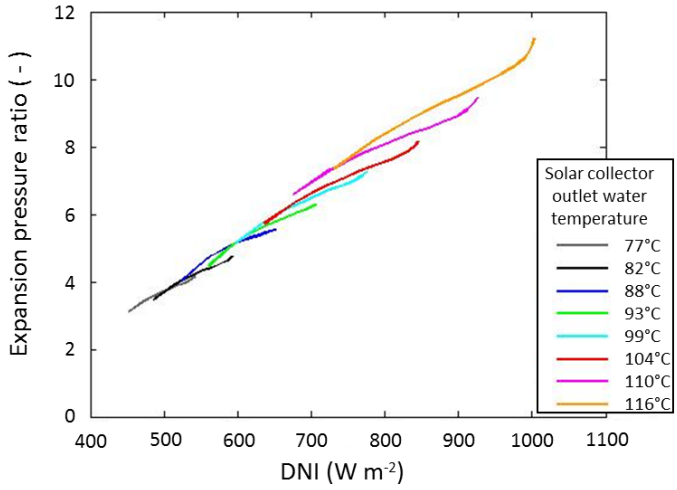

- a -

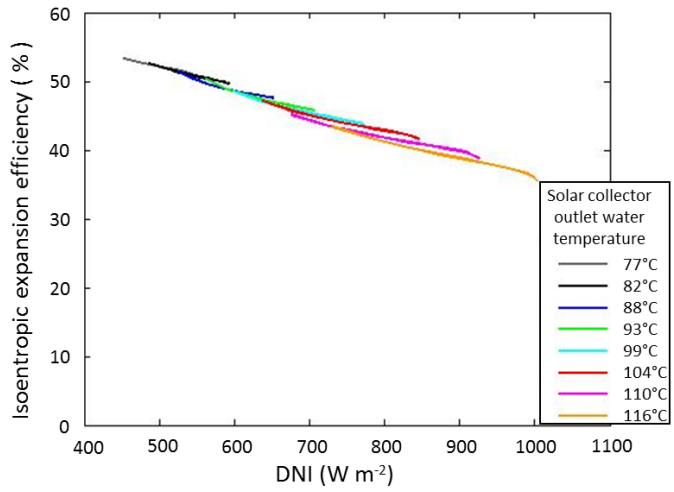

- b -

Figure 90– Pressure ratio (a) and isentropic expansion efficiency (b) of the expander in the solar-powered ORC system with direct vaporization of the OWF in the solar collector field as a function of the solar input (DNI). The curves refer different values of the collector outlet water temperature providing the same reduced temperature difference in the collectors.

The pressure ratio available for the expansion process is increased to values ranging from 3 bar to 11 bar as the DNI increases (Figure 90 – a). This increase is particularly evident at the higher solar input due to the non-linear trend of the saturation pressure with the temperature. Consequently, the expander is working far away from its design point and the isentropic efficiency results lower than the previous simulation (Figure 90 – b). At low DNIs the blowback losses are modest and the expander works near its peak of efficiency (52%), however, as the DNI increases, the isentropic expansion decreases down to 35% due to the increased pressure ratio.

In this configuration, the net electrical output of the ORC unit is calculated by subtracting the electrical consumption of the pump $P_{p,ORC}$ from the electrical power generated by the electrical generator $P_{g,ORC}$:

$$P_{el} = P_{g,ORC} - P_{p,ORC} = \dot{m}_{OWF}\left(\Delta h_{exp,is}\,\eta_{is,exp}\,\eta_{el} - \Delta h_{p,is}\frac{1}{\eta_{is,p}\,\eta_{el}}\right) \qquad \textit{Eq. 4.30}$$

Figure 91 reports the trend of the electrical power output of the ORC: it increases with the DNI from 1.7 kW_{el}, for 450 W m^{-2}, to 4.4 kW_{el} at 1000 W m^{-2}. It can be noticed that the trend is more regular as compared to the first configuration (see Figure 77) due to the monotonous decrease in the efficiency of the expander as the DNI increases.

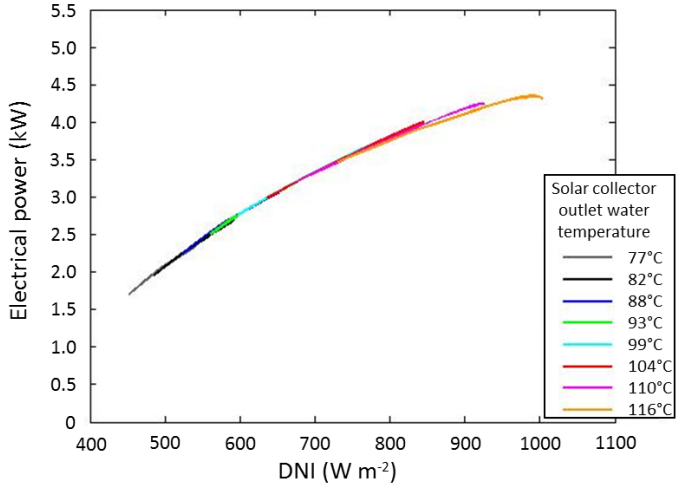

Figure 91 – Net electrical power generated by the solar-powered ORC system with direct vaporization of the OWF in the solar collector field as a function of the solar input (DNI). The curves refer different values of the collector outlet water temperature providing the same reduced temperature difference in the collectors.

When this result is compared with that obtained in the previous simulation, it can be observed that the configuration with direct vaporization exhibits higher electrical power for most of the cases considered (Figure 92). Only at DNI values over 900 W $m^{-2,}$ the solar-powered ORC system with intermediate heat transfer show allows generating more electricity. However, it has to be mentioned that these differences are quite small. This trend is mostly due to the stronger influence of the poor expansion isentropic efficiency in the second configuration.

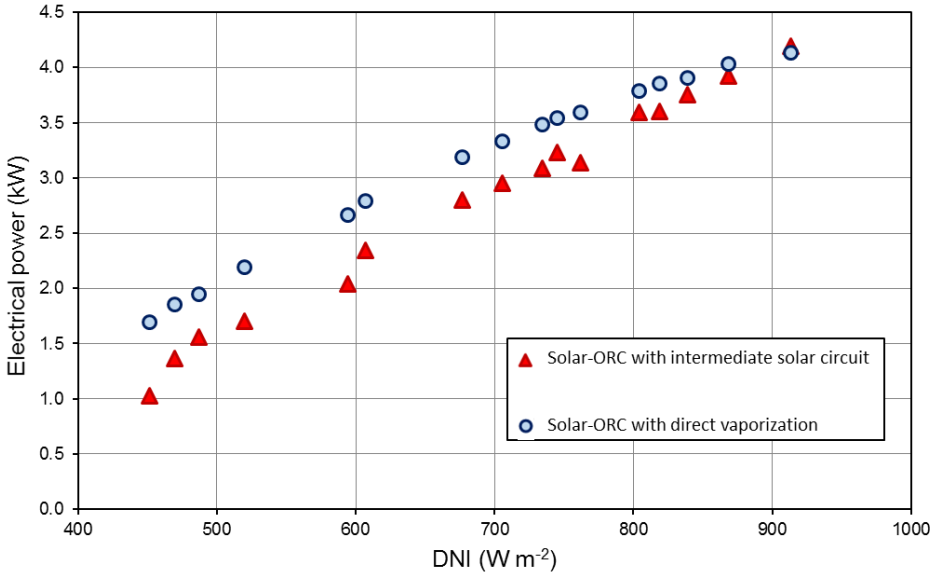

Figure 92 – Net electrical power generated by the solar-powered ORC systems with direct vaporization of the OWF (blue dots) and intermediate heat transfer loop (red triangles) as a function of the solar input (DNI).

With respect to the considered solar-powered ORC system, the supplied heat flow rate provided by the thermal input to the ORC unit is the heat flow rate gained by the OWF in the solar collector field:

$$q_{in} = \dot{m}_{OWF}\, \Delta i_{OWF,col} \qquad \textit{Eq. 4.31}$$

where $\Delta i_{OWF,col}$ is the enthalpy difference between inlet and outlet conditions of the OWF in the collectors. Hence, the conversion efficiency of the ORC unit in this case becomes:

$$\eta_{ORC} = \frac{P_{el}}{q_{in}} = \frac{P_{el}}{\dot{m}_{OWF}\, \Delta h_{OWF,col}} \qquad \textit{Eq. 4.32}$$

Unlike what is achieved with the first configuration in which an asymptotic trend is observed, the conversion efficiency of the ORC unit, plotted in Figure, present a maximum in the middle

part of the considered DNI range. This can be explained in the light of the increase evaporation temperature with the DNI and the contextual decrease of the isentropic expansion efficiency: initially the increase of the evaporation temperature results more influence than the reduction in in the expansion performance, implying an increasing trend until the peak is reached, afterwards the decrease if the isentropic efficiency becomes dominant.

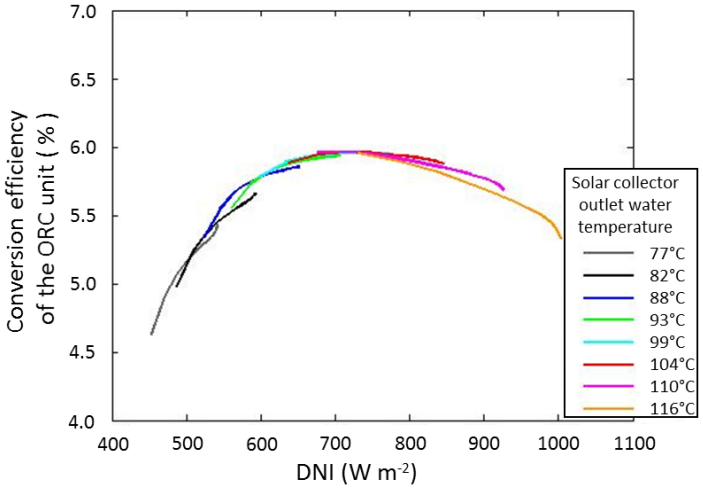

Figure 93 –Conversion efficiency of the ORC unit in the solar-powered ORC system with direct vaporization of the OWF in the solar collector field as a function of the solar input (DNI). The curves refer different values of the collector outlet water temperature providing the same reduced temperature difference in the collectors.

The efficiency of the solar collector field can be calculated by applying *Eq. 3.1* to the considered case:

$$\eta_{col} = \frac{\dot{m}_{OWF}\,\Delta h_{OWF,col}}{DNI\;A_a} \qquad \textit{Eq. 4.33}$$

Because of the assumption made on the reduced temperature difference, the solar collectors operate with a thermal efficiency ranging from 76% to 78%.

By extending the conversion efficiency analysis to the thermal collectors, it is possible to evaluate the overall conversion efficiency of the solar-powered ORC system given by the product between the solar collector efficiency and the conversion efficiency of the ORC unit (Eq. 4.27). The overall conversion efficiency is plotted against the solar input (DNI) in Figure 95. Similar to what observed for the configuration with an intermediate solar circuit, the overall

conversion efficiency of the solar-powered ORC during this simulation varies between 3.6% and 4.6%.

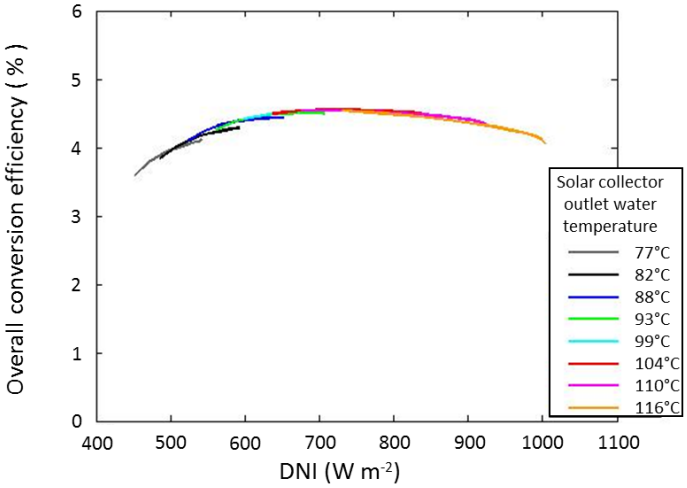

Figure 94Figure 89 – Overall conversion efficiency of the solar-powered ORC system with direct vaporization of the OWF in the solar collector field as a function of the solar input (DNI). The curves refer different outlet water temperature providing the same reduced temperature difference in the collectors.

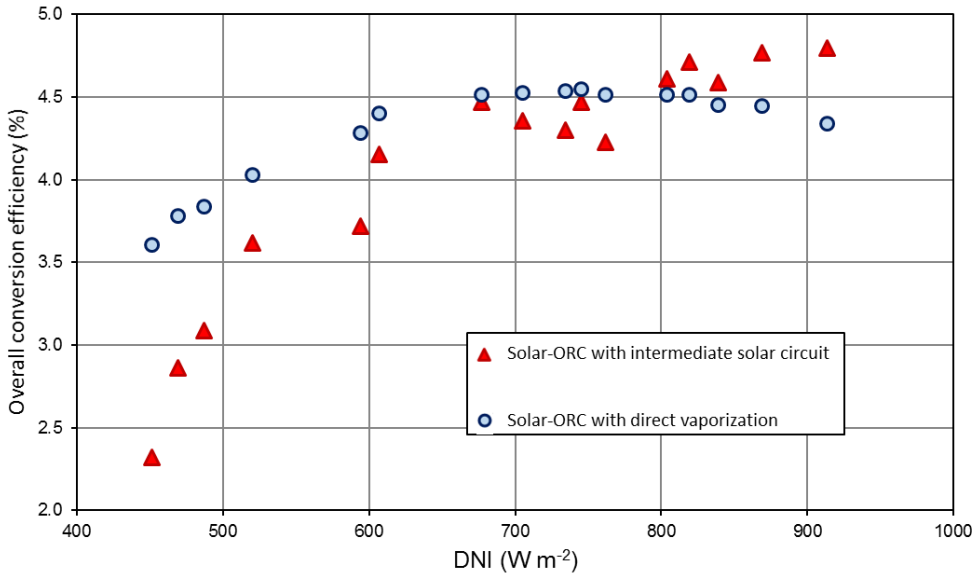

Figure 95 – Overall Conversion efficiency of the ORC unit in the solar-powered ORC systems with direct vaporization of the OWF (blue dots) and intermediate heat transfer loop (red triangles) as a function of the solar input (DNI).

In particular, the performance of the electric power generated by the two configurations is linear with the increase of the DNI. As shown in Figure 95. The values obtained in the present simulation are very similar close to those obtained with the configuration presenting an intermediate heat transfer circuit, however, at low DNI the performance of the configuration with direct vaporization of the DNI are significantly higher. As the DNI increases the difference between the two configurations reduces and for DNI over 800 W m^{-2} the overall efficiency of the configuration with intermediate heat transfer loop present becomes higher. Again, this trend is a direct consequence of the adoption of the same expansion device in both solar-powered ORC configurations which strongly penalizes the configuration with direct vaporization of the OWF whereas the first configuration operates at pressure ratios centred closer to the design point of the expander.

The exergetic efficiency of the ORC unit in the solar-powered ORC systems with direct vaporization of the OWF is evaluated through the following expression:

$$\eta_{ex,ORC} = \frac{P_{el}}{\dot{m}_{OWF}\left(\Delta i_{OWF,col} - T_{amb,ref}\Delta s_{OWF,col}\right)} \qquad \textit{Eq. 4.34}$$

where, P_{el} is the net electrical output of the ORC (Eq. 4.30) and $\Delta h_{OWF,col}$ and $\Delta s_{OWF,col}$ are the specific enthalpy and entropy differences between the inlet and outlet conditions of the hot OWF in the collector. The reference ambient temperature $T_{amb,ref}$ is assumed 21 °C. In this way, the conversion process of solar radiation into heat is not considered.

The exergetic efficiency of the ORC unit is plotted in Figure 96 and exhibits a monotonous decrease as the DNI increases reflecting the trend of exergetic expansion efficiency (Figure 97).

As expected, the expander constitutes the components that most influences the exergetic performance of the ORC unit in the case of direct vaporization of the OWF, causing from 63% to 69% of the total exergy destruction in the ORC unit. The condenser generates between 22% and 26% of the total irreversibility generated in the ORC unit, while the percentages of the total exergy destruction caused by the electrical generator and the circulating pump range respectively between 3.8% and 7.5% and 0.5% and 1.4%

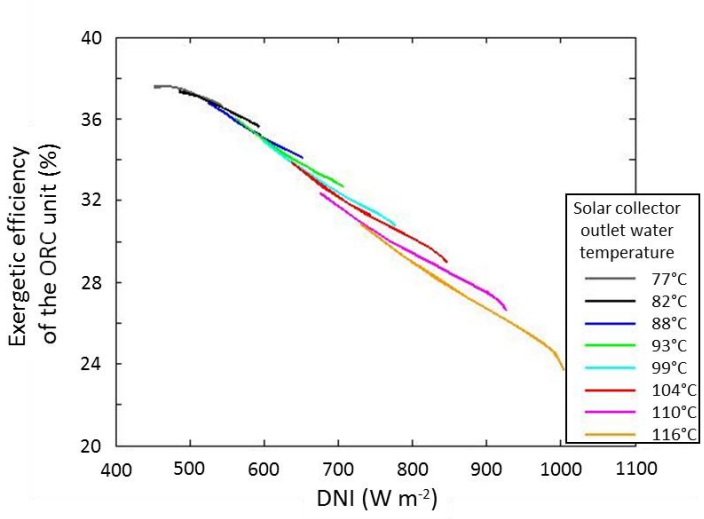

Figure 96– Exergetic efficiency of the ORC unit in the solar-powered ORC system with direct vaporization of the OWF in the solar collector field as a function of the solar input (DNI). The curves refer different values of the collector outlet water temperature providing the same reduced temperature difference in the collectors.

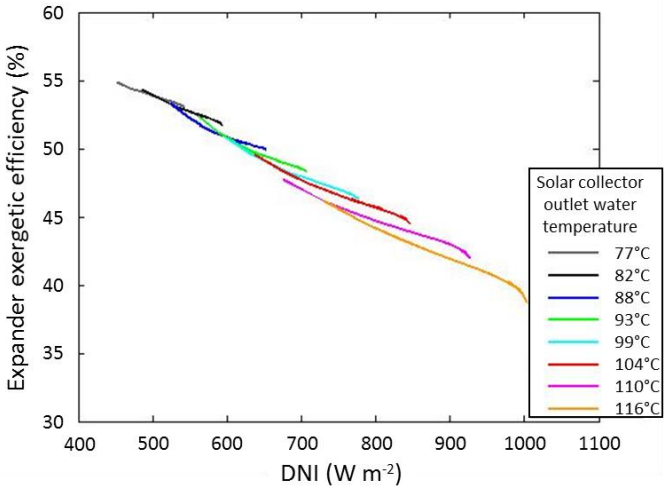

Figure 97 – Exergetic efficiency of the expander in the solar-powered ORC system with direct vaporization of the OWF in the solar collector field as a function of the solar input (DNI). The curves refer different values of the collector outlet water temperature providing the same reduced temperature difference in the collectors.

To compute the overall exergetic performance of the solar power ORC system, the conversion of the solar radiation available at the concentrator aperture area into heat is included in the analysis. Once the exergy difference between inlet and outlet conditions of the halogenated

fluid in the collector field is known, and the exergetic flux connected to the solar radiation is evaluated adopting the formulation of *Petela* [200] (Eq. 4.22), the exergetic efficiency of the solar collectors is calculated as:

$$\eta_{ex,col} = \frac{\left(\dot{E}_{OWF,out} - \dot{E}_{OWF,in}\right)_{col}}{\dot{E}_{sol}} = \frac{\dot{m}_{OWF}\left(\Delta h_{OWF,col} - T_{amb,ref}\,\Delta s_{OWF,col}\right)}{DNI\,A_a\left(1 + \frac{1}{3}\left(\frac{T_{amb,ref}}{T_{Sun}}\right)^4 - \frac{4}{3}\frac{T_{amb,ref}}{T_{Sun}}\right)} \qquad \textit{Eq. 4.35}$$

The overall exergetic efficiency of the solar-powered ORC system can be calculated as the product between the exergetic efficiency of the solar collector field and the ORC unit:

$$\eta_{ex,solar-ORC} = \eta_{ex,ORC}\ \eta_{ex,col} \qquad \textit{Eq. 4.36}$$

The overall exergetic efficiency in the simulation was between 3.8% and 4.9%. Figure 98 reports the trend of the overall conversion efficiency when the DNI is varied.

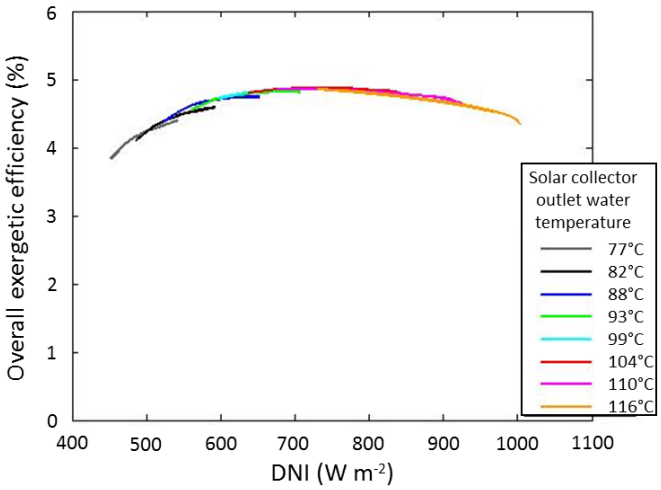

Figure 98 – Overall exergetic efficiency of the solar-powered ORC system with direct vaporization of the OWF in the solar collector field as a function of the solar input (DNI). The curves refer different values of the collector outlet water temperature providing the same reduced temperature difference in the collectors.

The solar field causes between 86% and 94% of the total exergy destruction in the system. This result is very similar to that obtained with the solar-powered ORC system with intermediate heat transfer loop. As compared to this first configuration, the direct vaporization of the OWF provides higher overall exergetic efficiency except for the highest value of DNI considered in

the comparison where the poor performance of the expander reduced the overall efficiency of the ORC system with direct vaporization of the OWF.

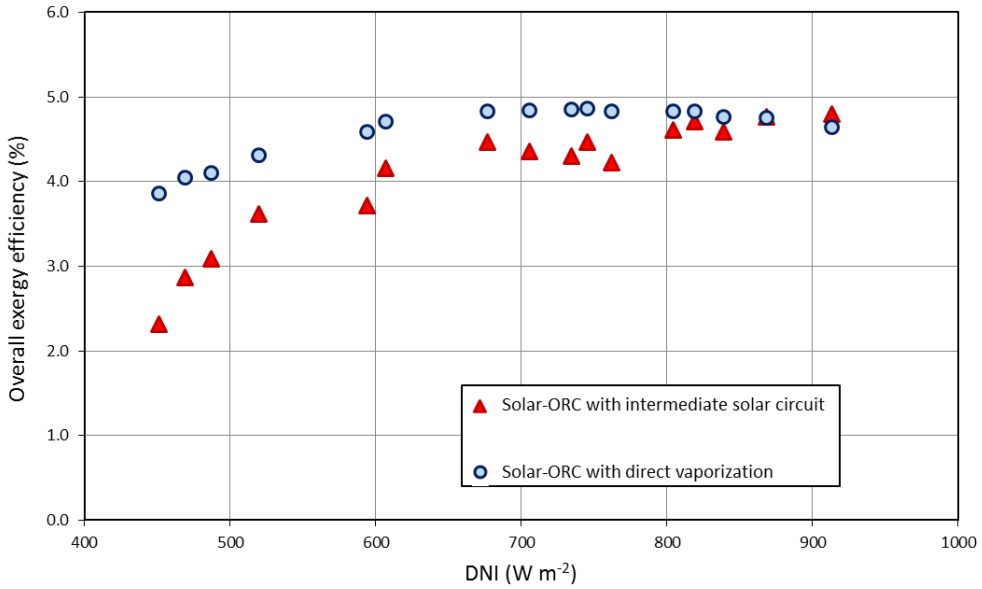

Figure 99 – Overall exergetic efficiency of the solar-powered ORC systems with direct vaporization of the OWF (blue dots) and intermediate heat transfer loop (red triangles) as a function of the solar input (DNI).

From the comparison between the solar-powered ORC systems with intermediate heat transfer loop and direct vaporization of the OWF, it can be concluded that the second configuration presents higher electrical output and overall conversion efficiency. Furthermore, the direct vaporization of the OWF can increase the exergetic performance of a solar-powered ORC. Only at the highest values of DNI, which corresponds to the highest pressure ratio at the expander, the low value of the isentropic expansion efficiency causes a decrease in the performance. It is expected that the adoption of an expander that shows peak performance at higher values of pressure ratio could increase dramatically the overall performance of the solar-powered ORC with direct vaporization of the OWF and the advantage of this configuration over the system with intermediate heat transfer loop would be magnified.

Chapter 5 Planar volumetric receiver for absorbing nanofluid

In conventional solar thermal collectors, the solar radiation is absorbed and transferred to a heat transfer fluid by means of a metallic absorber plate. To achieve high performance, solar collectors should enhance the absorption from the Sun and increase the heat transfer rate to the fluid. The addition of nanoparticles in a base-fluid can dramatically enhance its optical properties, in particular, its absorption properties. Thus, nanofluids could be successfully used in solar collectors to absorb directly the solar radiation in their volume and avoid using an absorber plate.

This Chapter presents the results of the numerical and experimental investigations on the application of nanofluids as a volumetric absorber in a concentrating direct absorption solar collector (DASC): an aqueous suspension of single-wall carbon nanohorns (SWCNHs) is chosen as the nanofluid. A model of a solar receiver with a planar geometry aimed to be installed in a parabolic trough concentrator is developed: the radiative transfer equation in participating media and the energy equation are numerically solved to predict the thermal performance of the receiver. An indirect experimental validation is performed by using measurements in the same parabolic trough concentrator: the simulated performance of the direct absorption receiver has been compared with experimental data of a conventional surface-absorption receiver under the same operating conditions. Moreover, the model is used to compare the calculated performance of the volumetric receiver and that of a selective surface receiver under the same operating conditions. From this numerical investigation, the guidelines for the design and optimization of a flat volumetric receiver for a solar concentrating collector are drawn. According to the numerical results, a direct absorption receiver has been designed and set up to investigate the capability of the nanofluid to absorb the concentrated sunlight. The receiver exhibits a flat geometry and has been designed for installation on a full-scale

linear concentrating collector presenting an asymmetrical parabolic trough, where the concentrated solar flux locally reaches 100 kW m^{-2} under clear-sky conditions. A SWCNHs suspension in distilled water with a concentration of 0.02 g L^{-1} is prepared at the Institute of Condensed Matter Chemistry and Technology for Energy (ICMATE) of the National Council of the Research (CNR) in Padova. The thermophysical properties, measured at the Construction Technologies Institute (ITC) of the CNR in Padova, are the same as those of the base-fluid, but the presence of carbon nanoparticles greatly enhances the optical characteristics, such as optical extinction. The characterization of the optical properties of the nanofluid is performed at the Italian National Institute of Optics (INO) of the CNR in Florence. An experimental investigation on the capability of the nanofluid in collecting solar radiation and verify its stability when exposed to concentrated and non-concentrated solar flux with and without circulation is carried out.

5.1 Direct absorption solar collector with nanofluid

In conventional solar thermal collectors, the photothermal conversion happens in a two-steps process: the solar radiation heats up an absorber surface provided by a selective coating and then, part of the heat is transferred to the working fluid, driven by a temperature difference. The thermal performance of a solar collector can be evaluated by accounting the thermal and optical losses. Thermal energy is lost from the collector to the surroundings by conduction, convection, and infrared radiation, while optical losses take account of the non-unitary transmittance and absorbance of the transparent cover and absorber medium, respectively. To achieve high performance, solar collectors should enhance the absorption from the Sun and increase the heat transfer rate to the fluid decreasing optical losses to the surroundings such as reflection of Sun radiation and heat transfer from the system to the surroundings [204]. In typical configurations, conductive and convective thermal resistances between the absorber and the fluid makes the effectiveness of solar-to-thermal energy conversion quite limited because of high heat losses from the surface absorber to the surroundings. Innovative absorber elements for flat and concentrating collectors providing enhanced heat transfer have been proposed in the literature. For instance, the performance of a roll-bond absorber in a flat plate solar collector has been discussed in the work of *Del Col et al*. [205]. *Bortolato et al.* [89] proposed the use of flat bar-and-plate absorber in an asymmetrical small parabolic trough.

An alternative method to reduce the interface thermal resistance is to replace the absorber surface with the volumetric absorption in the working fluid. In this kind of devices, the absorption of the solar radiation occurs directly in the fluid volume instead of being limited to the receiving surface. The main advantage of direct absorption of solar radiation is to avoid the thermal resistance between absorber surface and heat transfer fluid. Figure 100 reports a schematic comparison between a conventional solar thermal collector and a direct absorption solar collector in terms of thermal resistances as can be found in the work of *Taylor et al.* [206]. As compared to the conventional surface-absorption solar collectors, the total thermal resistance is lower, the fluid bulk represents the hottest element, the optical efficiency increases and the convection heat losses diminish because of the lower surface temperature. Direct

absorption solar collectors may, therefore, lead to higher thermal efficiency and lower cost due to the absence of a selective surface.

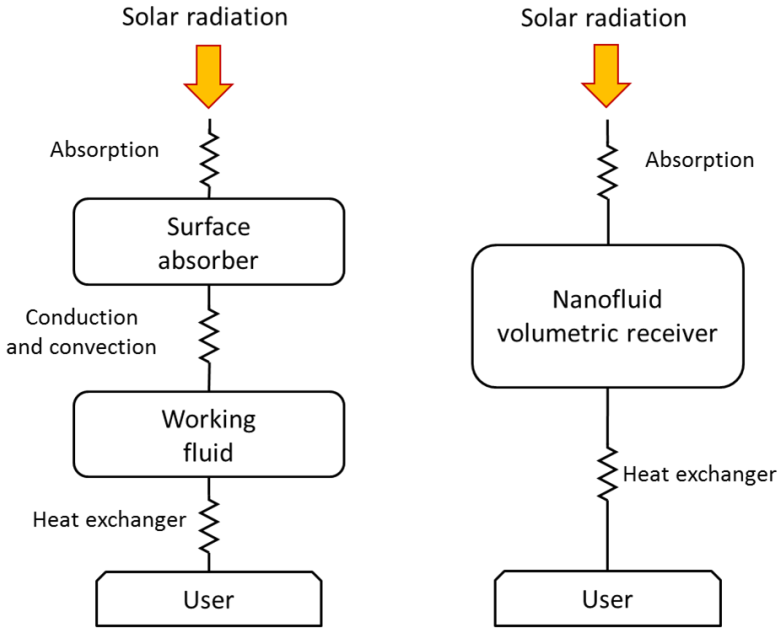

Figure 100 – Resistance network for the heat gain: comparison between conventional solar thermal collector (left) and direct absorption solar collector (right).

The concept of direct absorption of solar radiation was presented in the 70's as a simplification of conventional collector design to potentially enhance the efficiency by absorbing solar radiation within the fluid volume [207]. *Minardi and Chuang* [208] were the first to present a direct absorption solar collector using a suspension of micro-sized carbonaceous particles in shellac, known as India Ink, as a volumetric receiver. However, the microparticle-based fluids used were unsafe, toxic and unstable, causing fouling of hydraulic loops, clogging of pumps and erosion issues. The application of nanofluids, which consist of dispersions of solid nanoparticles with a diameter less than 100 nm in a base-fluid, in DASCs may overcome these drawbacks: the presence of a small amount of nanoparticles should facilitate the preparation of stable fluids, entails a negligible change in viscosity and minimizes mechanical erosion and chemical corrosion [209]. Furthermore, nearly total absorption of the solar spectrum energy can be achieved by properly tuning the kind and concentration of nanoparticles in the base-fluid. Only in the last decades, thanks to the technological progress in the production of

nanoparticles and preparation of nanofluids with improved functional properties with respect to the base-fluid [210], the research community has found a renewed interest in DASCs.

5.1.1 Nanofluids as direct absorbing media

A nanofluid is a fluid containing nanometer-sized particles, called nanoparticles. These fluids are engineered colloidal suspensions of nanoparticles in a base-fluid [211]. The nanoparticles used in nanofluids are typically made of metals, oxides, carbides, or carbon nanotubes [212]. Common base-fluids include water, ethylene glycol and oil. *Choi et al.* [210] conceived nanofluids as a substitute of the traditional medium in processes that require highly efficient heat transfer. At first, they have been proposed as working fluids in surface-absorption solar thermal collectors, since they were supposed to possess superior thermal properties as compared to the conventional working fluids. Numerous experimental and theoretical works on the application of nanofluids as heat transfer fluid in solar thermal systems have been done, as reported by *Lomascolo et al*. [213] and by *Kakaç et al.* [214]. Actually, ambiguous results have been obtained when assessing the enhancement of thermal convection by adding nanoparticles in a fluid. Knowledge of the rheological behaviour of nanofluids is found to be critical in deciding their suitability for convective heat transfer applications [215,216]. A discussion on the actual heat transfer enhancement of nanofluids is also provided in the work of *Mohamad* [217]. On the other hand, some nanofluids present peculiar optical properties that allow their use as absorbing and heat transfer medium in DASCs presenting good prospect to successfully enhance the solar collector efficiency.

In order to explore the possible use of a fluid as absorbing medium in DASCs, it is crucial to characterize its optical properties. Conventional fluids adopted in solar thermal collectors have been shown extremely low absorptive properties over the solar spectrum. *Otanicar et al*. [218] investigated the optical properties possible candidates as base-fluid for direct absorption receivers (water, propylene glycol, ethylene glycol and Therminol VP-1). Experimentally, they measured transmittance spectra for all four fluids, and they have found strong absorption bands at 950–1000 nm and at 1200 nm for water, ethylene glycol and propylene glycol. Although water results the best solar absorber of the four fluids, it can absorb only 13% of the incident solar energy.

Numerous studies have demonstrated that the optical properties of the base-fluid can be dramatically enhanced even with very low amounts of specific nanoparticles, much smaller than that required to vary the thermophysical properties of the heat transfer fluid [219]. A recent review on this topic is provided by *Gorji and Ranjibar* [220]. In the last years, many researchers have tried to determine the most suitable nanoparticle to be used in DASCs. *Javadi et al.* [204] acknowledged that there is the lack of study on the effects of nanofluids optical properties such as transmittance and extinction coefficient on the performance of solar collector. Recently, *Leong et al.* [219] presented an overview of current applications of nanofluids in solar systems. The authors discussed several issues that need further investigation and highlighted that type of particles, size, shape and volume concentration in the base-fluid play important roles on the definition of the optical characteristics of nanofluids; thus, there is much room to tailor the optical properties of a nanofluid according to with its application.

Extinction represents the energy reduction of incident beams. The extinction coefficient is the imaginary part of the complex refractive index. It depends on the size and nature of the nanoparticle, dielectric constant of the medium and temperature distribution and nanoparticle concentration. The extinction coefficient can be expressed as a combination of the absorption and scattering coefficients. Absorption characterizes the loss in intensity of incident light when passing through the working medium. The absorbance of the nanofluid takes account of both nanoparticles and base-fluid absorption characteristics, however, it cannot be computed as a simple summation of their absorption capacities [221]. Scattering takes account of all deviations and redirection mechanism of light from its original trajectory due to the presence of solid particles in a radiative participating medium such as nanofluid. The effect of scattering is related to the probability of a light beam to hit a solid particle and it increases with the volume concentration and dimension of solid particles. According to *Taylor et al*. [222], the effect of scattering is negligible if the particles volume fraction is less than 0.6%. Furthermore, scattering has minimal effect when the nanoparticles size is lower than 10 nm [223].

Table 10 a summarize the most important works on optical characterization of nanofluids presenting nanoparticles of different origin, size and concentration dispersed in different base-fluids.

Table 10 – Summary of the studies of optical properties of nanofluid.

Investigator(s) (Year)	Nanoparticles /base-fluid (Surfactant)	Nanoparticle size	Nanoparticle concentration
Otanicar et al. (2009)	Water, EG, PG, Therminol VP-1	-	-
Taylor et al. (2011)	TiO_2, Al, Ag, Graphite, Cu / Water; Al, Ag, Cu Graphite / Thermiol VP- 1	30 nm (TiO_2), 20nm (Al), 30nm(Ag), 30 nm (Graphite), 30 nm(Cu)	0.5 (TiO_2) , 0.1 (Al), 0.004 (Ag), 0.5 -0.1 - 0.0025 (Graphite), 0.004 (Cu) vol%
Han et al. (2011)	Carbon black / Water	50-500 nm	up to 7.5 vol%
He et al. (2011)	TiO_2/ ,CNT/H_2O	5–10 nm (TiO_2), 10–50 x 100–1000 nm (CNT)	4.3 wt% (TiO_2), 0.25, 0.5, 1 wt% (CNT)
Sani et al. (2011)	SWCNHs / EG	2-5 x 30-50 nm	0.06 g/L
Mercatelli et al. (2011)	SWCNHs / Water (SDS)	Dahlia-like and bud-like shapes	0.3 g/L
Mercatelli et al. (2011)	SWCNHs / Water, Glycol	Dahlia-like and bud-like shapes	0.005 - 0.06 vol%
Gan & Qiao (2012)	Al Al_2O_3 / Ethanol	25 nm(Al_2O_3) 80 nm (Al)	0.1 wt%
Jai Poinern et al. (2012)	fCNSs / Water	210 nm	n/a
Saidur et al. (2012)	Al / Water	1–20 nm	0.1–8.0 vol%
Mercatelli et al. (2012)	SWCNHs / Water	2-5 x 30-50 nm	0.3 g/L
Meng et al. (2012)	MWCNTs / Glycol	n/a	0.5, 1.0, 2.0, 4.0 wt%
He et al. (2013)	Cu / Water (surfactant)	25 nm	0.02 - 0.001 vol%
Lee & Jang (2013)	MWCNTs / Water	53 nm	0.0005–0.005 vol%
Zhu et al. (2013)	AlN, TiN, ZrC, ZnO / Water, Dispersant, E80 Arabic gum	40 nm (AlN), 29 nm (TiN), 40 nm (ZrC), 10nm (ZnO)	0.02,0.06 (AlN), 0.02 (TiN), 0.1 (ZrC), 0.02 (ZnO) vol%
Zhang et al. (2014)	Ni/C, Ni, Cu / Ionic liquid (HMIM)	40 nm	10 - 40 ppm

Hordy et al. (2014)	MWCNTs / Water, PG, Therminol VP-1	30 x 4000 nm	0 - 53 mg/L
Sajid et al. (2014)	Al_2O_3 / Water	13 nm	0.03, 0.05 and 0.08 vol%
Xuan et al. (2014)	TiO_2, TiO_2-Ag / Water	20/30 nm	0.5, 1.0, 1.5 vol%
Said et al. (2014)	TiO_2, Al_2O_3 / Water (various surfcatant)	21nm (TiO_2) 13 nm (Al_2O_3)	0.1, 0.3% vol%
Karami et al. (2014)	MWCNTs / Water	10 x 5000–10000	0 - 150 ppm
Hordy et al. (2015)	MWCNTs / Water	31 x 4000 nm	220 mg/L
Liu et al. (2015)	Graphene / Ionic liquid [HMIM]BF4	n/a	0.0005 - 0.01 wt%
Wu et al. (2015)	Si, SiC core and Au, Ag, Cu, Al shell / Water	n/a	n/a
Milanese et al. (2016)	Al_2O_3, CuO, TiO_2, ZnO, CeO_2, $Fe2O_3$ / Water	n/a	0.05, 0.1, 0.5, 1 vol%.
Karami et al. (2016)	CuO / EG and Water (30:70)	< 40 nm	0.01 vol%
Menbari & Alemrajabi (2016)	CuO and γ-Al2O3/ Water, EG, EG and water (mixture)	<100 nm (CuO) <40 nm (γ-Al_2O_3)	0.02 - 0.06 (γ-Al_2O_3) 0.0005 - 0.002 (CuO) vol%
Song et al. (2016)	functionalized Al2O3 / Water, ethyl alcohol	30 nm	0.01 vol%
Menbari et al. (2016)	CuO and γ-Al_2O_3/ Water, EG, EG and water (mixture)	<100 nm (CuO), <40 nm (γ-Al_2O_3)	0.02 - 0.06 (γ-Al_2O_3) 0.0005 - 0.002 (CuO) vol%

Taylor et al. [224] experimental and theoretical investigated the optical properties of different fluids (Graphite, Al, Cu, Ag, Au suspended in water or Therminol VP-1,). The results of this study reveal that for nanofluid layer thickness greater than 10 cm and particles volume fractions less than 10^{-5} ppm, over 95% of incident sunlight can be absorbed. Absorption at shorter wavelengths occurs due to the presence of the nanoparticles whereas at longer wavelengths it occurs mostly in the base-fluid. *Saidur et al.* [225] investigated the optical performance of four nanofluids with different concentrations of aluminium particles suspended in water. Despite

the lower extinction coefficient, absorption in visible light and shorter wavelengths was enhanced. The extinction coefficient resulted linearly proportional to the volume fraction of the nanoparticles in the suspension. *Gan and Qiao* [226] investigated the radiative properties of various nanofluid fuels (Al and Al_2O_3 in ethanol) for combustion systems, or to be used to directly collect solar thermal energy. They demonstrated that radiation absorption can be significantly enhanced by adding a small amount of nanoparticles such as Al to the base-fluid. However, at high particle-loading rates, such enhancement was mitigated by the increasing aggregation of nanoparticles. *He et al.* [227] measured the transmittance of Cu–H_2O nanofluids over the solar spectrum (250–2500 nm). The factors influencing transmittance of nanofluids, such as particle size, mass fraction and optical path were investigated. The transmittance of Cu–H_2O nanofluids (0.1 wt.%) was closes to zero, and the highest temperature of it can increase up to 25.3% compared with deionized water. In the study presented by *Zhu et al.* [228], an investigation on thermal radiative properties of different nanofluids (AlN, ZnO, ZrC, and TiN – water suspensions) have been performed. The effects of dispersants, mass fractions, and nanoparticle materials on the radiative properties of nanofluids within the wavelength range from 300 nm to 2500 nm were analysed. It resulted that dispersants can reduce the transmittance of water by less than 5 % within the visible spectrum. The solar weighted absorptances of AlN-, ZnO-, ZrC-, and TiN-water nanofluids were 45 %, 31 %, 87 %, and 99 %, respectively, when the liquid film was 10 mm thick. ZnO- and AlN-water nanofluids were semi-transparent in the wavelength range of 300 nm to 1400 nm and opaque in the wavelength range of 1400 nm to 2500 nm, whereas ZrC- and TiN-water nanofluids were able to absorb most of the solar radiation. *Zhang et al*[229] characterized the solar radiation absorption of ionic liquid-based nanofluid with different nanoparticle (Ni/C, Ni, Cu) with similar average size at the same volume fraction of 10 ppm. They observed that the optical absorption property can be greatly enhanced by adding a low volume fraction of nanoparticles (10 ppm to 40 ppm). Ni/C nanofluid exhibits the lowest transmittance and highest extinction coefficient as compared with those containing Ni and Cu nanoparticles.

Other researchers have investigated the use of nanofluids containing metallic oxide as direct absorption media for solar radiation. The paper of *Sajid et al.* [230] investigated the effect of time on optical properties of water-based alumina nanofluid. They noted a significant decrease

with time in the extinction coefficient of nanofluid within visible to near-infrared region. *Said et al.* [231] compared the optical properties of TiO_2 and Al_2O_3 water-based nanofluid. After the best surfactant for both nanofluids, it has been observed that TiO_2 nanofluids higher extinction coefficient for a wide range of wavelengths compared to that of Al_2O_3 based nanofluid although they are less stable. Recently, *Milanese et al.* [232] investigated the optical behaviours of different oxide nanoparticle (Al_2O_3, CuO, TiO_2, ZnO, CeO_2, Fe_2O_3) in aqueous solution. Although it has been noted some differences among the nanofluids, in all measurements the transmittance rises passing from visible to infrared region. In some cases, the extinction distance increased up to values larger than the typical thickness of solar collectors. The best results have been obtained with TiO_2 nanoparticles, which, at very low concentration (0.05 vol%), were capable to absorb completely solar radiation within 1 cm of depth. Analysis of the optical properties for absorption of solar radiation of copper oxide in ethylene glycol and water mixture (30%:70%) was performed by *Karami et al.*[233]. The absorbed energy fraction of CuO 0.01%vol nanofluid resulted four times greater than that of base-fluid in the whole wavelengths for solar energy , ranging from 200 nm to 2500 nm. *Song et al.* [234] conducted an investigation on optical properties of alumina nanofluids with different aggregation properties. In this study, they were able to investigate the underlying correlation between the size distribution of the aggregate in nanofluid and their resulting absorbance. Particle size distribution resulted an important factor affecting optical property of nanofluid. It was found that inhibited aggregation and resultant smaller aggregated particle size could lead to larger absorption coefficient.

At the beginning of the last decade, several authors have studied different shapes and structures of carbon-based nanoparticles to enhance the optical properties of the base-fluid. In the following the main results of the optical characterization of carbon-based nanofluids are presented, except for nanofluid with Single-wall Carbon Nanohorns which will be discussed in a separated Paragraph. The work of *Han et al.* [235] revealed that carbon black nanofluids show a good absorption ability of solar energy and could effectively enhance the solar absorption efficiency. For volume fraction up to 6%, carbon black nanofluid exhibits amply enhanced absorption of solar radiation in the wide range of the solar spectrum (200–2500 nm). Nanoparticles of functionalized carbon nanospheres (fCNS) have been studied by *Poinern et*

al. [236]. All the fCNS nanofluids had favourable photothermal responses to solar irradiation over the exposure period, showing the potential to improve the photothermal properties of the solar absorbing fluid. In their study, *Lee and Jang* [237] reported that the extinction coefficient of multi-wall carbon nanotubes (MWCNTs) glycol-based nanofluids linearly increases from 0.6 cm^{-1} to 3.83 cm^{-1} with the increase in volume fraction (0.0005–0.005 vol%) within 633 nm wavelength. The influences of the mass fraction of MWCNTs and temperatures on photothermal properties, thermal conductivity and rheological behaviour were investigated by *Meng et al.* [238]. Strong absorption has been observed at a wavelength range from 200 nm to 2500 nm. With 0.5 wt% nanofluids, 18% enhancement of photothermal conversion efficiency as compared to that of base-fluid. An experimental study to investigate the light-heat conversion characteristics of two nanofluids TiO_2 and CNT in water suspension were performed by *He et al.* [239]. Tests were conducted under two different weather conditions. The experimental results showed a very good light-heat conversion characteristic of the CNT-water nanofluid with the weight concentration of 0.5%. *Karami et al.* [240] reported a substantial increase in the extinction coefficient when a small amount of MWCNTs is added into the base-fluid (water). Strong absorption bands for these nanofluids at 900–1000 nm and again at 1200 nm have been observed. At nearly 1400 nm the nanofluids are essentially opaque to incoming radiation, which are similar to the base-fluid. The presence of 150 ppm MWCNTs increases the extinction coefficient of pure water by about 4.1 cm−1. *Hordy et al.* [241] studied the optical and stability properties of MWCNT nanofluid with different base-fluid (water, propylene glycol and Therminol VP-1). High optical absorption in solar spectrum range has been observed. Long-term stability (up to 8 months) at room temperature has been demonstrated for the glycol-based nanofluids. After heating up to 85°C and 170°C, no particle agglomeration has been found for the aqueous and glycol-based nanofluids, respectively. *Liu et al.* [242] combined numerical and experimental studies to predict temperature profiles based on direct absorption, convective heat transfer loss and thermal re-emission at high temperatures by graphene-ionic nanofluids. In their work, a one-dimensional transient heat transfer model was developed. The results showed that the receiver efficiency increases with the solar concentration and receiver height, but conversely with the graphene concentration under concentrated incident solar intensity.

The optical behaviour of composite nanofluids was firstly investigated by *Xuan et al.* [243] comparing the optical properties of TiO_2, Ag and TiO_2/Ag composite nanoparticles suspended in water. Due to the localized surface plasmon resonance (LSPR) effect excited on the Ag surface, the optical absorption of TiO_2/Ag plasmonic nanofluid was remarkably enhanced. Experiments revealed that TiO_2/Ag plasmonic nanofluid exhibits a higher temperature compared with that of TiO_2 based nanofluid. The effect of nanoparticle concentration on the photothermal performance of TiO_2/Ag plasmonic nanofluid was also studied in this paper. *Wu et al.* [244] investigated the optical and thermal radiative properties of plasmonic nanofluids containing composite nanoparticles with Si, SiC cores and Au, Ag, Cu and Al shells. Their results revealed that through an appropriate selection of composite radius ratio with required size and concentration of the nanoparticles, the effect of localized surface plasmon resonance could be fully utilized for efficient solar energy absorption at visible and infrared wavelengths. *Menbari et al*. in two different works [245,246] investigated the optical behaviour of a new class of oxide-based nanofluids (γ-Al_2O_3/CuO binary nanofluids) for direct absorption. From their results, it can be concluded that any changes in each component (CuO and γ-Al_2O_3) affect both the optimal conditions of stability and the properties of the nanofluid. The extinction coefficient of the binary nanofluids is approximately equal to the sum of the extinction coefficients of the constituent components. Optical coefficients were shown to be direct functions of the nanoparticle volume fraction. The extinction coefficient of the binary nanoparticles dispersed in water is greater than those of the binary nanoparticles dispersed in ethylene glycol or the mixture of ethylene glycol–water.

5.1.2 Single-Wall Carbon Nanohorns-based nanofluid

Single-wall Carbon Nanohorns (SWCNHs) are tiny graphene sheet, wrapped to form a horn-shaped cone with a cone opening angle of around 20°. These SWCNHs are derived from single-wall carbon nanotubes and ended by a five-pentagon conical (half-fullerene) cap with about 30–50 nm in tubule length and about 3–5 nm in diameter [247]. Generally, thousands of SWNHs associate with each other to form the ‘dahlia-like' and ‘bud-like’ structured aggregates which have an average diameter of about 80–120 nm. The former consists of tubules and

graphene sheets protruding from its surface like petals of a dahlia, while the latter is composed of tubules developing inside the particle itself [248] (Figure 115).

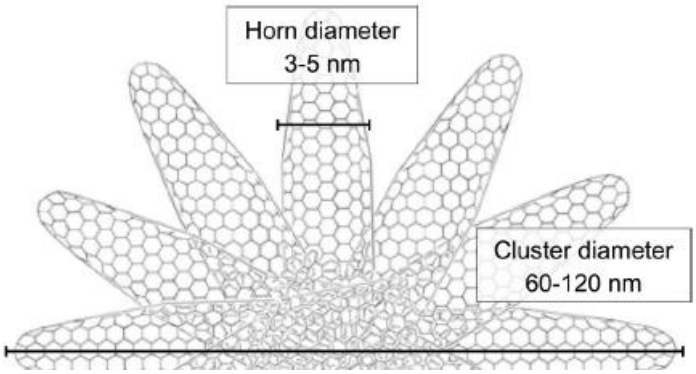

Figure 101 – Graphic representation and dimensions 'dahlia-like' structured aggregate of single-wall carbon nanohorns (SWCNH). (Carbonium [249] *Padova, Italy).*

The absence of potentially toxic metal catalyst in the synthesis of SWCNHs and their mass production at room temperature are two key advantages of carbon nanohorns over carbon nanotubes [250]. Furthermore, their dispersion in water is favourited due to their heterogeneous surface structure.

The use of single-wall carbon nanohorns for energy applications was recently reviewed by *Zhang et al.* [251]. SWCNHs are promising candidates as nanoparticles for nanofluid in DASCs, among other applications. *Sani et al.* [252] investigated the optical and thermal properties of nanofluids consisting in aqueous suspensions of single-wall carbon nanohorns at different concentrations, from 0.001 g L^{-1} to 0.05 g L^{-1}. The observed nanoparticle-induced differences in optical properties appeared promising, leading to a considerably higher sunlight absorption. The light transmittance level of the nanofluids decreased significantly even at very low concentrations (Figure 102). Furthermore, they found that the thermal conductivity of the nanofluids was higher than pure water. At 0.1 g L^{-1} SWCNHs concentration the thermal conductivity increased up to 10% with respect to that of water. The authors concluded that both these effects, together with the possible chemical functionalization of carbon nanohorns, make these nanofluids very interesting for increasing the overall efficiency of the sunlight exploiting device.

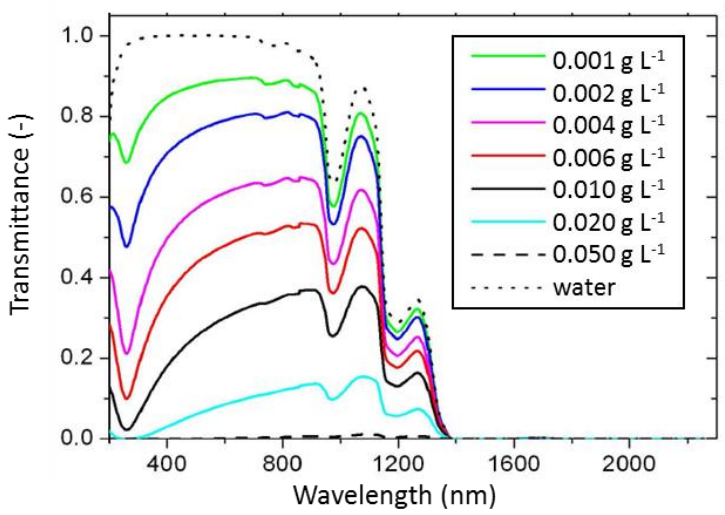

Figure 102 – Transmittance spectra for SWCNHs in water for different nanoparticle concentration. The pure water transmittance spectrum is also shown, for comparison (dotted black line) [252].

Further research of *Sani et al*. [253] disclosed that water could be replaced by glycols or water/glycol mixtures to protect against freeze damage and/or to increase the temperature for high-temperature solar collectors. They concluded that even with glycol as base-fluid, SWCNH could enhance remarkably the sunlight absorption with respect to pure glycol. Moreover, SWCNHs-ethylene glycol suspension possessed longer time stability and lower ability to agglomerate than amorphous carbon black particles-ethylene glycol suspensions. The photonic properties improvement of SWCNHs-based nanofluid can lead to a significant increase in the light extinction level even at very low concentration. A comparison of the absorbing energy capabilities of SWCNH suspensions in ethylene glycol (solid line and solid symbols) and water (dashed line and hollow symbols) is provided in Figure 103. *Mercatelli et al.* [254,255] investigated the potentiality of utilizing SWCNHs with different agglomeration shapes in two different base-fluids (water and ethylene glycol) and nominated that as a good choice for exploiting solar radiation in DASCs. Only about 5% of the total extinction is scattered by SWCNHs. Scattering behaviour of SWCNHs shows little dependence on the agglomerated nanohorns morphology (dahlia-like or bud-like). In a sequent publication, *Mercatelli et al.* [254] continued their work on SWCNHs based nanofluid. They concluded that these nanoparticles have a very low scattering albedo (not higher than 5% for red and near-infrared wavelengths) as compared to Indian inks (about 10% to 16% scattering) and therefore the

absorption effect was strongly prevailing. Furthermore, SWCNHs suspensions show good stability properties as confirmed by preliminary measurements they performed over a period of 1 year

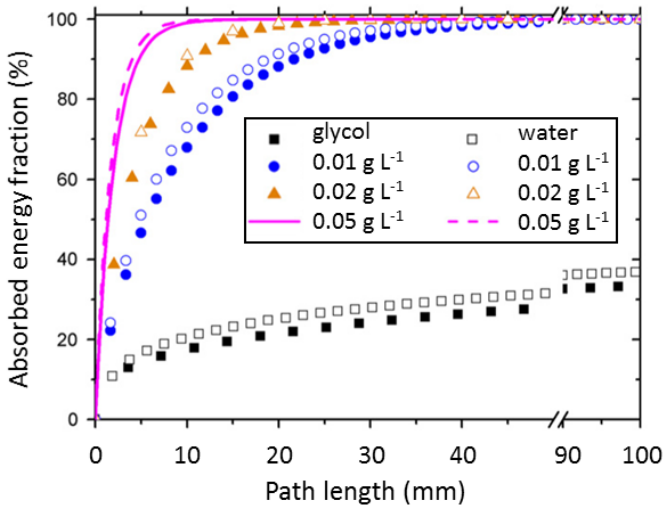

Figure 103 – Comparison of the absorbing energy capabilities of SWCNH suspensions in ethylene glycol (solid line and solid symbols) and water (dashed line and hollow symbols) [253].

Recently, *Moradi et al* [256] performed numerical simulations of a nanofluid-based solar receiver. The results showed that the use of nanohorn-based nanofluids implied an increase in temperature distribution inside the fluid which had its maximum inside the bulk fluid. This result suggested that such nanofluid-based solar collectors are quite competitive compared to traditional collectors employing black surface tubes, where the maximum temperature is always reached at the surface. *Sani et al.* found that the overall sunlight absorption properties of SWCNHs-based nanofluids could be improved by silver nanoparticles which present good thermal properties. Thanks to the favourable and different spectral characteristics of SWCNHs and silver nanoparticles, the optical properties of the resulting nanofluid can be tuned by changing both absolute and relative concentrations of nanoparticles, according to the desired absorption length. This result is interesting for designing solar receivers with novel geometries and optimized performances.

Experimental stability analysis of SWCNHs-water nanofluids was carried out by *Fedele et al*. [257], at different concentrations, i.e. 0.01%, 0.1%, 1% by mass. The nanoparticles were mechanically dispersed in water at different concentrations. In order to stabilize the nanofluids, SDS was added as a dispersant in different concentration. The ratio between nanoparticles and dispersant mass was 1:1. A ratio of 1:3 was also considered for the lowest concentration (0.01% by mass). Samples were measured almost every day for 30 days without and after shaking the fluid, to evaluate the size distribution changes due to natural and the size distribution changes after mechanically recovering the settled particles. In the latter case if a change in nanoparticles size occurs, indicating a nanoparticle's aggregation, then it affects the thermophysical properties of the nanofluid. The suspension containing 0.01 wt.% of SWCNHs and 0.03 wt.% of SDS showed a very stable behaviour for 39 days. Water-SWCNHs containing 0.1 wt.% SDS showed a constant diameter for both the static and stirred sample even after 25 days, suggesting a good stability of the fluid. Analogous behaviour was shown by water-SWCNHs containing 1 wt.% SDS. In the work of *Bobbo et al.* [258] viscosity data of the same nanofluids considered by *Fedele et al.* [257] were presented. The experimental measurements were performed at atmospheric pressure and temperatures ranging between 283.2 K and 353.2 K. The nanofluid showed a Newtonian behaviour at each composition. Negligible variations on the viscosity of the nanofluids in relation to water were observed at nanoparticles concentrations up to 0.1% in mass fraction. On the contrary, a significant increase was measured for nanoparticles concentration of 1% in mass fraction, making this nanofluid unsuitable for heat transfer applications. The thermal conductivity of the nanofluid presenting 0.1% concentration by mass resulted very similar to that of pure water.

5.2 Overview on the application of nanofluid in DASCs

Several reviews on the application of nanofluid in solar energy were published in the last years. In the paper of *Mahian et al.* [259], current applications, future work and challenges of nanofluids in solar energy have been discussed. They concluded that experimental and numerical studies on solar collectors, in some cases, have been shown that the efficiency could be increased remarkably by the use of nanofluids.

Javadi et al. [204] surveyed the main experimental and numerical works on the improvement of solar collectors by using nanofluids. The review of *Verma et al.* [260] focused on the progress of nanofluid application in solar collectors. Both experiments and models were reviewed. *Sarsam et al.* [261] limited their revision on the use of nanofluids in conventional solar collectors. After providing an overview of the experimental and numerical works that can be found in the literature, the authors identified the most significant challenges on using nanofluids in flat plate solar collectors. *Muhammad et al.* [262] reviewed the use of nanofluids as heat transfer fluids and as volumetric absorbing fluids for enhancing the thermal performance of stationary solar collectors. The authors also discussed the impact of nanofluid usage in a solar collector based on economic and environmental viewpoints.

Other reviews on nanofluids in solar energy were presented by *Bozorgan and Shafahi* [263], *Abdin et al.*[264]*, Nagarajan et al.* [265], *Hussein* [266] and *Hossain et al.* [221].

5.2.1 Numerical studies on nanofluids as absorbing media in DASCs

From all these reviews, it can be observed that in the last decade much effort has been made to perform both experimental and numerical studies. The most relevant numerical studies on the application of nanofluids in DASCs are presented in this paragraph and listed in Table 11.

Tyagi et al. [267] studied theoretically the use of Al_2O_3 water-based nanofluids in low-temperature DASC. Using a steady-state two-dimensional model for heat transfer, they investigated the effects of different parameters on the efficiency of the collector. The results revealed that the efficiency increases slightly with an increase in the size of the nanoparticles.

Table 11 – Summary of the numerical studies on the application of nanofluids for direct solar absorption.

Investigator(s) (Year)	Application	Nanoparticles / Base-fluid
Tyagi et al. (2009)	Microscale DASC	Aluminium / Water
Otanicar et al. (2010)	DASC	CNTs, graphite, and silver / Water
Khullar and Tyagi (2011)	PTC DASC	Al / Water, Al / PG, Al / EG, Al / Therminol® VP-1
Khullar et al. (2012)	PTC DASC	Aluminium / Therminol® VP-1
Veeraragavan et al. (2012)	Concentrating DASC	Graphite / Therminol® VP-1
Ladjevardi et al. (2013)	DASC	Graphite / Water
de Risi et al. (2013)	Transparent PTC receiver	CuO+Ni / Nitrogen
Luo et al. (2014)	DASC	TiO_2, Al_2O_3, Ag, Cu, SiO_2, graphite, CNT / Texatherm® oil
Rahman et al. (2014)	Quarter-circular DASC	MWCNTs / Water
Parvin et al. (2014)	DASC	Cu / Water
Hewakuruppu et al. (2015)	DASC	MWCNTs / Water
Cregan and Myers (2015)	DASC	Al / Water
Gorji & Ranjbar (2015)	DASC	Graphite / Water
Moradi et al. (2015)	DASC	SWCNHs / Water
Chen et al. (2016)	DASC without mass flow	Ag, Au, TiO_2 / Water
Delfani et al. (2016)	DASC	MWCNTs / Water + glycol
Gorji and Ranjbar (2016)	DASC	Graphite, magnetite and silver / Water
Jeon et al. (2016)	DASC	Au-nanorods / CTAB
Jin et al. (2016)	DASC without mass flow	Au / Water
Lee et al. (2016)	DASC	MWCNTs / Water
Li et al. (2016)	Concentrating DASC	MWCNTs / Water
Menbari et al. (2016)	PTC DASC	CuO / Water

Otanicar et al. [222], based on the work of *Tyagi et al.* [267], have numerically evaluated the thermal performance of DASC for low-temperature applications based on nanofluids made

from a variety of nanoparticles. In addition, the numerical model was compared with experimental data of a solar collector with direct absorption nanofluids. The experimental and numerical results demonstrated an initial rapid increase in efficiency with volume fraction, followed by a levelling off in efficiency as volume fraction continues to increase. They observed efficiency improvements up to 5% in solar thermal collectors by utilizing nanofluids for the absorption mechanism. *Khullar and Tyagi* [268] numerically investigated aluminium nanoparticles dispersed in different base-fluids (water, ethylene glycol, propylene glycol and Therminol® VP-1) for their suitability as working fluid in direct absorption linear parabolic solar collectors finding very similar results for all four nanofluids. In the work of *Khullar et al.* [269], the idea of harvesting solar radiation through the usage of nanofluid-based parabolic solar concentrating collectors has been numerically explored. *Veeraragavan et al.* [270] have analytically investigated the effect of heat losses, solar concentration, nanoparticle loading and channel height on the efficiency of a volumetric flow receiver. Absorption of the solar radiation was modelled as a volumetric heat release inside the flowing nanofluid. They apply the developed model to a case study with graphite nanoparticles suspended in Therminol® VP-1. *Ladjevardi et al.* [271] investigated the applicability of graphite nanofluids in direct solar energy absorption. They developed a numerical code to study the effects of particles size and volume fraction on the extinction coefficient and efficiency of the solar collector.

A model of transparent PTC based on gas-phase nanofluids has been presented by *de Risi et al.* [272]. The proposed solar collector has been modelled by means of a discretization in space under the assumptions of quasi steady-state conditions. The model has then been used to run an optimization procedure to define the best geometry of the receiver. In the work of *Luo et al.* [273], simulations were performed to investigate the performance of oily suspensions of different nanoparticles as direct absorbers. *Rahman et al.* [274] proposed an innovative design of quarter-circular plate DASC with variable tilt angle and solid volume fraction of carbon nanotube (CNT) nanofluids. A wide range of solid volume fraction and tilt angle was numerically explored. A numerical investigation on the heat transfer performance and entropy generation of forced convection through a DASC was conducted by *Parvin et al.* [275]. *Hewakuruppu et al.* [276] introduced the concept of a nanofluid-based selective DASC, where short wavelength absorption was maximized, but long wavelength emission was minimized, as

happened with advanced surface absorbers. The limitations in developing selective direct absorption solar receivers have been numerically evaluated. In the paper of *Cregan and Myers* [277], an approximated analytical solution to the steady-state, two-dimensional problem for the efficiency of an inclined nanofluid-based DASC was presented. For the first time, the model included all the wavelength-dependent optical parameters. *Gorij and Ranjbar* [278] numerically determined the flow of nanofluid and the temperature distribution in a DASC using a computational flow dynamics (CFD) model. Response surface methodology was applied to understand the effect of varying collector dimensions on thermal efficiency and entropy generation of the DASC design. *Moradi et al.* [256] performed a three-dimensional analysis of the flow and the temperature fields in a DASC using a CFD tool. A one-dimensional transient heat transfer analysis was carried out by *Chen et al.* [279] to analyse the effects of the nanoparticles volume fraction, channel height, irradiation time, solar flux, and nanoparticles material on the photothermal conversion efficiency of a solar collector without mass flow. To validate the model, the numerical results were compared with the experimental data obtained with silver nanofluids. The thermal performance of a low-temperature flat plate DASC has been numerically and experimentally investigated by *Delfani et al.* [280]. A two-dimensional model has been developed to examine the effects of internal emissivity of the bottom wall, nanoparticles volume fraction, collector height and nanofluid mass flow rate on the temperature distribution inside the collector. *Gorji and Ranjbar* [281] presented a numerical and experimental study focused on the application of nanofluids made from a variety of nanoparticles in a low-flux DASC. A numerical model was developed by solving the radiative transfer and the energy equations in ANSYS® Fluent 15.0 adopting a non-grey band discrete ordinates (DO) method. The model was then validated through experiments with a lab-scale DASC. *Jeon et al.* [282] presented a numerical study on the use of a blended plasmonic nanofluid in a flat plate volumetric solar collector. The numerical model was developed using COMSOL® Multiphysics. In order to evaluate the photothermal conversion efficiency of gold nanofluids in a cylindrical tube without mass flow, *Jin et al.* [283] employed a new transient three-dimensional model. The radiative transfer equation adopting Mie's scattering theory and heat transfer equations were solved using a finite element method powered by COMSOL® Multiphysics. The actual solar spectrum on the ground was implemented in the model. The results of the model were compared with the experimental data obtained under natural solar

irradiation conditions. The work of *Lee et al.* [284] provided a comparative investigation of the thermal efficiency of a volumetric receiver using MWCNTs - water nanofluid and a surface receiver with conventional fluid. Experiments were conducted to validate the numerical results. *Li et al.* [285] experimentally and numerically investigated the potential to deliver heat in the range of 100 °C – 250 °C using a low-profile concentrating solar thermal collector. They compared the thermal performance of a cylindrical volumetric absorber filled with a MWCNTs based nanofluid and a conventional tubular surface absorber using concentrating Fresnel lenses and compound parabolic reflectors. The CFD model was developed in ANSYS® CFX. In the publication of *Menbari et al.* [245], both analytically and experimentally investigations on the effects of the volume fraction and the mass flow rate of a CuO – water nanofluid on the efficiency of a direct absorption PTC were presented. A theoretical descriptive model was initially developed and later it was extended to solve the coupled radiative transfer and energy equations. Finite difference technique was employed for the numerical solution of the problem. Standard terrestrial solar spectral irradiance distribution according to ASTM G-173-03 [286] was used in this study.

5.2.2 Experimental studies on nanofluids as absorbing media in DASCs

The study of the available open literature reveals that, to date, the experimental investigation of nanofluids in full-scale DASCs is in its infancy and a large effort is required to promote the development of this technology and solve existing issues. Experimental works available in literature mainly deal with tests on laboratory scale solar collectors which provide critical insights into the photothermal conversion mechanisms and useful indications for the design of larger DASCs. Tests under solar simulators at low and medium solar concentrations and no-flow conditions have been performed at low temperature (below 100°C). They involved the measurement of temperature distribution in the fluid bulk over time and stagnation temperature or peak temperature achieved. In some cases, an efficiency defined as the ratio of internal energy increase to the total incident solar energy in a given time frame is also reported. *Lenert and Wang* [287] performed tests under solar simulators at medium solar concentrations and no-flow conditions and at low temperature (below 350 K). The outcomes of their study provided a perspective about the best usage of nanofluids as volumetric receivers in concentrated solar

applications. In the work of *Chen et al.* [288], experiments allowed assessing the optimum nanoparticles concentration in terms of peak temperature, photothermal conversion efficiency and specific absorption rate of gold, silver and gold-silver blended based nanofluid irradiated by a low concentrating (10 Suns) solar simulator. Initial values of the specific absorption rate, which describes the energy absorbed per unit volume of nanoparticle and time under no-flow conditions, may represent a qualitative parameter to preliminary assess the application of a nanofluid in a DASC. These works allowed assessing the optimum nanoparticle concentrations or size, leading to higher stagnation or peak temperature in a given nanofluid and comparing the absorption properties of different nanofluids. Similar tests have been carried out in no-flow devices with larger dimensions such as transparent glass cells [289] or glass-in-glass evacuated tubes, as in the work of *Chen et al.* [290] where sunlight absorption of silver nanofluids in no-flow glass-in-glass evacuated tubes has been experimentally investigated. *Jin et al.* [283] reported that the efficiency obtained using gold nanoparticles in water inside a glass-in-glass evacuated tube under natural sunlight decreased with increasing solar irradiance. An experimental study under stagnation was performed by *Xu et al.* [291] using water with magnetic iron nanoparticles as the working medium in glass-in-glass evacuated tubes. Some authors presented the trend over time of the specific absorption rate, which compares the absorption capability of the nanofluid to that of the pure base under no-flow conditions. Actually, initial values of specific absorption rate may represent a qualitative parameter to preliminary assess the application of a nanofluid in a DASC.

In few papers on no-flow laboratory and full-scale collectors, direct steam generation in nanofluids under concentrated solar irradiance has been analysed through measurements of temperature distribution, mass change or water evaporation rate and steam pressure [292-295]. Researchers agreed that, given the solar flux achievable in existing solar collectors, the steam generation is unlikely due to nanobubbles formation around the particles whereas it is linked to the highly localized solar absorption in the focal area, according to the mechanisms of classical nucleation theory. In experimental investigations with nanofluids flowing across lab-scale devices, the mass flow rate is low enough so that the thermal efficiency can be defined considering measurable temperature rises. *Otanicar et al.* [222] performed tests with aqueous nanofluids containing graphite nanoparticles, silver nanoparticles and carbon nanotubes at low

temperature (up to 45 °C) on a direct absorption micro-collector under 1000 W m^{-2} irradiance. *Lee et al.* [284] compared the performance of a surface absorption and a direct absorption lab device under concentrated irradiance (22 Suns). A suspension of multi-wall carbon nanotubes in water has been considered for these tests. *Taylor et al.* [222] tested a direct absorption mini-receiver of a parabolic dish concentrating collector having a geometric concentration ratio of around 400 Suns and working with graphite nanoparticles in Therminol oil at temperatures up to 250 °C. The results univocally showed that it exists an optimum nanoparticle concentration beyond which the efficiency levels off or even decreases. In fact, at low particle mass fractions, part of the incident irradiance is not absorbed by the nanofluid. On the other hand, at high particle concentrations, nanofluid may become unstable, while absorption occurs at the top layer of the nanofluid, resembling thus the thermal behaviour of a conventional surface absorber. There are few studies concerning the application of nanofluids in small prototypes of full-scale DASCs. To the best of the author' knowledge, available investigations on nanofluid-based non-concentrating direct absorption technologies regard only flat plate solar collectors. *Gupta et al.* [296] investigated the performance of a full-scale DASC under natural sunlight with an alumina-based aqueous nanofluid. The collector consisted of a glass box sustained by a wooden frame and had a size of 1.54 m x 0.9 m x 0.2 m. Tests were performed according to a standardized steady-state test procedure, within a timeframe short enough to avoid nanoparticles aggregation and sedimentation. Flow rates from 1.5 to 2.5 L min^{-1} were considered and higher performance was achieved at 2 L min^{-1} and an alumina concentration of 0.005 vol%. *Karami and coworkers* [280,297] tested a DASC for domestic water heating with either CuO nanoparticles or multi-wall carbon nanotubes in water and ethylene glycol mixture. The 0.6 m x 0.6 m prototype consisted of a toughened glass embedded in an aluminium body and presented a channel depth of 0.01 m. Nanoparticles volume fractions from 25 to 100 ppm were employed in test runs, performed according to a standardized steady state method procedure. Data were collected around solar noon at nanofluids inlet temperatures from 30 °C to 50 °C and volumetric flow rates from 54 to 90 L h^{-1}. Using both nanofluids, the collector thermal efficiency increased with volume fraction and flow rate but with an asymptotic trend. The same prototype of volumetric flat plate collector and the same test procedure were considered by *Vakili et al.* [298] to investigate the application of three nanofluids with nanoplatelets weight fractions of 0.0005, 0.001 and 0.005, finding that the efficiency increased.

As a general trend, the efficiency curve for the investigated DASCs resulted as a straight line and exhibited high optical efficiency, up to 93% when using graphene nanoplatelets in water [298], but the stagnation point was at quite low reduced temperature differences, within 0.033 and 0.047 m^2 K W^{-1}.

With respect to the use of nanofluids as working fluids and direct absorbers in concentrating solar collectors, *Leong et al.* [299] observed that the researchers have been given small attention to these collectors. However, some the studies described in the literature concern applications in small prototypes involving low concentrated solar fluxes (lower than 12 kW m^{-2}) have been presented. *Muraleedharan et al.* [300] examined the performance of Al_2O_3 dispersions in Therminol with concentrations from 0.025 to 0.1 %vol and a constant flow rate of 0.5 L s^{-1}. The single-axis tracking collector comprised four linear Fresnel lenses (0.55 m x 0.18 m) focusing the direct solar irradiance on four evacuated glass-in-glass tube receivers with external and internal diameter of 15 mm and 10 mm, respectively. It was arranged in a test rig equipped with a storage tank, where the collector outlet temperature and the net stored energy were measured as a function of time. Results showed that using the highest nanoparticles concentration, the 28 liters tank temperature increased from 25°C to 130°C within 3.5 hours. *Li et al.* [301] compared the performance of a surface (black-chrome coated copper tube) and a volumetric solar absorber (glass tube) arranged in a low-profile solar concentrating collector consisting of a linear Fresnel lens, a glass envelope, a compound parabolic concentrator and an absorber element with a geometrical concentration ratio of about 5 and with an internal tracking system. Suspensions of multi-wall carbon nanotubes in water and Therminol with a concentration of 50 mg L^{-1} were chosen as working fluids. Tests were carried out under standardized steady-state outdoor conditions at a mass flow rate of 0.02 kg s^{-1} and at inlet temperatures up to 250 °C, including the use of vacuumed and non-vacuumed absorbers and of borosilicate and ITO-coated low emissivity glass tubes. Results highlighted that the performance of the surface absorber was higher than that of the volumetric receiver. The authors pointed out that there is much room for reducing the heat losses in the direct absorption solar absorber while maintaining its cost-effectiveness as compared to a conventional surface absorber. *Menbari et al.* [245] presented the application of a CuO-water nanofluid in a direct absorption parabolic trough solar collector. The single-axis tracking parabolic concentrator had

a reflectance of 65%, an aperture width of 0.8 m and a length of 1 m. The evacuated tubular receiver consisted of two concentric glass tubes having a diameter of 36 mm and 20 mm, respectively. The estimated peak of concentrated solar flux was around 12 kW m^{-2}. Experimental tests were performed at inlet temperatures within 22°C - 25°C. The results indicated that the thermal efficiency of the concentrating collector increased with mass flow rate and nanoparticles volume concentration, achieving a maximum value of 50% at 100 L h^{-1} and 0.008 vol%. Similar trends were obtained by the same authors when studying the use of different binary nanofluids in the mentioned parabolic trough collector [246]. The nanofluids contained CuO and γ-Al_2O_3 in water and in a mixture of water and ethylene glycol. The results showed that that highest efficiency of 50% was achieved using the 0.2 vol % Al_2O_3 - 0.008 vol% CuO-water nanofluid at a mass flow rate of 100 L h^{-1} and an inlet temperature around 30°C.

5.3 Modelling of a direct absorption receiver under concentrated solar radiation

The application of aqueous suspensions of nanoparticles as volumetric absorbers in a concentrating direct absorption solar collector is numerically investigated. The suspension of single-wall carbon nanohorns (SWCNHs) in water is the chosen nanofluid. In numerical analysis such as computational fluid dynamics (CFD), the classical theory of single-phase fluids can be applied to a nanofluid, where its physical properties are taken as a function of properties of both constituents and their concentrations [302]. Here, the optical and thermal behaviours of the nanofluid are modelled for a single-phase fluid according to the properties available in the literature.

In order to gain a critical insight into the field application of direct absorption receivers under concentrated solar irradiance, a three-dimensional CFD model of a flat volumetric receiver is developed. The directional and spatial distribution of the concentrated solar radiation coming from a parabolic trough concentrator is applied to the receiver geometry. The radiative heat transfer equation (RTE) in the participating media is solved adopting the non-grey discrete ordinates (DO) method. The RTE, and the mass and momentum conservation equations are computed using the commercial package ANSYS® Fluent. The developed model is very useful to evaluate the effects of nanoparticles concentration, flow field and inlet temperature on the thermal performance of the direct absorption solar parabolic trough collector. From this numerical investigation, the guidelines for the design and optimization of a volumetric receiver for a solar concentrating collector are drawn. Moreover, the model is used to compare the calculated performance of the volumetric receiver and that of a selective surface receiver under the same operating conditions. An indirect experimental validation is performed by using measurements in the same parabolic trough concentrator.

5.3.1 Model description

The physical domain is a flat receiver for the direct absorption of solar irradiance. The receiver is conceived to be mounted on the focal region of the asymmetrical parabolic trough solar

concentrator installed at the Solar Energy Conversion Lab of the Department of Industrial Engineering at the University of Padua. Figure 104 reports a sketch of the receiver modelled in this study. With respect to the flow channel of the nanofluid, two clear low-iron glass sheets, having a thickness of 3 mm, form the upper wall (where the concentrated solar irradiance arrives) and the lower wall. The side wall consists of a polyether-ether-ketone (PEEK) frame, which contains the inlet and the outlet sections for the working fluid. PEEK is a semicrystalline thermoplastic with excellent mechanical and chemical resistance properties that are retained to high temperatures. The channel depth of the receiver can be set to 12 mm or 18 mm. The glass sheets are embedded in two stainless steel frames, which give mechanical stiffness to the structure. Both upper and lower windows have a width of 64 mm and a length of 500 mm. The configuration of the receiver has been designed with the primary aim of evaluating the optical performance of the nanofluid, thus, it is not aimed to maximize the efficiency of the photothermal process.

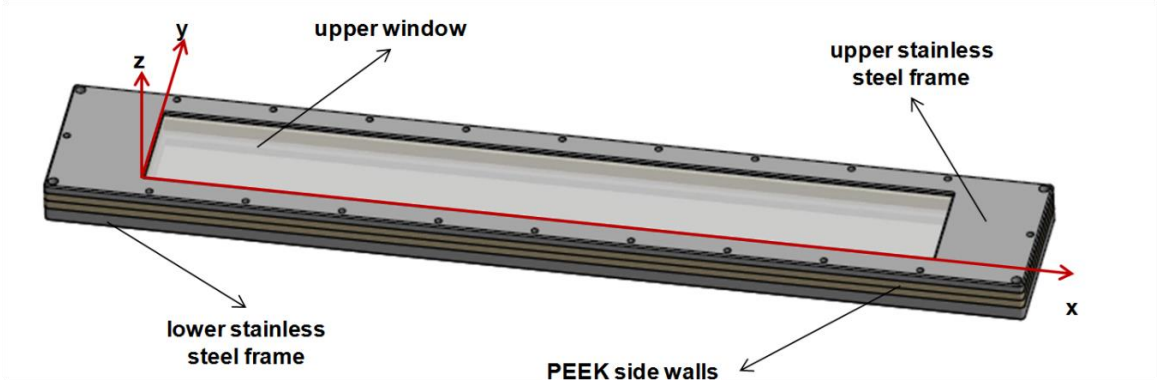

Figure 104 – Sketch of the receiver for direct absorption of solar concentrated irradiance and global Cartesian system employed in CFD modelling [303].

Assuming a steady-state, incompressible flow of a Newtonian fluid inside the receiver a solution of the Navier-Stokes equations is obtained numerically in a CFD code powered by ANSYS® Fluent. The shear stress transport (SST) formulation of the k-ω turbulence model is implemented in the model since it was reported to be more accurate and reliable for a wide class of flow regimes than the standard and the BSL k-ω models [304]. Since the Reynolds number in the simulations is up to 13000, the low Reynolds number correction to the turbulent

viscosity has been applied to account for the transitional flow regime. The effect of the gravity has also been considered in the model. The no-slip shear condition has been adopted at the fluid-wall interface.

When the source term *S* in the energy balance takes into account only thermal radiation, it can be expressed as [305]:

$$S = \int_0^\infty \alpha_\lambda(\lambda) \left(\int_0^{4\pi} I_\lambda(\lambda, \omega)\ d\omega \right) d\lambda - 4\pi \int_0^\infty \alpha_\lambda(\lambda)\, I_{bb,\lambda}(\lambda)\, d\lambda \qquad \textit{Eq. 5.1}$$

In Eq. 5.1, I_λ and $I_{bb,\lambda}$ are the radiation intensity and the blackbody re-emission intensity, α_λ is the spectral absorbance of the nanofluid, ω is the solid angle and λ is the wavelength of the radiation. To account for the energy source term, it is necessary to solve the Radiative Transfer Equation (RTE) which describes the balance of radiative energy through the scattering, absorption and emission due to the interaction with the participating media in the domain. In the nanofluid, the RTE is employed to evaluate the spectral attenuation of radiation within the depth of a semi-transparent particulate medium. According to what reported by *Modest* [306], the radiation intensity $I_\lambda(\check{r},\hat{s})$ for a steady-state, absorbing, emitting and scattering medium at the position $\check{r}$ in the direction $\hat{s}$ is given by:

$$\frac{dI_\lambda(\check{r},\hat{s})}{ds} = -(\alpha_\lambda + \sigma_\lambda)\, I_\lambda(\check{r},\hat{s}) + \alpha_\lambda I_{bb,\lambda}(T,\check{r},\hat{s}) + \left(\frac{\sigma_\lambda}{4\pi} \int_0^{4\pi} I_\lambda(\check{r},\hat{s})\ \Phi_\lambda(\hat{s}\cdot\hat{s}')d\omega \right) \qquad \textit{Eq. 5.2}$$

where σ_λ is the spectral scattering coefficient, Φ_λ is the scattering phase function and $\hat{s}'$ is the scattering direction vector. The finite volume method chosen for solving the RTE in ANSYS® Fluent is the discrete ordinates (DO) radiation method since it is appropriate to account for the optical complexity of the problem. The solution of the RTE adopting the DO method leads to a close coupling of surface temperature and radiative energy, due to the use of the same mesh for radiative transfer, energy, mass and momentum conservation problems. As reported by *Moghimi et al.* [305], this implies that the DO can be applied to complex geometries for different participating media such as non-grey, anisotropically scattering, non-isothermal, absorbing and emitting media. The present study concerns a direct absorption receiver, where

the concentrated radiation enters through a semi-transparent window and interacts with an absorbing, emitting and scattering participating medium. Due to the different optical properties of the involved materials, the energy equation and the radiative transfer equation are uncoupled, thus the energy and radiation intensities are solved one by one, assuming prevailing values for other variables. Within the considered wavelength range, the optical properties of the participating materials, i.e. glass and nanofluid, vary significantly, thus, they cannot be acceptably modelled as grey bodies. In this work, the spectral dependence of the optical properties of the participating media is captured by dividing the radiation spectrum of interest into different bands. Within each band, the media are assumed as having the optical behaviour of grey media. Then the non-grey DO model solves the radiation transfer equation for a number of discrete solid angles, each associated with a direction: the finer the angular discretization, the higher the computational effort. By changing the division of the octant of the angular space from 5 to 7 solid angles along the polar extent and by maintaining the 3 solid angles along the azimuthal extent, the model exhibits negligible effects (0.2%) on the thermal performance of the receiver. Moreover, a 3x3 pixelation is applied on each control angle, as recommended in this kind of problems [304].

Due to the presence of an incompressible flow, the pressure-based solver has been considered. In order to improve the convergence speed, the momentum equations and the pressure-based continuity equation are solved in a coupled manner using the SIMPLE algorithm together with a standard pressure spatial discretization due to the complex nature of the flow conditions involving turbulence. The Green-Gauss node based gradient is adopted since it is known to be more accurate than the cell-based gradient particularly on irregular unstructured meshes [304]. A second-order upwind spatial discretization scheme has been chosen to solve the energy problem to assure a more accurate solution. For the other scalar equations, a first-order upwind spatial discretization scheme is set.

A convergence criterion has been imposed on the residuals of the governing equations: they should be less than 10^{-5} for continuity and flow field parameters, less than 10^{-6} for discrete ordinate radiation intensities and less than 10^{-7} for energy equation. When these conditions are reached, the total heat flux balance is checked. In the simulations, the deviation for the heat flow rate is never above 1%.

The computational domain consists of the portion of volume from the inlet of the absorption region under the upper window to the outlet chamber realized between the PEEK layers downstream the absorption region, the two glass sheets, the stainless steel frames and the PEEK walls. This domain has been used for simulations to analyse the thermal performance of the present direct absorption solar collector. The inlet and the outlet sections are supposed adiabatic and a symmetry condition has been applied on the centreline plane of the receiver, to reduce the number of finite volume elements. ANSYS® ICEM has been employed for the mesh generation. A structured mesh is applied to the participating media. To model adequately the regions where the higher gradients of radiation intensity and velocity occur, a refinement of the mesh has been done near the upper windows and near the other solid walls of the fluid channel. The non-participating media, where only conduction heat transfer takes place, are meshed in an unstructured way. To evaluate the sensitivity of the numerical solution to the cells number, the results obtained from the meshes generated with 1.5×10^6 cells and 2.6×10^6 cells have been compared: no significant difference in terms of thermal performance of the receiver has been observed. Hence, in order to reduce the computational cost, the mesh including 1.5×10^6 cells has been adopted for all the simulations.

Preliminary CFD simulations considering the volume of fluid from the inlet pipe upstream the receiver up to one-third of the channel length has been conducted in order to obtain the velocity field profile at the inlet of the receiver for a given mass flow rate. An SST k-ω turbulence model has been included in these simulations as well as the gravitational effect. The obtained velocity profile and the inlet temperature have been applied as boundary conditions to the inlet section of the channel.

The heat losses on the external surfaces towards the surroundings are due to thermal convection and radiation. The temperature of the external free stream has been imposed equal to 300 K, while the sky temperature is set equal to 293 K. The emissivity of each material has been specified (for glass sheets, the external emissivity is set 0.9). As done in many previous publications [280-282], the external convective heat transfer coefficient is set equal to 10 W m^{-2} K^{-1}: this assumption is needed because external conditions may vary.

The solar direct irradiance incident onto the upper window of the receiver is derived from the previous study on the present asymmetrical concentrator. A value for the total optical error of 5 mrad has been prudently considered and the desired number of ray intersections has been set equal to $3x10^6$. The optical model in SolTrace [107] as Monte Carlo ray-tracing tool (see Chapter 3) is used to define a dimension of the front window the present receiver (64 mm wide) to achieve an intercept factor of 98%. A direct normal irradiance of 900 W m-2 has been assumed to calculate the reduced temperature difference and to define the solar flux distribution profile. The resulting incident radiant power is equal to 1234 W for all the simulated cases. Furthermore, the Monte Carlo ray-tracing tool helps in the definition of two input quantities: the average profile of the solar flux distribution and the direction of each ray hitting the upper glass surface along the receiver width. According to the generated mesh, a code has been developed in Matlab® environment to calculate the average direction of the incident concentrated irradiance on each facet of the upper glass sheet. These directions were then included as a boundary condition of the upper external surface. The resulting mean angle of incidence of the concentrated solar beams is around 24°. The profile of the concentrated solar flux distribution in a wavelength band is obtained proportionally to the average profile for the whole solar spectrum, considering the percent content of solar irradiance in each band.

The radiation spectrum considered in the model extends from 300 nm to 100000 nm, including the solar spectrum and the infrared wavelengths, in order to account for the thermal emission. The considered direct and circumsolar spectral irradiance are defined as given in the standard ASTM G-173 [286]. Assuming the reflectance of the parabolic mirror constant within the solar spectrum, the concentration of solar radiation entails only an increase of the spectral intensity proportional to the concentration ratio. According to this hypothesis, the incident direct irradiance is divided in the different wavelength bands implemented in the DO method.

Two types of glass have been considered for the model of the direct absorption receiver. In both cases, the thermophysical properties of glass are supposed temperature independent. The first type of glass sheets is provided with an anti-reflective treatment, to achieve high transmittance in the wavelength range between 300 nm and around 2500 nm, which is the most interesting band for solar thermal applications. Generally, anti-reflective treatment is obtained by deposing thin films with different refraction indexes. In ANSYS® Fluent code, the

reflectance of a semi-transparent surface at the interface between two different media results as a function of the refraction indexes of the media, the incident angle and the transmission angle. From the spectral transmittance of this type of glass, equivalent refraction index and extinction coefficient have been defined for each grey band, assuming that the percent reflected irradiance is around twice that of absorbed irradiance.

The second type of glass is a floated borosilicate glass without anti-reflective coating. In this case, the manufacturer provides both the spectral dependence of transmittance and refraction index up to 2500 nm, so that the absorbance can be easily derived. In the wavelength range between 2500 nm and 100000 nm, each kind of glass is supposed to be opaque, thus, a minor part of the incident irradiance is reflected and the remainder is absorbed. Figure 105 reports the nominal spectral transmittance of the two types of glass, as provided by the manufacturers.

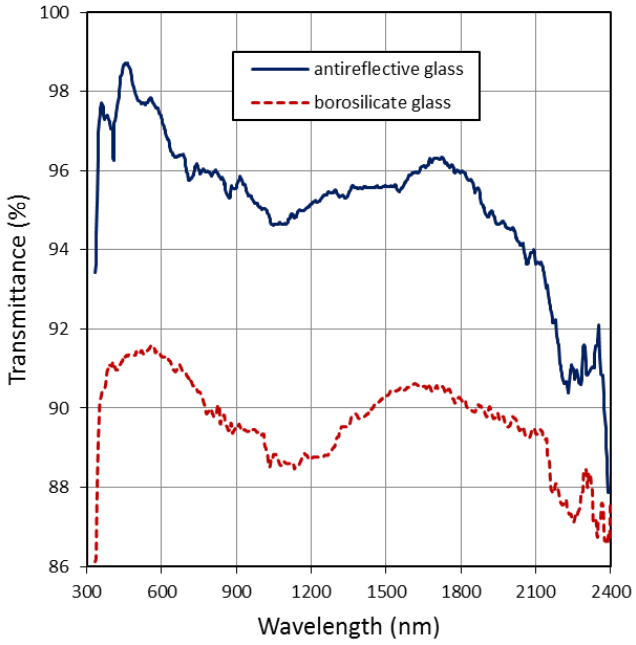

Figure 105 – Nominal spectral dependence of the transmittance for the two types of glass considered in this paper: clear low-iron glass with an anti-reflective coating (blue) and of the borosilicate glass (red).

The fluid acting as solar radiation absorber is an aqueous suspension of single-wall carbon nanohorns (SWCNHs). *Sani and coworkers* [252-255] illustrated the preparation procedure and measured thermal and optical properties of these nanofluids at different concentrations.

These suspensions proved to be very promising for increasing the efficiency of solar thermal collectors. Based on the data reported in the works referenced above and considering the geometry of the receiver, four different concentrations have been considered: 0.05 g L^{-1}, 0.02 g L^{-1}, 0.01 g L^{-1} and 0.006 g L^{-1}. Due to the small amount of nanoparticles suspended in these fluids, the thermophysical properties are assumed equal to those of pure water. Density, thermal conductivity, specific heat and dynamic viscosity have been calculated using NIST REFPROP® version 9 database [109], within the working temperature range from 300 K to 413 K, at which the nanofluid proved to be stable [254]. The temperature dependence of each thermophysical property is captured by using a polynomial interpolation, which is then implemented in the numerical code.

With regard to the optical properties, the small concentration of nanoparticle entails a negligible variation of the refraction index from the base-fluid, as shown by *Taylor et al*. [224]. On the other hand, *Sani et al.* [252] demonstrated that the presence of SWCNHs causes an outstanding increase of the extinction coefficient as compared to the pure base-fluid in the wavelength range from 300 nm to 1400 nm. At higher wavelength, water absorption becomes dominant. The extinction coefficient represents, in its general form, the sum of the absorption and scattering coefficient. The development of the present model accepts the conservative hypothesis of considering the scattering coefficient of the nanofluid equal to 5% of the extinction coefficient for a given wavelength [253]. Therefore, since the mutual influence in radiation among nanoparticles is very limited, the effect of in-scattering within the nanofluid can be reasonably neglected. When a wavelength band from 630 nm to 2100 nm is considered, the absorbance of the nanofluid is considered equal to the average absorbance within the limited range between 630 nm and 1400 nm. This conservative hypothesis is taken so that the radiative balance is not affected by the very high absorbance of water. Table 12 summarizes the properties of the participating materials, considering the band discretization.

Regarding the non-participating media, i.e. stainless steel and PEEK, it is necessary to specify the values of density, specific heat, thermal conductivity and emissivity. The thermophysical properties are needed for the computation of the conduction heat transfer. The emissivity is required to characterize the opaque surfaces at the interfaces between the participating and the non-participating materials. The reflection of the radiation incident on these interfaces is

considered completely diffuse. Table 13 summarizes the properties of the non-participating materials, considering the band discretization. It is worth mentioning that the emissivity of the PEEK for wavelengths higher than 2000 nm is taken from the work of *Gülhan and Braun* [307], while no data seems to be available for the emissivity at lower wavelengths, hence it is assumed equal to that of PTFE.

Table 12 – Properties of the participating materials implemented in ANSYS® Fluent code

Participating materials								
	Thermophysical properties				Optical properties			
	ρ (kg m^{-3})	c_p (J kg^{-1} K^{-1})	k (W m^{-1} K^{-1})	μ (Pa s)	λ (nm)	n (-)	a (m^{-1})	σ [(a)] (m^{-1})
Nanofluid 0.05 g L^{-1}	ρ (T)	c_p (T)	k (T)	μ (T)	300-630	1.340	878	40
					630-2100	1.321	594	
					2100-2400	1.288	1973	
					Over 2400	1.25	3244	
Nanofluid 0.02 g L^{-1}	ρ (T)	c_p (T)	k (T)	μ (T)	300-630	1.340	310	18
					630-2100	1.321	262	
					2100-2400	1.288	1973	
					Over 2400	1.25	3244	
Nanofluid 0.01 g L^{-1}	ρ (T)	c_p (T)	k (T)	μ (T)	300-630	1.340	151	13
					630-1100	1.328	102	
					1100-1300	1.323	164	
					1300-2100	1.314	496	
					2100-2400	1.290	1973	
					Over 2400	1.260	3244	
Nanofluid 0.006 g L^{-1}	ρ (T)	c_p (T)	k (T)	μ (T)	300-630	1.340	91	11
					630-1100	1.328	66	
					1100-1300	1.323	136	
					1300-2100	1.314	577	
					2100-2400	1.290	1973	
					Over 2400	1.260	3244	
Glass + AR coating	2200	830	1.2	-	300-630	1.223	1.65	0
					630-2100	1.31	2.85	
					2100-2400	1.43	4.5	
					Over 2400	1.45	5000	
Float glass	2200	830	1.2	-	300-630	1.48	1.7	0
					630-2100	1.475	9	
					2100-2400	1.46	27.9	
					Over 2400	1.46	5000	

[(a)] scattering coefficient cannot be expressed as a function of the wavelength in ANSYS® FLUENT

Table 13 – Properties of the non-participating materials implemented in ANSYS® FLUENT code.

Non-participating materials					
	Thermophysical properties			Optical properties	
	ρ (kg m^{-3})	c_p (J kg^{-1} K^{-1})	k (W m^{-1} K^{-1})	*Wavelengths* (nm)	ε (-)
PEEK	1800	1700	0.2	300-630	0.12[(b)]
				630-2100	0.12[(b)]
				2100-2400	0.12[(b)]
				Over 2400	0.95
Stainless steel	7900	501	13	300-630	0.4
				630-2100	0.4
				2100-2400	0.4
				Over 2400	0.25

[(b)] PEEK emissivity for wavelengths up to 2000 nm is assumed equal to that of PTFE.

5.3.2 Results of the simulations

Several simulations have been performed with the aim of investigating the effect of glass optical properties, nanofluid inlet temperature, mass flow rate and nanoparticles concentration on the efficiency of the device. When analysing the effect of the inlet temperature, the thermal behaviour of the direct absorption receiver has been compared against that of a traditional surface receiver. The latter uses a copper sheet provided with a selective coating that replaces the top glass sheet. In the numerical simulations, the mass flow rate ranges from 98 kg h^{-1} to 378 kg h^{-1} and the inlet temperature varies from 300 K to 413 K. Simulations have been performed in the receiver configuration described above, but the bottom glass may be replaced with an insulating layer or a reflective surface. Table 14 lists the cases of the present numerical simulations: the channel depth is equal to 12 mm if not otherwise specified.

Two simulations have been carried out to evaluate the effect of the optical properties of the two glasses at a nanoparticles concentration of 0.05 g L^{-1}, a mass flow rate of 378 kg h^{-1} and 300 K nanofluid inlet temperature. In order to completely absorb the incident radiation, a channel depth of 12 mm is considered. In fact, as reported in the work by *Sani et al.* [252], the investigated nanofluid is able to absorb all the incident irradiance within a penetration depth of 10 mm. This is confirmed from Figure 106: the incident radiation is totally extinct before reaching the bottom glass sheet.

Table 14 – Operating conditions of the present numerical simulations.

Cases	SWCNHs concentration, c ($g\ L^{-1}$)	Inlet temperature, T (K)	Mass flow rate, $\dot{m}$ ($kg\ h^{-1}$)	Notes
1	0.05	300	378	upper and lower borosilicate glass
2-4	0.05	300, 345, 393	378, 371, 358	upper and lower anti-reflective glass
5-7	0.05	300, 345, 393	106, 104, 98	upper and lower anti-reflective glass
8-11	0.05	300, 345, 393, 413	378, 371, 358, 351	upper anti-reflective glass + insulated and reflective bottom
12-15	0 (pure water)	300, 345, 393, 413	378, 371, 358, 351	copper with selective coating + insulated bottom
16	0.02	393	358	upper and lower anti-reflective glass
17	0.02	393	358	upper anti-reflective glass + insulated and reflective bottom
18	0.01	393	358	upper anti-reflective glass + insulated and reflective bottom
19	0.01	393	358	Anti-reflective glass + insulated and reflective bottom + channel depth of 18 mm
20	0.006	393	358	upper anti-reflective glass + insulated and reflective bottom
21	0.006	393	358	Anti-reflective glass + insulated and reflective bottom + channel depth of 18 mm

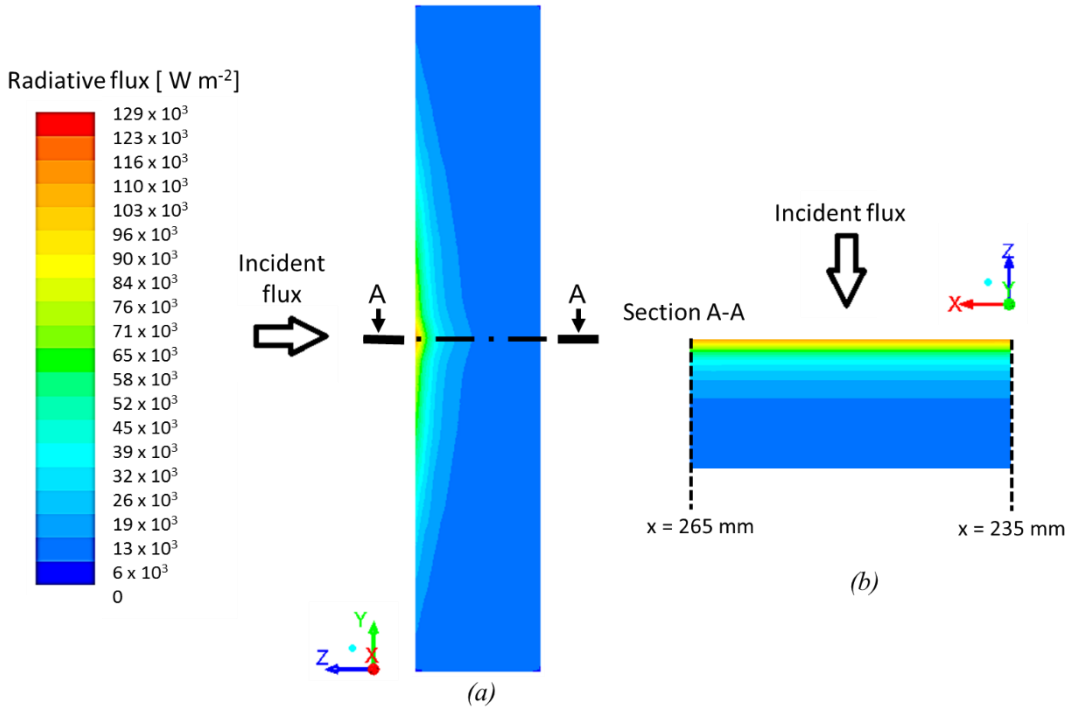

Figure 106 – Extinction of incident radiation (W m^{-2}) when considering a concentration c = 0.05 g L^{-1} of SWCNHs in water and a channel depth of 12 mm (Case 2 in Table 14): cross-section of the channel (a); central part of the symmetry plane of the receiver (b). The fluid flows along the x-axis.

Under these conditions, given that the increase of the fluid temperature inside the receiver is lower than 3 K, the reduced temperature difference (Eq. 3.2) is very close to zero. This means that, in both cases, the calculated performance of the receiver is not significantly affected by the heat dissipation. The efficiency of the receiver results equal to 96.3% when the anti-reflective glass is employed and 93.9% for the borosilicate glass. The resulting efficiencies of the receiver in these cases reasonably represent the average transmittance of the two types of glass in the solar spectrum. They result slightly higher than the average values calculated from the spectral transmittance graphs provided by the manufacturers, which, however, are referred to normal incidence in air. This can be explained by the following considerations. First, the average angle of incidence of the concentrated solar flux is around 24°, which means that the glass transmittance is negligibly affected by the non-normal incidence of the focused solar beams. Secondly, the glass is in contact with air on one side and with water on the other side. As illustrated, the reflectance can be obtained from the refractive indexes of two interfacing

media: the higher the difference of these indexes, the higher the amount of reflected radiation. On the back side of the upper window, the reflectance at the interface between glass and nanofluid (which has the same refraction index of water) is lower than that calculated at the front interface between air and glass. In light of the above, the assumptions made during the numerical simulations on the anti-reflective glass seem to be reasonable.

Simulations are performed considering a nanofluid with a concentration of SWCNHs of 0.05 g L^{-1} entering the receiver with an insulated bottom at temperatures of 300 K, 345 K, 393 K and 413 K, within the temperature range where the stability of the nanofluid has been experimentally demonstrated. Therefore, the reduced temperature difference ranges from 0.001 K m^2 W^{-1} to 0.128 K m^2 W^{-1}. A channel depth of 12 mm is considered. Since the inlet velocity profile remains the same in all the cases while the density of the nanofluid varies as a function of temperature, the mass flow rate decreases from 378 kg h^{-1} to 351 kg h^{-1}. This percent deviation of around 7% meets the requirements of the standard ISO 9806:2013 [110] for testing solar collectors, which recommends that the mass flow rate shall not vary more than 10% from one test period to another. To determine the efficiency of the linear solar concentrating collector η_{col}, the receiver efficiency η_{rec} calculated accordingly to Eq. 3.8 is multiplied by the intercept factor (98%) and by the nominal reflectance of the back-silvered parabolic mirrors (96%). Hence, the collector thermal efficiency obtained from the numerical simulations can be plotted as a function of the reduced temperature difference to define the efficiency curve (Figure 107). The thermal efficiency of the collector (including the optical losses of the concentrating trough) decreases from 90.6% at 0 K m^2 W^{-1} to 77.2% at 0.128 K m^2 W^{-1}: this represents a really promising result. For comparison, the same graph in Figure 107 reports the efficiency curve obtained from an experimental study of an aluminium flat bar-and-plate absorber having a width of 70 mm and mounted on the same concentrator [89] In this device, the surface absorption of the concentrated solar flux is promoted by a black thickness insensitive selective coating and the channel where the operating fluid flows is provided by an offset-strip turbulator to enhance the heat transfer. From Figure 107, it can be observed that, despite the innovative concept of the bar-and-plate receiver, adopting an advanced minichannel geometry, the efficiency is lower than that numerically calculated for the volumetric receiver. In particular, the higher optical efficiency (at $T_m^* = 0$ K m^2 W^{-1}) attained using the volumetric receiver is due

to the direct absorption of all the concentrated solar flux by the nanofluid within the channel depth.

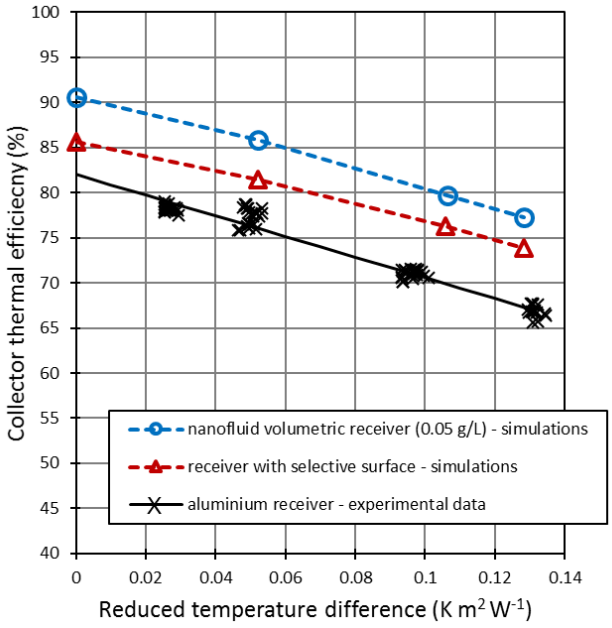

Figure 107 – Comparison of the efficiency curves of the solar linear concentrating collector: numerical simulations of the nanofluid volumetric receiver (Cases 8-11 in Table 14); numerical simulations of the selective surface receiver (Cases 12-15 in Table 14) and experimental data of a bar-and-plate receiver.

Regarding the bar-and-plate receiver, the absorption is limited by the absorbance of the employed black coating which is around 90%. Furthermore, the trend of the efficiency with increasing reduced temperature difference is related to the heat losses towards the surrounding external ambient. It is worth to mention that the volumetric receiver exhibits a better thermal insulation than the bar-and-plate receiver, which is provided by a layer of rockwool only on the rear. On the other hand, the thermal emittance coefficient of the selective coating is equal to 45%, while the emittance coefficient of the top glass window in the volumetric receiver configuration is assumed equal to 90%.

In order to present a fairer comparison, the graph includes also the efficiency curve obtained from the simulations of a surface-absorption receiver that has the same geometry of the volumetric receiver and works with water. The concentrated solar flux is absorbed by the selective coating of a top copper sheet, which has a solar absorbance of 94% and a thermal emittance of 11%. As can be seen from Figure 107., in the considered temperature range, the

thermal efficiency of the collector using the volumetric receiver once again is higher than that using the selective surface. This can be explained by the fact that the direct absorption of solar concentrated irradiance by the fluid bulk reduces the optical losses and avoids the thermal resistance between the absorber plate and the fluid in the surface-absorption receiver. In other words, as Figure 108 demonstrates, when working at the same ambient conditions, the temperature of the external surface of the volumetric receiver's top glass is lower than the external copper selective surface of the conventional receiver.

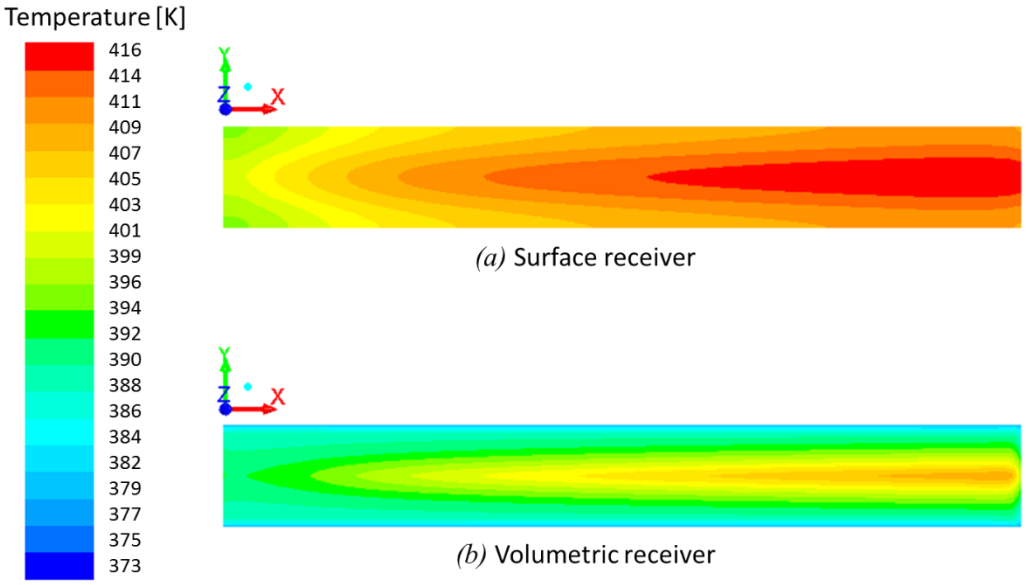

Figure 108 – Contours of temperature (K) of the external top surface when the fluid enters the receiver at 393 K: (a) surface-absorption receiver (Case 14 in Table 14); (b) volumetric receiver working with a nanofluid with a concentration c = 0.05 g L^{-1} of SWCNHs in water (Case 10 in Table 14). For both the receivers, the rear is thermally insulated.

When the working fluid enters the receiver at 393 K, the calculated average external top surface temperature is equal to 393.5 K for the volumetric receiver and to 408.8 K for the surface-absorption receiver (Figure 108). Comparable results were obtained by *Lee et al.* [284], despite the differences in the materials, optical characteristics, system configuration and considered nanofluids. In their work, a surface receiver with conventional base-fluids and a volumetric receiver with water-based MWCNTs nanofluids have been compared by means of analytical

and experimental approaches. Based on their analysis, the efficiency of the nanofluid-based volumetric receiver resulted 10% higher than that of the surface receiver.

Because of the non-uniform distribution of the concentrated solar flux, at a given cross-section of the external top surface, the maximum temperature is reached in the centre. The contours plots reported in Figure 109 refer to a cross-section of the flow channel at 2 cm from the outlet.

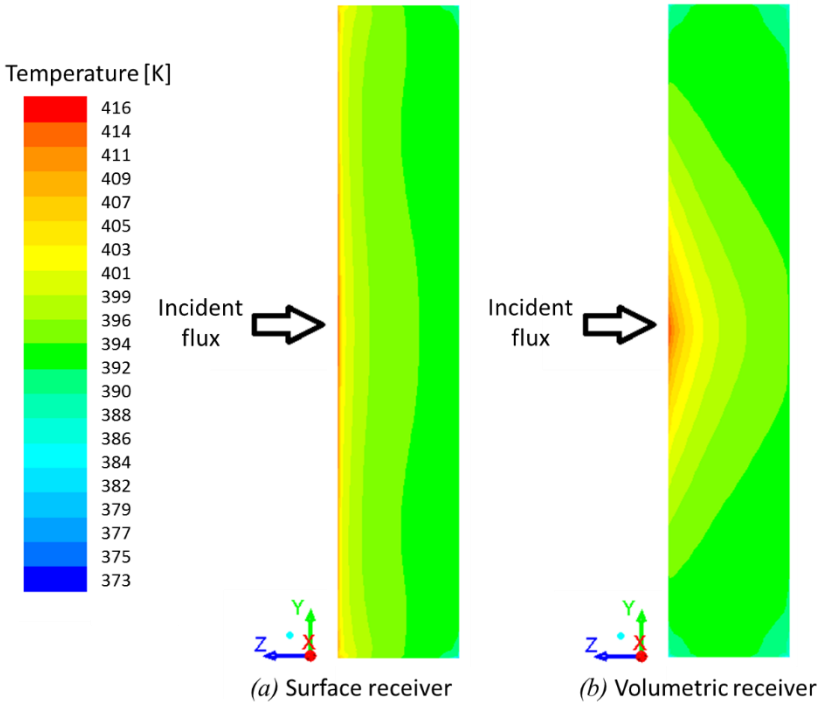

Figure 109 – Contours of temperature (K) of the fluid cross-section at 2 cm from the outlet: (a) surface-absorption receiver (Case 14 in Table 14); (b) volumetric receiver working with a nanofluid with a concentration c = 0.05 g L^{-1} of SWCNHs in water (Case 10 in Table 14). For both the receivers, the fluids enter at 393 K and the rear is thermally insulated.

Furthermore, due to the heating of the working fluid, the peak temperature on the top surface is attained close to the outlet section of the channel. There, the calculated temperature gradient along *y* on the top of the volumetric receiver is higher than the one of the surface-absorption receiver. Since the peak temperature may affect the thermal performance of the volumetric receiver, especially when longer receivers are investigated, it may be useful to analyse and compare the temperature distributions of the two receivers at a cross-section of the fluid channel close to the outlet. Regarding the volumetric receiver, in agreement with the extinction

of incident radiation reported in Table 12, only the layers of nanofluid close to the centreline of the upper window display a significant temperature increase. While the average fluid temperature on the outlet section is equal to 395.5 K, at the interface with the upper window, just before the outlet, the fluid reaches a maximum temperature of 414 K. This indicates that the investigated concentration of 0.05 g L^{-1} may not be the optimal one because the receiver thermal behaviour at the outlet tends to that observed for a surface-absorption receiver. Hence, there may be room for optimization using lower SWCHNs concentrations.

The mass flow rate, ranging from 378 kg h^{-1} to 351 kg h^{-1} in the present simulations, is such that the Reynolds number related to the fluid cross-section results higher than 10000 when working with an inlet temperature over 393 K, whatever the channel depth. In order to investigate the effects of the nanofluid flow rate inside the channel of the receiver, simulations are conducted at even lower inlet velocity, with a constant SWCNHs concentration of 0.05 g L^{-1} and three different inlet temperatures of the nanofluid (300 K, 345 K and 393 K). The lower values of mass flow rate have been defined in agreement with the standard ISO 9806:201, where a mass flow rate equal to 0.02 kg s^{-1} per square meter of the aperture area is established for testing conventional liquid heating solar collectors. The aperture area in the present analysis has been computed as the product of the concentrator aperture width (2.9 m) and the volumetric receiver length (0.5 m). Since the thermophysical properties of the nanofluid vary as a function of temperature and the inlet velocity profile remains the same in all the cases, the mass flow rate decreases from 106 kg h^{-1} to 98 kg h^{-1} when increasing the fluid inlet temperature. The simulations have been performed considering a configuration of the receiver with upper and lower anti-reflective glass and 12 mm channel depth. At the lower mass flow rate (98 - 106 kg h^{-1}), the difference between the outlet and the inlet temperature is around 3.6 times the one attained when considering the higher mass flow rate (358 - 378 kg h^{-1}). The results show that the receiver efficiency is negligibly affected by the operating mass flow rate for the considered geometry. Nevertheless, the temperature distribution within the nanofluid close to the channel outlet is substantially worsened when working at the lower mass flow rate. With respect to the simulations performed at 393 K inlet temperature and at 98 kg h^{-1}, the peak temperature at the channel cross-section at 2 cm from the outlet is 476 K, as reported in Figure 110.

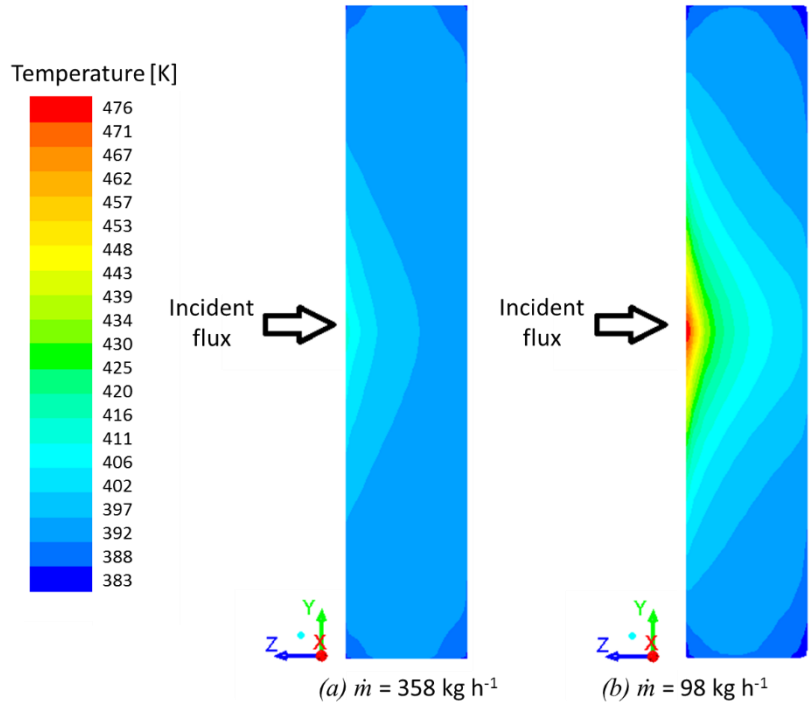

Figure 110 – Contours of temperature (K) of the fluid cross-section at 2 cm from the outlet of the volumetric receiver working with a nanofluid with a concentration c = 0.05 g L-1 of SWCNHs in water at (a) ṁ = 358 kg h-1 (Case 4 in Table 14); (b) ṁ = 98 kg h-1 (Case 7 in Table 14). For both the receivers, the fluids enter at 393 K and the rear is made of glass.

This temperature distribution can be explained by considering that the nanofluid needs a longer time to cross the channel, thus it absorbs a higher amount of solar energy and gets extremely hot just below the top glass window close to the receiver outlet. In a longer volumetric receiver, this could lead to a lower efficiency. Moreover, since the thermal gradient between the two faces of the upper window increases when the nanofluid flow rate is reduced, a lower lifetime of the glass may be expected. For these considerations, the numerical studies at lower SWCNHs concentrations in water have been performed considering the higher mass flow rate.

The nanoparticles concentration in the nanofluid should be carefully optimized because its value can be used to adjust the absorbance of the nanofluid. An increase of nanoparticles concentration in the nanofluid results in a shorter absorption path for the absorption of the radiation inside the fluid. The higher concentration of the absorbed energy causes an increase of the temperature on the top surface and therefore the heat losses to the environment increase.

As concluded by *Moradi et al.* [256], this characteristic makes the thermal behaviour of the direct absorption receiver similar to that of a surface absorber, as in this case the maximum of the temperature distribution is always located at the top surface. For this reason, the thermal efficiency of the volumetric absorber working with a SWCNHs concentration higher than 0.05 g L^{-1} is expected to be lower than that obtained at 0.05 g L^{-1} concentration and therefore it is not further investigated. On the other hand, when considering a SWCNHs concentration lower than 0.05 g L^{-1}, in the receiver configuration with front and bottom glass, the 12 mm depth is not enough to attain a 100% absorbed solar energy fraction. Therefore, part of the incident radiation is lost from the bottom window. This effect can be seen in Figure 111 reporting the extinction of the incident concentrated radiation on the cross-section of the channel when using aqueous suspensions of SWCHNs with concentration ranging from 0.05 g L^{-1} to 0.006 g L^{-1}.

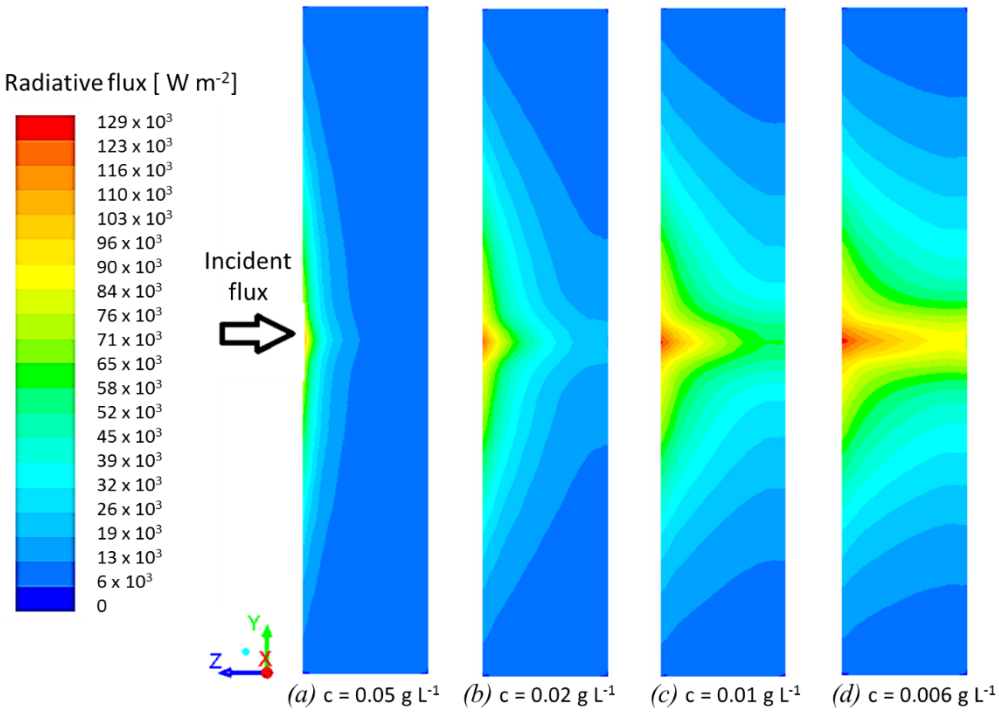

Figure 111 – Extinction of incident radiation (W m-2) at a cross-section of the 12 mm deep channel considering different concentrations of SWCNHs in water: (a) c= 0.05 g L^{-1} (Case 10 in Table 14); (b) c= 0.02 g L^{-1} (Case 17 in Table 14); (c) c= 0.01 g L^{-1} (Case 18 in Table 14); (d) c= 0.006 g L^{-1} (Case 20 in Table 14).

At a concentration of 0.02 g L^{-1} SWCNHs in water, the penetration distance is around 20 mm [255] and, within the 12 mm deep channel, around 95% of the incident radiation is absorbed. Consequently, for the case of 393 K inlet temperature in the configuration with upper and lower glass windows, the efficiency of the receiver is 83.5% at 0.05 g L^{-1} concentration while it is 79.5% at 0.02 g L^{-1} concentration. When employing a nanoparticles concentration lower than 0.05 g L^{-1}, it may result appropriate to arrange a reflective layer on the rear part of the receiver. Actually, this reflecting surface may be either specular reflective or Lambertian reflective. In this way, the fraction of transmitted radiation intensity is sent back to the absorbing nanofluid and this would increase the overall efficiency. If this expedient is not sufficient to obtain a good efficiency, a deeper channel should be adopted.

To prove the validity of this argument, the results of two numerical simulations have been compared, considering an inlet temperature of 393 K, to account for the heat dissipation towards the surrounding ambient. In the first case, the performance of a nanofluid with a SWCNHs concentration of a 0.05 g L^{-1} has been evaluated inside a receiver where the bottom window has been replaced with an insulated bottom made of PEEK without any reflective surface. In the second case, a nanofluid with the lower concentration of 0.02 g L^{-1} has been considered in a receiver provided with an insulated bottom having the properties of PEEK and supposing a specular reflective surface at fluid-bottom wall interface. The specular reflectance of this interface is assumed 95%. At the highest concentration (0.05 g L^{-1}), the efficiency increases by around 1.5%, reaching the value of 84.8%: this small difference can be explained by the reduction in thermal losses from the lower part of the receiver thanks to the presence of the insulating layer. On the other hand, at a SWCNHs concentration of 0.02 g L^{-1}, the predicted efficiency of the receiver increases by 5.4% up to 84.9%. This increase is partly due to the reduced heat losses from the rear of the receiver, but primarily to the longer optical path of the solar irradiance within the nanofluid bulk.

Numerical simulations implementing nanofluids with further reduced SWCNHs concentrations of 0.01 g L^{-1} and 0.006 g L^{-1} show that the adoption of the reflective and thermally insulating layer on the rear part of the 12 mm deep receiver leads to lower receiver efficiency of 81.8% and 76.0%, respectively. Nevertheless, as the SWCNHs concentration decreases, the temperature distribution close to the outlet of the receiver is more and more uniform and the

peak temperature is closer to the outlet average temperature. As an example, Figure 112 reports the temperature contours in the channel cross-section of the 12 mm deep receiver, at a distance of 48 cm from the inlet, resulting from the simulations performed with all the investigated nanofluids entering at 393 K.

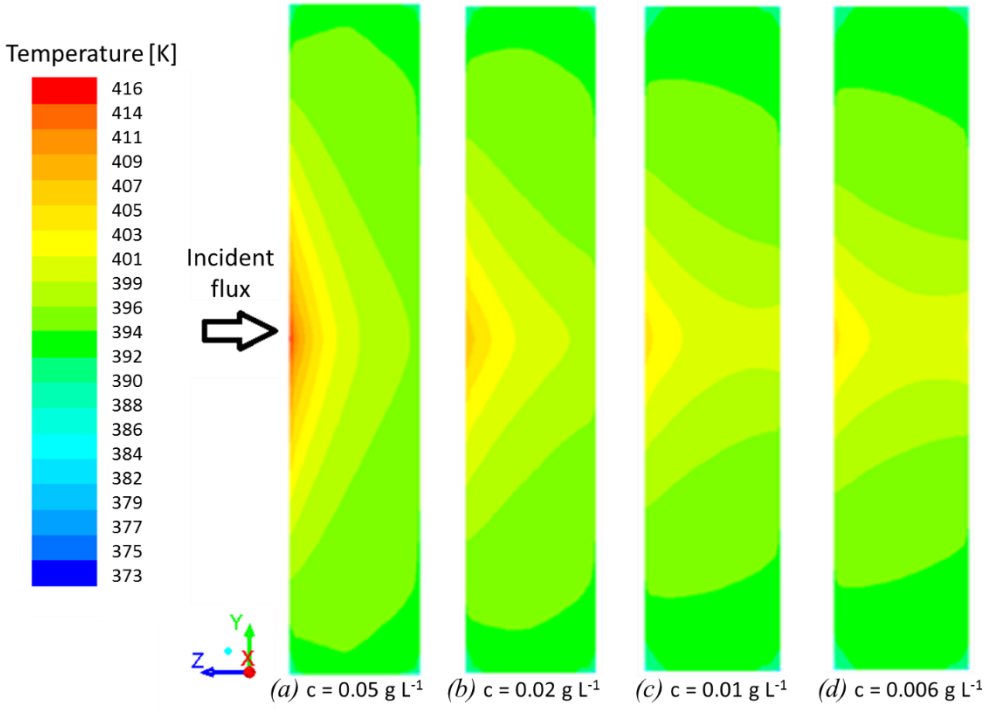

Figure 112 – Contours of temperature (K) of the fluid cross-section at 48 cm from the inlet of the volumetric receiver working with nanofluids with different concentrations of SWCNHs in water (a) c= 0.05 g L^{-1} (Case 10 in Table 14); (b) c= 0.02 g L^{-1} (Case 17 in Table 14); (c) c= 0.01 g L^{-1} (Case 18 in Table 14); (d) c= 0.006 g L^{-1} (Case 20 in Table 14). All the simulations refer to 393 K inlet temperature; the receiver is provided with thermal insulation and reflecting layer on the rear.

The presence of a thermal insulation and a reflective layer on the rear has been considered according to the above-mentioned analyses. The calculated peak temperatures are equal to 407 K, 405 K and 403 K when implementing 0.02 g L^{-1}, 0.01 g L^{-1} and 0.006 g L^{-1} as SWCNHs concentrations in water, respectively (Figure 112).

Similar results, displaying a decrease of the receiver thermal efficiency when decreasing the nanoparticles concentration have been already reported in the scientific literature, even with different types of nanoparticles [246,256,281,283,284].

In order to increase the receiver efficiency with SWCNHs based nanofluids having lower concentrations (0.01 g L^{-1} and 0.006 g L^{-1}), simulations have been performed considering a receiver with the insulated and reflective bottom and an increased depth of 18 mm. Once again, the nanofluids enter the channel at 393 K. In both the studied cases, the receiver efficiency increases reaching 84.2 % for 0.01 g L^{-1} nanoparticle concentration and 80.7% for 0.006 g L^{-1}. Thus, adjusting the receiver configuration, it is possible to decrease the SWCHNs concentration in the nanofluid down to 0.01 g L^{-1} without significant performance penalization.

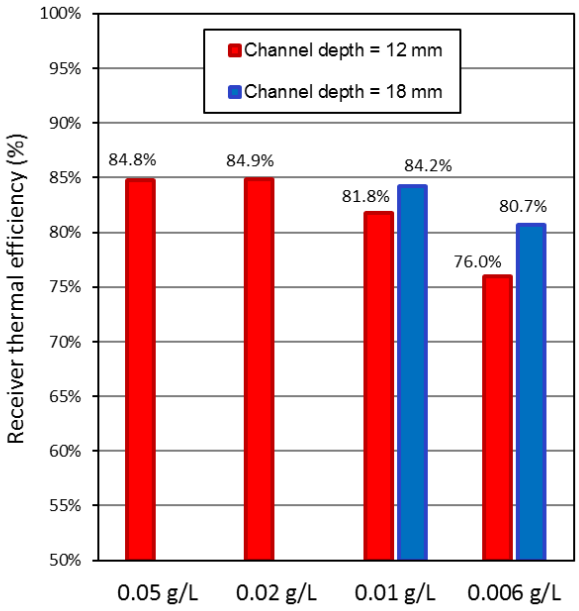

Figure 113 – Calculated receiver efficiencies at varying SWCHNs concentrations c (g L^{-1}) and channel depths obtained from the simulations: receiver with a reflective bottom and 393 K inlet temperature of the nanofluid (Cases 10, 17, 18, 19, 20 and 21 in Table 14).).

The graph of Figure 113 sums up the calculated receiver efficiencies for a constant nanofluid inlet temperature of 393 K as a function of the SWCHNs concentration and the channel depth in a configuration with thermal insulated and reflective bottom. In a future perspective, the use of a very low SWCHNs concentration nanofluid may facilitate the establishment of production methodologies to achieve a long-term stable working fluid. Furthermore, it could contribute to the cost-effectiveness of the direct absorption receiver for solar concentrating collectors. However, it is worth to mention that the employed nanoparticles are available on the market at a cost lower than 5 €/g.

5.4 Design of a direct absorption solar receiver using nanofluid as direct absorbing media

A new volumetric planar receiver has been designed and fabricated to test the direct absorption of the concentrated solar radiation in a volume of single-wall carbon nanohorn (SWCNH)-based aqueous nanofluid. The geometry of the volumetric receiver is not optimized to maximize the energy efficiency of the collector, but the design of this test section is aimed at developing a receiver that allows the evaluation of the optical capability of nanofluids to absorb a high concentrated solar flux within their volume.

Two clear low-iron glass sheets, having a thickness of 3 mm, form the front (where the solar irradiance is concentrated) and the rear surfaces of the receiver. The width of the front window of the receiver is 64 mm to achieve an intercept factor of 98%. The glass on the rear part of the channel is used to trap only the solar radiation absorbed by the nanofluid, and hence allowing the measurement of the heat gain due to the mere nanofluid optical absorption. The numerical analyses presented in the previous Paragraph highlighted that the optical properties of the front glass window, play a key role in the definition of the optical characteristics of the volumetric solar receiver. The glass sheets are provided with an anti-reflective coating, to achieve high transmittance in the wavelength range between 300 nm and 2400 nm, which is the most interesting for solar thermal applications. A sample of the glass used in the receiver has been optically characterized. The resulting spectral dependence of the glass transmittance is shown in Figure 114. The glass sheets are embedded in two stainless steel frames, which give mechanical stiffness to the full structure. A thin layer of PTFE is interposed between glass and frames, to protect the glass itself. The front steel frame has a thickness of 6 mm, while the rear steel frame is 10 mm thick to host the threads for the tube fittings for nanofluid inlet and outlet.

The test section is aimed to tests the solar absorption capability of nanofluids consisting of suspensions of single-wall carbon nanohorns in distilled water with a concentration of 0.02 g ranging from 0.02 g L^{-1} to 0.05 g L^{-1}. This range of concentration of SWCNHs was chosen based on the results of the simulations presented above. In fact, it has been observed that increasing the nanoparticles concentration makes the receiver thermal behaviour more and more similar to that of a surface-absorption device leading to increased heat losses in full-size

receivers. Furthermore, the optimization of the nanoparticles concentration should lead to the lowest possible concentration so as to simplify the production method, address possible long-term stability issues, improve the thermal behaviour and the cost-effectiveness of the receiver.

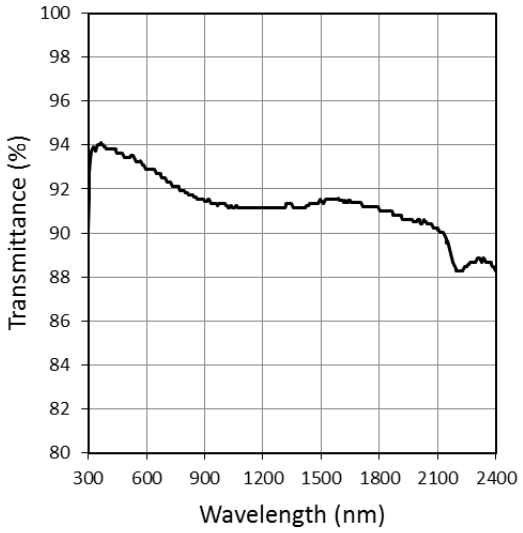

Figure 114 – Spectral transmittance characterization of the glass used in the test section.

In the design of any direct absorption receiver, it is crucial that the channel depth meet the optical penetration depth of the nanofluid which depends on the nanoparticles concentration. With this purpose, according to the results of *Sani et al*. [253] a modular configuration which allows varying the channel depth between 12 mm and 18 mm is adopted to define the geometry of the new volumetric receiver. The modular structure presents two or three PEEK frames that can be combined to form the side walls of the flow channel. The choice to use PEEK as the frame's material is due to its excellent mechanical and chemical resistance properties up to 240°C and its good thermal insulation (0.25 W m^{-1} K^{-1} thermal conductivity). Inlet and the outlet semicircular chambers for the nanofluid are obtained by shaping the PEEK frames and are connected to two threaded holes in the stainless steel frame on the rear part of the receiver. A diffuser is interposed between the PEEK frames to cause a localized pressure loss which allows a uniform distribution of the nanofluid across the section of the flow channel. The nanofluid enters the receiver through the inlet section, accumulates in the semi-circularly shaped chamber between the PEEK frames and passes through the diffusor before flowing along the channel where it gets exposed to the concentrated solar radiation and lastly exits from

the receiver. A CFD analysis has been carried out in ANSYS Fluent® to find the optimal geometry of the diffuser in order to provide an even flow distribution in the receiver [308]. All the layers of the receiver are kept together by tightening several bolts and nuts on the stainless steel frames. Viton® fluoroelastomer chords have been placed between the glass sheets and the PEEK frames, and on the inlet and outlet connections to guarantee hydraulic sealing of the volumetric receiver. Sketches of the proposed receiver are reported in Figure 115.

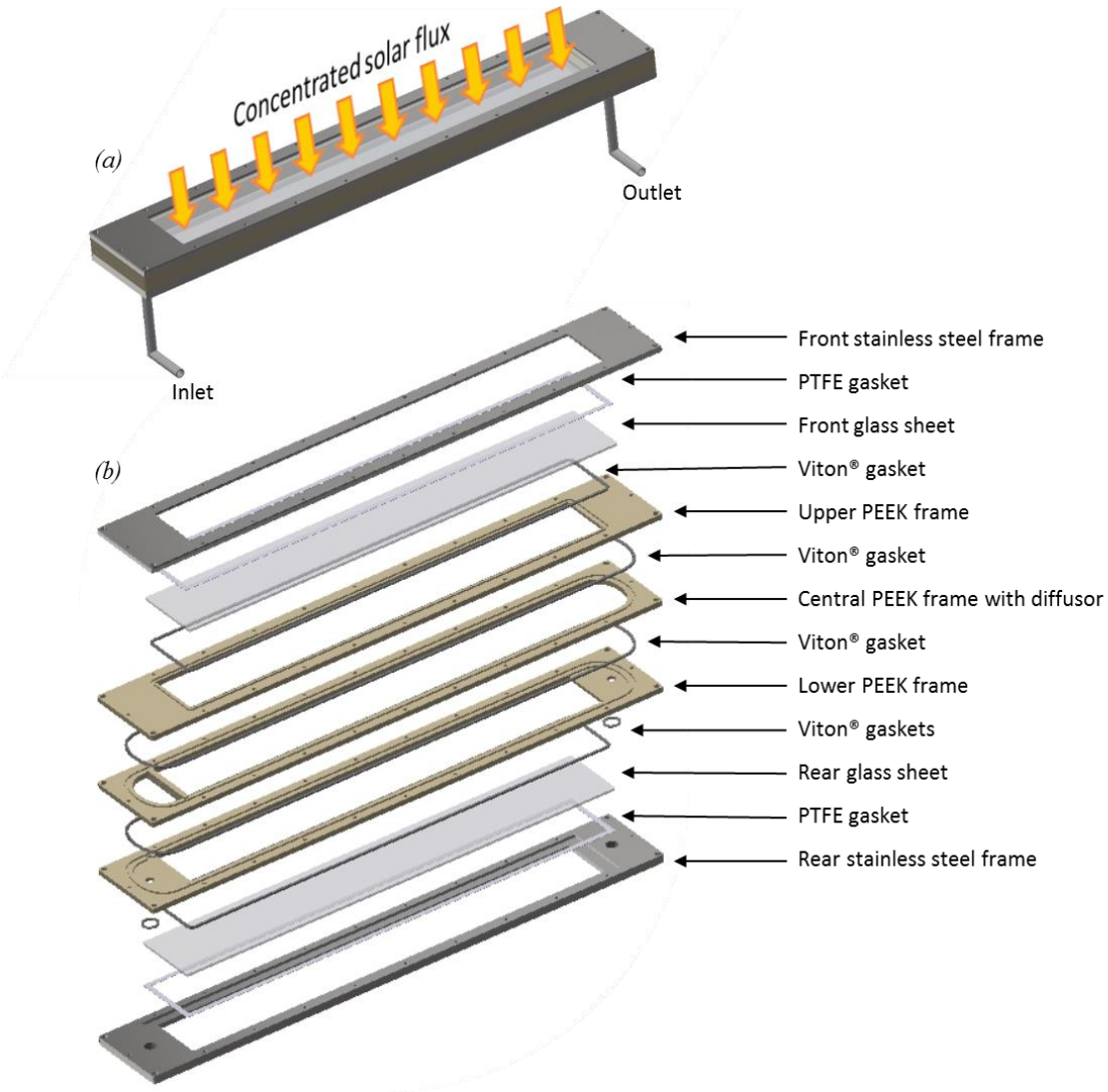

Figure 115 – Compact (a) and exploded (b) views of the volumetric receiver for direct absorption of solar concentrated irradiance.

Once the width and the depth of the channel are defined, it is possible to calculate the mass flow rate which allows a turbulent flow regime. In the previous numerical simulations, it has been observed that this flow condition may lead to a safer and more efficient operation. In fact, at low mass flow rates, the nanofluid had more time to absorb and convert concentrated solar flux into heat causing high thermal gradients on the glass. The length of the glass window is set to 500 mm to allow operating pressure up to 2.5 bar (). Nevertheless, this limited length permits to collect sufficient radiative thermal power in order to be measured by means of the nanofluid temperature difference between inlet and outlet of the receiver with a low measurement error.

5.5 Experimental characterization of a direct absorption receiver in a full-scale solar concentrating collector

An experimental investigation using a single-wall carbon nanohorn (SWCNH)-based aqueous nanofluid in the designed direct absorption receiver has been conducted. The nanofluid used here, present a SWCNHs concentration of 0.02 g L^{-1} and although it displays excellent optical properties and potentially low cost, has never been tested in a full-scale solar collector under realistic operating conditions. During the tests, the channel depth of 18 mm has been adopted. This depth assures the extinction of more than 95% of the incident light under laboratory conditions [252]. Several experiments have been set up to investigate the capability of this nanofluid in collecting solar radiation and verify its stability when exposed to concentrated and non-concentrated solar flux with and without circulation.

5.5.1 Nanofluid preparation and optical characterization

The concentration of nanoparticles in the base-fluid has been observed to have a significant impact on the optical behaviour of the nanofluid. In fact, at low particle mass fractions, part of the incident irradiance is not absorbed by the nanofluid. On the other hand, at high particle concentrations, nanofluid may become unstable, while absorption occurs at the top layer of the nanofluid, resembling thus the thermal behaviour of a conventional surface absorber. Therefore, it is fundamental to characterize the optical properties of the chosen nanofluid at its specific concentration in order to meet the optical characteristics of the considered volumetric absorber. Furthermore, the stability of nanofluids is fundamental for the maintenance of thermal, rheological and optical properties during their application in DASCs. When dispersed in a liquid, nanoparticles tend to aggregate and precipitate, leading to a variation in the fluid composition and, consequently, in its properties. Hence, the optimization of the nanofluid preparation method is essential [257].

Dahlia-like aggregates of single-wall carbon nanohorns were provided by the company Carbonium S.r.l. and were produced by a process based on rapid condensation of carbon atoms without any catalyst and with highly reduced production costs [309] and an estimated market

price lower than 3 €/g. The morphological characterization of the nanoparticles was performed by Field Emission - Scanning Electron Microscopy (FE-SEM) with a SIGMA Zeiss instrument (Carl Zeiss SMT Ltd, UK). Figure 116 reports an example of FE-SEM micrograph for SWCNHs powder. The mean dimension of carbon nanohorns, evaluated by means of the software ImageJ IJ 1.46r, was equal to 80 ± 6 nm. The aggregation is due to the drying process in preparing the specimen to perform FE-SEM observation.

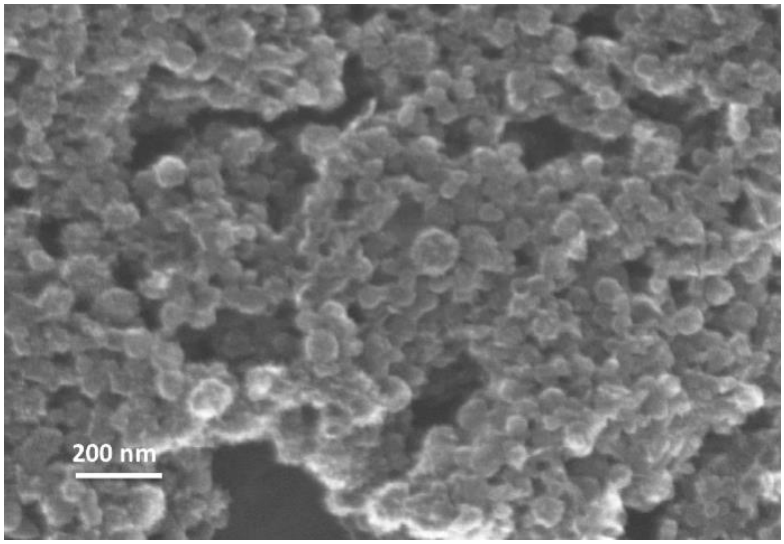

Figure 116 – FE-SEM micrograph of carbon nanohorn powder.

The SWCNHs suspension for tests in a DASC was prepared at the Institute of Condensed Matter Chemistry and Technology for Energy (ICMATE) of the National Council of the Research (CNR) in Padova, Italy. The nanofluid preparation described in the work of *Bortolato et al*. [310] is schematically summarized in Figure 117. The suspension containing 0.02 g L^{-1} of SWCNHs in a water solution where sodium dodecyl sulfate (SDS) was chosen as a surfactant (SWCNH:SDS = 4:1 by weight) was prepared according to the following procedure. First, 250 ml of a solution containing 0.005 g L^{-1} of SDS in water was prepared, afterward, 0.05 g L^{-1} of SWCNHs were dispersed in this solution by a first homogenization with an ultrasonic processor (VCX 130, Sonics & Materials) at 20 kHz and 65 W for 10 min. Therefore, a high-pressure homogenizer (Panda, GEA Niro Soavi, 1000 bar) was employed for 15 min to optimize the dispersion. Finally, all batches prepared were diluted to achieve 7 liters of the 0.02 g l^{-1} of SWCNHs suspension.

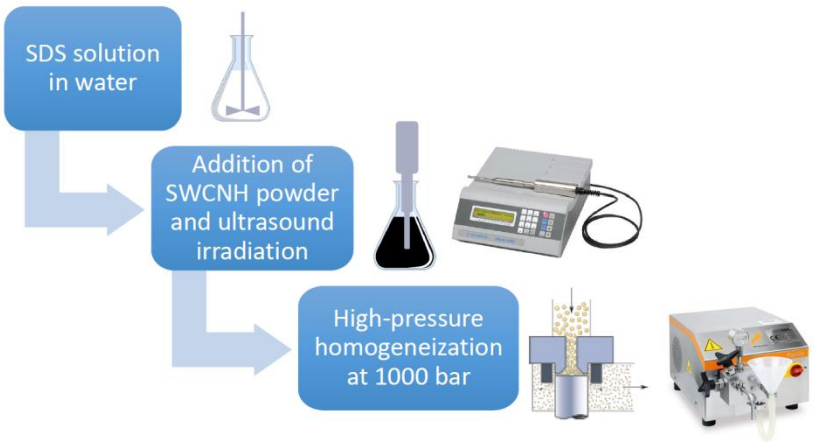

Figure 117 – Schematic of the SWCNHs -water/SDS nanofluid preparation.

The use of SDS as surfactant results fundamental to achieve a stable nanofluid under laboratory conditions. In fact, the ζ-potential for suspensions with SDS as surfactant resulted much higher in modulus (-44 mV) than that for suspensions without SDS (about -8 mV). Furthermore, the homogenization process was optimized: samples of nanofluids have been produced considering various homogenization times (from 0 to 60 min homogenization) and, for each sample, a quantitative analysis on SWCNHs size distribution in water was carried out by Dynamic Light Scattering (DLS, Zetasizer Nano, Malvern). This analysis reveals the possible presence of unwanted settling and clustering phenomena. The measurements were performed for 15 days on a static sample (*i.e.* not undergone to stirring before measurements) and a 15 min homogenization processing has been found to be the optimum in terms of stability. Figure 118 reports the mean aggregate size measured by means of the DLS technique for 15 days in suspensions for non-homogenized (0 min) and for 15 min homogenized sample: the decreasing of aggregate size and the stability with time of the sample after 15 min homogenization can be clearly observed in this Figure.

The suspension stability with temperature was qualitatively evaluated by placing samples in an autoclave at 150°C and about 5 bar for 24 hours. Only the samples prepared with homogenization showed no aggregation and/or settling after this test. Figure 119 shows a SEM micrograph of the homogenized sample, where no modifications of carbon nanohorns morphology were detected as compared to the only sonicated sample.

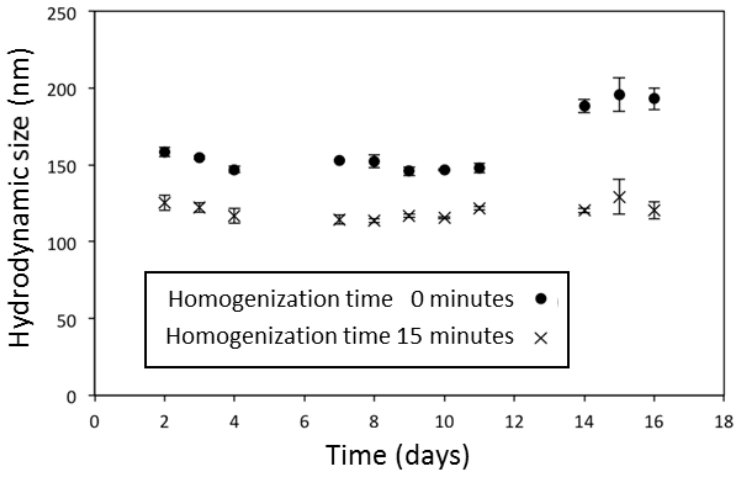

Figure 118 – Mean aggregate size of SWCNHs measured by DLS for 15 days in aqueous suspensions for non-homogenized (0 min) and for 15 min homogenized sample.

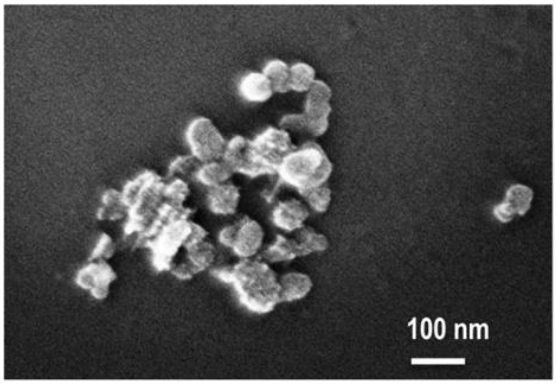

Figure 119 – SEM micrograph of 15 min homogenized nanofluid sample.

The compatibility and stability of the SWCNHs suspension with the materials used in the test rig have been verified in laboratory tests conducted by immersion of samples of the material in the prepared suspension. No aggregation and/or settling has been observed. Considering the very low SWCNHs concentration, the thermophysical properties (thermal conductivity and viscosity) were verified to be analogous to the base-fluid (water).

According to a preliminary optical characterization [253] of SWCNHs nanofluid under laboratory test conditions, the suspension containing 0.02 g L^{-1} of SWCNHs in water assures the complete extinction of the incident light in a depth greater than about 24 mm (Figure 120).

From the same Figure 120, it can be appreciated how SWCNHs dramatically change optical properties of the fluid, as pure water has a considerable lower sunlight absorption.

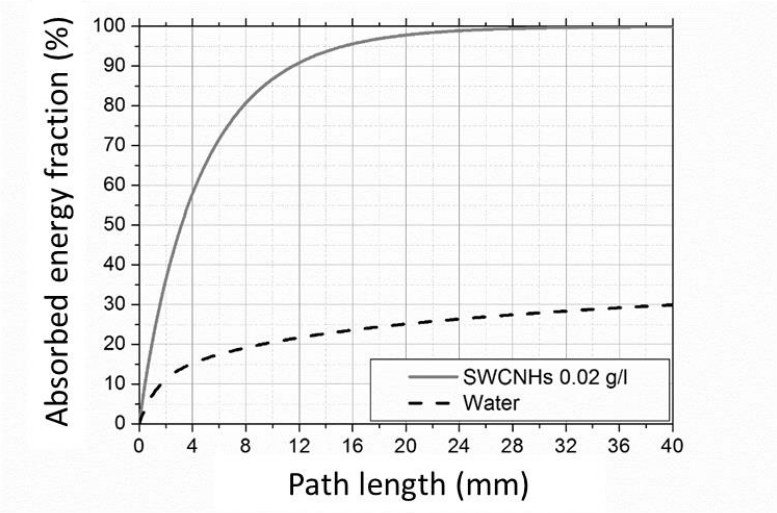

Figure 120 – Comparison of the absorbing energy capabilities of a suspension containing 0.02 g L^{-1} of SWCNHs in water (continue line) and pure water (dashed line).

For diagnostic purposes, considering the different preparation technique of the present suspension with the one presented in [253], the optical extinction spectra have been measured in the spectral range 200-2500 nm on the sample studied in this experiment, by the Italian National Institute of Optics (INO) of the National Council of the Research (CNR) in Florence, Italy. The measurement is carried out using a double-beam spectrophotometer (Perkin Elmer Lambda 900) and holding the sample in cells with 50 ÷1140 μm-thicknesses [311].

Figure 121 reports the spectral extinction coefficient of the suspension tested in the concentrator (0.02 g L^{-1} of SWCNHs in water) in the spectral range 200-1400 nm. A good agreement with previous works was found. It should be noticed that for carbon nanohorn suspensions, the extinction coefficient gives a good approximation of absorption properties since the optical scattering can be considered negligible [255] In fact, as shown by *Mercatelli et al.* [254], SWCNHs have a very low scattering albedo (not higher than 5% for red and near-infrared wavelengths) as compared to Indian inks.

Before the test campaign, in order to avoid any effects due to exposure of the nanofluid to the external environment, the fluid has been kept at ambient temperature in a tank protected by the sunlight.

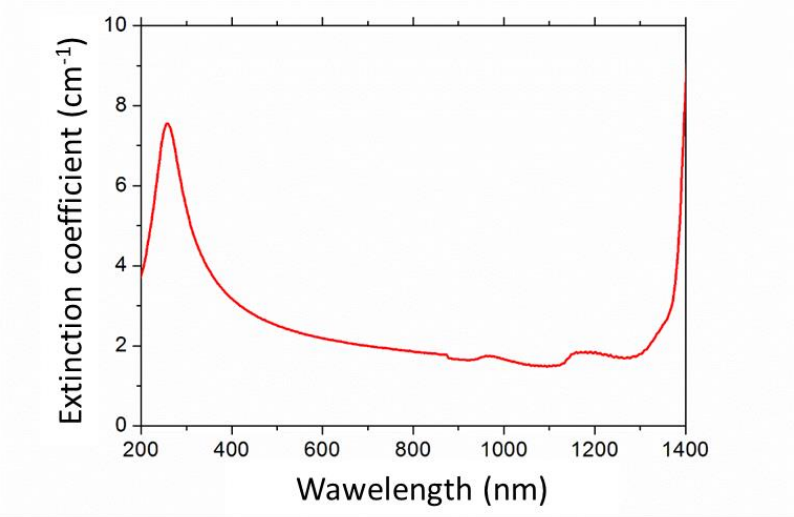

Figure 121 – Experimental extinction coefficient of a suspension containing 0.02 g L^{-1} of SWCNHs in water, 15 minutes homogenization time.

5.5.2 Experimental apparatus

The first experiment on the nanofluid is performed under the concentrated solar flux in the focal region of the asymmetrical parabolic trough installed in the Solar Energy Conversion Lab of the Industrial Engineering Department, at the University of Padova.

The designed planar volumetric receiver is placed in the central section of the first mirrors row of the parabolic trough. This position assures that the front window of the receiver is exposed to the most uniform concentrated solar radiation along the flow channel length because its distribution is not affected by border effect. In order to minimize the incidence angle of the concentrated beams, the front surface of the flat receiver is tilted at 45° to the plane containing the focal line and the vertex line of the parabolic trough. The receiver is mounted on two vertical aluminium supports sustained by a horizontal bar parallel to the focal line of the parabolic trough concentrator. The ends of the receiver's front steel frame are equipped with reflecting aluminium layers to avoid any contribution of solar flux absorption (Figure 122).

The support structure is placed to avoid any shadow on the reflecting surface of the concentrator.

A first class Kipp & Zonen CHP1 pyrheliometer mounted on a high precision EKO Instruments STR-22G solar tracker is used to measure the direct normal irradiance (DNI). The wind speed on the horizontal plane is measured by an anemometer while the ambient air temperature is gauged by a Pt100 RTD.

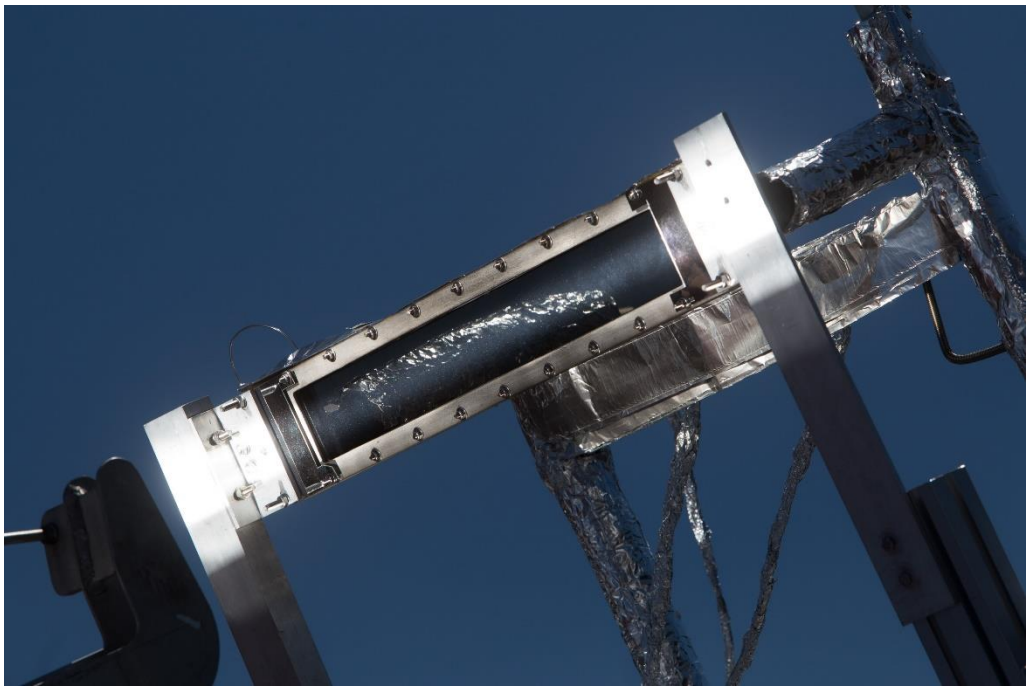

Figure 122 – Volumetric receiver arranged on the vertical supports under concentrated solar radiation during a test run.

The test facility includes a primary loop arranged on board the concentrating collector and a secondary cooling loop. Both loops are thermally insulated by a 13 mm thick extruded elastomeric foam to limit heat losses towards the surroundings. The pipes and the instrumentations on board the collector are shielded from the concentrated solar beams that can strike them during the initial positioning. In the primary loop (Figure 123), after exiting the receiver, the nanofluid enters a tube-in-tube heat exchanger that acts as a heat sink: the heat flow rate provided by the concentrated solar irradiance is taken away by a secondary water flow. A parallel pipe with a regulation valve is included to eventually bypass the heat exchanger

and reduce the heat transfer from the nanofluid to the secondary loop for operation at temperatures higher than 100°C. Afterward, the nanofluid is sent to an independently controlled rotary vane pump (Nuert PR4ASXV) magnetically coupled to a variable speed electric motor. This pump is used to set the mass flow rate, which is measured by a Coriolis effect mass flow meter (Siemens SITRAN FC MASS2100).

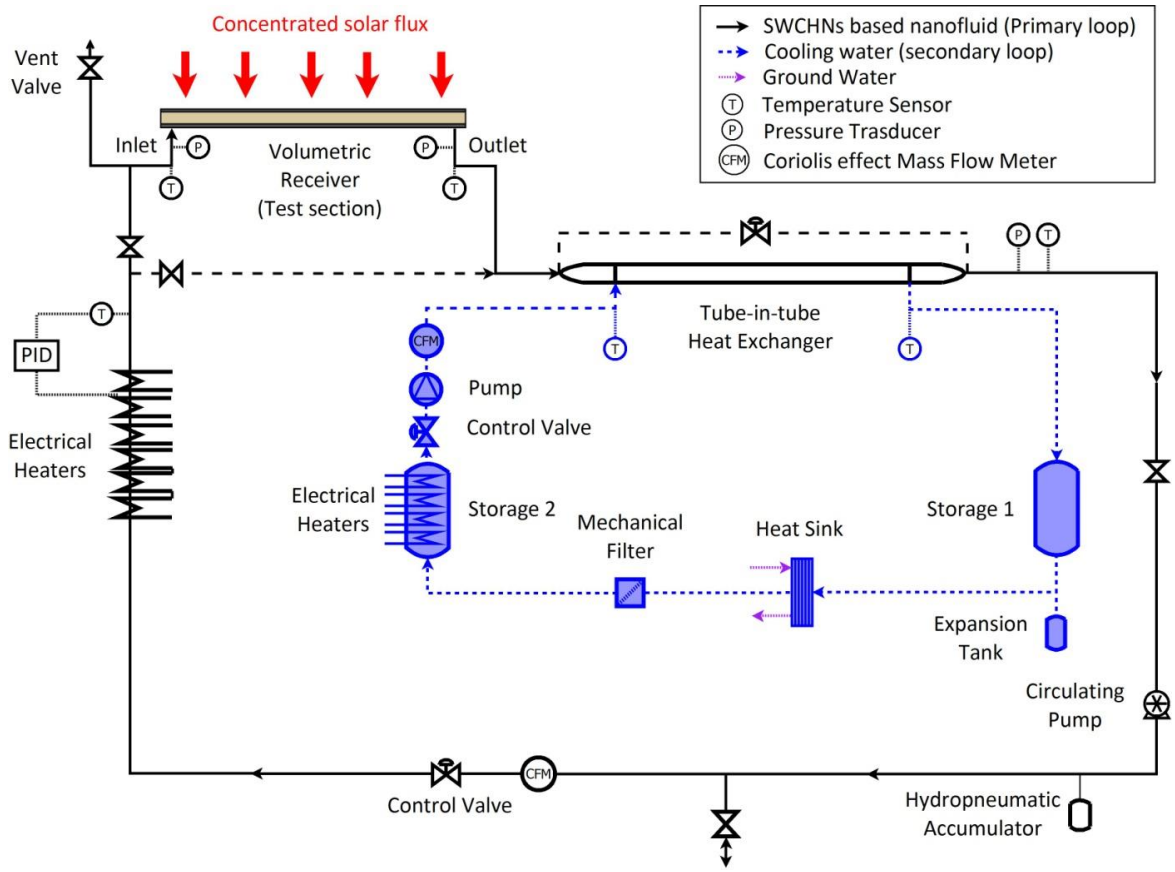

Figure 123 – Schematic of the experimental test rig.

The pressure of the primary loop is regulated by a hydropneumatics accumulator with a fluoroelastomer membrane. Before entering the receiver, the nanofluid passes through a preheating section which consists of a heating wire wrapped around a stainless steel tube. The electrical heater is connected to a solid-state relay which is governed by a PID temperature controller. The PID controller uses a T-type thermocouple as a probe to monitor the trend of the external wall temperature of the stainless steel pipe downstream of the preheating section. Three high precision absolute pressure transmitters (STS ATM.1ST) have been connected to

the primary loop pressure taps to gauge the pressure at the inlet and outlet of the receiver and at the outlet of the tube-in-tube heat exchanger. The temperatures of the nanofluid at inlet and outlet of the receiver and downstream of the heat exchanger are measured by Pt100 resistance temperature detectors (RTDs). A vent valve sits at the highest point of the primary loop to eventually remove the non-condensable gases trapped in the circuit. In the secondary cooling loop (Figure 123), the water coming from the tube-in-tube heat exchanger enters the first storage and passes through a plate heat exchanger, where the heat gained from the primary loop is wasted to the groundwater of the building central plant. Afterward, the cooling water enters a second storage that is provided with four electrical heaters. The controls on the secondary mass flow rate and inlet temperature are useful to achieve constant conditions of the primary working fluid at the inlet of the receiver. An Agilent 34970A Data Acquisition / Data Logger Switch Unit registers the electrical signal coming from the sensors and transmitters with a sampling rate of 3 seconds.

A second experiment is carried out to establish the capability of the nanofluid in collecting solar radiation and verify its stability when exposed to non-concentrated solar radiation with and without circulation. To determine the energy performance of the nanofluid as a direct absorber for non-concentrated solar radiation, the test apparatus presented above has been modified to match the necessities dictated by the new test conditions. First, the solar tracking system of the concentrator has been modified in order to position the rear window of the absorber perpendicular to the direct normal radiation coming from the Sun. To avoid any unwanted reflection of the solar radiation from the solar concentrator, the front window of the receiver has been shielded by a metal plate. Due to the much lower intensity of the global irradiance compared to the concentrated solar flux for which the receiver was originally conceived, the temperature increase in the nanofluid during its passage in the volumetric receiver results barely detectable by the RTDs placed at the inlet and outlet of the receiver. For this reason, a new technique to measure the absorption efficiency of the volumetric receiver based on its radiative balance has been adopted. A schematic representation of the modified apparatus is reported in Figure 124. A first pyranometer, Kipp & Zonen CM11, is mounted on the same receiving plane (rear windows) of the test section, while a second device (Kipp & Zonen CM11) is installed on the metal shield facing the front glass windows (Figure 125).

These radiometers allow measuring the incident and the transmitted irradiance through the test section. Proper covers are adopted to protect the sensor of the second pyranometer from the solar radiation coming from the spaces between receiver's rear plate and metal shield.

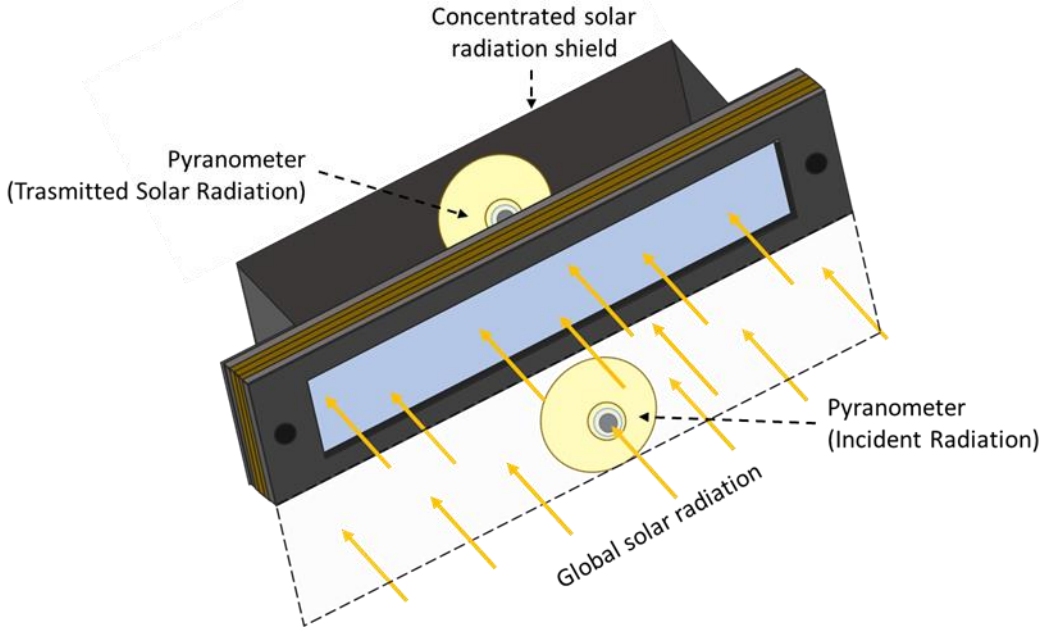

Figure 124 – Schematic representation of the modified test section during test runs under non-concentrated solar radiation.

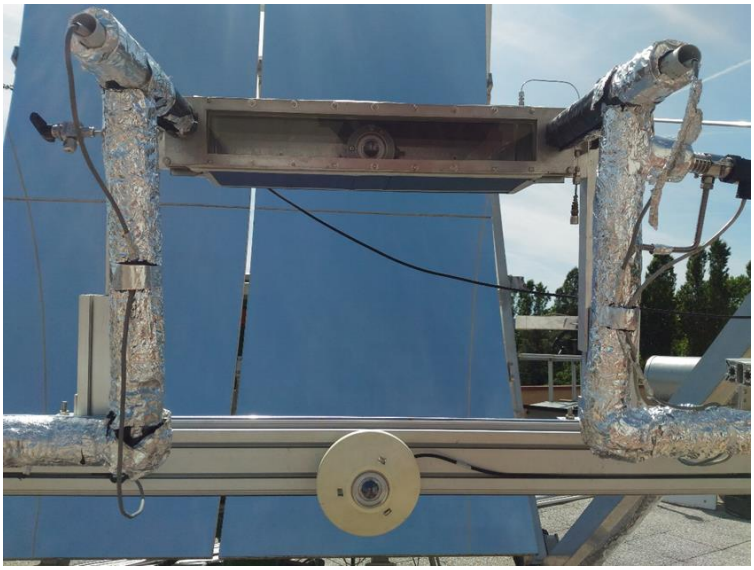

Figure 125 – Pyranometers for the measurement of the incoming solar radiation on the receiving plane and the transmitted solar radiation through the test section. The picture was taken before the circuit was filled with the nanofluid.

5.5.3 Experimental procedure and data reduction

Before the test runs, the primary loop is evacuated and then it is filled with the nanofluid by using a centrifugal pump. The residual air content is removed by circulating the nanofluid at high mass flow rate while keeping the vent valve open. During both experimental campaigns, a preconditioning period of 20 minutes has been observed as indicated in the standard [110]. During each test sequence, the measured data are averaged every 5 minutes: in other words, each measured value presented is the average value of 100 recordings while the collector is working under steady-state conditions, according to the specifications of EN ISO 9806:2013. Experimental test runs were conducted at a nanofluid mass flow rate of about 350 kg h^{-1}, which allows to a transition flow regime in the receiver. Working with lower mass flow rates leads to a higher residence time of the nanofluid in the receiver and to an increased mean temperature. Furthermore, a laminar flow regime may cause a significant temperature gradient across the front glass windows and thus increases the risk of cracks formation in the glass induced by thermal stresses.

All the measured quantities recorded by the data logger are reduced in a MathWorks Matlab® ambient by calculating the fluid properties with NIST Refprop Version 9.0 [109]

During the tests under concentrated solar radiation, the experimental data are collected and reduced according to the quasi-dynamic test method described in the European Standard EN ISO 9806:2013. Prior to the test, the distribution of concentrated solar flux has been experimentally defined using the solar flux mapping system including a water-cooled heat flux microsensor mounted on a semi-automatic two-axes linear system as described in Chapter 2. By using the experimental technique described and the measurement of the direct normal irradiance (DNI), it is possible to calculate the radiative power incident on the front windows of the volumetric receiver. This parameter allows the definition of the receiver thermal efficiency η_r Eq. 3.8, which represents the capability of the absorbing device in converting concentrated solar energy into useful thermal energy and it is independent on the optical and tracking characteristics of the solar concentrator. The performance of a solar collector is evaluated by plotting the thermal efficiency of the receiver η_r and the collector η_{col} (Eq. 3.1) as a function of the reduced temperature difference (Eq. 3.2). The concentration of the

nanoparticles in the nanofluid has been monitored collecting samples of the bulk nanofluid at the beginning and at the end of each test sequence.

During the under non-concentrated solar radiation, the efficiency of the receiver is evaluated based on the radiative balance of the receiver. The irradiance fraction $I_{abs,gross}$ absorbed by the test section can be calculated from the difference between the incident irradiance I_{inc} and the transmitted irradiance I_{trans} through the receiver:

$$I_{abs,gross} = I_{inc} - I_{trans} \qquad \textit{Eq. 5.3}$$

The subscript '*gross'* in the symbol for the absorbed irradiance $I_{abs,gross}$ refer to the fact this term does not represent the mere absorption of the solar irradiance in the nanofluid but takes into account also optical and thermal losses of the receiver. Hence, in the calculation of the efficiency of the receiver, the term $\eta_{r,losses}$ accounting of these losses has been introduced:

$$\eta_r = \eta_{r,gross} - \eta_{r,losses} = \frac{I_{inc} - I_{trans}}{I_{inc}} - \eta_{r,losses} \qquad \textit{Eq. 5.4}$$

The evaluation of the term $\eta_{r,losses}$ has been based on the results obtained from preliminary tests conducted on the test section when the nanofluid was replaced by nitrogen under very similar ambient conditions (T_m^* near 0 K W^{-1} m^2). During these preliminary test, light and heavy types of side cover for the rear pyranometer have been tested. No significant difference between the two types of covers has been detected, and the average ratio between absorbed and incident irradiance resulted of 19%. When the side cover was removed the ratio decrease down to 16%. The consistency of the measurement conducted with the two pyranometers Kipp & Zonen CM11 was check through a direct comparison of the irradiance measured by the two instruments. Good agreement was observed between the two set of measurements with an error within 0.2%, which results much lower than their experimental uncertainties.

5.5.4 Experimental uncertainty analysis

An uncertainty analysis has been performed in agreement with the guidelines provided by the "Guide to the Expression of Uncertainty in Measurement" [37]. Type A uncertainty arises from the statistical analysis of repeated observations and, in the present tests, it comes out considering 100 readings collected over the averaging time of 5 minutes. A list of the Type B

uncertainties of the measured parameters considered in these experiments is reported in Table 15 (confidence level of 95%).

Table 15 – Type B uncertainty (confidence level 95%) of measured parameters during the experimental campaign on the use of SWCNHs – water nanofluid in a volumetric solar receiver.

Ambient air temperature		± 0.1°C
Fluid temperature in primary and secondary loops		± 0.035°C
Nanofluid mass flow rate		± 0.3 kg h^{-1}
Pressure of the fluid in the primary loop		± 0.023 bar
Direct normal irradiance		
	Temperature response	±0.5% of measured value
	Non-linearity	±0.2% of measured value
	Spectral response	±2% of measured value
	Zero offset B	±1 W/m^2
Incident and transmitted irradiances		
	Directional response	±10 W/m^2
	Temperature response	±1% of measured value
	Non-linearity	±0.5% of measured value
	Spectral response	±2% of measured value
	Zero offset B	±2 W/m^2
Wind speed		± (0.1 m/s + 1% of measured value)

The uncertainty analysis, here adopted for the pyrheliometer and the pyranometers to measure incident and absorbed irradiances, is based on the procedure described by *Padovan and Del Col* [11], who show how to apply the method by ISO [37] to the irradiance measurements with thermopile pyranometers. The type B uncertainty of the RTDs in the primary loop results from the calibration procedure performed using high precision four-wire RTDs calibrated up to 150°C. As described in the previous Chapters, the combined standard uncertainty of the parameters that are not directly measured can be calculated by applying the law of error propagation. The expanded experimental uncertainty is obtained by multiplying the relevant standard uncertainty by a coverage factor equal to 2, which corresponds to a level of confidence of 95%.

5.5.5 Experimental results under concentrated solar radiation

The first experimental campaign has been carried out under the concentrated solar flux of the asymmetrical parabolic trough using the same load of SWCNHs nanofluid with a concentration of 0.02 g L^{-1} in two clear-sky days. A total of 71 data points has been collected. During the tests, the thermal efficiency of the receiver has been evaluated under similar ambient conditions. In the first test day, the direct normal irradiance was between 920 W m^{-2} and 960 W m^{-2} and the ambient air temperature between 27°C and 29°C. The direct normal irradiance during the second test varied between 780 W m^{-2} and 680 W m^{-2} with an ambient air temperature around 36°C. The nanofluid in the primary loop has been maintained at a mass flow rate close to 350 kg h^{-1} for both test sequences and its temperature at the inlet of the receiver was equal to 33°C. The average difference between the mean temperature of the nanofluid and the ambient air temperature was 7 K and -2 K during the first and the second test sequences, respectively. That means that the collected data are only slightly affected by the heat losses, therefore the calculated collector thermal efficiencies are mostly affected by the optical efficiency of the present direct absorption concentrating collector.

Figure 126 depicts the volumetric receiver efficiency η_r (Eq. 3.9) with the corresponding error bands against the exposure time of the nanofluid under concentrated solar irradiance. The expanded experimental uncertainty on the receiver efficiency ranges between ±3.5% and ±5.5%. The time in the horizontal axis of Figure 126 represents the actual exposure time of the nanofluid to the concentrated solar radiation. During the first test day, the receiver efficiency did not vary significantly and a maximum value of 87% has been achieved. This efficiency is lower than what was expected from the optical characterization tests on the nanofluid performed in the laboratory (Figure 120). A plausible reason for this could be the saturation of absorption in the nanofluid at high incident intensities. This phenomenon has been recently checked at two discrete wavelengths in the green and infrared regions, finding that SWCNHs show a non-linear optical effect at higher energy densities than the radiative flux measured in the present experiment. However, no indication so far is available regarding the optical effect at high radiative intensity in the whole solar spectrum. Another possible explanation may be addressed to some kind of instability of the nanofluid due to the mere circulation in the apparatus. From Figure 126, a continuous decrease of the performance of the nanofluid-based

device during the second test day can be seen. After eight hours under solar concentrated radiation, the receiver efficiency was equal to 69%. This result clearly indicates that a progressive degradation of the optical properties occurs when the nanofluid is exposed at high concentrated solar flux. The degradation of the absorption capacity of the nanofluid is due to the instability of the SWCNHs suspension in the present concentrating collector. In fact, when monitoring the aspect of the nanofluid inside the receiver channel during the experimental campaign, the change in the working fluid aspect indicates a variation of the nanoparticles concentration due agglomeration and precipitation phenomena.

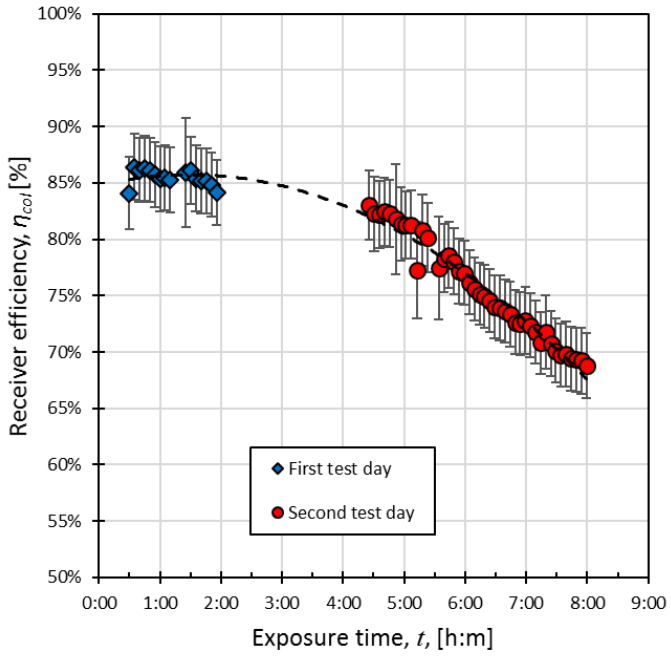

Figure 126 – Experimental receiver efficiency versus exposure time of the receiver under concentrated solar radiation (First test day: DNI: 920 – 960 W m^{-2}, T_{amb}: 27 – 29°C; Second test day: DNI: 680 – 780 W m^{-2}, T_{amb}: 35 – 38°C).

Figure 127 presents three pictures of the flow channel (volumetric absorber) taken respectively, at the beginning of the test campaign (before being exposed to the concentrated solar radiation), between the first and the second test day (exposure time 3 h) and at the end of the test campaign (exposure time 8 h). When taking these picture, samples of the bulk nanofluid has been collected in order to characterize the concentration of the SWCNHs in the aqueous solution. As can be observed on the top picture, which shows the initial conditions of the nanofluid with

a nanoparticles concentration of 0.02 g L^{-1}, the flow channel appears dark and opaque. In the central picture, the paper behind the receiver can be clearly seen and the nanofluid looks like a semi-transparent brownish liquid. The analysis of the corresponding sample reveals that this change in colour and transparency is due to the reduction of the SWCNHs concentration down to 0.01 g L^{-1}. In the bottom picture, the nanofluid has lost almost completely its initial colour, resembling the aspect of pure water. The nanoparticles concentration of the sample corresponding to this last picture results equal to 0.004 g L^{-1}. These concentrations of SWCNHs into suspension reported in Figure 127 have been estimated from the absorbance corresponding to the interband π plasmon peak at the wavelength of about 260 nm, typical of SWCNHs and other graphene-based nanostructure [312], as shown in Figure 128.

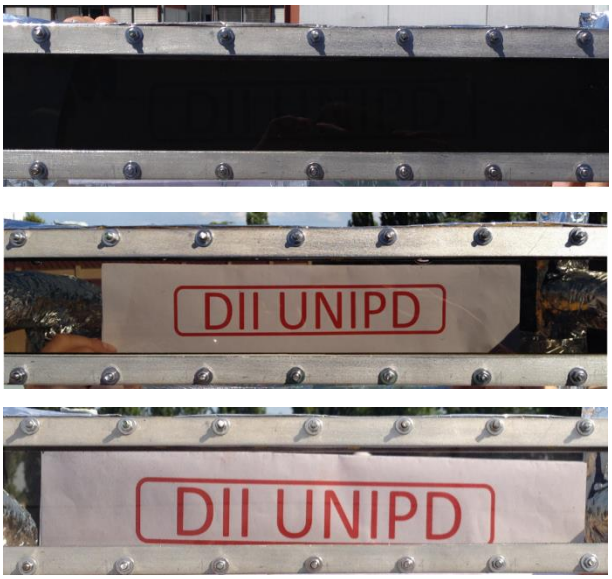

Exposure time = 0 h
(Concentration 0.02 g L^{-1})

Exposure time = 3 h
(Concentration 0.01 g L^{-1})

Exposure time = 8 h
(Concentration 0.004 g L^{-1})

Figure 127 – Pictures of the nanofluid volume in the flow channel of the receiver taken at different exposure times.

The concentrations have been calculated using the Lambert-Beer law:

$$A = \varepsilon_\lambda \, l \, C \qquad \textit{Eq. 5.5}$$

where A is the absorbance, ε_λ is the molar extinction coefficient, l is the beam path length and C is the concentration. Optical transmittance spectra at room temperature have been obtained using a double-beam UV–vis spectrophotometer (Perkin Elmer Lambda 35) from 200 nm to

1100 nm wavelength. The SWCNHs suspensions have been held in quartz cuvettes, with 1 mm beam path length.

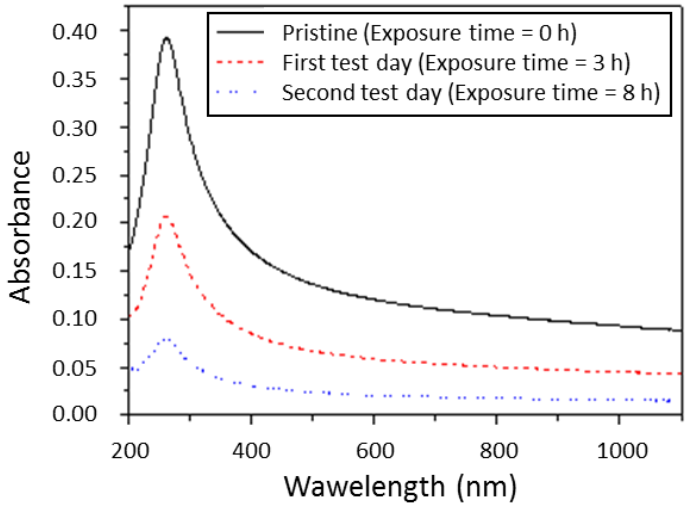

Figure 128 – Absorbance spectra of SWCNHs in the original suspension (pristine) and after the first and second test runs.

A possible explanation for the observed instability of the SWCNHs suspension is the rapid degradation of the polymeric surfactant when exposed to the highly concentrated solar radiation. Another possibility is the irreversible desorption of surfactant molecules from the surface of nanoparticles due to the local overheating. Both mechanisms can lead to a decreased ζ-potential of the suspension due to the loss of charge on the surface of nanoparticles, besides to the loss of steric stabilization, and thus to the agglomeration of the SWCNHs. DLS measurements after the test runs revealed that the average size of aggregates shifted from 143 nm for the original suspension to 95 nm and 81 nm after the first and second test day, respectively. This means that the biggest aggregates or particles tend to coalesce and precipitate, thus not participating to radiation absorption into the collector. ζ-potential measurements showed a reduction in absolute value from -44 mV to -35 mV and -32 mV after the first and second test day, respectively.

Beyond the encountered stability issue, the initial performance of the volumetric receiver is very promising. In Figure 129, a comparison between the performance achieved using the present volumetric receiver and the flat bar-and-plate surface-absorption receiver mounted on

the same asymmetrical parabolic trough is reported. The plot shows the collector experimental thermal efficiencies (Eq. 3.1) against the reduced temperature difference. Furthermore, the efficiency curve for the concentrating collector including the bar-and-plate surface-absorption receiver is also depicted (dashed line). In the present tests with the volumetric receiver, the reduced temperature difference was between -0.006 K m^2 W^{-1} and 0.009 K m^2 W^{-1}. The expanded experimental uncertainty on the collector thermal efficiency ranges between ±2.8% and ±4.9% while the maximum expanded experimental uncertainty on the reduced temperature difference is of ±0.0003 K m^2 W^{-1}.

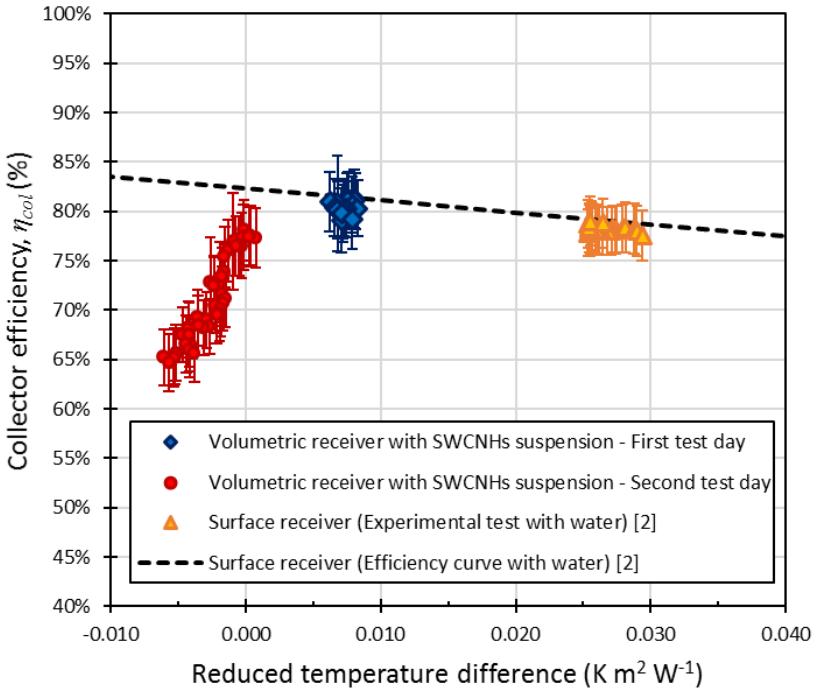

Figure 129 – Comparison of experimental thermal efficiencies of parabolic trough collector using the present volumetric receiver (red circles and blue diamonds) against the same collector using a surface receiver and water as the working fluid (yellow triangles).

Figure 129 shows that the two systems present the same thermal efficiency at 0.0075 K m^2 W^{-1}. This corresponds to the average reduced temperature difference during the first test campaign. As mentioned in Paragraph 5.4, the design of the volumetric receiver was not aimed to maximize the photothermal conversion efficiency, thus there is margin to increase the values of the thermal efficiency of the present DASC. For example, by replacing the glass on the rear

of the receiver with a reflective material and an insulation layer as suggested by the numerical results obtained in Paragraph 5.3.

5.5.6 Experimental results under non-concentrated solar radiation

As mentioned above, the observed instability in the nanofluid during the test performed under concentrated solar radiation may be explained by a rapid degradation of the polymeric surfactant or an irreversible desorption of surfactant molecules from the surface of nanoparticles. This trend could be a hint of surfactant degradation during the exposure to concentrated solar flux. Furthermore, it is not clear how the fluid circulation can contribute to the aggregation of the SWCNs. In order to detect the causes of the nanoparticle agglomeration occurring in the nanofluid, some new experiments have been performed.

5.5.6.1 Experimental results under non-concentrated solar radiation with circulation

A first experimental investigation was carried out with the aim to establish the capability of the nanofluid in collecting solar radiation and verify its stability when exposed to non-concentrated solar radiation. Three test sequences were performed during two consecutive clear-sky days collecting 64 experimental data. The first test sequence was carried out in the afternoon of the first test day. The incident irradiance on the receiver plane was between 850 W m^{-2} and 980 W m^{-2} and the ambient air temperature between 27°C and 31°C. The second day, tests have been performed during the morning and the afternoon. In the morning test sequence, the incident irradiance ranged from 880 W m^{-2} to 1005 W m^{-2} with an ambient air temperature between 24°C and 28°C. In the afternoon, the intermittent passage of clouds led to less stable conditions with an incident irradiance that varied between 330 W m^{-2} and 840 W m^{-2} with an average ambient temperature around 31 °C. The nanofluid in the primary loop has been maintained at a mass flow rate close to 350 kg h^{-1} for all test sequences and its temperature at the inlet of the receiver was around 35°C. The average difference between the mean temperature of the nanofluid and the ambient air temperature was 8 K and -2 K during the first and the second test sequences, respectively. That means that the reduced temperature difference resulted between -0.0017 K W^{-1} m^2 and 0.0239 K W^{-1} m^2 (uncertainty ±0.0006 K W^{-1} m^2) thus, the calculated efficiencies are mostly affected by the optical efficiency of the collector. In this regard, the

preliminary tests conducted with nitrogen in the test section can be considered suitable for the evaluation of the term $\eta_{r,losses}$ in Eq. 5.4.

Figure 130 depicts the volumetric receiver efficiency η_r (Eq. 5.4) with the corresponding error bands against the exposure time of the nanofluid under non-concentrated solar irradiance. The expanded experimental uncertainty on the receiver efficiency ranges between ±9.7% and ±12.3%. The receiver efficiency curve resulting from the test under concentrated solar radiation (dashed line) is also reported in this Figure. The horizontal axis refers to the actual exposure time of the nanofluid to solar radiation.

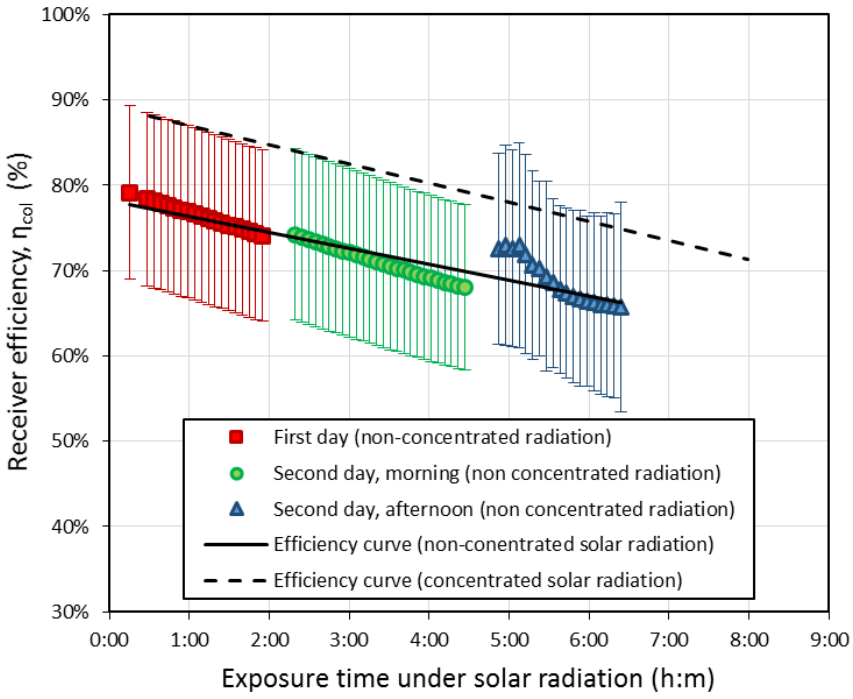

Figure 130 – Experimental receiver efficiency versus exposure time of the receiver under non-concentrated solar radiation. The efficiency curves refer to the test under non-concentrated (continuous line) and concentrated solar radiation (dashed line).

Figure 130 shows that a continuous decrease of the performance of the nanofluid-based device is present during the tests under non-concentrated solar radiation. During the first test day, the receiver efficiency decreases already from the maximum value of 79% down to 74%. After six hours and a half under solar radiation, the receiver efficiency was equal to 66%. This result shows that the progressive degradation of the optical properties occurs also when the nanofluid

is exposed to non-concentrated solar radiation and circulated in the test loop. Figure 131 reports six pictures of the samples of the nanofluid collected respectively at the beginning and at the end of each test sequence. As can be observed, a progressive change in colour and transparency occurs from the first to the last sample revealing that the degradation of the optical properties of the nanofluids is still caused by its instability (nanoparticles agglomeration).

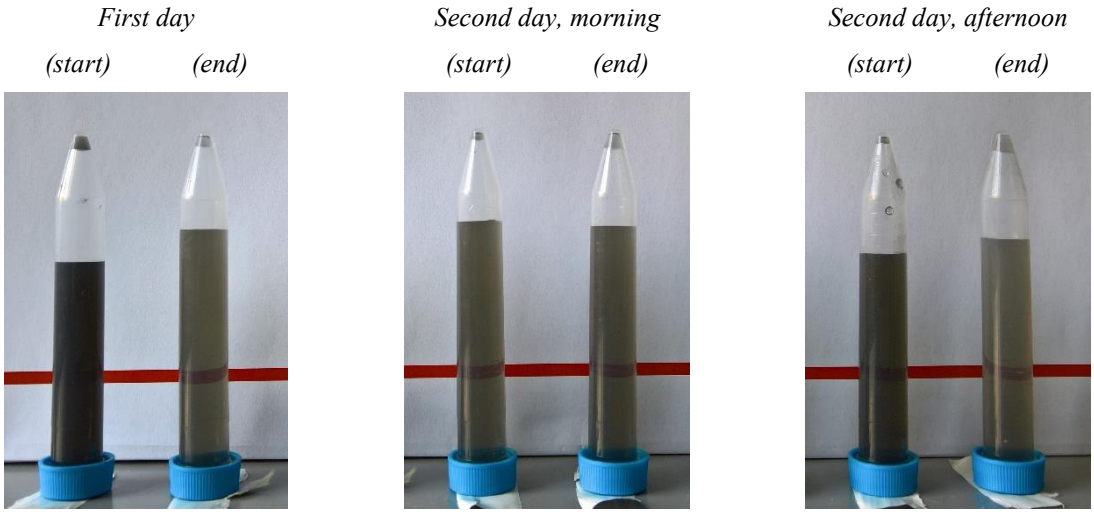

Figure 131 – Pictures of the nanofluid samples collected at the beginning and the end of each test sequence performed under non-concentrated solar radiation.

The SWCNHs concentrations in the suspension reported in Figure 132 have been calculated using the Lambert-Beer law (Eq. 5.5) from the absorbance value corresponding to their interband π plasmon peak at the wavelength of about 260 nm, as shown in Figure 133. It must be mentioned that the higher SWCNHs concentration in the sample collected at the beginning of the last test sequence (second day, afternoon) as compared to that collected at the end of the second test sequence (second day, morning) is due to the circulation of the nanofluid present in the bypass section during a manoeuvre operated between the morning and the afternoon test sequences. Apart from the initial circulation of the nanofluid at a high mass flow rate to remove the residual air content, the fluid present in the bypass section was not circulated and has not been exposed to solar radiation at all. Thus, it is expected that this nanofluid at the time of the manoeuvre possessed a higher SWCNHs concentration than that of the nanofluid circulating in the test section, which was subject to both circulation and exposition to sunlight. The

increased SWCNHs concentration may explain the higher efficiencies of the receiver displayed in the initial period of the last test sequence (Figure 130).

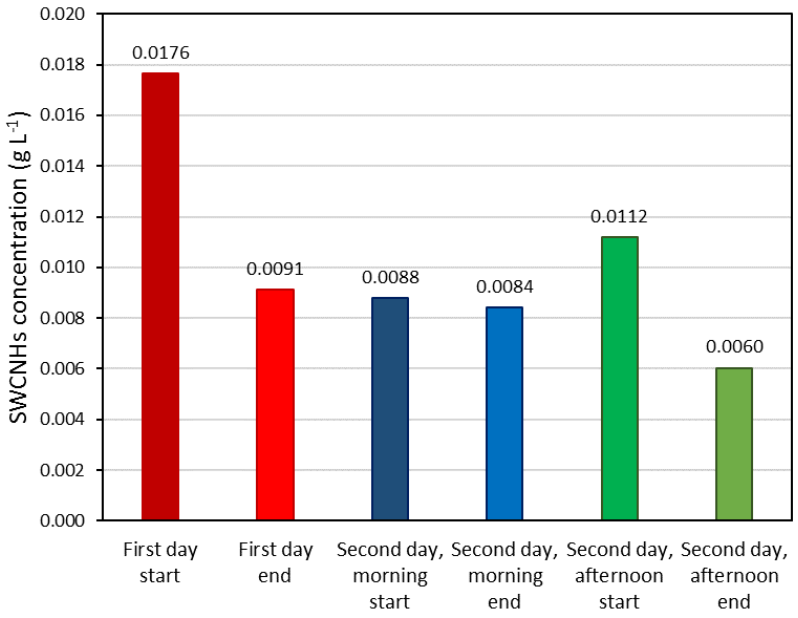

Figure 132 – Concentration of SWCNHs in the nanofluid at the start and the end of each test sequence under non-concentrated solar radiation.

By comparing the experimental efficiency of the receiver measured during the test under non-concentrated solar radiation with the efficiency curve obtained from the tests under concentrated solar radiation, it can be observed that the decreasing trend of the thermal performance of the receiver is very similar. Furthermore, even if the solar radiation incident on the receiver was significantly lower, no slowing down in the degradation of the absorption capacity of the nanofluid is observed. The difference in the efficiency value between the two experimental campaigns can be justified by the lower initial SWCNHs concentration (0.0176 g L^{-1}) of the nanofluid collected during the second experiment as compared to that starting value (0.02 g L^{-1}) measured for the test under concentrated solar radiation. Furthermore, the adoption of different procedures and measurement techniques for the estimation of the thermal performance of the receiver can constitute a further source of the detected efficiency discrepancies. In particular, the term $\eta_{r,losses}$ in Eq. 5.4 can be overestimated because it accounts

optical losses of the receiver, especially of the rear glass, which may not occur when the circuit was filled with nanofluid.

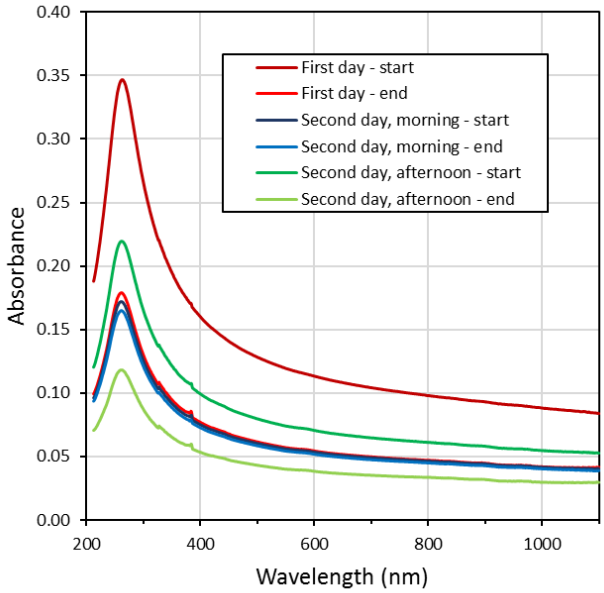

Figure 133 – Absorbance spectra of SWCNHs in the nanofluid at the start and the end of each test sequence under non-concentrated solar radiation.

The experimental results presented above show that the decrease of the thermal efficiency of the receiver over the exposure time when the SWCNH based nanofluid is circulated in the test loop and exposed to non-concentrated solar radiation has a very similar trend to that resulting from the experiments under concentrated solar radiation due to the instability (nanoparticles agglomeration) of the nanofluid. Hence, it can be concluded that the exposure of the nanofluid to an intense concentrated solar flux is not the cause of nanofluids degradation.

5.5.6.2 Experimental results under non-concentrated solar radiation without circulation

In order to investigate the effects on the absorption capability of the nanofluid caused by the mere exposure to solar radiation, a new experiment was set up. The volumetric receiver has been filled with a new load of nanofluid having a SWCNHs concentration of 0.02 g L^{-1}. The receiver has been exposed to solar radiation without circulating the nanofluid. Incident and transmitted irradiances through the receiver have been measured as well as temperature and pressure of the nanofluid in the receiver. The experiment has been carried out during ten non-

consecutive days during which the receiver has been exposed to non-concentrated solar radiation for a cumulative time equal to 65 hours. The signals of the measuring devices were acquired every 3 s and were averaged over a period of 5 minutes

Figure 134 display the measured gross receiver efficiency as a function of the exposure time. The variations in the efficiency during each test sequence are mainly due to the variability in the environmental conditions (air temperature and sky cover) and were all within the experimental uncertainty ±10%. It is interesting to note that during each test, a stable condition has been reached after a period of around 20-30 minutes. This period is in line with the preconditioning period suggested by the European Standard EN ISO 9806:2013. A slightly decreasing trend of the gross efficiency of the receiver can be observed in Figure 134. The average efficiency slightly decreases from of 99.2% down to 98.3%. This decrease is significantly smaller with respect to those detected in the previous experiments.

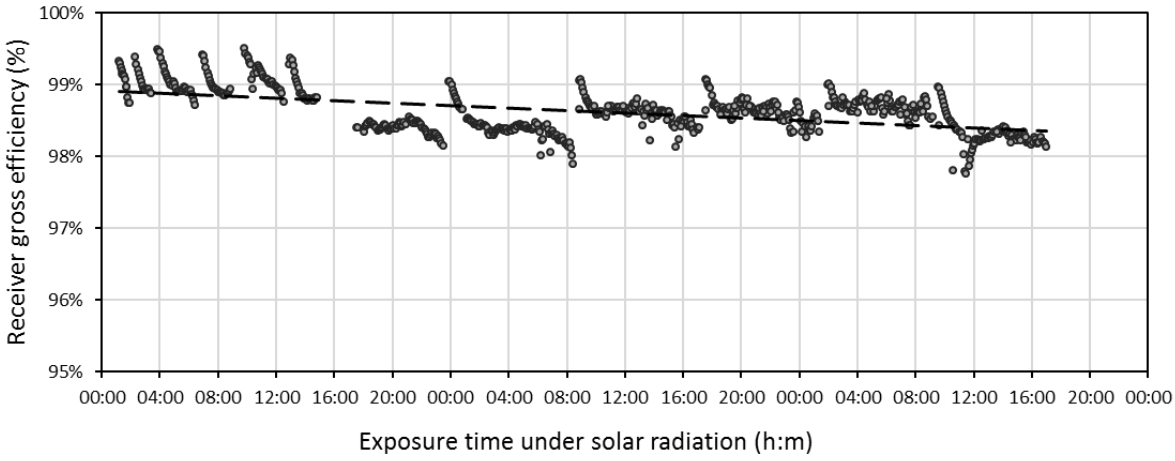

Figure 134 – Experimental receiver gross efficiency versus exposure time of the receiver under non-concentrated solar radiation without circulation of the nanofluid.

These results show that the mere exposure of the nanofluid to the solar radiation does not significantly affect the gross efficiency of the receiver, therefore it is reasonable to suppose that the interaction between solar radiation and aqueous suspension of SWCNs presents negligible effects on the stability of the nanofluid and on its optical absorption capability over short period under solar radiation.

5.5.6.3 Experimental results in circulation without exposure to solar radiation

According to the experimental results obtained when the nanofluid has been exposed to concentrated solar radiation with and without circulation, the instability of the nanofluid may be caused by the mechanical stress induced in the nanofluid by its circulation in the nanofluid in the experimental circuit on board of the solar concentrator. To investigate this aspect, the nanofluid used to performs the tests under non-concentrated solar radiation has been circulated for 12 hours in the collector circuit without being exposed to sunlight at a mass flow rate close to 350 kg h^{-1}. The average temperature of the receiver during these tests was 35°C, while the ambient air was 29°C. The initial SWCNHs concentration in the nanofluid was equal to 0.006 g L^{-1}, which was the last concentration measured during the test under non-concentrated solar radiation with circulation. Figure 135 shows the nanofluids samples collected at different times during the circulation test with the respective value of SWCNHs concentration in the nanofluid. The concentrations have been calculated using the Lambert-Beer law (Eq. 5.5) from the absorbance value corresponding to the interband π plasmon peak at the wavelength of about 260 nm.

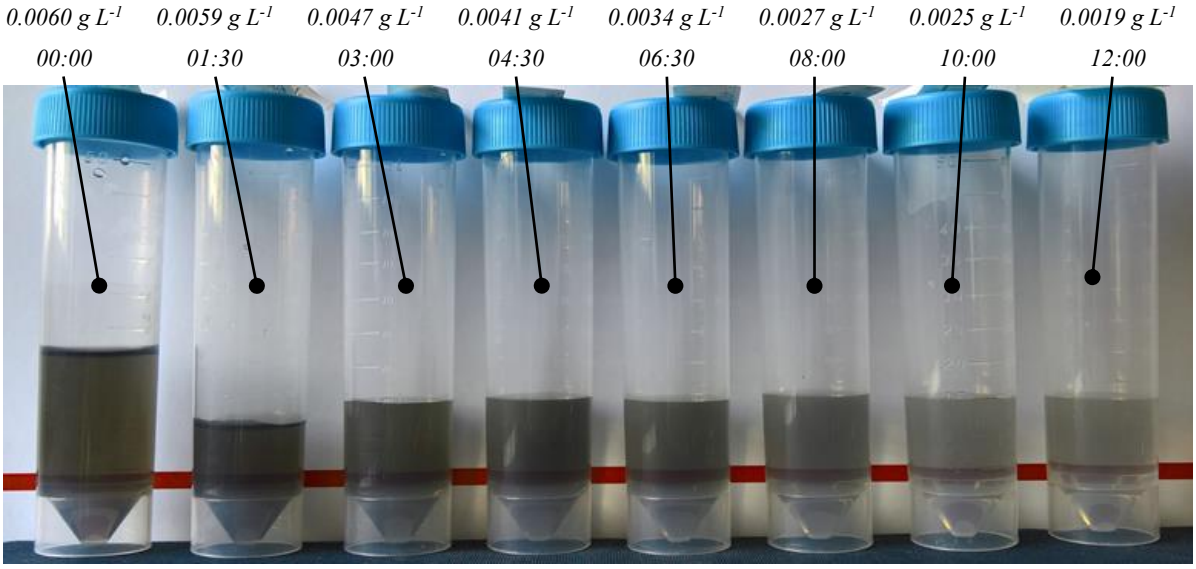

Figure 135 – Picture of the samples collected during the circulation test on the nanofluid. The concentration of SWCNHs in the nanofluid (g L^{-1}) and the circulation time (hh:mm) are reported above each sample.

The chart in Figure 136 reports the SWCNHs concentration suspended in water for the collected samples as a function of the circulation time. For the sake of completeness, also the concentration obtained from the test under non-concentrated solar radiation with circulation and that of the pristine are represented in this Figure.

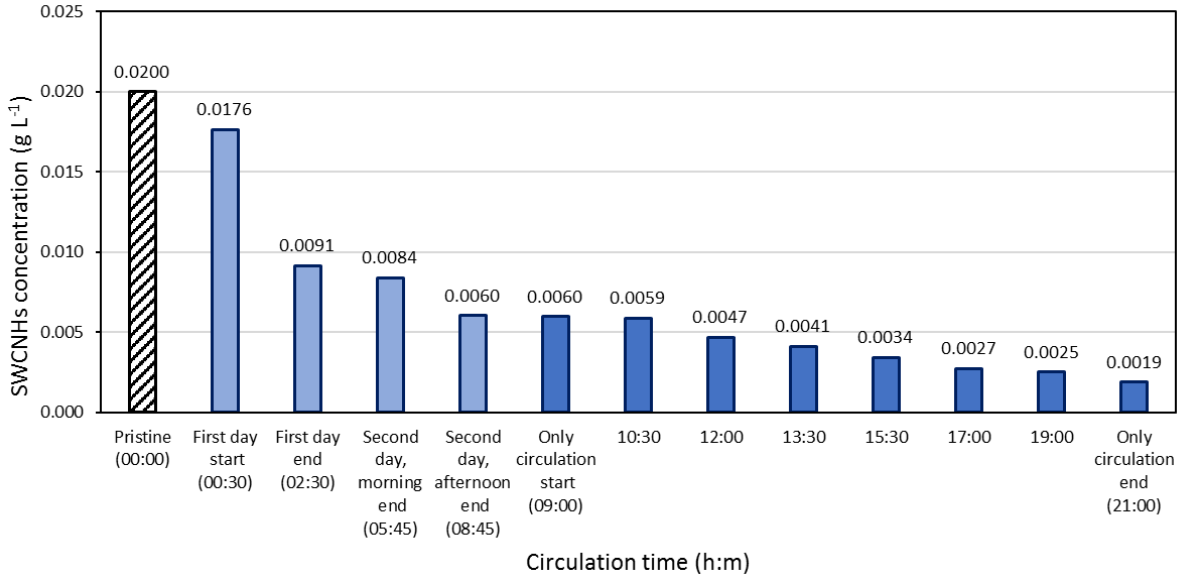

Figure 136 – Concentration of SWCNHs in the nanofluid versus circulation time.

From the values of the nanoparticles concentration reported in Figure 135 and Figure 136, it is clear that the agglomeration in the nanofluid still occurs when the nanofluid is circulated in the experimental test circuit without being exposed to the solar radiation. The decrease of the concentration is not linear with time. After 21 hours of circulation since the nanofluid was filled in the circuit, the SWCNHs concentration results 10 times smaller than the value of the pristine (0.02 g L^{-1}). Compared to the value (0.006 g L^{-1}) measured at the beginning of the test without exposition to sunlight, the concentration at the end of the test is decreased by a factor 3 (0.002 g L^{-1}). These results suggest that the instability of the nanofluid detected in the previous tests may be addressed to the mechanical stress in the nanofluid when circulated in the test loop.

Conclusions

In this thesis, the results of the investigation on advanced technologies for linear concentrating solar collector conducted in the Solar Energy Conversion Lab of the Industrial Engineering Department, at the University of Padova, were presented.

The study started with the analysis of different estimation procedures for the assessment of the solar radiation availability in concentrating systems in two sites (Padova and Trisaia). This study has shown that sky variability affected the accuracy of the considered separation models in the estimation of short-term (minute and hour) and long-term (day, month and season) direct normal irradiance, proving the high sensitivity of the correlations to the sky conditions. Furthermore, the considered models showed different behaviour for the two sites under investigation even under clear-sky conditions; this suggested that their accuracy was also affected by local climatic and atmospheric conditions, which can be site-dependent. With regard to the indirect derivation of the direct normal irradiance from measurements of global and diffuse horizontal irradiances, it showed good accuracy in estimating the direct normal irradiance even when the diffused irradiance was measured with a shadow-band, provided that the systematic error due to the thermal offset was evaluated and corrected. Therefore, the presented indirect procedure can constitute a valid and cheaper method to produce short- and long-term data of direct normal irradiation when measurements from pyrheliometers are not available.

In the second step, the solar flux map on the focal region of the asymmetrical parabolic trough linear concentrator has been experimentally determined by adopting a reliable and repeatable direct method. The solar flux mapping system includes a water-cooled heat flux microsensor mounted on a two-axis semi-automatic linear handling system to scan the concentration region. To define the solar flux map, the collected data of sensor position and heat flux have been numerically interpolated by a biharmonic spline interpolant over a grid with a spatial resolution

of 0.1 mm x 0.1 mm. The heat flux data were collected with different spatial sampling on the focal region. A sensitivity analysis considering different interpolants has demonstrated that the results were insensitive to the chosen interpolant and that the number of collected data was high enough for an accurate definition of the concentrated solar flux distribution. According to the results, as expected, the solar flux distribution was strongly non-uniform along the width of the concentration region. The study provided the values of the optical efficiency and the intercept factor for different values of width of a receiver installed in the asymmetrical parabolic trough concentrator. This information is a key aspect for the proper design of new receivers. The intercept factor resulted 100% for receiver's widths larger 75 mm, while it decreased to 98% for a 65 mm width and when a width lower than 45 mm was considered, the intercept factor resulted below 90%. A numerical model to predict the optical performance of the investigated parabolic trough has been developed using a Monte Carlo ray-tracing tool. From the comparisons between experimental data and numerical predictions, it has been concluded that a value between 4.5 mrad and 5 mrad is suitable for modelling the total optical error using a Gaussian distribution

An innovative bar-and-plate flat aluminium absorber receiver has been designed and tested during both liquid heating and direct vaporization of water and of a halogenated fluid in the considered linear concentrator. The obtained results were in line with some medium-temperature concentrating collectors currently available on the market. The performance during the two tests conducted with the two fluids was similar with an experimental optical efficiency between 82% and 80%. During the test conducted on water, the thermal efficiency at 0.160 $W^{-1} m^2$ reduced temperature difference was around 64%. The efficiency curves derived considering only the liquid heating tests or the whole collected database in single- and two-phase tests on water were in very good agreement. Furthermore, the two datasets overlapped at reduced temperature differences between 0.130 K $W^{-1} m^2$ and 0.140 $W^{-1} m^2$. Therefore, the present new test procedure proposed for direct steam generation tests was validated and can be adopted to characterize the thermal performance of a concentrating collector with two-phase flow. Moreover, the solar collector was able to vaporize the low-GWP halogenated fluid R1233zd(E) at 7.5 bar saturation pressure and outlet vapor quality between 0.37 and 0.98 with a mean efficiency of 73%. At the saturation pressure of 10.5 bar and outlet vapor quality

between 0.35 and 0.88, the mean efficiency of the collector was equal to 70%. Mass flow rate and the subcooling of the halogenated fluid entering the receiver displayed a negligible influence on the performance of the collector. When the outlet vapor quality was below 0.7, the measured surface temperatures on the back of the absorber back were close to the saturation temperature of the vaporizing fluid, without any hot spot associated with thermal dry out. However, at higher vapor quality, the efficiency of the collector was not affected by the presence of dry out. This demonstrates that the present bar-and-plate absorber is suitable for direct steam generation even at low mass flow rate. Regarding the hydraulic performance, despite the presence of the turbulator in the channel, a low pressure drop during direct vaporization of the fluid was measured. A numerical model to predict the performance of the receiver during liquid heating and vaporization of a fluid has been developed and validated against the experimental data. The estimated thermal performance of the collector was in good agreement with the experimental tests. The prediction of the thermal efficiency of the collector displayed error within 5%. The numerical prediction was less accurate for the experimental points where the phenomenon of dry out is occurring. The numerical simulation on the direct vaporization of the halogenated fluid up to 130°C in the collector showed that is possible to obtain outlet vapor quality between 0.55 and 0.6 with a thermal efficiency higher than 60%.

A new numerical steady-state model was developed for a small size ORC system powered by a low-temperature water flow. The system configuration and the installed components were inspired by the design of a commercially available machine which constitutes a valid example of the current state-of-art in the design of ORC system for distributed generation from low- to medium-temperature heat sources. The model has been validated by comparing the numerical predictions with the datasheet of a commercial unit with a similar size working with R245fa. Since no information on the control of the working fluid flow rate and on the geometry of the components in the ORC unit were available by the manufacturer, some assumptions on these aspects have to be made. No data were available to validate the expander model, which strongly affects the performance of the ORC unit throughout the operational range. Nevertheless, the validation of the ORC model showed that the relative prediction error on the electrical power output of the machine resulted 12% lower on average than the data declared by the manufacturer. Next, the model of the flat receiver has been integrated into the ORC model to

evaluate its performance by coupling the aforementioned concentrating solar system with direct vaporization of the R1233zd(E) or by using an intermediate solar circuit to heat pressurized water and evaporate this organic fluid in a separate heat exchanger. The comparison highlighted the advantages offered by the direct vaporization of the organic working fluid in the solar receiver which presented higher electrical output and conversion efficiency. Furthermore, the direct vaporization of the organic fluid increased the exergy performance of the solar-powered ORC in most of the simulated conditions.

The last step of this thesis regards the application of aqueous suspensions of single-wall carbon nanohorns as volumetric absorbers in a concentrating direct absorption solar collector. This application has been numerically and experimentally investigated. A three-dimensional model has been developed in commercial software for computational fluid dynamics simulations to estimate the performance of a direct absorption receiver. The calculated performance of a volumetric receiver working with a concentration of SWCHNs equal to 0.05 g L^{-1} has been compared with calculated and experimental performance of two conventional surface-absorption receivers working under the radiative flux of the same asymmetrical parabolic trough solar concentrator. The comparison showed that, under the same ambient, solar irradiance and mass flow rate conditions, at fluid inlet temperature up to 140°C (413 K), the efficiency of the volumetric collector was higher than those of the collectors involving a selective surface absorber. An optical efficiency equal to 90.6% has been estimated for the volumetric concentrating solar collector. Numerical analyses on the effects of the optical properties of the glass window, inlet temperature, mass flow rate and nanoparticles concentration have been performed. The following guidelines for the design and optimization of a flat volumetric receiver for a solar concentrating collector are drawn:

- increasing the nanoparticles concentration makes the receiver thermal behaviour more and more similar to that of a surface-absorption device; this may lead to increased heat losses in full-size receivers;
- at low mass flow rates, the nanofluid has more time to absorb and convert concentrated solar flux into heat causing high thermal gradients on the glass; a turbulent flow regime condition leads to a safer and more efficient operation;

- the channel depth of the direct absorption receiver must meet the optical penetration depth of the nanofluid depending on the nanoparticles concentration;
- the optimization of the nanoparticles concentration should lead to the lowest possible concentration to simplify the production method, address possible long-term stability issues, improve the thermal behaviour and the cost-effectiveness of the receiver.

According to guidelines provided by the numerical results, a direct absorption receiver has been designed and manufactured to investigate the capability of the nanofluid to absorb the concentrated sunlight. The receiver exhibits a flat geometry and has been designed for installation on a full-scale linear concentrating collector presenting an asymmetrical parabolic trough. A low-cost nanofluid containing 0.02 g L^{-1} of SWCHNs in distilled water was prepared and its thermal and optical properties were characterized. The nanofluid optical capability to absorb high concentrated solar fluxes has been experimentally investigated using this suspension as working fluid and volumetric absorber in a parabolic trough direct absorption solar collector. Tests have been performed according to a standardized procedure with the nanofluid flowing in the designed receiver at 83.4 kg m^{-2} s^{-1} specific mass flow rate and temperature close to that of the ambient air to minimize the effect of the heat losses. The nanofluid flow channel is 18 mm deep, displaying glass windows both on the front and on the rear of the receiver. In order to characterize the performance of the volumetric receiver, its efficiency was compared with previous data obtained with a surface absorber. Although the geometry of the receiver was designed for testing purposes and not optimized for thermal efficiency, the initial performance of the volumetric receiver reached 82% and was similar to that of a surface receiver, using a flat bar-and-plate with an inner turbulator and mounted on the same parabolic trough concentrator. Thus, the results demonstrated that there is much room for further improvements. Although during the first two hours of exposure to concentrated solar radiation, the receiver thermal efficiency did not vary significantly, a continuous decrease in the efficiency of the direct absorption receiver was found, down to 65% after 8 hours of exposure. Furthermore, a change in colour and transparency of the nanofluid in the receiver was observed. Spectrophotometric analysis of specimens of bulk nanofluid taken at different exposure times revealed that the concentration of SWCNHs decreases due to coalescence and precipitation of the biggest aggregates. After 3 hours of exposure, the SWCNHs concentration in water was halved and, after 8 hours, it was of 0.004 g L^{-1}. Further experiments revealed the

instability of the nanofluid (nanoparticles agglomeration) was still present when the nanofluid was circulated in the same circuit and exposed to non-concentrated solar radiation. Furthermore, the decrease in the thermal efficiency of the receiver over the exposure time during these tests displayed a very similar trend to that resulting from the experiments under concentrated solar radiation. On the other hand, when the nanofluid was not circulated, but still exposed to the sunlight, the nanoparticles did not show any agglomeration and the performance of the receiver was extremely stable. These results suggested that the only exposure of the nanofluid under solar radiation was not a cause for the aggregation of the nanoparticles. Moreover, it was observed that the agglomeration of the nanoparticles was still present when the nanofluid was circulated and not exposed to the solar radiation. Thus, a possible reason for the instability of the nanofluid can be the mechanical stress on the nanofluid when it was circulated.

Future perspectives

In the future, thanks to the low cost and the high flexibility of the bar-and-plate technology, it is expected that an optimization study conducted on the presented bar-and-plate flat absorber can lead to the development of market competitive, high-performance receivers for linear concentrating. For example, some improvement can be obtained by arranging the flat absorber as a part of a cavity receiver and by adopting a solar selective coating with a low thermal emittance.

Regards direct solar absorbers, from the literature it emerges that this technology is still in its infancy. However, given the good ground in terms of solar absorption of the carbon-based nanofluids, further investigations are needed to get stable nanofluid for future market competitive direct absorption solar collectors. The functionalization of the SWCNHs offers some alternatives to increase the stability of the nanofluid and may be an interesting topic for future research. Furthermore, the investigated volumetric solar receiver tested here was not conceived to maximize its thermal performance and there is much room for improvement, such as the adoption of a reflective insulated rear part of the receiver.

References

[1] Rabl A. Optical and thermal properties of compound parabolic concentrators. Solar Energy 1976;18:497-511.

[2] Al-Sulaiman FA. Exergy analysis of parabolic trough solar collectors integrated with combined steam and organic Rankine cycles. Energy Conversion and Management 2014;77:441-9.

[3] Solar industrial process heat. State of the art. 2006.

[4] Vannoni C,., Battisti R, Drigo S. Potential for solar heat in industrial processes. 2008.

[5] Cabrera FJ, Fernández-García A, Silva RMP, Pérez-García M. Use of parabolic trough solar collectors for solar refrigeration and axial-flow' applications. Renewable and Sustainable Energy Reviews 2013;20:103-18.

[6] Fernández-García A, Zarza E, Valenzuela L, Pérez M. Parabolic-trough solar collectors and their applications. Renewable and Sustainable Energy Reviews 2010;14:1695-721.

[7] Galvez J, Malato Rodriguez S. Medium temperature solar concentrators (parabolic trough collectors. ;1.

[8] Blanco M, Santigosa LR. Advances in Concentrating Solar Thermal Research and Technology. 1st ed. GB: Woodhead Publishing Ltd, 2016.

[9] Duffie JA, Beckman WA. Solar engineering of thermal processes. 4th Edition ed. Hoboken, New Jersey, U.S.A.: John Wiley & Sons Inc., 2014.

[10] Myers DR. Comparison of direct normal irradiance derived from silicon and thermopile global hemispherical radiation detectors. Proceedings of SPIE Aug 18, 2010;7773.

[11] Padovan A, Del Col D. Measurement and modeling of solar irradiance components on horizontal and tilted planes. Solar Energy 2010;84:2068-84.

[12] Dugaria S, Padovan A, Sabatelli V, Del Col D. Assessment of estimation methods of DNI resource in solar concentrating systems. Solar Energy 2015;121:103-15.

[13] Gueymard CA, Myers DR. Evaluation of conventional and high-performance routine solar radiation measurements for improved solar resource, climatological trends, and radiative modeling. Solar Energy 2009;83:171-85.

[14] Kotti MC, Argiriou AA, Kazantzidis A. Estimation of direct normal irradiance from measured global and corrected diffuse horizontal irradiance. Energy 2014;70:382-92.

[15] Vick BD, Myers DR, Boyson WE. Using direct normal irradiance models and utility electrical loading to assess benefit of a concentrating solar power plant. Solar Energy 2012;86:3519.

[16] Mohammed J, Yandt M, Wilkins M, Muron A, Hall TJ, Haysom JE et al. Collection and storage of direct spectral irradiance and DNI datasets with high temporal resolution for CPV energy yield assessments. PVSC 2013:2320-5.

[17] Cogliani E, Ricchiazzi P, Maccari A. Generation of operational maps of global solar irradiation on horizontal plan and of direct normal irradiation from Meteosat imagery by using SOLARMET. Solar Energy 2008;82:556-62.

[18] Viana TS, Rüther R, Martins FR, Pereira EB. Assessing the potential of concentrating solar photovoltaic generation in Brazil with satellite-derived direct normal irradiation. Solar Energy 2011;85:486-95.

[19] Amillo A, Huld T, Müller R. A New Database of Global and Direct Solar Radiation Using the Eastern Meteosat Satellite, Models and Validation. Remote Sensing 2014;6:8165-89.

[20] Polo J, Antonanzas-Torres F, Vindel JM, Ramirez L. Sensitivity of satellite-based methods for deriving solar radiation to different choice of aerosol input and models. Renewable Energy 2014;68:785-92.

[21] Bachour D, Perez-Astudillo D. Deriving solar direct normal irradiance using lidar-ceilometer. Solar Energy 2014;110:316-24.

[22] Gueymard CA. Impact of on-site atmospheric water vapor estimation methods on the accuracy of local solar irradiance predictions. Solar Energy 2014;101:74-82.

[23] Remund J, Müller SC. Uncertainty of meteonorm long term DNI means and future trends. Proceedings of 17th SolarPACES Conference 2011.

[24] Bertrand C, Vanderveken G, Journee M. Evaluation of decomposition models of various complexity to estimate the direct solar irradiance over Belgium. Renewable Energy 2015;74:618-26.

[25] Muneer T. Solar radiation and daylight models. 2nd ed. ed. Oxford: Elsevier Butterworth Heinemann, 2004.

[26] Erbs DG, Klein SA, Duffie JA. Estimation of the diffuse radiation fraction for hourly, daily and monthly-average global radiation. Solar Energy 1982;28:293-302.

[27] Maxwell EL. A quasi-physical model for converting hourly global horizontal to direct normal insolation. 1987.

[28] Perez R, Seals R, Zelenka A, Ineichen P. Climatic evaluation of models that predict hourly direct irradiance from hourly global irradiance: Prospects for performance improvements. Solar Energy 1990;44:99-108.

[29] Skartveit A, Olseth JA, Tuft ME. An hourly diffuse fraction model with correction for variability and surface albedo. Solar Energy 1998;63:173-83.

[30] Perez RR, Ineichen P, Maxwell EL, Seals RD, Zelenka A. Dynamic global-to-direct irradiance conversion models. ASHRAE Transactions 1992;98:354-69.

[31] Orgill JF, Hollands KGT. Correlation equation for hourly diffuse radiation on a horizontal surface. Solar Energy 1977;19:357-9.

[32] Kasten F. A simple parameterization of two pyrheliometric formulae for determining the linke turbidity factor. Meteorolgische Rundschau 1980;33:123-7.

[33] Dugaria S, Padovan A, Sabatelli V, Del Col D. Assessment of estimation methods of DNI resource in solar concentrating systems. Solar Energy 2015;121:103-15.

[34] LeBaron BA, Michalsky JJ, Perez R. A simple procedure for correcting shadowband data for all sky conditions. Solar Energy 1990;44:249-56.

[35] International Organization for Standardization. ISO 9060:1990 Solar energy - specification and classification of instruments for measuring hemispherical solar and direct solar radiation. Genève: ISO, 1990.

[36] International Organization for Standardization. ISO 9847:1992 Solar energy -- Calibration of field pyranometers by comparison to a reference pyranometer. 1992.

[37] International Organization for Standardization. ISO/IEC Guide 98-3:2008 Uncertainty of measurement -- Part 3: Guide to the expression of uncertainty in measurement (GUM:1995). Geneve, Switzerland, 2008.

[38] Reda I. Method to Calculate Uncertainties in Measuring Shortwave Solar Irradiance Using Thermopile and Semiconductor Solar Radiomenters. National Renewable Energy Laboratory 2011.

[39] Vignola F, Long C, Reda I. Evaluation of Methods to Correct for IR Loss in Eppley PSP Diffuse Measurements. Optical Modeling and Measurements for Solar Energy Systems: Proceedings of the Conference, 26-28 August 2007, San Diego, California Jan 1, 2007.

[40] Meyer R, Gueymard CA, Ineichen P. Standardizing and benchmarking of modeled DNI products. Proceedings of 17th SolarPACES Conference 2011.

[41] Gueymard CA. Progress in direct irradiance modeling and validation. Proceedings of 39th ASES National Solar Conference 2010 2011.

[42] Padovan A, Del Col D. Assessment of models of direct normal irradiance in northern Italy. Proceedings of 17th SolarPACES Conference 2011.

[43] Kleissl J. Solar Energy Forecasting and Resource Assessment. 1st ed. US: Academic Press, 2013.

[44] Ineichen P. Validation of models that estimate the clear sky global and beam solar irradiance. Solar Energy 2016;132:332-44.

[45] REN21. Renewables 2017 Global Status Report. 2017.

[46] Tiwari GN, Tiwari A, Shyam. Handbook of Solar Energy : Theory, Analysis and Applications. Singapore: Springer, 2016.

[47] Rabl A. Comparison of solar concentrators. Solar Energy 1976;18:93-111.

[48] Hoffschmidt B, Alexopoulos S, Göttsche J, Sauerborn M, Kaufhold O. 3.06 - High Concentration Solar Collectors. In: Sayigh A, editor. Comprehensive Renewable Energy, Oxford: Elsevier; 2012, p. 165-209.

[49] Dudley VE, Kolb GJ, Sioan M, Kearney D. Report SAND94-1884 - Test results: SEGS LS-2 Solar Collector. Sandia National Laboratories 1994.

[50] Lupfert E, Geyer M, Schiel W, et al. Eurotrough: A new parabolic trough collector with advanced light weight structure Proceedings of the Solar Thermal 2000 International Conference. 2000.

[51] Menand G. NREL research helps deliver clean, solar electricity to thousands of homes in the southwest. CSP Today 2006.

[52] Riffelmann K-, Kötter J, Nava P, et al. HELIOTROUGH – A new collector generation for parabolic trough power plants. Prooceding of SolarPACES Symposium 2009 Berlin 2009.

[53] Schweitzer A, Schiel W, Abul-Ella Z, et al. ULTIMATE TROUGH – The next generation collector for parabolic trough power plants. Proceedings of SolarPACES Symposium 2010 Perpignan 2010.

[54] Abengoa Solar. http://www.abengoasolar.com/

[55] Prinsloo G, Dobson R. Solar tracking. Stellenbosch, South Afruca, 2014.

[56] Chong KK, Wong CW. General formula for on-axis sun-tracking system and its application in improving tracking accuracy of solar collector. Solar Energy 2009;83:298-305.

[57] Daniel Cotfas, Petru Cotfas, Socrates Kaplanis, Doru Ursutiu, Cornel Samoila. SUN TRACKER SYSTEM VS FIXED SYSTEM. Bulletin of the Transilvania University of Brasov. Mathematics, Informatics, Physics. Series III 2008;1:545.

[58] Ronda High-Tech S.r.l. Ronda High-Tech Reflective Panel. Technical data sheet, material characteristic and tests. 2012:23.

[59] Montecchi M. Riflettanza solare dello specchio Fast Glass basato su. ENEA 2010:6. Vetro extra-chiaro Pilkington Microwhite 1.0 mm

[60] Baig H, Sarmah N, Heasman KC, Mallick TK. Numerical modelling and experimental validation of a low concentrating photovoltaic system. Solar Energy Mater Solar Cells 2013;113:201-19.

[61] Khanna S, Singh S, Kedare SB. Explicit expressions for temperature distribution and deflection in absorber tube of solar parabolic trough concentrator. Solar Energy 2015;114:289-302.

[62] Khanna S, Singh S, Kedare SB. Effect of Angle of Incidence of Sun Rays on the Bending of Absorber Tube of Solar Parabolic Trough Concentrator. Energy Procedia 2014;48:123-9.

[63] Khanna S, Kedare SB, Singh S. Analytical expression for circumferential and axial distribution of absorbed flux on a bent absorber tube of solar parabolic trough concentrator. Solar Energy 2013;92:26-40.

[64] Eck M, Uhlig R, Mertins M, Häberle A, Lerchenmüller H. Thermal load of direct steam-generating absorber tubes with large diameter in horizontal linear fresnel collectors. Heat transfer engineering 2007;28:42-8.

[65] Winter C-, Sizmann RL, Vant-Hull LL. Solar Power Plants : Fundamentals, Technology, Systems, Economics. 1st ed. Berlin/Heidelberg: Springer, 1991.

[66] Röger M, Herrmann P, Ulmer S, Ebert M, Prahl C, Göhring F. Techniques to Measure Solar Flux Density Distribution on Large-Scale Receivers. Journal of Solar Energy Engineering 2014;136:031013.

[67] Ballestrín J, Burgess G, Cumpston J. 18 - Heat flux and temperature measurement technologies for concentrating solar power (CSP). In: Lovegrove K, Stein W, editors. Concentrating Solar Power Technology: Woodhead Publishing; 2012, p. e4.

[68] Ballestrin J. A non-water-cooled heat flux measurement system under concentrated solar radiation conditions. Solar Energy 2002;73:159-68.

[69] Ferriere A, Rivoire B. An instrument for measuring concentrated solar-radiation: a photo-sensor interfaced with an integrating sphere. Solar Energy 2002;72:187-93.

[70] Parretta A, Antonini A, Armani M, Nenna G, Flaminio G, Pellegrino M. Double-cavity radiometer for high-flux density solar radiation measurements. Appl Opt 2007;46:2166-79.

[71] Fernández-Reche J, Sánchez MAM, Cañadas I, Chenlo F, Rodríguez J, Ballestrín J. Concentrating PV: An Alternative to Calorimeters for Measuring High Solar Flux Densities. J Sol Energy Eng 2008:130-4.

[72] Riffelmann K, Neumann A, Ulmer S. Performance enhancement of parabolic trough collectors by solar flux measurement in the focal region. Solar Energy 2006;80:1303-13.

[73] Pérez-Rábago CA, Marcos MJ, Romero M, Estrada CA. Heat transfer in a conical cavity calorimeter for measuring thermal power of a point focus concentrator. Solar Energy 2006;80:1434-42.

[74] Estrada CA, Jaramillo OA, Acosta R, Arancibia-Bulnes CA. Heat transfer analysis in a calorimeter for concentrated solar radiation measurements. Solar Energy 2007;81:1306-13.

[75] Jaramillo OA, Pérez-Rábago CA, Arancibia-Bulnes CA, Estrada CA. A flat-plate calorimeter for concentrated solar flux evaluation. Renewable Energy 2008;33:2322-8.

[76] Ballestrín J, Monterreal R. Hybrid heat flux measurement system for solar central receiver evaluation. Energy 2004;29:915-24.

[77] Ho CK, Khalsa SS. A Photographic Flux Mapping Method for Concentrating Solar Collectors and Receivers. Journal of Solar Energy Engineering 2012;134:041004.

[78] Lüpfert E, Riffelmann K, Price H, Burkholder F, Moss T. Experimental Analysis of Overall Thermal Properties of Parabolic Trough Receivers. Journal of Solar Energy Engineering 2008;130:21007.

[79] Xiao J, Wei X, Lu Z, Yu W, Wu H. A review of available methods for surface shape measurement of solar concentrator in solar thermal power applications. Renewable and Sustainable Energy Reviews 2012;16:2539-44.

[80] Schiricke B, Pitz-Paal R, Lüpfert E, Pottler K, Pfänder M, Riffelmann K et al. Experimental Verification of Optical Modeling of Parabolic Trough Collectors by Flux Measurement. Journal of Solar Energy Engineering 2009;131:011004.

[81] Bortolato M., Dugaria S., Del Col D. Concentrated flux measurement apparatus for an asymmetrical parabolic trough solar concentrator. in ISES SWC 2015 Conference Proceedings 2016.

[82] Lovegrove K, Stein W. Concentrating Solar Power Technology : Principles, Developments and Applications. Cambridge: Woodhead Publishing, 2012.

[83] Hager JM, Simmons S, Smith D, Onishi S, Langley LW, Diller TE. Experimental Performance of a Heat Flux Microsensor. Journal of Engineering for Gas Turbines and Power 1991;113:246-50.

[84] Song X, Huan K, Dong W, Wang J, Zang Y, Shi X. Research on infrared radiation characteristics of Pyromark1200 high-temperature coating. 2014.

[85] Ballestrín J, Ulmer S, Morales A, Barnes A, Langley LW, Rodríguez M. Systematic error in the measurement of very high solar irradiance. Solar Energy Mater Solar Cells 2003;80:375-81.

[86] Vatell Corporation. HFM-6, HFM-7 & HFM-8 Operator's manual – Version 1.0 . 2015.

[87] National Renewable Energy Laboratory. SolTrace. 2012.

[88] Neumann A, Witzke A, Jones SA, Schmitt G. Representative Terrestrial Solar Brightness Profiles. Journal of Solar Energy Engineering 2002;124:198-204.

[89] Bortolato M, Dugaria S, Del Col D. Experimental study of a parabolic trough solar collector with flat bar-and-plate absorber during direct steam generation. Energy 2016;116, Part 1:1039-50.

[90] Montes MJ, Rubbia C, Abbas R, Martínez-Val JM. A comparative analysis of configurations of linear Fresnel collectors for concentrating solar power. Energy 2014;73:192-203.

[91] Zhu G, Wendelin T, Wagner MJ, Kutscher C. History, current state, and future of linear Fresnel concentrating solar collectors. Solar Energy 2014;103:639-52.

[92] Pye J, Morrison GL, Behnia M. Transient Modelling of Cavity Receiver Heat Transfer for the Compact Linear Fresnel Reflector. Jun 14, 2003.

[93] Reynolds DJ, Jance MJ, Behnia M, Morrison GL. An experimental and computational study of the heat loss characteristics of a trapezoidal cavity absorber. Solar Energy 2004;76:229-34.

[94] Wang P, Liu DY, Xu C. Numerical study of heat transfer enhancement in the receiver tube of direct steam generation with parabolic trough by inserting metal foams. Appl Energy 2013;102:449-60.

[95] Muñoz J, Abánades A. Analysis of internal helically finned tubes for parabolic trough design by CFD tools. Applied Energy 2011;88:4139-49.

[96] Cheng ZD, He YL, Cui FQ. Numerical study of heat transfer enhancement by unilateral longitudinal vortex generators inside parabolic trough solar receivers. International Journal of Heat and Mass Transfer 2012;55:5631-41.

[97] Ghadirijafarbeigloo S, Zamzamian AH, Yaghoubi M. 3-D Numerical Simulation of Heat Transfer and Turbulent Flow in a Receiver Tube of Solar Parabolic Trough Concentrator with Louvered Twisted-tape Inserts. Energy Procedia 2014;49:373-80.

[98] Mwesigye A, Bello-Ochende T, Meyer JP. Heat transfer and thermodynamic performance of a parabolic trough receiver with centrally placed perforated plate inserts. Applied Energy 2014;136:989-1003.

[99] Mwesigye A, Bello-Ochende T, Meyer JP. Multi-objective and thermodynamic optimisation of a parabolic trough receiver with perforated plate inserts. Applied Thermal Engineering 2015;77:42-56.

[100] Reddy KS, Ravi Kumar K, Ajay CS. Experimental investigation of porous disc enhanced receiver for solar parabolic trough collector. Renewable Energy 2015;77:308-19.

[101] Rojas ME, de Andrés MC, González L. Designing capillary systems to enhance heat transfer in LS3 parabolic trough collectors for direct steam generation (DSG). Solar Energy 2008;82:53-60.

[102] Almanza R, Jiménez G, Lentz A, Valdés A, Soria A. DSG Under Two-Phase and Stratified Flow in a Steel Receiver of a Parabolic Trough Collector. Journal of Solar Energy Engineering 2002;124:140.

[103] Almanza R, Lentz A, Jiménez G. Receiver behavior in direct steam generation with parabolic troughs. Solar Energy 1997;61:275-8.

[104] Flores V, Almanza R. Direct steam generation in parabolic trough concentrators with bimetallic receivers. Energy 2004;29:645-51.

[105] Aldali Y, Muneer T, Henderson D. Solar absorber tube analysis: thermal simulation using CFD. International Journal of Low-Carbon Technologies 2013;8:14-9.

[106] Lambda Research Corporation. TracePro. https://www.lambdares.com/tracepro/

[107] National Renewable Energy Laboratory, (NREL). *SolTrace version 2012.7.9* www.nrel.gov/csp/soltrace. 2012.

[108] Manglik RM, Bergles AE. Heat transfer and pressure drop correlations for the rectangular offset strip fin compact heat exchanger. Experimental Thermal and Fluid Science 1995;10:171-80.

[109] Lemmon EW, Huber ML, McLinden MO. NIST Standard ReferenceDatabase 23: Reference Fluid Thermodynamic and Transport Properties - REFPROP. 9.0. 2010.

[110] Comitè Europeen de Normalisation, (CEN). Solar energy - Solar thermal collectors - Test methods (ISO 9806:2013). 2013.

[111] Xu L, Wang Z, Li X, Yuan G, Sun F, Lei D et al. A comparison of three test methods for determining the thermal performance of parabolic trough solar collectors. Solar Energy 2014;99:11-27.

[112] ANSI/ASHRAE Standard 93-2010 (RA 2014). Methods of testing to determine the thermal performance of solar collectors 2014.

[113] Sardeshpande VR, Chandak AG, Pillai IR. Procedure for thermal performance evaluation of steam generating point-focus solar concentrators. Solar Energy 2011;85:1390-8.

[114] Bouvier J, Michaux G, Salagnac P, Nepveu F, Rochier D, Kientz T. Experimental characterisation of a solar parabolic trough collector used in a micro-CHP (micro-cogeneration) system with direct steam generation. Energy 2015;83:474-85.

[115] Juhasz JR, Simoni LD. A review of potential working fluids for low temperature organic rankine cycles in waste heat recovery. Proceedings of 3rd International Seminar on ORC Power Systems 2015:Paper 177.

[116] Meeker D. Mirage. Steady - State Finite Element Heat Conduction Solver - User’s Manual. 2005.

[117] Forristall R. Heat Transfer Analysis and Modeling of a Parabolic Trough Solar Receiver Implemented in Engineering Equation Solver. 2003.

[118] Özışık MN. Radiative transfer and interactions with conduction and convection. United States, 1973.

[119] Rohsenow WM. Handbook of heat transfer. 3. ed. ed. New York [u.a.]: McGraw-Hill, 1998.

[120] Sparrow EM, Abraham JP, Tong JCK. Archival correlations for average heat transfer coefficients for non-circular and circular cylinders and for spheres in cross-flow. International Journal of Heat and Mass Transfer 2004;47:5285-96.

[121] Liu Z, Winterton RHS. A general correlation for saturated and subcooled flow boiling in tubes and annuli, based on a nucleate pool boiling equation. International Journal of Heat and Mass Transfer 1991;34:2759-66.

[122] Cooper MG. Heat Flow Rates in Saturated Nucleate Pool Boiling-A Wide-Ranging Examination Using Reduced Properties. In: Anonymous Advances in Heat Transfer: Elsevier B.V; 1984, p. 157-239.

[123] Dittus FW, Boelter LMK. Heat transfer in automobile radiators of the tubular type. International Communications in Heat and Mass Transfer 1985;12:3-22.

[124] Friedel L. Improved friction pressure drop correlations for horizontal and vertical two-phase pipe flow. Proceedings of European Two Phase Flow Group Meeting 1979.

[125] Incropera FP, De Witt DP. Introduction to heat transfer. 4. ed. ed. New York [u.a.]: Wiley, 2002.

[126] Gnielinski V. New equations for heat and mass transfer in turbulent pipe and channel flows. International Chemical Engineering 1976;16:359-68.

[127] Angelino G, Gaia M, Macchi E. A review of Italian activity in the field of organicRankine cycles. VDI Berichte - Proceedings of the International VDI Seminar 1984:465-82.

[128] Gaia M. (Keynote lecture) 30 years of ORC development. ORC 2011 - 1st International Seminar on ORC Power Systems M. Gaia. 30 years of ORC development. 2011. Keynote lecture at the ORC2011 - 1st International Seminar on ORC Power Systems - Delft (NL), September 22-23. Availableonline: www.kcorc.org/en/literature/orc2011-proceedings.

[129] Chen H, Goswami DY, Stefanakos EK. A review of thermodynamic cycles and working fluids for the conversion of low-grade heat. Renewable and Sustainable Energy Reviews 2010;14:3059-67.

[130] Saleh B, Koglbauer G, Wendland M, Fischer J. Working fluids for low-temperature organic Rankine cycles. Energy 2007;32:1210-21.

[131] He C, Liu C, Gao H, Xie H, Li Y, Wu S et al. The optimal evaporation temperature and working fluids for subcritical organic Rankine cycle. Energy 2012;38:136-43.

[132] Macchi E, Perdichizzi A. Efficiency prediction for axial-flow turbines operating with non conventional fluids. Journal of Energy power 1981;103:718-24.

[133] Lakew AA, Bolland O. Working fluids for low-temperature heat source. Applied Thermal Engineering 2010;30:1262-8.

[134] Kontomaris K. Organic Rankine Cycle System Analysis for Low GWP Working Fluids. Proceeding of 15th International Refrigeration and Air Conditioning Conference 2014.

[135] Regulation (EU) No 517/2014 of the European Parliament and of the Council of 16 April 2014 on fluorinated greenhouse gases and repealing Regulation (EC) No 842/2006 Text with EEA relevance. 2014.

[136] ASHRAE publishes 2010 editions of refrigerant safety standards. Frozen Food Digest 2010;26:18.

[137] Datla BV, Brasz J. Organic Rankine Cycle System Analysis for Proceedings of International Refrigeration and Air Conditioning Conference 2012.

Low GWP Working Fluids.

[138] Cataldo F, Mastrullo R, Mauro AW, Vanoli GP. Fluid selection of Organic Rankine Cycle for low-temperature waste heat recovery based on thermal optimization. Energy 2014;72:159-67.

[139] Orosz M, Mueller A, Quoilin S, Hemond H. Small Scale Solar ORC system for distributed power. 2009.

[140] Rayegan R, Tao YX. A procedure to select working fluids for Solar Organic Rankine Cycles (ORCs). Renewable Energy 2011;36:659-70.

[141] LI D, ZHANG S, WANG G. Selection of organic Rankine cycle working fluids in the low-temperature waste heat utilization. Journal of Hydrodynamics, Ser. B 2015;27:458-64.

[142] Peris B, Navarro-Esbri J, Moles F, Gonzalez, Mota-Babiloni A. Experimental characterization of an ORC (organic Rankine cycle) for power and CHP (combined heat and power) applications from low grade heat sources. Energy 2015;82:269-76.

[143] Molés F, Navarro-Esbrí J, Peris B, Mota-Babiloni A, Barragán-Cervera Á, Kontomaris K(. Low GWP alternatives to HFC-245fa in Organic Rankine Cycles for low temperature heat recovery: HCFO-1233zd-E and HFO-1336mzz-Z. Applied Thermal Engineering 2014;71:204-12.

[144] Molés F, Navarro-Esbrí J, Peris B, Mota-Babiloni A, Barragán-Cervera Á, Kontomaris K(. Low GWP alternatives to HFC-245fa in Organic Rankine Cycles for low temperature heat recovery: HCFO-1233zd-E and HFO-1336mzz-Z. Applied Thermal Engineering 2014;71:204-12.

[145] Datla BV, Brasz J. Comparing R1233zd and R245fa for low temperature ORC applications. Proceeding of international refrigeration and air conditioning conference 2014.

[146] Eyerer S, Wieland C, Vandersickel A, Spliethoff H. Experimental study of an ORC (Organic Rankine Cycle) and analysis of R1233zd-E as a drop-in replacement for R245fa for low temperature heat utilization. Energy 2016;103:660-71.

[147] Molés F, Navarro-Esbrí J, Peris B, Mota-Babiloni A. Experimental evaluation of HCFO-1233zd-E as HFC-245fa replacement in an Organic Rankine Cycle system for low temperature heat sources. Applied Thermal Engineering 2016;98:954-61.

[148] Guillaume L, Legros A, Desideri A, Lemort V. Performance of a radial-inflow turbine integrated in an ORC system and designed for a WHR on truck application: An experimental comparison between R245fa and R1233zd. Applied Energy 2017;186:408-22.

[149] Weiss AP. Volumetric expander versus turbine - which is the better choice for small ORC plants. Proceeding of 3rd International Seminar on ORC Power Systems.

[150] Branchini L, De Pascale A, Peretto A. Systematic comparison of ORC configurations by means of comprehensive performance indexes. Applied Thermal Engineering 2013;61:129-40.

[151] Glavatskaya Y, Podevin P, Lemort V, Shonda O, Descombes G. Reciprocating Expander for an Exhaust Heat Recovery Rankine Cycle for a Passenger Car Application. Energies 2012;5:1751-65.

[152] Lemort V, Guillaume L, Legros A, Declaye S, Quoilin S. A comparison of piston, screw and scroll expanders for small scale Rankine cycle systems. Apr 2013.

[153] Astolfi M. Techno-economic Optimization of Low Temperature CSP Systems Based on ORC with Screw Expanders. Energy Procedia 2015;69:1100-12.

[154] Bao J, Zhao L. A review of working fluid and expander selections for organic Rankine cycle. Renewable and Sustainable Energy Reviews 2013;24:325-42.

[155] Badr O, O'Callaghan PW, Hussein M, Probert SD. Multi-vane expanders as prime movers for low-grade energy organic Rankine-cycle engines. Applied Energy 1984;16:129-46.

[156] Badr O, Naik S, O'Callaghan PW, Probert SD. Expansion machine for a low power-output steam Rankine-cycle engine. Applied Energy 1991;39:93-116.

[157] Kane M, Larrain D, Favrat D, Allani Y. Small hybrid solar power system. Energy 2003;28:1427-43.

[158] Lemort V. Contribution to the Characterization of Scroll Machines in Compressor and Expander Modes. 2008.

[159] Quoilin S, Declaye S, Lemort V. Expansion Machine and fluid selection for the Organic Rankine Cycle. Jul 2010.

[160] Singh R, Srinivasan J. Modified refrigerant compressor as a reciprocating engine for solar thermal power generation. International Journal of Energy Research 1988;12:69-74.

[161] Dunbar MK. Altering the volumetric expansion ratio of a Lysholm helical screw expander. 1984.

[162] Stošić N. Review Article: Screw Compressors in Refrigeration and Air Conditioning. HVAC&R Research 2004;10:233-63.

[163] Leibowitz H, Smith IK, Stošic N. Cost effective small scale ORC Systems for power recovery from low grade heat sources. Proceedings of IMECE2006 ASME International Mechanical Engineering Congress and Exposition.

[164] Heliex Power. http://www.heliexpower.com/

[165] ElectraTherm. https://electratherm.com/

[166] Quoilin S, Lemort V, Lebrun J. Experimental study and modeling of an Organic Rankine Cycle using scroll expander. Applied Energy 2010;87:1260-8.

[167] Eneftech Innovation SA. http://www.eneftech.com/

[168] Eck M, Zarza E, Eickhoff M, Rheinländer J, Valenzuela L. Applied research concerning the direct steam generation in parabolic troughs. Solar Energy 2003;74:341-51.

[169] Delgado-Torres AM, García-Rodríguez L. Comparison of solar technologies for driving a desalination system by means of an organic Rankine cycle. Desalination 2007;216:276-91.

[170] Baral S, Kim D, Yun E, Kim KC. Experimental and Thermoeconomic Analysis of Small-Scale Solar Organic Rankine Cycle (SORC) System. Entropy 2015;17:2039-61.

[171] NREL – CSP. https://www.nrel.gov/csp/

[172] Vélez F, Segovia J, Martín C, Antolín G, Chejne F, Quijano A. A technical, economical and market review of Organic Rankine Cycles for the conversion of low-grade heat for power generation. Renewable and Sustainable Energy Reviews 2012;16:4175-89.

[173] Pikra G, Salim A, Prawara B, Purwanto AJ, Admono T, Eddy Z. Development of Small Scale Concentrated Solar Power Plant Using Organic Rankine Cycle for Isolated Region in Indonesia. Energy Procedia 2013;32:122-8.

[174] Enrico Bocci, Mauro Villarini, Luca Bove, Stefano Esposto, Valerio Gasperini. Modeling Small Scale Solar-powered ORC Unit for Standalone Application. Mathematical Problems in Engineering 2012;2012:1-10.

[175] Lemort V, Quoilin S, Cuevas C, Lebrun J. Testing and modeling a scroll expander integrated into an Organic Rankine Cycle. Applied Thermal Engineering 2009;29:3094-102.

[176] Quoilin S, Orosz M, Hemond H, Lemort V. Performance and design optimization of a low-cost solar organic Rankine cycle for remote power generation. Solar Energy 2011;85:955-66.

[177] Quoilin S, Lemort V, Lebrun J. Experimental study and modeling of an Organic Rankine Cycle using scroll expander. Applied Energy 2010;87:1260-8.

[178] SAITOH T, YAMADA N, WAKASHIMA S. Solar Rankine Cycle System Using Scroll Expander. Journal of Environment and Engineering 2007;2:708-19.

[179] Wang XD, Wang JL, Zhao XZ, Zhao L, Zhang WZ, Wu W. Performance evaluation of a low-temperature solar Rankine cycle system utilizing R245fa. Solar Energy 2010;84:353-64.

[180] Wang XD, Wang JL, Zhao L. Experimental investigation on the low-temperature solar Rankine cycle system using R245fa. Energy Conversion and Management 2011;52:946-52.

[181] Wang JL, Wang XD, Zhao L. An experimental study on the recuperative low temperature solar Rankine cycle using R245fa. Applied Energy 2012;94:34-40.

[182] Helvaci HU, Khan ZA. Experimental study of thermodynamic assessment of a small scale solar thermal system. Energy Conversion and Management 2016;117:567-76.

[183] Delgado-Torres AM, García-Rodríguez L. Analysis and optimization of the low-temperature solar organic Rankine cycle (ORC). Energy Conversion and Management 2010;51:2846-56.

[184] Delgado-Torres AM, García-Rodríguez L. Design recommendations for solar organic Rankine cycle (ORC)–powered reverse osmosis (RO) desalination. Renewable and Sustainable Energy Reviews 2012;16:44-53.

[185] Clemente S, Micheli D, Reini M, Taccani R. Energy efficiency analysis of Organic Rankine Cycles with scroll expanders for cogenerative applications. Applied Energy 2012;97:792-801.

[186] Mago PJ, Chamra LM, Srinivasan K, Somayaji C. An examination of regenerative organic Rankine cycles using dry fluids. Applied Thermal Engineering 2008;28:998-1007.

[187] Martin H. A theoretical approach to predict the performance of chevron-type plate heat exchangers. Chemical Engineering & Processing: Process Intensification 1996;35:301-10.

[188] Amalfi RL, Vakili-Farahani F, Thome JR. Flow boiling and frictional pressure gradients in plate heat exchangers. Part 1: Review and experimental database. International Journal of Refrigeration 2016;61:166-84.

[189] Amalfi RL, Vakili-Farahani F, Thome JR. Flow boiling and frictional pressure gradients in plate heat exchangers. Part 2: Comparison of literature methods to database and new prediction methods. International Journal of Refrigeration 2016;61:185-203.

[190] Longo GA, Zilio C, Righetti G. Condensation of the low GWP refrigerant HFC152a inside a Brazed Plate Heat Exchanger. Experimental Thermal and Fluid Science 2015;68:509-15.

[191] Webb RL. Convective Condensation of Superheated Vapor. Journal of Heat Transfer 1998;120:418.

[192] Ng KC, Bong TY, Lim TB. A thermodynamic model for the analysis of screw expander performance. Heat Recovery Systems and CHP 1990;10:119-33.

[193] Ng KC, Lim TB, Bong TY. Analysis of screw-expander performance. Journal of process mechanical engineering 1988.

[194] Bamgbopa MO, Uzgoren E. Quasi-dynamic model for an organic Rankine cycle. Energy Conversion & Management 2013;72:117-24.

[195] Mayekawa Manufacturing Co.

[196] Quoilin S, Orosz M, Hemond H, Lemort V. Performance and design optimization of a low-cost solar organic Rankine cycle for remote power generation. Solar Energy 2011;85:955-66.

[197] Ibarra M, Rovira A, Alarcón-Padilla DC, Zaragoza G, Blanco J. Performance of a 5 kWe Solar-only Organic Rankine Unit Coupled to a Reverse Osmosis Plant. Energy Procedia 2014;49:2251-60.

[198] Jeter SM. Maximum conversion efficiency for the utilization of direct solar radiation. Solar Energy 1981;26:231-6.

[199] Spanner DC. Introduction to thermodynamics. , 1964.

[200] Petela R. Exergy of undiluted thermal radiation. Solar Energy 2003;74:469-88.

[201] Bejan A. Advanced engineering thermodynamics. 3. ed. ed. Hoboken, NJ: Wiley, 2006.

[202] Tchanche BF, Papadakis G, Lambrinos G, Frangoudakis A. Fluid selection for a low-temperature solar organic Rankine cycle. Applied Thermal Engineering 2009;29:2468-76.

[203] Barse KA, Mann MD. Maximizing ORC performance with optimal match of working fluid with system design. Applied Thermal Engineering 2016;100:11-9.

[204] Javadi FS, Saidur R, Kamalisarvestani M. Investigating performance improvement of solar collectors by using nanofluids. Renewable and Sustainable Energy Reviews 2013;28:232-45.

[205] Del Col D, Padovan A, Bortolato M, Dai Prè M, Zambolin E. Thermal performance of flat plate solar collectors with sheet-and-tube and roll-bond absorbers. Energy 2013;58:258-69.

[206] Taylor RA, Phelan PE, Otanicar TP, Walker CA, Nguyen M, Trimble S et al. Applicability of nanofluids in high flux solar collectors. Journal of Renewable and Sustainable Energy 2011;3:15.

[207] Arai N, Itaya Y, Hasatani M. Development of a “volume heat-trap” type solar collector using a fine-particle semitransparent liquid suspension (FPSS) as a heat vehicle and heat storage medium Unsteady, one-dimensional heat transfer in a horizontal FPSS layer heated by thermal radiation. Solar Energy 1984;32:49-56.

[208] Minardi JE, Chuang HN. Performance of a “black” liquid flat-plate solar collector. Solar Energy 1975;17:179-83.

[209] Celata GP, D’Annibale F, Mariani A, Sau S, Serra E, Bubbico R et al. Experimental results of nanofluids flow effects on metal surfaces. Chem Eng Res Design 2014;92:1616-28.

[210] Choi SUS, Eastman JA. Enhancing thermal conductivity of fluids with nanoparticles. ASME FED 1995;231:99-103.

[211] Buongiorno J. Convective Transport in Nanofluids. Journal of Heat Transfer 2005;128:240-50.

[212] Taylor R, Coulombe S, Otanicar T, Phelan P, Gunawan A, Lv W et al. Small particles, big impacts: A review of the diverse applications of nanofluids. J Appl Phys 2013;113:011301.

[213] Lomascolo M, Colangelo G, Milanese M, de Risi A. Review of heat transfer in nanofluids: Conductive, convective and radiative experimental results. Renewable and Sustainable Energy Reviews 2015;43:1182-98.

[214] Kakaç S, Pramuanjaroenkij A. Single-phase and two-phase treatments of convective heat transfer enhancement with nanofluids – A state-of-the-art review. International Journal of Thermal Sciences 2016;100:75-97.

[215] Witharana S, Chen H, Ding Y. Stability of nanofluids in quiescent and shear flow fields. Nanoscale Research Letters 2011;6:231.

[216] Chen H, Witharana S, Jin Y, Kim C, Ding Y. Predicting thermal conductivity of liquid suspensions of nanoparticles (nanofluids) based on rheology. Particuology 2009;7:151-7.

[217] Mohamad AA. Myth about nano-fluid heat transfer enhancement. International Journal of Heat and Mass Transfer 2015;86:397-403.

[218] Otanicar TP, Phelan PE, Golden JS. Optical properties of liquids for direct absorption solar thermal energy systems. Solar Energy 2009;83:969-77.

[219] Leong KY, Ong HC, Amer NH, Norazrina MJ, Risby MS, Ku Ahmad KZ. An overview on current application of nanofluids in solar thermal collector and its challenges. Renewable and Sustainable Energy Reviews 2016;53:1092-105.

[220] Gorji TB, Ranjbar AA. A review on optical properties and application of nanofluids in direct absorption solar collectors (DASCs). Renewable and Sustainable Energy Reviews 2017;72:10-32.

[221] Sajid Hossain M, Saidur R, Mohd Sabri MF, Said Z, Hassani S. Spotlight on available optical properties and models of nanofluids: A review. Renewable and Sustainable Energy Reviews 2015;43:750-62.

[222] Otanicar TP, Phelan PE, Prasher RS, Rosengarten G, Taylor RA. Nanofluid-based direct absorption solar collector. Journal of Renewable and Sustainable Energy 2010;2:033102.

[223] Noguez C. Optical properties of isolated and supported metal nanoparticles. Optical Materials 2005;27:1204-11.

[224] Taylor R, Phelan P, Otanicar T, Adrian R, Prasher R. Nanofluid optical property characterization: towards efficient direct absorption solar collectors. Nanoscale Res Lett 2011;6:1-11.

[225] Saidur R, Leong KY, Mohammad HA. A review on applications and challenges of nanofluids. Renewable and Sustainable Energy Reviews 2011;15:1646-68.

[226] Gan Y, Qiao L. Radiation-enhanced evaporation of ethanol fuel containing suspended metal nanoparticles. International Journal of Heat and Mass Transfer 2012;55:5777-82.

[227] He Q, Wang S, Zeng S, Zheng Z. Experimental investigation on photothermal properties of nanofluids for direct absorption solar thermal energy systems. Energy Conversion and Management 2013;73:150-7.

[228] Zhu Q, Cui Y, Mu L, Tang L. Characterization of Thermal Radiative Properties of Nanofluids for Selective Absorption of Solar Radiation. Int J Thermophys 2013;34:2307-21.

[229] Zhang L, Liu J, He G, Ye Z, Fang X, Zhang Z. Radiative properties of ionic liquid-based nanofluids for medium-to-high-temperature direct absorption solar collectors. Solar Energy Materials and Solar Cells 2014;130:521-8.

[230] Sajid MH, Said Z, Saidur R, Adikan FRM, Sabri MFM, Rahim NA. A time variant investigation on optical properties of water based Al2O3 nanofluid. International Communications in Heat and Mass Transfer 2014;50:108-16.

[231] Said Z, Saidur R, Rahim NA. Optical properties of metal oxides based nanofluids. International Communications in Heat and Mass Transfer 2014;59:46-54.

[232] Milanese M, Colangelo G, Cretì A, Lomascolo M, Iacobazzi F, de Risi A. Optical absorption measurements of oxide nanoparticles for application as nanofluid in direct absorption solar power systems – Part I: Water-based nanofluids behavior. Solar Energy Materials and Solar Cells 2016;147:315-20.

[233] Karami M, Akhavan-Behabadi MA, Raisee Dehkordi M, Delfani S. Thermo-optical properties of copper oxide nanofluids for direct absorption of solar radiation. Solar Energy Materials and Solar Cells 2016;144:136-42.

[234] Song D, Wang Y, Jing D, Geng J. Investigation and prediction of optical properties of alumina nanofluids with different aggregation properties. International Journal of Heat and Mass Transfer 2016;96:430-7.

[235] Han D, Meng Z, Wu D, Zhang C, Zhu H. Thermal properties of carbon black aqueous nanofluids for solar absorption. Nanoscale Research Letters 2011;6:457.

[236] Poinern GEJ, Brundavanam S, Shah M, Laava I, Fawcett D. Photothermal response of CVD synthesized carbon (nano)spheres/aqueous nanofluids for potential application in direct solar absorption collectors: a preliminary investigation. Nanotechnology, science and applications 2012;5:49-59.

[237] Lee S, Jang SP. Extinction coefficient of aqueous nanofluids containing multi-walled carbon nanotubes. International Journal of Heat and Mass Transfer 2013;67:930-5.

[238] Meng Z, Wu D, Wang L, Zhu H, Li Q. Carbon nanotube glycol nanofluids: Photo-thermal properties, thermal conductivities and rheological behavior. Particuology 2012;10:614-8.

[239] He Y, Wang S, Ma J, Tian F, Ren Y. Experimental Study on the Light-Heat Conversion Characteristics of Nanofluids. Nanoscience and Nanotechnology Letters 2011;3:494-6.

[240] Karami M, Akhavan Bahabadi MA, Delfani S, Ghozatloo A. A new application of carbon nanotubes nanofluid as working fluid of low-temperature direct absorption solar collector. Solar Energy Materials and Solar Cells 2014;121:114-8.

[241] Hordy N, Rabilloud D, Meunier J, Coulombe S. High temperature and long-term stability of carbon nanotube nanofluids for direct absorption solar thermal collectors. Solar Energy 2014;105:82-90.

[242] Liu J, Ye Z, Zhang L, Fang X, Zhang Z. A combined numerical and experimental study on graphene/ionic liquid nanofluid based direct absorption solar collector. Solar Energy Mater Solar Cells 2015;136:177-86.

[243] Xuan Y, Duan H, Li Q. Enhancement of solar energy absorption using a plasmonic nanofluid based on TiO2/Ag composite nanoparticles. RSC Advances 2014;4:16206.

[244] Wu Y, Zhou L, Du X, Yang Y. Optical and thermal radiative properties of plasmonic nanofluids containing core–shell composite nanoparticles for efficient photothermal conversion. International Journal of Heat and Mass Transfer 2015;82:545-54.

[245] Menbari A, Alemrajabi AA, Rezaei A. Heat transfer analysis and the effect of CuO/Water nanofluid on direct absorption concentrating solar collector. Appl Therm Eng 2016;104:176-83.

[246] Menbari A, Alemrajabi AA. Analytical modeling and experimental investigation on optical properties of new class of nanofluids (Al2O3-CuO binary nanofluids) for direct absorption solar thermal energy. Optical Materials 2016;52:116-25.

[247] Yudasaka M, Iijima S, Crespi VH. Single-Wall Carbon Nanohorns and Nanocones. In: Jorio A, Dresselhaus G, Dresselhaus MS, editors. Carbon Nanotubes. Topics in Applied Physics (vol 111), Berlin, Heidelberg: Springer; 2001.

[248] Kasuya D, Yudasaka M, Takahashi K, Kokai F, Iijima S. Selective Production of Single-Wall Carbon Nanohorn Aggregates and Their Formation Mechanism. J Phys Chem B 2002;106:4947-51.

[249] Carbonium Srl. http://www.carbonium.it/

[250] Karousis N, Suarez-Martinez I, Ewels CP, Tagmatarchis N. Structure, Properties, Functionalization, and Applications of Carbon Nanohorns. Chem Rev 2016;116:4850-83.

[251] Zhang Z, Han S, Wang C, Li J, Xu G. Single-Walled Carbon Nanohorns for Energy Applications. Nanomaterials 2015;5.

[252] Sani E, Barison S, Pagura C, Mercatelli L, Sansoni P, Fontani D et al. Carbon nanohorns-based nanofluids as direct sunlight absorbers. Opt Express 2010;18:5179-87.

[253] Sani E, Mercatelli L, Barison S, Pagura C, Agresti F, Colla L et al. Potential of carbon nanohorn-based suspensions for solar thermal collectors. Solar Energy Mater Solar Cells 2011;95:2994-3000.

[254] Mercatelli L, Sani E, Giannini A, Di Ninni P, Martelli F, Zaccanti G. Carbon nanohorn-based nanofluids: characterization of the spectral scattering albedo. Nanoscale Research Letters 2012;7:96.

[255] Mercatelli L, Sani E, Fontani D, Zaccanti G, Martelli F, Di Ninni P. Scattering and absorption properties of carbon nanohorn-based nanofluids for solar energy applications. Journal of the European Optical Society - Rapid publications 2011;6.

[256] Moradi A, Sani E, Simonetti M, Francini F, Chiavazzo E, Asinari P. Carbonnanohorn based nanofluids for a direct absorption solar collector for civil application. Journal of Nanoscience and Nanotechnologies 15 2015:3488-95.

[257] Fedele L, Colla L, Bobbo S, Barison S, Agresti F. Experimental stability analysis of different water-based nanofluids. Nanoscale Research Letters 2011;6:300.

[258] Bobbo S, Fedele L, Benetti A, Colla L, Fabrizio M, Pagura C et al. Viscosity of water based SWCNH and TiO2 nanofluids. Experimental Thermal and Fluid Science 2012;36:65-71.

[259] Mahian O, Kianifar A, Kalogirou SA, Pop I, Wongwises S. A review of the applications of nanofluids in solar energy. International Journal of Heat and Mass Transfer 2013;57:582-94.

[260] Verma SK, Tiwari AK. Progress of nanofluid application in solar collectors: A review. Energy Conversion and Management 2015;100:324-46.

[261] Sarsam WS, Kazi SN, Badarudin A. A review of studies on using nanofluids in flat-plate solar collectors. Solar Energy 2015;122:1245-65.

[262] Muhammad MJ, Muhammad IA, Che Sidik NA, Muhammad Yazid, Muhammad Noor Afiq Witri. Thermal performance enhancement of flat-plate and evacuated tube solar collectors using nanofluid: A review. International Communications in Heat and Mass Transfer;76:6-15.

[263] Bozorgan N, Shafahi M. Performance evaluation of nanofluids in solar energy: a review of the recent literature. Micro and Nano Syst Lett 2015;3:1-15.

[264] Abdin Z, Alim MA, Saidur R, Islam MR, Rashmi W, Mekhilef S et al. Solar energy harvesting with the application of nanotechnology. Renewable and Sustainable Energy Reviews 2013;26:837-52.

[265] Nagarajan PK, Subramani J, Suyambazhahan S, Sathyamurthy R. Nanofluids for Solar Collector Applications: A Review. Energy Procedia 2014;61:2416-34.

[266] Hussein AK. Applications of nanotechnology in renewable energies—A comprehensive overview and understanding. Renewable and Sustainable Energy Reviews 2015;42:460-76.

[267] Tyagi H, Phelan P, Prasher R. Predicted Efficiency of a Low-Temperature Nanofluid-Based Direct Absorption Solar Collector. Journal of Solar Energy Engineering 2009;131:41004.

[268] Khullar V, Tyagi H. Enhancing optical efficiency of a linear parabolic solar collector through nanofluids. AIP Conference Proceedings1391 2011:353-5.

[269] Khullar V, Tyagi H, Phelan P, Otanicar T, Singh H, Taylor R. Solar Energy Harvesting Using Nanofluids-Based Concentrating Solar Collector. Journal of Nanotechnology in Engineering and Medicine (Transactions of the ASME) 2012;3:1-9.

[270] Veeraragavan A, Lenert A, Yilbas B, Al-Dini S, Wang EN. Analytical model for the design of volumetric solar flow receivers. International Journal of Heat and Mass Transfer 2012;55:556-64.

[271] Ladjevardi SM, Asnaghi A, Izadkhast PS, Kashani AH. Applicability of graphite nanofluids in direct solar energy absorption. Solar Energy 2013;94:327-34.

[272] de Risi A, Milanese M, Laforgia D. Modelling and optimization of transparent parabolic trough collector based on gas-phase nanofluids. Renewable Energy 2013;58:134-9.

[273] Luo Z, Wang C, Wei W, Xiao G, Ni M. Performance improvement of a nanofluid solar collector based on direct absorption collection (DAC) concepts. International Journal of Heat and Mass Transfer 2014;75:262-71.

[274] Rahman MM, Mojumder S, Saha S, Mekhilef S, Saidur R. Effect of solid volume fraction and tilt angle in a quarter circular solar thermal collectors filled with CNT–water nanofluid. International Communications in Heat and Mass Transfer 2014;57:79-90.

[275] Parvin S, Nasrin R, Alim MA. Heat transfer and entropy generation through nanofluid filled direct absorption solar collector. International Journal of Heat and Mass Transfer 2014;71:386-95.

[276] Hewakuruppu YL, Taylor RA, Tyagi H, Khullar V, Otanicar T, Coulombe S et al. Limits of selectivity of direct volumetric solar absorption. Solar Energy 2015;114:206-16.

[277] Cregan V, Myers TG. Modelling the efficiency of a nanofluid direct absorption solar collector. International Journal of Heat and Mass Transfer 2015;90:505-14.

[278] Gorji TB, Ranjbar AA. Geometry optimization of a nanofluid-based direct absorption solar collector using response surface methodology. Solar Energy 2015;122:314-25.

[279] Chen M, He Y, Zhu J, Wen D. Investigating the collector efficiency of silver nanofluids based direct absorption solar collectors. Applied Energy 2016;181:65-74.

[280] Delfani S, Karami M, Behabadi MAA. Performance characteristics of a residential-type direct absorption solar collector using MWCNT nanofluid. Renewable Energy 2016;87, Part 1:754-64.

[281] Gorji TB, Ranjbar AA. A numerical and experimental investigation on the performance of a low-flux direct absorption solar collector (DASC) using graphite, magnetite and silver nanofluids. Solar Energy 2016;135:493-505.

[282] Jeon J, Park S, Lee BJ. Analysis on the performance of a flat-plate volumetric solar collector using blended plasmonic nanofluid. Solar Energy 2016;132:247-56.

[283] Jin H, Lin G, Bai L, Amjad M, Bandarra Filho EP, Wen D. Photothermal conversion efficiency of nanofluids: An experimental and numerical study. Solar Energy 2016;139:278-89.

[284] Lee S, Choi TJ, Jang SP. Thermal efficiency comparison: Surface-based solar receivers with conventional fluids and volumetric solar receivers with nanofluids. Energy 2016;115, Part 1:404-17.

[285] Li Q, Zheng C, Mesgari S, Hewkuruppu YL, Hjerrild N, Crisostomo F et al. Experimental and numerical investigation of volumetric versus surface solar absorbers for a concentrated solar thermal collector. Solar Energy 2016;136:349-64.

[286] American Society for Testing and Materials, (ASTM). Standard Tables for Reference Solar Spectral Irradiances: Direct Normal and Hemispherical on 37° Tilted Surface (ASTM G173–03). 2003.

[287] Lenert A, Wang EN. Optimization of nanofluid volumetric receivers for solar thermal energy conversion. Solar Energy 2012;86:253-65.

[288] Chen M, He Y, Huang J, Zhu J. Synthesis and solar photo-thermal conversion of Au, Ag, and Au-Ag blended plasmonic nanoparticles. Energy Conversion and Management 2016;127:293-300.

[289] Bandarra Filho EP, Mendoza OSH, Beicker CLL, Menezes A, Wen D. Experimental investigation of a silver nanoparticle-based direct absorption solar thermal system. Energy Conversion and Management 2014;84:261-7.

[290] Chen M, He Y, Huang J, Zhu J. Investigation into Au nanofluids for solar photothermal conversion. Int J Heat Mass Transfer 2017;108, Part B:1894-900.

[291] Xu G, Zhao S, Zhang X, Zhou X. Experimental thermal evaluation of a novel solar collector using magnetic nano-particles. Energy Conversion and Management 2016;130:252-9.

[292] Wang X, He Y, Cheng G, Shi L, Liu X, Zhu J. Direct vapor generation through localized solar heating via carbon-nanotube nanofluid. Energy Conversion and Management 2016;130:176-83.

[293] Ni G, Miljkovic N, Ghasemi H, Huang X, Boriskina SV, Lin C et al. Volumetric solar heating of nanofluids for direct vapor generation. Nano Energy 2015;17:290-301.

[294] Jin H, Lin G, Bai L, Zeiny A, Wen D. Steam generation in a nanoparticle-based solar receiver. Nano Energy 2016;28:397-406.

[295] Fu Y, Mei T, Wang G, Guo A, Dai G, Wang S et al. Investigation on enhancing effects of Au nanoparticles on solar steam generation in graphene oxide nanofluids. Appl Therm Eng 2017;114:961-8.

[296] Gupta HK, Agrawal GD, Mathur J. An experimental investigation of a low temperature Al2O3-H2O nanofluid based direct absorption solar collector. Solar Energy 2015;118:390-6.

[297] Karami M, Akhavan-Bahabadi MA, Delfani S, Raisee M. Experimental investigation of CuO nanofluid-based Direct Absorption Solar Collector for residential applications. Renewable and Sustainable Energy Reviews 2015;52:793-801.

[298] Vakili M, Hosseinalipour SM, Delfani S, Khosrojerdi S, Karami M. Experimental investigation of graphene nanoplatelets nanofluid-based volumetric solar collector for domestic hot water systems. Solar Energy 2016;131:119-30.

[299] Leong KY, Ong HC, Amer NH, Norazrina MJ, Risby MS, Ku Ahmad KZ. An overview on current application of nanofluids in solar thermal collector and its challenges. Renewable and Sustainable Energy Reviews 2016;53:1092-105.

[300] Muraleedharan M, Singh H, Suresh S, Udayakumar M. Directly absorbing Therminol-Al2O3 nano heat transfer fluid for linear solar concentrating collectors. Solar Energy 2016;137:134-42.

[301] Jeon J, Park S, Lee BJ. Analysis on the performance of a flat-plate volumetric solar collector using blended plasmonic nanofluid. Solar Energy 2016;132:247-56.

[302] Maïga SEB, Palm SJ, Nguyen CT, Roy G, Galanis N. Heat transfer enhancement by using nanofluids in forced convection flows. International Journal of Heat and Fluid Flow 2005;26:530-46.

[303] Dugaria S, Bortolato M, Del Col D. Nanofluids application in direct absorption solar collectors: review and numerical model. in Proceeding of ECOS 2016 - The 29th international conference on efficiency, cost, optimization, simulation and environmental impact of energy systems ECOS, June 19-23, Portoroz, Slovenia 2016;Paper 469.

[304] ANSYS Incorporated. Ansys Fluent - Theory Guide, Release 13.0. 2010.

[305] Moghimi MA, Craig KJ, Meyer JP. A novel computational approach to combine the optical and thermal modelling of Linear Fresnel Collectors using the finite volume method. Solar Energy 2015;116:407-27.

[306] Modest MF. Chapter 10 - The Radiative Transfer Equation in Participating Media (RTE). In: Modest MF, editor. Radiative Heat Transfer (Third Edition), Boston: Academic Press; 2013, p. 279-302.

[307] Gülhan A, Braun S. An experimental study on the efficiency of transpiration cooling in laminar and turbulent hypersonic flows. Exp Fluids 2011;50:509-25.

[308] Dugaria S, Bortolato M, Del Col D. Modelling of a direct absorption solar receiver using carbon nanotube nanofluids under concentrated solar radiation. Renewable Energy 2017.

[309] MAURO SCHIAVON. Device and method for production of carbon nanotubes, fullerene and their derivatives. 2006.

[310] Bortolato M, Dugaria S, Agresti F, Barison S, Fedele L, Sani E et al. Investigation of a single-wall carbon nanohorn-based nanofluid in a full-scale direct absorption parabolic trough solar collector. Energy Conversion and Management 2017;150:693-703.

[311] Sani E, Dell'Oro A. Optical constants of ethylene glycol over an extremely wide spectral range. Optical Materials 2014;37:36-41.

[312] Hu J, Zeng H, Wang C, Li Z, Kan C, Liu Y. Interband small pi] plasmon of graphene: strong small-size and field-enhancement effects. Phys Chem Chem Phys 2014;16:23483-91.